GHENT UNIVERSITY

FACULTY OF SCIENCES

ATOMIC LAYER DEPOSITION FOR LITHIUM-ION BATTERIES

FELIX MATTELAER

Members of the Jury:

Dr. Ville Miikkulainen (University of Helsinki)
Dr. Geert Rampelberg (Ghent University)
Prof. Dr. Jan Ryckebusch (Ghent University, chair)
Prof. Dr. Mohammadhosein Safari (UHasselt)
Prof. Dr. Katrien Strubbe (Ghent University)
Prof. Dr. Philippe Vereecken (KU Leuven & imec)

Promotors:
Dr. Jolien Dendooven
Prof. Dr. Christophe Detavernier

Thesis submitted for the degree of
Doctor in Sciences: Physics
May 2017

CONTENTS

Part I

PREFACE

FOREWORD

The uses of atomic layer deposition as a thin-film deposition technique in the field of lithium-ion batteries are investigated in this thesis. The driving force behind this work has been SOS-Lion, a cross-university SBO project spanning the four years from 2013 to 2016 meant to investigate all-solid-state 3D thin-film lithium-ion batteries. However, the findings in this work can be applied to more than that application, and aid in the development of better lithium-ion batteries or beyond lithium-ion batteries.

The work presented here was primarily carried out at the Department of Solid State Sciences in Ghent University, and more specifically at the CoCooN research group under the supervision of prof. Christophe Detavernier and dr. Jolien Dendooven from end 2012 to the beginning of 2017.

The results of this research are published in 6 peer-reviewed publications, which make up the bulk of this thesis. A broad introduction chapter and a general experimental chapter are presented to initiate the reader into the world of energy storage in batteries, and experimental techniques in solid state sciences. The results are split into two parts, ALD for lithium-ion battery electrodes (papers 1-4) and ALD for lithium-ion battery surface modifications (papers 5-6), which both contain the respective papers and introductory chapters to provide a broader background, literature study and a brief summary of the highlights of the papers.

I hope to have succeeded in presenting my work in a coherent and interesting way for both specialist and novel readers alike, and that it may inspire young researchers after me to further dig into these topics.

Enjoy!

Felix Mattelaer
May, 2017

NEDERLANDSE SAMENVATTING

INTRODUCTIE EN DOELSTELLINGEN

Lithium-ion batterijen (LIB) zijn tegenwoordig het hart van de meeste elektronica. Ze zijn zeer breed toepasbaar, wat blijkt uit hun gebruik gaande van energieopslag op grote schaal zoals net-opslag en uitbalanceren van energieproductie, over elektrische en hybride wagens, tot elektrisch gereedschap en draagbare elektronica zoals laptops en smartphones. Daarnaast duiken echter nieuwe toepassingen op voor kleinere lithium-ion batterijen: energieopslag op microchips, bijvoorbeeld bij autonome sensoren en in implantaten. Nieuwe trends zoals nano-architecturen en het afstappen van vloeibare componenten in de batterij duiken op om aan deze recente toepassingen te voldoen. Daarbovenop moet zowel de gevestigde als nieuwe batterijchemie voldoen aan steeds strengere eisen zoals een betere levensduur van de batterij, sneller op- en ontladen, betere veiligheid en biocompatibiliteit.

Atomaire laag depositie (ALD) is een depositietechniek waarbij dunne films worden gegroeid uit opeenvolgende gas-oppervlak interacties. Deze interacties zijn zelf-terminerend, wat ALD-groei een aantal interessante eigenschappen oplevert; zoals een zeer accurate controle over de dikte van de films (nanometerresolutie), lage depositietemperaturen en een uitmuntende conformaliteit van de afgezette films. Deze unieke aspecten stelden ALD in staat om zijn plaats in de microchip industrie te verzegelen. Andere toepassingsdomeinen zoals katalyse en energieopslag kunnen daarenboven ook hun voordeel halen uit deze interessante depositietechniek, maar voor deze toepassingen is ALD tot heden nog vooral te vinden in de academische wereld. In dit werk wordt de toepassing van atomaire laag depositie voor lithium-ion batterijen onderzocht, en twee potentiële toepassingsgebieden worden voorgesteld:

- Recente batterijconcepten zoals de 3D dunne-film lithium-ion batterij zijn bijzonder veelbelovend dankzij de hoge energie- en vermogensdensiteiten en verbeterde veiligheid, wat ze interessant maakt voor vele toepassingen zoals bijvoorbeeld energieopslag op microchips. Conformele depositietechnieken zijn nodig om dunne films af te zetten op deze 3D-structuren. Atomaire laag depositie is bijna uniek in de depositie van dunne films op structuren met zeer complexe vormfactoren.

- De degradatie van batterijen kan al problematisch zijn voor klassieke lithium-ion batterijen, maar de uitdagingen worden des te groter voor nieuwe batterijarchitecturen en materialen. Eén van de manieren op dit aan te pakken is het veranderen of stabiliseren van de oppervlaktechemie. Aangezien de elektrodes in een lithium-ion batterij een complexe architectuur zijn, zowel in een traditionele batterij als bij nieuwe batterijconcepten, is ook hier een conformele depositietechniek zoals atomaire laag depositie aangewezen.

ATOMAIRE LAAG DEPOSITIE VOOR DUNNE-FILM ELEKTRODES

Atomaire laag depositie en controle over de fase van mangaanoxides

Een ALD-proces voor mangaandioxide (MnO_2) was reeds gerapporteerd aan het begin van dit onderzoek door Nilsen *et al*. Het desbetreffende proces maakte gebruik van $Mn(thd)_3$, i.e. manganese tris(2,2,6,6-tetramethyl-3,5-heptanedionato), als mangaanprecursor en ozon als oxidant. Het groeitempo van dit proces lag echter zeer laag (0.1 tot 0.2 Å/cyclus), wat aanleiding gaf tot de ontwikkeling van drie nieuwe *plasma-enhanced* ALD (PE-ALD) processen. Met deze processen was het mogelijk om een temperatuuronafhankelijk groeitempo te bereiken van 0.2 Å/cyclus. Interessant genoeg bepalen de oxidatieve of reductieve eigenschappen van de plasmacomponenten de oxidatietoestand van het mangaan in de afgezette films. MnO_2 kon worden afgezet met ozon, en lagere oxides met een plasma reagent: Mn_3O_4 (H_2O plasma), Mn_3O_4/MnO (H_2 plasma) or MnO (NH_3 plasma).

De oxidatie en reductie van deze films werden onderzocht in inerte, reducerende en oxiderende gassen met *in-situ* X-stralen diffractie. Door het oxideren en reduceren van de films konden alle mangaanoxides gesynthetiseerd worden, inclusief Mn_2O_3 waarvoor geen ALD-proces werd gevonden met de $Mn(thd)_3$ precursor.

Toepassingen van ALD mangaanoxides

De vier ALD-gegroeide films werden getest als dunne-film elektrodes. Gezien hun verschillende oxidatietoestanden werd ook een verschillend elektrochemisch gedrag geobserveerd: MnO_2 gedroeg zich als een positieve elektrode, en de MnO-houdende films als negatieve elektrodes. Helaas was het groeitempo een beperkende factor op de filmdikte, die maximaal haalbaar ongeveer 30 nm was. Dit beperkt de toepassing van deze films als dunne-film elektrodes. Daarbovenop was de depositie van ALD

mangaanoxides nauwelijks conformeel, waardoor geen 3D dunne-film elektrodes konden worden onderzocht.

Twee andere toepassingen werden geëvalueerd, waarvoor ultradunne films voldoende waren. MnO_2 en Mn_2O_3 werden onderzocht als dunne-film katalysatoren voor het splitsen van water, en een activiteit vergelijkbaar met een platina/carbon black benchmark werd geobserveerd. Verder werden ultra-dunne MnO_2 films ook onderzocht als beschermende seed-lagen op TiN, een current-collector die gevoelig bleek te zijn aan oxidatie in zure omgevingen. De seed-laag maakte het mogelijk om dikkere en elektrochemisch actieve MnO_2 films af te zetten via elektrodepositie.

Atomaire laag depositie van vanadiumoxides

Vanadiumoxide films werden gegroeid via ALD met TEMAV, $V(NEtMe)_4$, als vanadium precursor. Water, ozon en zuurstofplasma werden gebruikt als reagentia. Amorfe VO_2-lagen konden worden afgezet met water en ozon. Kristallijne V_2O_5-lagen waren gerapporteerd als resultaat van de depositie met het zuurstofplasma, maar dit proces werd hier gemodificeerd om amorf V_2O_5 af te zetten door de depositietemperatuur te verlagen ($<100\,^{\circ}C$) en met korte plasmapulsen te werken. Het kristallisatiegedrag en de opeenvolging van vanadiumoxide fasen werd onderzocht voor de twee types amorf VO_2 in oxiderende en inerte atmosferen. Dit werd gemonitord met *in-situ* X-stralen diffractie. De invloed van het substraat, de temperatuur, de atmosfeer en de initiële film op dit gedrag werd bepaald, wat resulteerde in het verkrijgen van alle kristallijne vanadiumoxide fasen in de Wadsley-serie (VO_2-V_2O_5).

Vanadiumoxides als dunne-film elektrodes

De kristallijne vanadium oxides die werden gesynthetiseerd lagen in de Wadsley-serie, i.e. VO_2(B), V_6O_{13}, V_4O_9, V_3O_7 and V_2O_5, en vertoonden bruikbare karakteristieken als lithium-ion batterij kathodes, met bijzonder hoge opslagcapaciteiten tot $1.4\,A\,h\,cm^{-3}$. Van de kristallijne films had V_4O_9 de hoogste capaciteitsdensiteit, terwijl VO_2(B) het beste compromis was tussen goede capaciteit, snel op- en ontladen en lange levensduur.

De amorfe VO_2 en V_2O_5 films werden vergeleken met hun kristallijne tegenpolen als batterij kathodes. Algemeen gesproken hebben de amorfe films een hogere capaciteit en kunnen ze bovendien sneller op- en ontladen worden. Dit werd gerelateerd aan de lagere densiteiten en gemakkelijkere diffusie van lithium ionen doorheen deze films. De capaciteit nam echter gestaag af bij herhaaldelijk op- en ontladen. Dit verval werd in ver-

band gebracht met het oplossen van vanadium uit de film wanneer de kathodes zich in de opgeladen toestand bevonden.

3D dunne-film elektrodes

In tegenstelling tot ALD van mangaanoxides is de conformaliteit van ALD van vanadiumoxides zeer goed. Bouwend daarop werden vanadiumoxide films afgezet op 3-dimensionale micro- en nanostructuren, namelijk silicium micropilaren en koolstof nanobuizen, waarbij oppervlaktecapaciteiten tot $\sim$100 µA h cm^{-2} werden aangetoond op beide structuren. De snelle op- en ontlaadkarakteristieken van de dunne-film elektrodes werden overgeërfd door de 3D-gestructureerde elektrodes.

ALD OM DE OPPERVLAKTECHEMIE VAN DE ELEKTRODES TE WIJZIGEN

Atomaire laag depositie wordt beschouwd als een interessante techniek om elektrode-oppervlakken in lithium-ion batterijen te stabiliseren of verbeteren. Het meest onderzochte materiaal is ALD-gedeponeerd Al_2O_3, maar andere materialen werden hiervoor ook geëvalueerd. In de meeste literatuur werd vooral de levensduur van de gemodificeerde elektrodes bestudeerd, en niet onderzocht wat het effect is op het snel op- en ontladen (*rate* capaciteit) van de elektrodes. In dit werk wordt dat laatste in detail ontrafeld voor ALD oppervlakte-modificaties, waarna een optimale ALD-film geëvalueerd wordt op een ALD-gedeponeerde nano-gestructureerde V_2O_5 dunne-film elektrode.

ALD oppervlaktemodificaties en de rate capaciteit

Om de rol van ALD-films op elektrode-oppervlakten van lithium-ion batterijen te bepalen werden twee dunne-film elektrodes gebruikt als eenvoudige modelsystemen. Anataas TiO_2 werd beschouwd als ideaal modelsysteem, aangezien geen solventdecompositie, elektrodedissociatie of grote volumeveranderingen verwacht werden voor dit materiaal. Amorfe ALD Al_2O_3- en TiO_2-lagen met een dikte van 0.5 tot 5.0 nm werden afgezet op het oppervlak van deze elektrode. ALD-gedeponeerd Al_2O_3 bleek bijzonder resistief te zijn ten opzichte van lithium, wat de rate capaciteit significant verzwakte. Aan de andere kant werd de ratecapaciteit van de dunne-film elektrode volledig behouden in het geval van een TiO_2-gemodificeerd elektrode-oppervlak.

Als tweede modelsysteem werd een dunne $LiMn_2O_4$-film op- en ontladen buiten het stabiliteitsgebied van het vloeibaar elektrolyt, waardoor

deze film een modelsysteem werd voor solventdecompositie. Een ALD Al_2O_3 van slechts 1 nm werd gebruikt gezien het resistieve karakter van deze films. Echter, met deze oppervlakte-modificatie vond nog steeds oxidatie van het solvent plaats, wat in combinatie met de impedantie van de ALD Al_2O_3-laag een sterk verzwakte ratecapaciteit opleverde. Een 5 nm ALD TiO_2-laag kon de solventdecompositie anderzijds wel grotendeels onderdrukken. Aangezien deze laag zelf niet resistief is voor lithiumtransfer, leverde dit een noemenswaardige verbetering op in de ratecapaciteit; m.a.w. deze elektrode kon sneller op- en ontladen worden.

ALGEMENE CONCLUSIES

Atomaire laag depositie werd onderzocht voor toepassingen in lithium-ion batterijen. Eerst werden films gegroeid uit bestaande en nieuw ontwikkelde ALD processen getest als lithium-ion batterij elektrodes. Als de depositie conformeel kon gebeuren, wat het geval was voor ALD vanadiumoxides, konden een nanogestructureerde elektrodes worden gevormd. Hierdoor verhoogde de capaciteit met een oppervlaktefactor terwijl de snelle op- en ontlaadkarakteristieken van de dunne-film elektrodes bewaard werden, wat tot zowel hoge capaciteiten als hoge vermogens opleverde.

Vervolgens werd atomaire laag depositie geëvalueerd voor de modificatie van elektrode-oppervlakten. De diffusie van lithium door de ALD oppervlaktelaag werd geïdentificeerd als kritische factor bij de keuze van coatingmateriaal, aangezien een slechte lithiumtransfer door de coating aanleiding geeft tot verzwakte batterijfunctionaliteiten, zoals het geval was voor ALD Al_2O_3-coatings.

Tenslotte werden de twee topics gecombineerd. Een oppervlak-gemodificeerde en nanogestructureerde elektrode werd gevormd door een ALD TiO_2 oppervlaktemodificatie op een ALD V_2O_5-elektrode gedeponeerd op koolstof nanobuizen, waarbij zowel hoge capaciteit, snel op- en ontladen als een lange levensduur van de elektrode gedemonstreerd werden.

ENGLISH SUMMARY

INTRODUCTION AND RESEARCH OBJECTIVES

Lithium-ion batteries (LIB) power most electronic devices today, and are applied in an extremely wide range of applications: large scale off-grid and grid-levelling solutions, electric and hybrid electric vehicles, modern power tools and portable electronics such as laptops and smartphones. Recently, even smaller batteries are coming into focus, such as small-scale microbatteries for on-chip storage, autonomous sensors and implantables. These emerging markets drive the lithium-ion battery towards new concepts and architectures, such as nano-structured electrodes and all-solid-state devices. Furthermore, evermore stringent demands are placed on existing and novel battery chemistries, such as improved cycle life, fast charging, high safety and biocompatibility.

Atomic layer deposition (ALD) is a deposition technique where thin films are deposited from sequential gas-surface reactions. Thanks to the self-limiting nature of these reactions, ALD provides interesting deposition characteristics such as sub-nanometre level thickness control, low deposition temperatures and excellent conformality. These unique features enabled ALD to become a well-established tool in semiconductor manufacturing. Other domains, such as catalysis or energy storage, can also benefit from these interesting coating characteristics. However, for these applications ALD is yet to break the bonds of academia into industry.

In this work, atomic layer deposition is investigated for uses in the field of lithium-ion batteries. Two application areas are proposed:

- Novel battery concepts such as the 3D thin-film lithium-ion battery are very promising in applications such as on-chip energy storage, as a result of their potential high power, high energy and good safety. To obtain these 3D thin-films, conformal deposition technique are required. Atomic layer deposition is one of the few techniques that can achieve conformal thin films in very high aspect ratio structures.

- As battery ageing for traditional lithium-ion batteries can already be problematic, novel architectures, battery concepts and material chemistries pose increasingly greater challenges in this direction. Surface coating has always been one of the concepts to overcome ageing and improve battery performance. To obtain a high quality surface coating on the complex structures of battery electrodes, even

in traditional batteries, a conformal deposition technique such as atomic layer deposition is paramount.

ATOMIC LAYER DEPOSITION FOR THIN FILM ELECTRODES

Atomic layer deposition and phase control of manganese oxides

An ALD process for the deposition of manganese dioxide was reported using the $Mn(thd)_3$ precursor, i.e. manganese tris(2,2,6,6-tetramethyl-3,5-heptanedionato), by Nilsen *et al* before the start of this PhD. As the growth rate of this particular process chemistry was reported to be very low (0.1 to 0.2 Å/cycle), three new plasma-enhanced ALD processes were developed. These processes obtained a higher, temperature independent growth rate of 0.2 Å/cycle. Interestingly, depending on the nature of oxidative or reductive species in the plasma (H_2, NH_3, H_2O) or ozone, films with different oxidations states were obtained: MnO_2 (ozone), Mn_3O_4 (H_2O plasma), Mn_3O_4/MnO (H_2 plasma) or MnO (NH_3 plasma).

The oxidation and reduction behaviour of these films in inert, reducing and oxidative atmospheres were studied using *in-situ* X-ray diffraction. In this way, all manganese oxide phases could be obtained, including the Mn_2O_3 phase which would not be obtained directly from (PE-)ALD growth with the $Mn(thd)_3$ precursor.

Applications of ALD manganese oxides

The four as-deposited films were characterised as thin-film electrodes. Their different oxidation states resulted in different electrochemical behaviour: MnO_2 behaved as a positive electrode, while the MnO-containing films could be used as negative electrodes. However, the slow growth rate limits the thickness of these films to $\leq$30 nm, restricting their use as thin-film electrodes. Furthermore, the conformality of these ALD processes was subpar, so 3D thin-film mangnanese oxide electrodes could not be demonstrated.

Two alternative applications were envisioned where only ultra-thin films were required. MnO_2 and Mn_2O_3 were examined as thin-film catalysts for water splitting, and performed comparably to platinum/carbon black, a benchmark catalyst. Ultra-thin MnO_2 films were also examined as a protective seed layer for the electrodeposition on oxidizable current collectors, which enabled the growth of thicker, electro-active MnO_2 films.

Atomic layer deposition of vanadium oxides

ALD of vanadium oxides was performed using TEMAV, i.e. $V(NEtMe)_4$, as a precursor for vanadium, while water, ozone and oxygen plasma were used as reagents. Amorphous VO_2 films were deposited with the first two. Oxygen plasma was reported to deposit crystalline V_2O_5, but the process was modified to lower temperatures ($<100\,^{\circ}C$) and lower precursor dosage to obtain amorphous V_2O_5. The crystallisation and phase change behaviour of these two flavours of amorphous VO_2 were investigated using *in-situ* XRD in atmospheres ranging from oxidizing to inert. The influence of the substrate, temperature, ambient and initial flavour of VO_2 were unravelled. All crystalline phases in the Wadsley series (VO_2-V_2O_5) could be obtained.

Vanadium oxides as thin-film electrodes

The ALD-derived crystalline films in the Wadsley series, i.e. VO_2(B), V_6O_{13}, V_4O_9, V_3O_7 and V_2O_5, showed good electrochemical activity as positive lithium-ion electrodes, with very high storage capacities up to $1.4\,A\,h\,cm^{-3}$. V_4O_9 demonstrated the highest capacity of the crystalline films, while VO_2(B) had the best trade-off between capacity, rate capability and cycle life.

Amorphous VO_2 and V_2O_5 were benchmarked as electrodes against their crystalline counterparts. The amorphous films generally demonstrate higher capacities and exhibit better rate capability thanks to lower densities and superior lithium diffusion coefficients. The cycle life for these amorphous films was not perfect, and capacity fading was related to vanadium dissolution at high state-of-charge.

3D thin-film electrodes

Contrary to the manganese oxide ALD, the conformality of the thermal vanadium oxides processes was excellent. Vanadium oxide films were deposited on micro- and nano-structured scaffolds, i.e. silicon micropillars and carbon nanotubes. Footprint capacities up to $\sim 100\,\mu A\,h\,cm^{-2}$ were demonstrated on both structures, with excellent rate capabilities inherited from the thin-film nature of the electrodes.

ATOMIC LAYER DEPOSITION FOR INTERFACE MODIFICATIONS

Atomic layer deposition is considered as an excellent candidate to modify and stabilize interfaces of lithium-ion battery particles or electrodes. ALD-deposited Al_2O_3 is the most studied surface modifier, but many other ALD films are also explored. In most published work, these coatings were investigated to extend the cycle life of various electrodes, but the effect on the rate capability is often omitted. Here, this influence on the electrode kinetics is studied in detail, and the best coating is evaluated on an ALD V_2O_5 3D nano-structured thin-film electrode.

ALD interface modifications and the rate capability

Two thin-film electrodes were used as simple model systems to unravel the role of ALD coatings on lithium-ion battery electrodes. Anatase TiO_2 was considered a near-ideal model system as it does not suffer from SEI formation, metal dissolution of large volume changes. 0.5 nm to 5.0 nm films of amophous ALD Al_2O_3 and TiO_2 were deposited on the surface of this electrode. ALD Al_2O_3 appeared to be very resistive towards lithium, and significantly deteriorated rate capabilities were found. ALD TiO_2 on the other hand retained the rate capability of the model electrode.

Overcharged thin-film $LiMn_2O_4$ was used as a model system for solvent decomposition. A 1 nm ALD Al_2O_3 film already posed a large impedance, and could not alleviate the solvent decomposition, resulting in severely degraded rate performance. 5 nm ALD TiO_2 on the other hand could prevent the solvent decomposition, which appreciably improved the rate capability compared to the uncoated electrode.

ALD-modified vanadium oxide 3D thin-film electrodes

A 3D thin-film electrode was constructed from an ALD-derived crystalline V_2O_5 film deposited on carbon nanotubes (CNTs). This V_2O_5/CNTs electrode suffered from capacity fading when charged to 2 V *vs* Li^+/Li, which was shown to be related to vanadium dissolution. The interface was modified with 5 and 25 cycles of ALD TiO_2, which maintained the excellent thin-film kinetics of the V_2O_5/CNTs electrodes. Vanadium dissolution was completely supressed with 25 cycles of ALD TiO_2, which resulted in a stabilized electrode capacity.

CONCLUSIONS

Atomic layer deposition was investigated for applications in lithium-ion batteries. First, electrodes grown from existing and novel ALD processes were evaluated. If the conformality of the deposition allows it, as was the case for ALD vanadium oxides, these electrodes can be nano-structured, which increases their footprint capacity and at the same time maintains the excellent rate capability of the thin-film electrodes, yielding high-energy and high-power electrodes.

Next, atomic layer deposition was evaluated for electrode surface modifications. The lithium diffusion through the deposited coatings needs to be considered when choosing a coating, as a poor lithium transfer can significantly degrade battery performance, as was shown for ALD Al_2O_3.

Finally, 3D nano-structured electrodes and interface modifications were combined in an ALD TiO_2/ALD V_2O_5/CNTs electrode, which exhibited excellent rate capability, high footprint capacity and an excellent cycle life, demonstrating both applications of atomic layer deposition for lithium-ion batteries.

Part II

INTRODUCTION

1

INTRODUCTION

We live in an electrical world. It is easily forgotten that we rely on electricity for almost everything in our daily lives, from our alarm clock the first thing in the morning to turning off the last light bulb in the evening. Close to everything we do is powered by electrical energy.

With the evermore increasing need to become mobile, wireless and connected, the need for energy storage has never been far behind. Numerous forms of energy storage are available, but batteries are the most well-known. A battery works by storing energy (electro)chemically in its system, which can be released in the form of electrical energy. Batteries have been around for centuries, quite literally; the first battery was invented by Alessandro Volta around 1800, over two centuries ago, by stacking several pairs of copper and zinc discs separated by cloth or cardboard soaked in brine, as displayed in figure 1.1.

1.1 BATTERIES

A battery consists of one or more electrochemical cells, made up of a positive electrode, a negative electrode and an ion-conducting electrolyte.

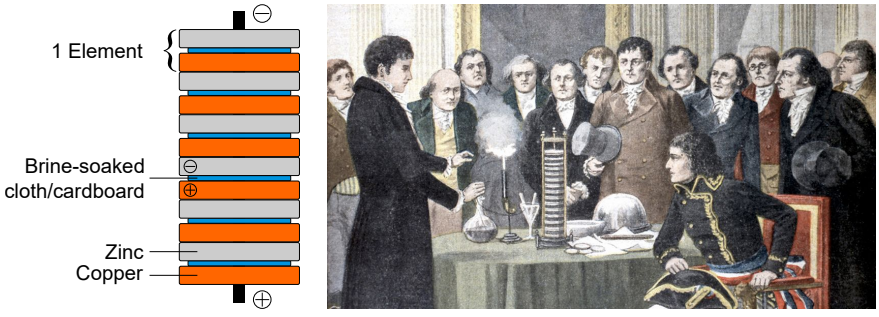

Figure 1.1: (left) The principle of a voltaic pile; (right) Volta presenting his voltaic pile as the first stand-alone power source to Napoleon Bonaparte.

Batteries are the most commonly used method for energy storage, thanks to their portability and versatility. This verstatility results from the various chemistries that can be used to construct a battery, and the wide range of physical volumes and charge storage sizes that it can be used for. Indeed, battery sizes can range from large-scale grid storage applications (MWh) [1], (hybrid) electric vehicles (for example, 40-85kWh for Tesla car batteries) [2] to consumer electronics (Wh storage for power tools, laptop and smartphones) and autonomous sensors (mWh to μWh) [3].

1.1.1 *The principle of Volta's battery*

The building blocks of the battery have not changed much since Volta's discovery in the 19th century. The basic components of Volta's cell in figure 1.1 are

- A current collector
- A positive electrode (copper disk)
- An electrolyte (brine, a solution of salt in water)
- A separator (cloth or cardboard)
- A negative electrode (zinc disc)
- A current collector

In the case of Volta's cell, the energy is released in the form of electrical current by dissolving zinc into the brine solution. Charge compensation happens by reducing hydrogen ions to neutral hydrogen at the copper disk's surface, which bubbles out of the battery, resulting in an electrochemical cell of 0.76 V. Not a lot can be accomplished with such a low voltage, which is why the Cu-electrolyte-Zn couples were stacked to Voltaic piles resulting, for example, to 4.56 V in the case of the pile in figure 1.1. This also explains the origin of the term 'battery', as these voltaic piles resembled the cannons employed in warfare at that time.

1.1.2 *Rechargeable batteries*

Since that time various battery types, or chemistries, have been developed to keep up with demands. Batteries are classified according to the reversibility of the reactions taking place in the battery, in other words, whether the battery is rechargeable or not. Volta's cell, like our current-day alkaline batteries (most cylindrical batteries in children's toys) and

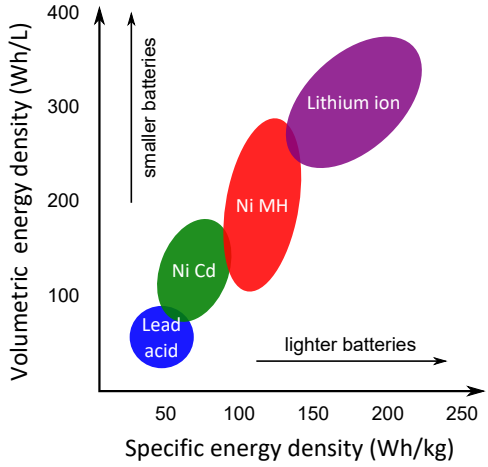

Figure 1.2: Comparison of the energy densities of several rechargeable battery types. Adapted from [4].

lithium-manganese dioxide batteries (the coin-cell type batteries in most watches) are primary or non-rechargeable batteries, meaning the battery can be used until one of its components runs out.

On the other hand, for some battery chemistries the electrochemical reactions ocurring within the battery can be reversed, so they can be re-used for anything from 5 times (simple rechargeable alkaline batteries) to 5000 times (state-of-the-art lithium-ion batteries). Four major secondary battery chemistries[1] exist (see also figure 1.2) [4]:

- **Lead-acid** is the cheapest battery chemistry if weight is not an important factor, but has a very low energy density. Invented in 1859, it's still used today in cars and large uninterruptible power supply (UPS) systems.
- **Nickel Cadmium (NiCd)** has been around since 1950, but also has a low energy density, significant self-discharge and contains toxic metals. NiCd batteries are still used today for applications such as power tools.
- **Nickel Metal Hydride (NiMH)** emerged in the 1970s as a less toxic alternative to the NiCd battery. It has a higher energy density (40 %

1 Other battery chemistries, such as lithium-air, lithium-metal and sodium batteries for example are in the focus for beyond-lithium-ion batteries, but haven't made it to the commercial stage yet.

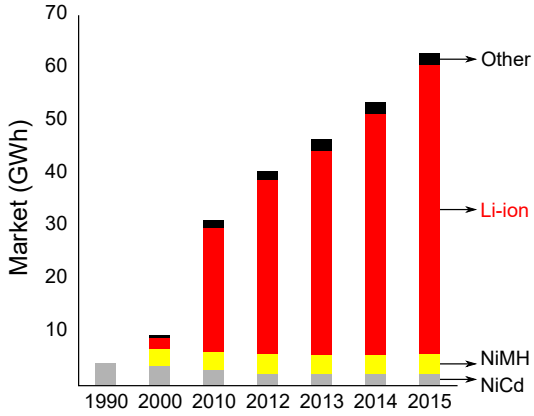

Figure 1.3: The evolution of the rechargeable battery market since the introduction of the lithium ion battery to the market by Sony in 1991 (2015 are estimations) [10].

higher than NiCd), but still suffers from high self-discharge, so it can only be found in niche markets such as satellite applications.

- **Lithium-ion batteries (LIB)** offer the highest energy density, more than twice that of NiCd batteries. They also do not suffer from memory effects and exhibit low self-discharge properties.

Amongst the rechargeable batteries, the lithium-ion battery is king. Since its proposition by Stanley Whittingham in the 1970s at Exxon [5, 6], further development by John Goodenough in 1980 at Oxford University [7] and commercialisation by Sony in 1991 [1, 8], the lithium-ion battery has taken the market by storm (figure 1.3). Not surprising, considering the superior properties it has over earlier battery chemistries, the lithium ion battery market is projected to rise further by more than 17 % yearly between 2016 and 2021 [9].

1.2 THE LITHIUM-ION BATTERY

Lithium-ion batteries are the commercially available batteries that provide the highest energy density to date. This is inherited from the properties of lithium itself. On the one hand, being only the third element in the periodic table makes it the third lightest element, and Li^+ one of the smallest single-charged ions. Furthermore, lithium has the lowest reduction potential of any element ($-3.02\,V$ *vs* the standard hydrogen electrode), resulting in much higher cell potentials (typically 3.6 V) compared to earlier rechargeable battery chemistries (Ni-based 1.2 V, lead acid 2.0 V).

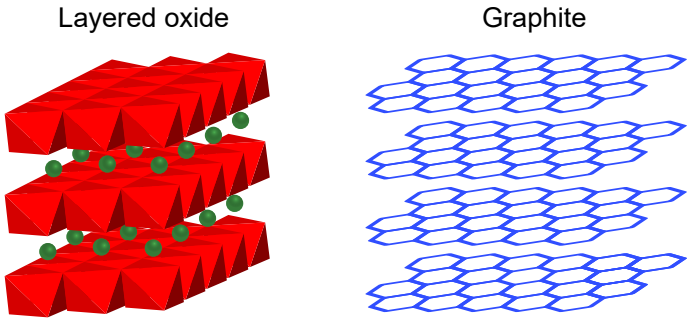

Figure 1.4: (left) Lithiated layered oxide structure found for many transition metal positive electrode materials ($LiMO_2$ with M=Co, Ni, Mn, and the spheres represent Li). (right) Layered structure of graphite.

1.2.1 *How the lithium-ion battery works*

The basic components of lithium-ion batteries are very similar to those of Volta's rudimentary battery:

- current collectors, usually aluminium for the positive electrode and copper for the negative electrode
- a negative electrode, usually carbon-based such as graphitic carbon
- an electrolyte, a lithium salt in (a mixture of) solvents
- a positive electrode, usually a transition metal oxide such as lithium cobalt oxide

The layered structure of the negative graphite electrode (figure 1.4) allows lithium ions to reside in between the sheets of graphite, a storage mechanism called *intercalation*. The lithium cobalt oxide in the positive electrode is a layered oxide, as shown in figure 1.4. This implies it has sites for lithium ions along certain planes within the crystal structure, which allows lithium ions to also be (de)intercalated there. Other lithium storage mechanisms exist, such as conversion and alloying with lithium, which will be briefly touched upon further.

The electrodes determine the potential and capacity of the cell. When an electrode such as $Li_{0.5}CoO_2$ is part of an electrochemical cell, an energy difference exists between the two electrodes which gives rise to the electrode potential (as will be explained in section 1.2.2). The driving force behind the lithium-ion battery is the equalisation of the energy in the system, which is done by electron transfer, effectively oxidizing and reducing components (typically the transition metals) in the electrodes. These

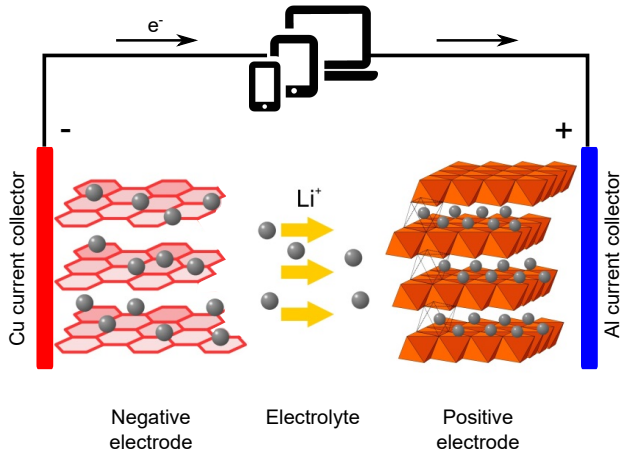

Figure 1.5: Lithium ion battery during discharge. Ions and electrons move in the opposite direction during charge. Figure adapted from [11].

electrons are transferred through the circuit, where they can perform (useful) work during the discharge of the battery. As electrons are negatively charged, this creates a charge imbalance, which is then compensated by the extraction or insertion of lithium ions from or into the electrode.

Each electrode has a specific electrode potential, which is the potential V of the electrode is lithium is used as a negative electrode. In a real cell, a negative electrode is paired with a positive electrode and the electrode potential is thus the difference between their electrode potentials:

$$V_{cell} = V_{positive} - V_{negative} \tag{1.1}$$

as long as no current is flowing. If a current flows, this potential is modified by charge transfer resistances for the ions at the interfaces and internal current resistance, causing the usable cell voltage to be lower than V_{cell}.

The second characteristic of the cell is the capacity, which corresponds to the number of lithium sites available in the electrodes. Often, only a fraction of the available lithium sites can be accessed reversibly, or only a fraction of the host lattice can be oxidized reversibly. To use the cell in a good rechargeable battery the depth of charge (DOC) or discharge (DOD) can be limited. Insertion electrodes typically have less potential lithium storage than conversion electrodes and alloying electrodes, but a better reversibility and coulombic efficiency.

In the charged state of the battery, the lithium is stored in the negative graphite electrode. When the battery is used as in figure 1.5, the nega-

tive electrode is used as anode[2] as it releases electrons and de-intercalates lithium ions:

$$LiC_6 \longrightarrow Li^+ + e^- + C_6 \tag{1.2}$$

At the same time, the positive electrode acts as a cathode; electrons are accepted to reduce the Co^{4+} to Co^{3+}, and the intercalation of lithium ions again balances the charge:

$$xLi^+ + xe^- + Li_{1-x}CoO_2 \longrightarrow LiCoO_2 \tag{1.3}$$

The electrolyte conducts the lithium ions, but does not conduct electrons. Since reaction 1.2 releases electrons, and reaction 1.3 consumes electrons, these reactions can only take place if a current can flow through an external circuit, connected to the device the battery is powering. The full reaction taking place is then:

$$Li_xC_6 + Li_{1-x}CoO_2 \underset{charge}{\overset{discharge}{\rightleftharpoons}} C_6 + LiCoO_2 \tag{1.4}$$

This reaction is reversible, which means that it can take place in both directions. The spontaneous direction is left to right as this lowers the energy of the system. However, if a current is forced in the opposite direction of figure 1.5, the cobalt is oxidized again. Charge neutrality implies that lithium ions must move back to compensate the electronic charge. This reversible dual intercalation mechanism is also known as the *rocking chair* battery [12, 13].

The battery in section 1.2.1 is an oversimplification of a real battery. A schematic representation of the components of a real lithium-ion battery is shown in figure 1.6. The classical lithium-ion battery found in cellphones and laptops is particle-based; i.e. the electrodes are constructed from active material particles, usually micron-sized. To keep these 'glued' together, a binder needs to be added. To ensure a good electronic current collection, a conductive agent is added, and a slurry made from these components makes up both electrodes. This slurry is spread onto the current collector foils, and is dried to obtain the porous structure of the electrode. The porosity provides channels for the liquid electrolyte to easily penetrate throughout the electrodes, ensuring sufficient ionic conductivity throughout the cell. The electrolyte is an electronically insulating liquid, but a non-reactive non-conductive porous membrane, called the separator, must be added to keep the positive and negative electrode from forming a

2 The 'cathode' and 'anode' terminology is confusing, since their role depends on whether the battery is charging or discharging. Here, we will use mostly negative and positive electrode where possible.

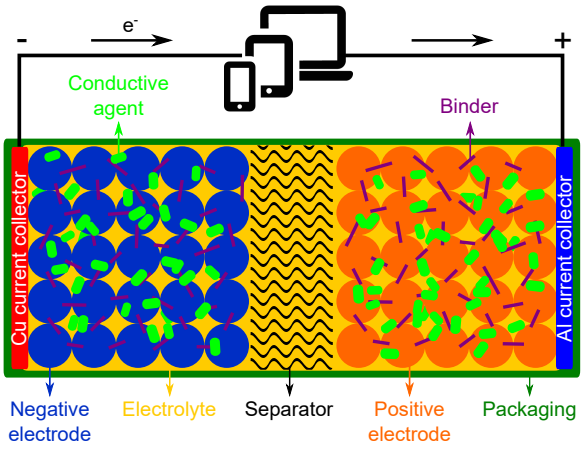

Figure 1.6: A schematic representation of the building blocks that a real lithium-ion battery is composed of.

direct contact and short-circuiting the battery. Finally, the whole assembly is packaged since the components are not stable in contact with ambient air: lithium is very reactive with moisture and oxygen, and the solvents making up part of the liquid electrolyte are usually flammable.

1.2.2 *The origin of the electrode potential*

Equation 1.1 in the previous section states that the potential of an electrochemical cell depends on the difference in electrode potentials of the negative and positive components. This section will give some physiochemical background to the origin on these electrode potentials, which can be found in the electrochemical potentials of its components.

An electrochemical potential is a quantity that defines how difficult it is, or how much work it takes, to move a chemical species to a well-defined location (concentration) and electrostatic surrounding. As all systems want to lower their energy, spontaneous reaction happen from higher to lower electrochemical potentials. The electrochemical potential $\tilde{\mu}_\alpha$ [J/mol] for compound α consists of a chemical potential and an electrostatic term:

$$\tilde{\mu}_\alpha = \mu_\alpha + z_\alpha F \phi_\alpha \tag{1.5}$$

where z_α is the valency (charge) of the species (if charged), F the Faraday constant [C/mol] and ϕ_α the local electrostatic potential [V]. The chemical potential μ_α [J/mol] can be written as

$$\mu_\alpha = \frac{\delta G}{\delta n} = \mu_\alpha^0 + RTln(a_\alpha) \tag{1.6}$$

with G the Gibbs free energy. The chemical potential can be separated into a term μ_α^0 [J/mol] which is the chemical potential at a set of standard conditions [J/mol], R the gas constant[J/mol.K], T the temperature [K] and a_α the activity.

Let us now return to a simple electrochemical cell, with lithium cobalt oxide as a positive electrode and lithium as the negative electrode. During discharge, he half-cell reaction on the positive side is

$$xLi^+ + xe^- + Li_{1-x}CoO_2 \longrightarrow LiCoO_2 \tag{1.7}$$

As the electrochemical potentials need to be balanced on both sides of this equation at reaction equilibrium, they can be written as

$$x\tilde{\mu}_{Li^+} + x\tilde{\mu}_{e^-} + \tilde{\mu}_{Li_{1-x}CoO_2} = \tilde{\mu}_{LiCoO_2} \tag{1.8}$$

The electrochemical potential for the electrons here are equal to the Fermi level. This allows us to calculate the electrode potential, as the electrode potential is the potential for a compound compared to the potential of the Li^+/Li electrode. Let us again consider the aforementioned electrochemical cell. The Fermi level, or electrochemical potential, for the positive electrode is thus

$$E_F^{positive} = \tilde{\mu}_{e^-}^{positive} = \frac{\tilde{\mu}_{LiCoO_2} - \tilde{\mu}_{Li_{1-x}CoO_2}}{x} - \tilde{\mu}_{Li^+} \tag{1.9}$$

where the marker 'positive' denotes that this is valid for the positive electrode. Fermi levels are typically expressed in units of electronvolt (eV), but this unit is equivalent to that of the (electro)chemical potential (J/mol) and differ only by the elementary charge e divided by the Faraday constant (e/F [mol]). Similarly, the Fermi level at the negative electrode is in this case

$$E_F^{lithium} = \tilde{\mu}_{e^-}^{lithium} = \tilde{\mu}_{Li} - \tilde{\mu}_{Li^+} \tag{1.10}$$

where the denotion 'lithium' means that this applies for the following reaction in this cell:

$$Li \longrightarrow Li^+ + e^- \tag{1.11}$$

Figure 1.7 visualizes these energy levels. In the charged state of the $Li/LiCoO_2$ cell, half of the cobalt in in the +4 oxidation state, and half

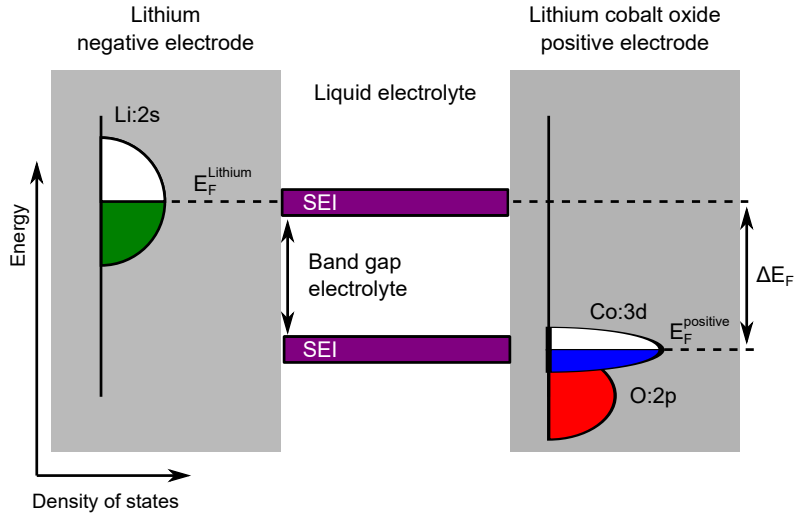

Figure 1.7: A qualitative schematic of the important electronic energy levels in a charged $Li/LiCoO_2$ cell.

is in the +3 oxidation state, resulting in a half-filled Co:3p orbital. Lithium itself is a metal, so always has a half-filled shell with the Fermi level fixed in the middle. If the battery is connected to a load, electrons can flow from the Li:2s shell to the Co:3p shell, effectively reducing the remaining Co^{4+} to Co^{3+} as the Co:3p is filled. To balance charge, the lithium ions generated by the release of electrons at the lithium electrode are simultaneously transferred through the electrolyte into the Li_xCoO_2 electrode. The open circuit potential, i.e. the potential in volts that is measurable at the two terminals of the cell, can thus be written as the difference in Fermi levels between the two electrode, by the charge of the electrons (-1) and the Faraday constant as

$$-FV_{halfcell} = E_F^{positive} - E_F^{lithium} = \tilde{\mu}_{e^-}^{positive} - \tilde{\mu}_{e^-}^{lithium} \tag{1.12}$$

Combining this equation with equations 1.5, 1.6, 1.9 and 1.10 finally gives us the Nernst Equation, which allows us to calculate the measurable cell potential, in this case $V_{halfcell}$, to quantities as standard chemical potentials, temperature, and activities of its components[3]:

$$V_{halfcell} = V_{halfcell}^0 - \frac{RT}{Fx} \ln \frac{a_{LiCoO_2}}{a_{Li_{1-x}CoO_2}} \tag{1.13}$$

3 The activity of lithium, a_{Li}, drops out of this equation as it is conventionally taken as unity in pure substances.

with $V^0_{halfcell}$ containing contributions of the standard chemical potentials of the compounds (in this case $LiCoO_2$, $Li_{1-x}CoO_2$ and lithium). This equation allows us to calculate the potential of the $LiCoO_2$/Li cell for every given state-of-charge.

If the lithium electrode is considered as a reference electrode, than this $V_{halfcell}$ can be considered as an electrode potential. The potential of a cell with a compound as both the negative and positive electrode, such as graphite and lithium cobalt oxide, then the potential of the full cell is simply the difference of the electrode potentials, as

$$\begin{aligned} V_{cell} &= V^{positive}_{halfcell} - V^{negative}_{halfcell} \\ &= \frac{(E_F^{positive} - E_F^{lithium}) - (E_F^{negative} - E_F^{lithium})}{-F} \\ &= \frac{E_F^{positive} - E_F^{negative}}{-F} \end{aligned} \tag{1.14}$$

1.2.3 *Characteristic properties of the lithium-ion battery*

A specific terminology is obligatory when discussing batteries. The characteristic properties of the battery are listed below with a short explanation.

- The **capacity** of the battery states how much charge it can hold and release, expressed in Coulomb (C) or ampere-hour (A h).
- **Terminal voltage** is the potential at which the battery can deliver its charge. This can be nearly constant, but typically this changes depending on how much charge is left in the battery. The terminal voltage is the difference between the electrode potential of the positive and negative electrodes.
- The **energy** in a battery is the amount of work it can perform, and is a product of the amount of charge it can deliver and the potential it can deliver the charge at (W h). Energy density is a measure of the density of charge storage within the electrodes or within the battery, and can be expressed in gravimetric ($W\,h\,g^{-1}$, charge per unit of weight) or volumetric units ($W\,h\,cm^{-3}$ or $W\,h\,l^{-1}$, charge per unit of volume).
- **Power** (and **Power density**) is a measure of the rate at which a battery can do work. This is expressed in units of Watt (W).
- **Rate**, or the **rate capability** is a measure of how fast the battery can be charged or discharged without loss of too much energy. Fast

charging often reduces the accessible capacity, and generates high currents, which can be detrimental for the battery. The rate capability is expressed in C-rate, where a C-rate of 1C corresponds to the current required to charge or discharge the battery to its theoretical capacity in 1 hour, while a C-rate of 10C indicates charge/discharging in 6 minutes (1/10th of an hour).

- **Cyclability** determines the number of cycles a battery can be used before the capacity drops to below a certain value (usually 80 % of the initial value). Many factors influence the cycle lifetime, such as charge and discharge rate, temperature, type of electrode and electrolyte materials, etc.
- **Coulombic efficiency** is the amount of charge delivered during discharge of the battery, compared to the amount of charge stored during charge. It is a measure of the reversibility of the reactions in the cell or at the electrodes, and has to be as close to 100 % as possible.
- **Self-discharge** is the amount of charge lost during storage of the battery.

1.3 RECENT TRENDS IN BATTERY ADVANCEMENT

While the lithium-ion battery is the best commercial battery out there, the work is never done. Moore's law already predicted in 1975 that the number of components per integrated circuit would double every two years, which they did[14]. Batteries have not followed: making the leap from lead-acid batteries to lithium-ion batteries increased the energy density five-fold, but only over a period of more than 30 years, which really required a revolution in materials science. Futhermore, the most commonly used lithium-ion battery (graphite-$LiCoO_2$) is little different from the one first commercialized in 1991. Several routes are being explored to advance energy storage, summarized in figure 1.8. It ranges from advances within the lithium-ion battery on a materials and design level (section 1.3.1) to technologies beyond classical lithium-ion batteries, such as solid-state, thin-film lithium-ion batteries or batteries beyond lithium-ion (section 1.3.2).

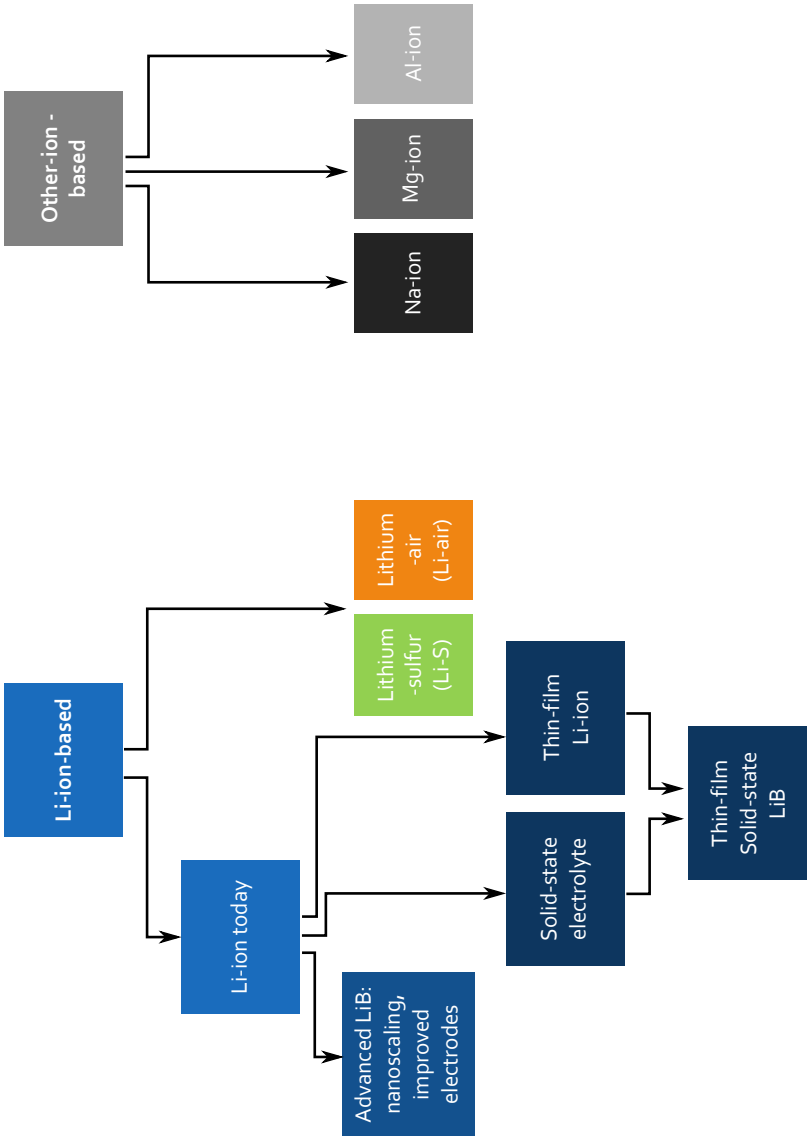

Figure 1.8: Possible advances in energy storage. Figure adapted from [15].

1.3.1 *Advances for the lithium-ion battery*

The lithium-ion battery itself is still being improved, which is evident from the almost 150 000 scientific papers published since its birth.[4] Most lithium-ion batteries on the market still consist of the original lithium-ion battery's composition, i.e. lithium cobalt oxide as the positive electrode, graphite as the negative electrode and the electrolyte made up from a lithium salt (such as $LiPF_6$ or $LiClO_4$) dissolved in a mixture of solvents (such as ethylene carbonate, dimethyl carbonate and propylene carbonate). New battery materials can reduce cost, increase energy or power density and enhance battery safety, three major concerns in the advancement of lithium ion batteries. The largest advances in materials science are found on the electrodes. An ideal electrode has to fulfil the following conditions:

- high (positive electrode) or low (negative electrode) potential, to maximize the terminal voltage
- high energy density
- (almost) 100 % reversible storage reactions
- small volume changes during charge and discharge
- non-toxic, abundant and inexpensive

Several types of charge storage hosts exist, either based on intercalation, conversion or alloying mechanisms. Graphite and lithium cobalt oxide are intercalation-type electrodes. In an intercalation-type material, specific lattice sites are available within the crystal structure of the host material, and lithium can diffuse to those sites over diffusion planes in the case of layered materials such as graphite and lithium cobalt oxide (see figure 1.4) or by three-dimensional channels in the case of an open structure such as spinel $LiMn_2O_4$. These materials have a low volume expansion, but also a relatively low energy density. A conversion anode stores lithium by the conversion of a metal oxide to a metal and lithium oxide, while alloying is the transformation of a metal to a lithium-metal compound. These storage modes typically offer much higher energy densities (up to an order of magnitude higher), but suffer from low coulombic efficiencies and severe volume expansions, respectively, rendering them less suited for continued cycling.

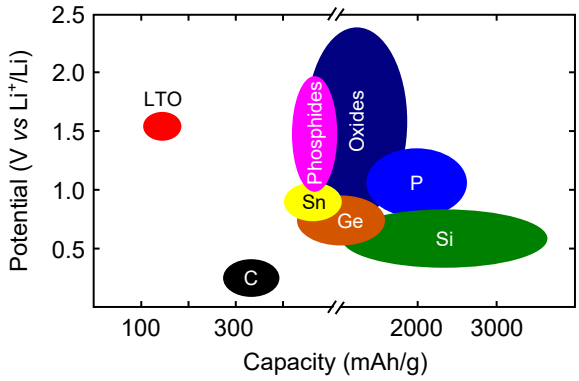

Figure 1.9: Capacity and electrode potential for negative electrodes. Figure adapted from [16].

1.3.1.1 *Negative electrode materials beyond graphite*

Graphite has reasonable storage capacity ($372\,\mathrm{mA\,h\,g^{-1}}$) and the advantage of a flat voltage plateau, but materials with much higher capacities are available, as shown in figure 1.9. While the low voltage plateau of graphite has the advantage of providing a high terminal voltage for the battery, most solvents in the liquid electrolytes are unstable at these potentials. During the first cycle, irreversible side reactions occur on the graphite electrode, forming an ill-defined layer called the *Solid Electrolyte Interface or Interphase* (SEI). This layer stabilizes the graphite-electrolyte interface for the duration of the battery life, but irreversibly consumes some of the lithium in the battery, rendering less lithium available to do the actual energy storage. Furthermore, this SEI layer is typically not resilient to elevated temperatures, limiting the operating window of the battery [17–20].

Keeping this in mind, two pathways are investigated to improve the negative electrode, or anode (during battery use). On the one hand, SEI formation can be avoided altogether by choosing a good anode with a higher electrode potential (above $1.58\,\mathrm{V}$ *vs* $\mathrm{Li^+/Li}$), which implies a lower electrochemical potential preferably within the band gap of the electrolyte. Lithium titanium oxide ($\mathrm{Li_4Ti_5O_{12}}$ or LTO) has a delithiation potential of $1.58\,\mathrm{V}$ *vs* $\mathrm{Li^+/Li}$. Despite this higher potential and lower capacity ($175\,\mathrm{mA\,h\,g^{-1}}$), it has been commercialized successfully because of its high temperature stability, high rate and extremely high cycle life, up to tens of thousands of

4 147 000, as determined by a google scholar search using the exact phrase "lithium ion battery" as terms, up to January 2017.

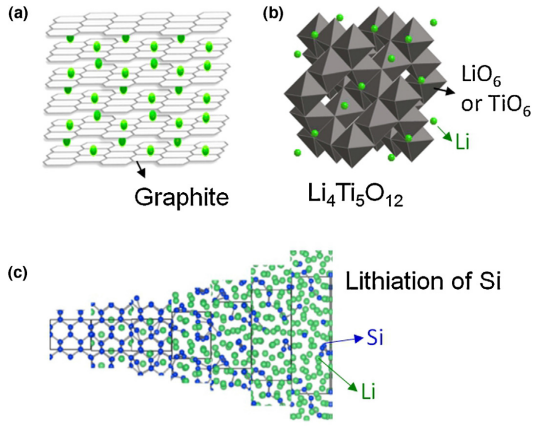

Figure 1.10: Crystal structures of (a) lithiated graphite, (b) lithium titanium oxide (LTO) and (c) silicon in various stages of lithiation, demonstrating the extreme volume change for the latter. Figure reproduced from [16].

cycles. The latter originates from the fact that LTO is an almost *zero-strain* electrode: it only expands 0.2 % upon lithiation, while graphite expands almost 10 %. However, despite the excellent properties of LTO, it has not pushed graphite from the position of anode for the 'standard' lithium ion battery, due to the low energy density and residual surface reactions.

Another interesting possibility is moving to extremely high capacity materials. Silicon for example can be used as a negative electrode material, and has a capacity of 3579 mA h g^{-1}, almost 10 times as high as graphite. However, the extremely large volume changes associated with the high storage capacity (up to 270 % volume expansion, as demonstrated in figure 1.10(c)) implies it does not offer a very long lifetime, caused by pulverisation of the anode particles. Furthermore, the low potential at which this electrode operates, triggers electrolyte decomposition similar to that on graphite, which is further enhanced by the pulverisation exposing fresh surface with every cycle. Unless measures are taken to stabilize the surface and the morphology, only a few cycles can be obtained from silicon [21]. Other high-capacity anodes, such as germanium, manganese and tin, suffer from similar issues [22].

Lithium itself can also be used as the negative electrode[5] with a whopping capacity of 3861 mA h g^{-1}, more than 10 times higher than graphite. Due to this high theoretical capacity, major effort has been made to make

5 Those batteries are typically called *lithium batteries* rather than *lithium-ion batteries*, since the lithium is stored as metallic lithium, rather than as an ion in an intercalation host material.

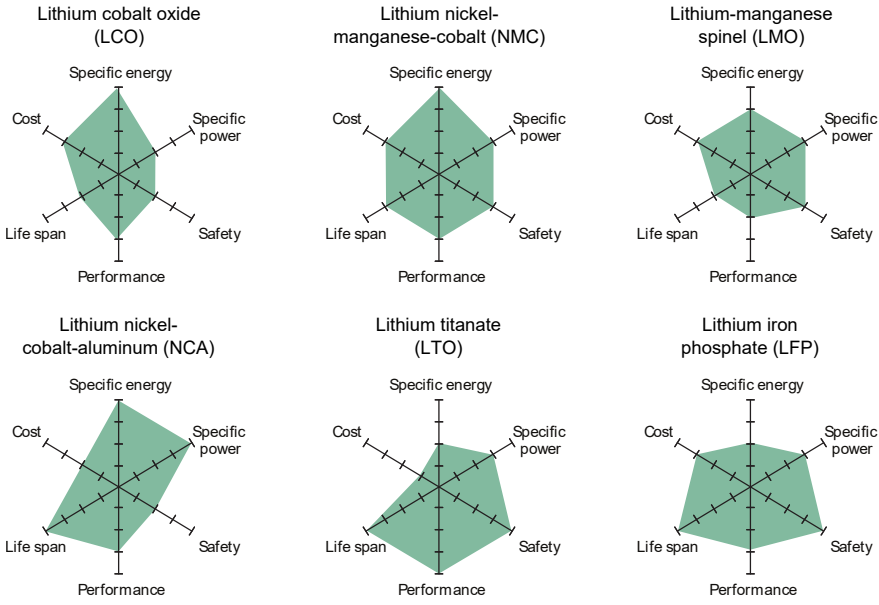

Figure 1.11: Properties and trade-off in cathode materials beyond lithium cobalt oxide. Edited from [2].

this possible. Unfortunately, uncontrollable dendritic Li growth and limited Coulombic efficiency during Li deposition/stripping inherent in these batteries has made it non-viable in a standard lithium-ion battery [23].

1.3.1.2 *Positive electrode materials beyond $LiCoO_2$*

Lithium cobalt oxide (LCO) has a high theoretical capacity of 274 mA h g^{-1} at 3.8 V *vs* Li^+/Li, relatively low self-discharge and relatively good cycling performance. However, the limited availability of cobalt makes it a high-cost cathode: the cost of current lithium-ion batteries is determined to a large extent by the price of the cobalt. Furthermore, it has a low thermal stability (thermal runaway above 200 °C), which poses a serious safety concern and resulted in the grounding of all Boeing 787 airplanes in 2013 [24]. This has as a consequence that LCO-based lithium-ion cells cannot be discharged at high rates, as the high current would heat the battery, limiting the power of LCO. Finally, even though LCO has a high theoretical capacity, only half of the theoretical capacity can actually be used, as delithiation beyond $Li_{0.5}CoO_2$ introduces lattice deformation detrimental to the cycle life of lithium cobalt oxide.

A whole range of oxides, sulphides, phosphates and fluorides have been investigated and commercialized. Figure 1.11 shows the properties of the mainly used and investigated positive electrodes. This figure clearly illustrates the trade-off present between cost, energy, power, safety and lifespan. To date, the holy grail of lithium-ion battery cathodes remains as elusive as the mythical unicorn, so the choice of cathode today mainly depends on prioritizing battery characteristics (for example, NMC is used for electric vehicles thanks to the high energy, translating into a good range).

Nickel, manganese and iron are the most popular transition metals for lithium-ion storage in the positive electrode, although titanium and vanadium have also been evaluated. Lithium nickel oxide ($LiNiO_2$) has the same crystal structure as LCO, and the lower cost of nickel makes it an interesting alternative. However, $LiNiO_2$ has a poor cycle life and an even lower thermal stability than LCO.

Lithium manganese oxide ($LiMn_2O_4$, LMO in particular) has also attracted much attention thanks to its even lower cost and the low toxicity of manganese compared to nickel and cobalt. Furthermore, the crystal structure of spinel LMO is three-dimensional rather than layered for LCO, meaning that lithium can diffuse into the electrode from every direction rather than through planes. However, despite the low cost and high safety, cycle life is not sufficient for LMO due to side reactions with the electrolyte, oxygen loss, Mn dissolution and irreversible phase transformations.

The key concept to unlocking novel cathode insertion materials has been found beyond the ternary compounds. Rather than simple metal oxides, with the metal being manganese, cobalt or nickel, mixtures of two or three of those (sometimes doped with Mg or Al) have shown excellent cycle life and electrochemical performance. For example, $LiNi_{0.8}Co_{0.15}Al_{0.05}O_2$ (NCA) has found its way to commercial use in Tesla car batteries as a cheaper alternative to LCO with a discharge capacity around 200 mA h g^{-1}. Higher voltage materials were obtained by mixing LMO and LNO to $LiMn_{1.5}Ni_{0.5}O_4$ (LMNO). LMNO has a higher electrode potential than LCO (4.7 V *vs* Li^+/Li), which translated to a higher power. A mixture of all three transition metals, such as $LiNi_{0.33}Mn_{0.33}Co_{0.33}O_2$ (NMC) has been commercialized successfully thanks to the high reversible storage capacity of up to 170 mA h g^{-1}.

1.3.1.3 *Nano-structuring the electrodes for higher performance*

Typical first-generation lithium-ion electrodes are constructed of electrode particles in the range of 10 µm to 100 µm, in combination with a binder and a conductive agent. While great advances in materials science on the

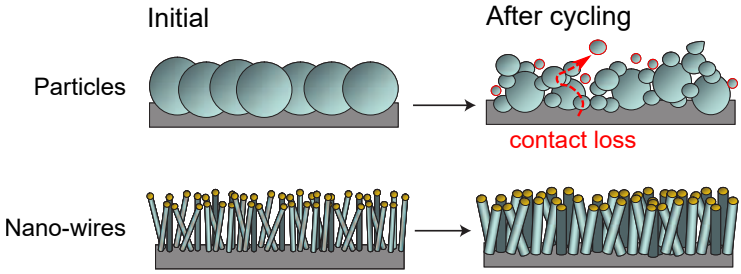

Figure 1.12: Schematic illustration of the mechanical stabilisation effect of nanoscaling silicon to silicon nanowires. Figure adapted from [33].

electrode level can enhance the energy density of the electrodes, the power density will be limited by slow diffusion of lithium in solid matter (around $D \sim 10^{-8}\,\mathrm{cm^2\,s^{-1}}$). To meet the demands of batteries for electric vehicles [25], or on-the-go charge storage on sensors in combination with energy harvesters [3], a leap forwards towards faster (dis)charging batteries will be required. The characteristic time scales within the electrode particle is given by $t = L^2/D$, with L the diffusion length, so these advances can be obtained by down-sizing the electrode particles from micron-sized to nano-sized [26, 27]. Similar enhancements can be achieved by replacing the particle structure altogether by a complex nanostructuring [28, 29], such as nanotubes [30, 31] or thin film electrodes [32].

Aside from faster and more performant batteries [34], nanoscaling can also provide structural stabilisation. A common problem with high capacity electrodes is the associated high volume change. This causes problems with delamination and fracturing, resulting in severe capacity fading [21, 35–37]. Moving from large particles to small nano-particles, or more complex nanostructures such as nanofibres [33, 38] or nanotubes [39–41], can effectively alleviate issues related to strain, as illustrated in figure 1.12. This results in an enhanced capacity retention [22, 33, 42].

Despite the merits of structuring the battery electrodes, some disadvantages are also still present. Apart from more difficult synthesis, higher cost, poorer inter-particle contact and generally lower density of active material in assembled electrodes, the interface-to-bulk ratio is much higher for nanostructured electrodes. While this high contact area with the electrolyte generates a high lithium-ion flux across the interface, side reactions with the electrolyte (for electrodes outside the stability window of the electrolyte) and metal dissolution (the main capacity fading mechanism for intercalation cathodes containing manganese and nickel) are also

proportional to the interface area [26]. Therefore, careful engineering of the interface is a necessary step in lithium-ion battery advancement [43].

1.3.1.4 *Ageing of lithium-ion batteries and interface engineering*

The ageing of lithium-ion batteries is still one of the most serious concerns of battery manufacturers and consumers alike. In chapter 13, a brief overview of the ageing processes is presented. To summarize, most ageing mechanisms, such as electrolyte decomposition, SEI formation, lithium plating, contact loss, metal dissolution and surface layer formation, occur at the surface of the electrode particles. To make matters worse, unlike what happens in Vegas, what happens at the interfaces does not necessarily stay at the interfaces, and dissolved cathode metals can be redeposited on the anode surface, triggering lithium plating and further SEI formation [44]. While the merits of nanostructuring the electrodes are clear from the above paragraphs, a larger surface area implies a greater electrode-electrolyte interface, causing interface-induced ageing for nano-structured electrodes to be much more severe.

To overcome this, interface engineering is widely investigated to stabilize the surface. The graphite-electrolyte interface can for example be stabilised by mild oxidation of the surface, or altering the surface with metal, metal oxides or other forms of carbon, which controls the SEI formation [45, 46]. High volume expansion anodes such as silicon suffer from contact loss and re-initiated SEI formation due to the creation of fresh anode surface upon cracking of the silicon particles. Here, coating does not only stabilise most of the surface, but can form a 'glue' to keep the pulverized anode particles connected to the electronic network, preventing contact loss [47, 48]. Cathode surfaces are usually not stabilised by a controlled SEI, but rather by a metal dissolution barrier, a barrier to prevent electrolyte decomposition or an HF-scavenger in the case of fluorine-based electrolytes, as schematically represented by figure 1.13 for a conformal Al_2O_3 coating on a cathode surface [49]. A wide range of coating materials (Li_2CO_3, MgO, Al_2O_3, $AlPO_4$, ZrO_2, SnO_2, TiO_2, ZnO, CoO, cathode materials, carbon, conductive coatings) can be deposited by an array of possible coating techniques (sol-gel, chemical vapour deposition, physical vapour deposition, pulsed laser deposition, ...) [46, 50].

1.3.2 *Beyond the classical lithium-ion battery*

Besides advances on a materials and engineering level for the classical particle-based lithium-ion battery, progress in energy storage can also be found beyond. For energy storage in medical implants for example, the

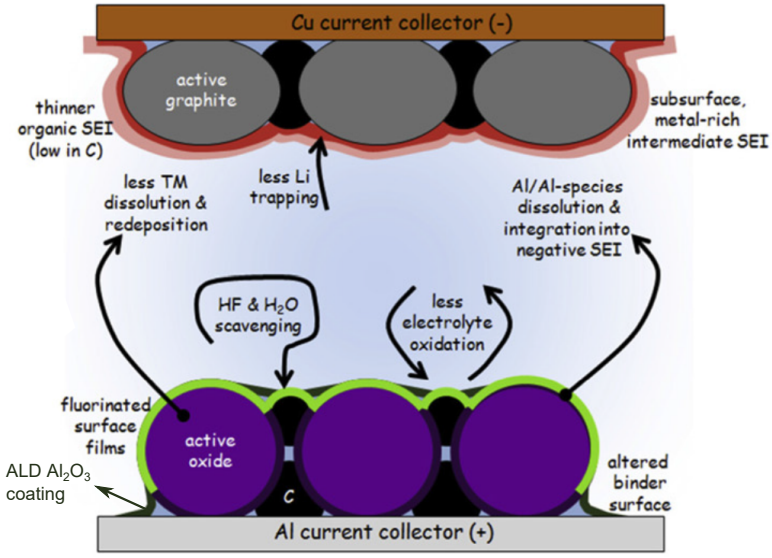

Figure 1.13: (Possible) beneficial effects of cathode surface coating. Figure reprinted from [49].

safety hazard (liquid electrolte leaking, flammable components) excludes liquid-electrolyte based batteries as a candidate [51]. On-chip energy storage requires integratability and flexibility, properties provided by thin-film batteries technology [52–54]. Furthermore, there is a growing consensus that for some applications, the energy density limits of lithium-ion battery may not be enough, and beyond-lithium-ion (BLI) chemistries are needed [55]. Several BLI battery chemistries are finding their way to the spotlight, such as magnesium- and sodium-based storage mechanisms, metal-air and metal-sulfur systems [1]. These novel technology nodes are very promising, but still face serious challenges, as will be discussed below.

1.3.2.1 *All-solid-state lithium-ion batteries & the solid electrolyte*

Classical lithium-ion batteries are comprised of a liquid electrolyte soaked into a separator and throughout the electrode (figure 1.6). This liquid electrolyte usually consists of a lithium salt in a mixture of organic solvent, and is an electronic insulator but a good lithium ion conductor ($1 \times 10^{-2}\,\mathrm{S\,cm^{-1}}$ to $10\,\mathrm{S\,cm^{-1}}$). The organic solvents used for these electrolytes are flammable, posing a serious safety issue for traditional lithium-

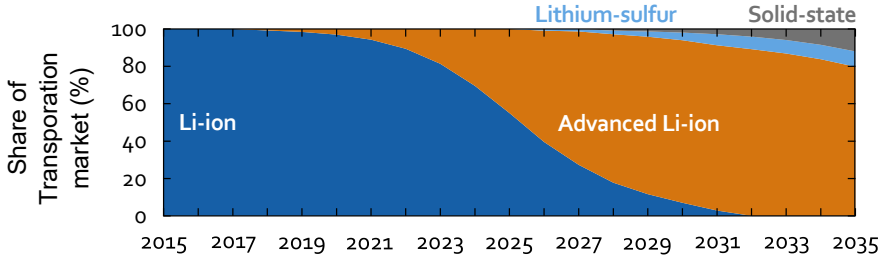

Figure 1.14: Predicted transportation market evolution beyond lithium-ion up to 2035. Figure reprinted from [15].

ion batteries. Batteries for medical implants naturally abide even more stringent safety regulations, and cannot contain a liquid electrolyte. Pacemaker batteries for example are all-solid-state devices, using a solid electrolyte rather than a liquid one. Besides the obvious safety risk, liquid electrolytes also suffer from several other limitations:

- The liquid **reduces the energy density** of the battery, as it requires a separator membrane to keep the electrodes from forming a direct contact, and requires bulky packaging to ensure no air can get to the electrolyte.
- A liquid battery **limits the miniaturisation** of the battery, as the membrane separator requires a certain thickness to maintain a good separating functionality.
- Although the electrolyte is an electronic insulator, the high fields at the interfaces with the electrodes are often outside of the stability window (band gap) of the solvent. This causes the already discussed **SEI formation**, which not only irreversibly consumes lithium, but hinders battery kinetics.

All-solid-state lithium ion batteries are being explored to alleviate these issues. As these compounds are solvent-free, this makes the flammable component redundant and alleviates the safety risks. Furthermore, they have high electronic resistivity, and good stability windows. The challenges for solid-state electrolytes are (1) ionic conductivity and (2) interface stability and matching [56]. Ionic conductivity of solid-state electrolytes is several orders of magnitude lower than that of their liquid counterparts: one of the benchmark solid-state electrolytes, nitrogen-doped lithium phosphate, has an ionic conductivity of only $3 \times 10^{-6}\,\mathrm{S\,cm^{-1}}$ [57]. Significant research effort is invested in finding a solid-state electrolyte with good properties and a high ionic conductivity. However, as the solid electrolytes do not

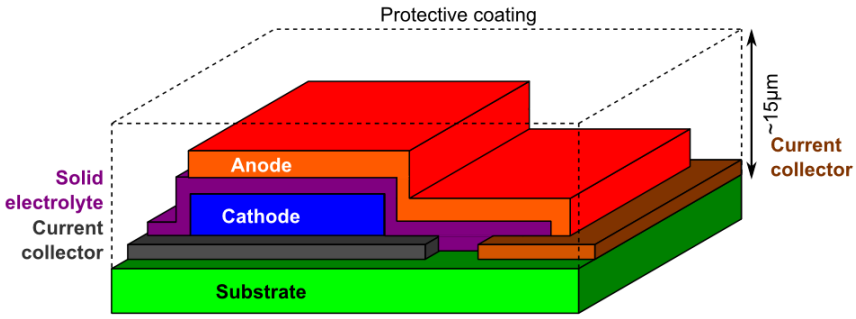

Figure 1.15: Schematic concept of thin-film battery on a flat substrate. Figure adapted from [58].

require a separator, they can be made much thinner, which (partially) compensates the low ionic conductivity. Optimistic market reports predict significant market interest for solid-state batteries: their market value for automotive applications is predicted to climb from $3 billion to $42 billion from 2030 to 2035 (figure 1.14), and solid-state batteries are predicted to take almost 40 % of the battery market for electronics by 2035 [15].

1.3.2.2 *Thin-film all-solid-state batteries*

The interface between the electrodes and the electrolytes is a critical component of the solid-state battery. Interface quality and stability has been found to be one of the determining factors for solid-state battery lifetimes [56]. The interfaces in particle-based batteries are very complex, making it tricky to control them. A possible solution is to move towards thin-film electrodes and electrolytes. This significantly simplifies the interfaces, and makes good quality and matching much more likely.

Another advantage of thin-film all-solid-state batteries is integratability in light of the Internet of Things. The *Internet of Things* (IoT) is defined as the internetworking of physical devices, vehicles, buildings, and other items. Embedded with electronics, software, sensors, actuators, and network connectivity, this enables these smart devices to collect and exchange data [59, 60]. Small wireless sensors need a power source, which can be provided by an energy harvester (for example a small solar cell) and an energy storage device to compensate for the intermittent nature of the energy harvester. As these devices are either on flexible substrates [52, 53] or on-chip devices [54], standard lithium-ion batteries will not stand, and thin-film all-solid-state batteries as the one in figure 1.15 may prove to be the solution to these challenges [58].

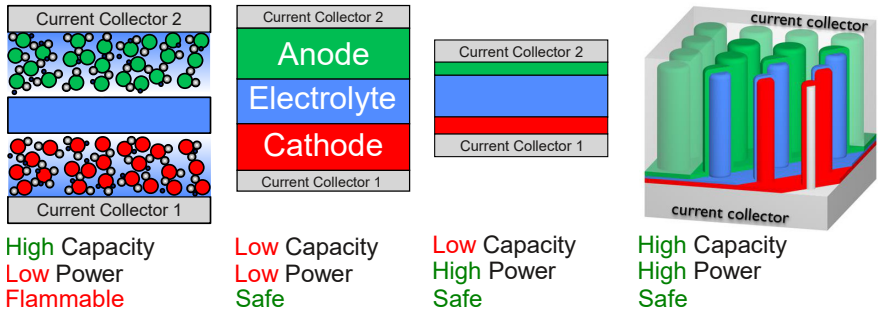

Figure 1.16: Properties of battery architectures. From left to right: classical battery, thin-film battery, truly thin-film battery, 3D thin-film battery. Figure adapted from [61].

For high-power applications, batteries like the one depicted in figure 1.15 will not suffice as the films are several μm thick, so the maximum currents will still be determined by lithium- or electron transport through the bulk of these films. The solution for this is similar to the high-power battery for the particle-based lithium-ion battery: downsizing. By making the layers thinner (from several μm to the nano-metre range), the diffusion lengths are shorter and the battery can be charged and discharged much faster. Of course, making the thin-film battery thinner implies less electrode material, and less storage capacity.

1.3.2.3 *3D Thin-film all-solid-state batteries*

For a battery powering a portable device as a laptop or a smart phone, the volume of the battery is a critical factor as downsizing the form factor of portable electronics is one of the main concerns of manufacturers. For (hybrid) electric vehicles, the same is true: the battery cannot be too large in volume, as it has to fit in the car it's envisioned to power. Thin-film batteries however find their application in powering on-chip devices. For on-chip power source, the actual volume of the battery affects the engineering of the device less than the footprint area. Therefore, the third dimension can be tapped into for higher capacity, and various concepts of 3D all-solid-state thin-film batteries have been proposed. While this builds on the thin-film properties of short diffusion lengths, and high power or high current densities, the 3D concepts increase the energy density per footprint area by the factor of surface area attributed to the 3D substrate. This way, a high capacity can be combined with high power, and integratability towards on-chip devices is maintained, making this the ideal battery architecture for internet-of-things related applications. This approach from

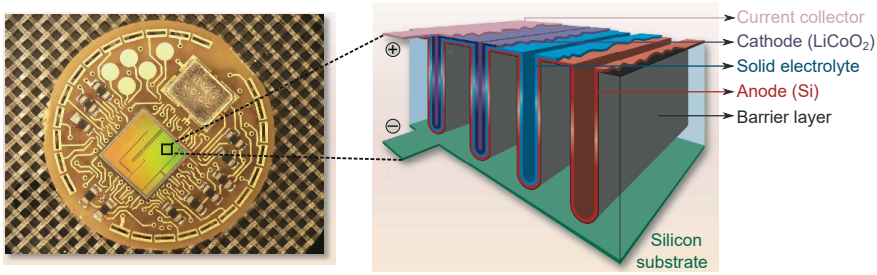

Figure 1.17: Three-dimensional, integrated thin-film all-solid-state battery on a sensor chip, with a 25-fold capacity enhancement compared to the planar thin-film battery as a result of the aspect ratio of the architecture. Figure adapted from [62–64].

classical liquid-based batteries to solid-state thin-film batteries, and culminating onto 3D thin-film batteries is schematically depicted in figure 1.16, indicating the properties of the various approaches. A reported example is shown in figure 1.17.

Deposition of a stack of thin layers on complex 3D high aspect ratio structures such as the one in figure 1.17 requires a good conformal deposition technique, able to deposit the various components of the battery. As the interfaces in thin-film all-solid-state batteries are even more important and critical compared to a liquid-based battery, thin interfacial modifications may also be required for these battery designs. A thin-film deposition technique with excellent conformality and control over film thickness and quality must be used. The use of Atomic Layer Deposition (ALD) for the components of the lithium-ion battery will be the focus of this PhD thesis, with special attention to negative and positive electrodes in part iii, and interfacial concepts in part iv. The use of ALD for all components will be introduced in section 1.4.

1.3.2.4 *Battery types beyond lithium-ion batteries*

Despite advances in classical lithium-ion batteries and the growing effort towards thin-film and/or solid-state lithium-ion batteries, energy storage over the next decades may decide to turn this page altogether. Figure 1.8 reveals some of the next-generation battery options. Two main concepts are examined: lithium-ion based, or alternative ion batteries.

The lithium-ion battery as described in section 1.2.1 is not the only way to use lithium-ions to store energy. Two alternative concepts exist as demonstrated in figure 1.18: lithium-air and lithium-sulfur batteries. The lithium-air battery is an open-system battery with one of the highest

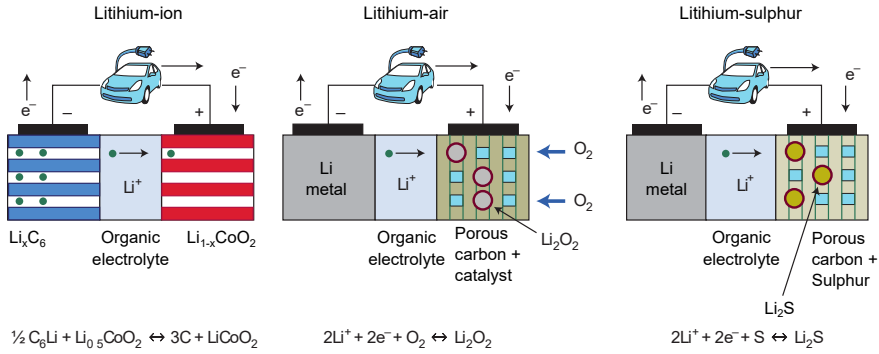

Figure 1.18: Schematic representation of lithium-ion, lithium-air and lithium-sulphur cells during discharge. Figure adapted from [65].

energy densities available today. Lithium metal is used as a negative electrode and carbon as a positive electrode, and during discharge lithium is oxidized using ambient oxygen on the surface of the positive electrode:

$$2\,\mathrm{Li} + \mathrm{O_2} \longrightarrow \mathrm{Li_2O_2} \tag{1.15}$$

During recharging the lithium peroxide is dissolved to let the free lithium ions move back to the lithium metal electrode. The fact that the lithium-air battery is an open, air-breathing system (no heavy packaging needed), as well as the low weight of both the lithium and carbon electrodes, allows the lithium-air batteries to provide an energy density around $1.0\,\mathrm{kW\,h\,kg^{-1}}$, close to that of gasoline ($1.7\,\mathrm{kW\,h\,kg^{-1}}$) and 5-10 times higher than that of the lithium-ion battery ($100\,\mathrm{W\,h\,kg^{-1}}$ to $200\,\mathrm{W\,h\,kg^{-1}}$) [55]. The high power density and open-system approach renders it particularly interesting for large-scale batteries, such as stationary storage or electric vehicles [62]. However, lithium-air is still in a research stage, and serious issues with electrolyte decomposition, energy efficiency, rechargeability, undesired reactions, cathode stability and dendrite formation need to be solved before this energy storage mode can be commercialised [1, 65, 66].

The lithium-sulphur battery (Li-S) on the other hand is a closed-system cell with an even higher energy density, composed of a lithium metal negative electrode and a sulphur composite positive electrode. During discharge, the cyclo-S_8 ring is opened and reacts to form various degrees of lithium-sulphur polysulphides, up to dilithium sulphide:

$$2\,\mathrm{Li^+} + 2\,\mathrm{e^-} + \mathrm{S} \rightleftharpoons \mathrm{Li_2S} \tag{1.16}$$

This reaction yields a theoretical energy density of $\sim 2500\,\mathrm{W\,h\,kg^{-1}}$, with the added advantages of a closed system approach (which does not depend on any external material supply), and the very high abundance, low

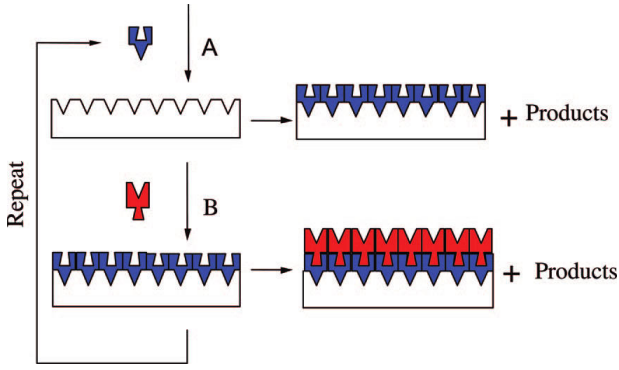

Figure 1.19: Schematic representation of the principle of atomic layer deposition, illustrating its self-limiting properties. Figure reprinted from [68, 69].

cost and non-toxicity of sulphur [65]. Similar to lithium-air, major challenges need to be overcome to bring Li-S from the research to the commercial stage, such as large volume changes, limited cycle life, the insulating nature of sulphur and lithium sulphide and low Coulombic efficiencies.

Finally, other ions than lithium can also be used to store energy. Sodium-, magnesium- and aluminium-based batteries have a similar energy density promise to that of lithium-ion, but have several potential advantages. First, the cost can be a tipping point towards beyond-lithium energy storage in the future. Sodium for example is far more abundant than lithium and offers an excellent geographical distribution, making the cost for bulk metal sodium almost an order of magnitude lower than for lithium metal, the latter of which is expected to increase in price over the coming years [55]. A secondary advantage to beyond-lithium ions, is double charging. Magnesium for example can be ionized twice to Mg^{2+}, and two electrons can be released from the insertion of a single Mg ion. This gives a higher volumetric energy density to a magnesium metal anode (3833 mA h cm^{-3}) compared to a lithium metal anode (2036 mA h cm^{-3}). However, serious challenges are still faced before lithium-ions will be replaced, such as reduced ion mobility in the electrolyte due to the higher charge density and the formation of passivating layers on the metal anodes [67].

1.4 ATOMIC LAYER DEPOSITION FOR THE LITHIUM-ION BATTERY

1.4.1 *Atomic layer deposition*

This thesis deals with possible applications of atomic layer deposition (ALD) for lithium ion batteries. The concept of ALD was invented both in Russia in the 1960s, and again completely independently invented in Finland 10 years later [70]. The language barrier, the different naming and the different end-goal applications explain why it was invented twice, without either team knowing from one another. The thin-film deposition technique fits in the class of Chemical Vapour Deposition (CVD) techniques, meaning it works by chemical interactions between a precursor vapour and the substrate surface. The principle that makes ALD different from other CVD techniques is illustrated by figure 1.19, and hinges on self-limiting reactions [68, 69]. A first precursor, called A, is introduced to the surface of the substrate in gaseous state. As figure 1.19 illustrates, it can react with the surface, but once this reaction has occured, it can not react with the formed surface any further. Next, gas A is removed from the reaction chamber, and a second precursor, gas B, is introduced to the substrate. It too can only react to the end-groups of precursor A, and not to itself. By cycling gas A - evacuation - gas B - evacuation, a film is grown which has a uniform thickness across the entire substrate. A more detailed, chemical and in-depth discussion of various reactor concepts, film properties and energy-enhanced ALD processes can be found in the string of review papers, published throughout the last decades [69, 71–76].

This method of deposition has several advantages and disadvantages compared to other conventional thin-film deposition techniques, such as sol-gel deposition, physical vapour deposition and chemical vapour deposition. The advantages are listed below.

- The **conformality** of ALD is inherited from the self-limiting nature of the gas-solid interactions. This sets it apart from other coating techniques, as shown schematically in figure 1.20. The conformality of ALD is one of the main stakeholders that have placed ALD in an almost unique position when it comes to depositing uniform and conformal thin-films on high-aspect ratio structures. Very few techniques can match the conformality and versatility of atomic layer deposition.

- **Digital thickness control** down to the sub-Å level, as a single ALD cycle produces one (sub)monolayer per cycle on the complete accessible surface.

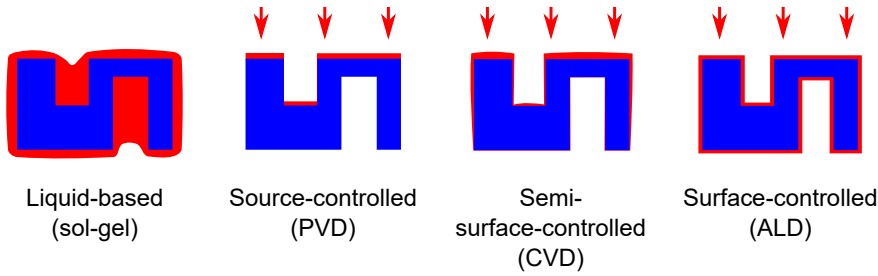

Figure 1.20: Schematic illustration of the degree of film uniformity and surface coverage conformality for several types of thin-film deposition classes. Figure adapted from Beneq.

- While many deposition techniques, such as solution-based techniques and chemical vapour deposition, require high temperatures (>400 °C), the energy required for most ALD processes can be relatively low (depending on the precursor chemistry), resulting in a **low substrate temperature**, typically from room temperature to 300 °C.
- The gas-phase nature of ALD allows reaction at every accessible surface-site, which results in the growth of **uniform and pinhole-free films**, for an ideal ALD process[6].
- The specific chemical exchange or combustion reaction chemistry allows ALD to grow films with a very **low impurity content**, almost uniquely so for such low growth temperatures.

Of course, there are also some disadvantages to atomic layer deposition, mainly related to its cost and deposition speed.

- The need for specialized (vacuum) equipment and carefully designed precursor molecules, constributes to the **high cost** of atomic layer deposition processes. While for the semiconductor industry the cost of the ALD coating is not a limiting factor, large-scale powder coating, requiring massive throughput and very large quantities of precursor, has not broken through the cost barrier yet.
- While the (sub)monolayer-mode growth has the advantage of excellent thickness control, it also strains the **deposition speed** and limits the realistic ALD **coating thickness**. Typical growth rates are in the range of 0.01 nm to 1 nm per cycle. Cycle speed can range from minutes (high-vacuum ALD) to fractions of seconds (purge-type and

6 Metal ALD is an example of non-ideal ALD, as the initial growth mode is nucleation controlled.

atmospheric ALD), which brings the growth time for a 100 nm film anywhere between several days for the slowest processes and high-vacuum type ALD, to several minutes for the fastest processes and reactor designs. Coatings of several μm thick, as the coatings required for the electrodes of traditional thin-film batteries, are just too thick for ALD.

- **Complexity of compounds**. While ALD is extremely suited to grow binary compounds such as oxides, sulphides and nitrides, it is significantly more difficult to grow ternary or quaternary compounds.

1.4.2 *Applications of ALD for lithium-ion batteries*

The properties of an ideal ALD process such as saturation, temperature window and linearity tests, and the characterisation of these characteristics, will be discussed in the next chapter. Here, we will discuss the use of ALD in the field of lithium-ion batteries, the topic of this PhD thesis. The main focus will be on ALD of electrode materials (part iii) and ALD for interface tuning and modification (part iv), which will be introduced more broadly in the respective chapters.

The first application of ALD for lithium-ion batteries was already reported in 2000, when V_2O_5 nanofilms were investigated as LIB cathodes [77]. Several years later, ALD resurfaced for anode-electrolyte interface modification (ALD of TiN on $Li_4Ti_5O_{12}$) [78]. Several excellent reviews have surfaced in recent years detailing the use of ALD for lithium ion batteries. The first were published in 2012, appearing online almost simultaneously in November 2011. Researchers from the university of Eindhoven (The Netherlands) focussed on application of ALD for nanostructured lithium-ion batteries [79], while at the same time a collaboration between the university of Western Ontario (Canada) and the Brookhaven National Lab (USA) detailed the emerging application of ALD for lithium-ion battery studies [80]. Several review papers have been published since that time, and the interested reader can glance through the following references: [81–85]. Atomic layer deposition for lithium ion batteries can be roughly categorised in three sections:

1. ALD of the **active components** of the battery (positive and negative electrodes, solid electrolytes)

2. ALD modification of the surfaces and **interfaces** (protective coatings, interface stabilisation, separator coatings)

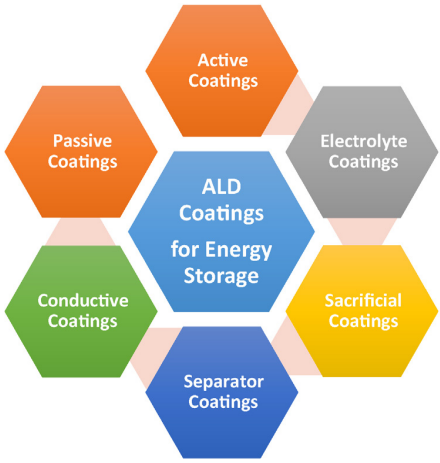

Figure 1.21: Different possible applications of ALD coatings in energy storage devices. Figure reproduced from [84].

3. ALD of **functional films** in the battery (current collectors) or of coatings for enhancing battery **manufacturability** (sacrificial coatings).

Active battery components

ALD coatings typically do not exceed several hundreds of nanometres, due to the limitations on cost and deposition speed (although the industrial use of thicker films, ∼1 µm, has been demonstrated in commercial batch tools). This implies that for the planar thin-film battery (thickness ∼10 µm, component thickness several μm, see figure 1.15), the electrode or electrolyte films are too thick to be grown using ALD. However, for nanostructured lithium-ion batteries (3D thin-film LIB), the electrodes can be made thinner, as described above, and are within the realm of ALD. Therefore, ALD has been used to procure an assortment of nanostructured electrodes, such as nano-laminates, coated nano-particles, nano-ribbons, nanotubes, nano-wires and 3D nano-films [79, 80].

The excellent film quality, control over composition and crystallinity provided by ALD allows electrodes and electrolytes grown by ALD to have a secondary application: the synthesis of thin, planar model systems. A uniform thin film with well-controlled properties allows the study of specific material characteristics: the thin-film system provides simplified one-dimensional currents and is unbothered by the complex interplay of various components of the classical battery, such as binder, conductive

additive, particle size, solvent composition, current collector adhesion and so on.

The electrolyte thickness in a typical thin-film battery is in the range of 500 nm to 2000 nm [63]. If the electrolyte film properties are excellent, as for LiPON grown by PVD [86] or ALD [87], the same functionality can be achieved at much lower thickness (several tens of nanometres), while the effective resistance can be reduced (since $R \sim d/\sigma$, with d the film thickness and σ the conductivity). This condition, in unison with the excellent uniformity, film purity and conformality, makes ALD suited not only to deposit solid-state electrolytes for thin-film batteries, but also as a component in a more classical battery.

Interface modifications & engineering of the surface properties

Furthermore, ALD can deposit films down to the monolayer level, which can be used to alter the surface properties of the substrate the film is deposited on, such as wettability, reactivity and the zeta-potential. Ultrathin ALD coatings have been heavily investigated since 2010, with the main focus on ALD Al_2O_3. The need for excellent conformality and absolute thickness control makes ALD almost uniquely suited to deposit these films, and the low thickness required to significantly enhance battery lifetimes makes the low growth rates and high cost of ALD less stringent. Surface modification has not only been applied to mediate various electrode issues (solvent oxidation, SEI formation, metal dissolution, structural stabilisation, and so on), but has for example also been shown to modify the wetting of separator membranes in classical batteries to allow for the use of polar solvents (such as PC), and increase the thermal stability of the separators [88].

From functional coatings to the all-ALD battery

Finally, ALD can also be used in nanostructured batteries to deposit functional coatings, such as current collectors, passivating films, sacrificial coatings and adhesion layers. The versitility of ALD makes it possible to deposit a complete functional lithium-ion battery using this single deposition technique. Last year, Létiche *et al.* [54] demonstrated the deposition of a half-cell 3D thin-film all-solid-state lithium-ion battery. They used silicon double-patterned microtubes, passivated with a 120 nm ALD Al_2O_3 film, coated with a 40 nm ALD Pt current collector. The electrode was an ALD TiO_2 film with a thickness ranging from 55 nm to 155 nm, and was covered with a thin-film ALD Li_3PO_4 solid electrolyte coating (20 nm to

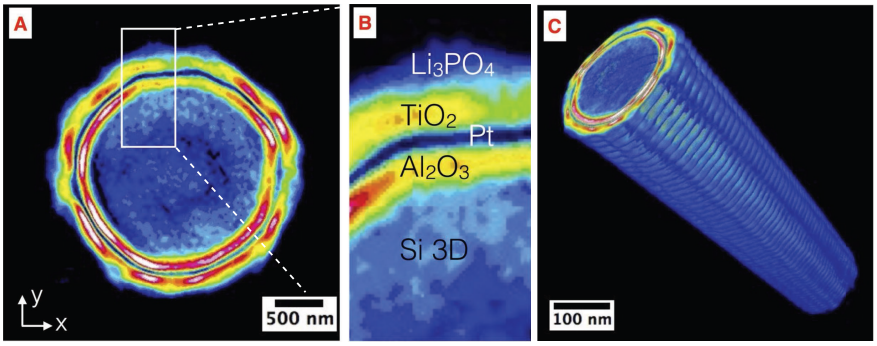

Figure 1.22: Transmission microscopy microtomography images of the ALD microbattery on a single silicon micropillar. Figure adapted from [54].

40 nm), as shown in figure 1.22. This battery demonstrates a 105x surface capacity enhancement by deposition onto the 3D scaffold [54].

For commercial applications, ALD is too slow (and too expensive) to be used for all components, except as a scientific proof-of-concept, in niche applications such as on-chip energy storage, or in medical implants. However, for certain critical components of the battery, the use of ALD can be justified. In that light, interface layers and solid-electrolyte layers will most likely emerge into commercial batteries, as the thickness, uniformity and conformality provided by ALD are almost unmatched by any other deposition techniques.

1.5 Goals and Outline of the Thesis

In this work, atomic layer deposition is evaluated for two aspects of the lithium-ion battery: nano-scaled and thin-film electrodes on the one hand, and interface engineering and protective coatings on the other hand. The goals of this research are as listed below:

- Evaluate ALD and post-ALD annealing as a tool to control the crystal phase and oxidation state in thin-film manganese and vanadium oxides, and unravel the influence of parameters such as ALD process gas, annealing temperature, ambient and substrate.
- Investigate whether ALD can be used for the deposition for lithium-ion battery thin film electrodes and, in particular, conformally coatings films for 3D thin-film electrodes for high power electrodes, in particular those based on manganese and vanadium oxides.

- Use ALD for the deposition of model-system electrodes to study the effect of oxidation state and crystalline nature on the electrochemical performance of lithium-ion battery electrodes.
- Study the effect of ultra-thin simple metal oxide coatings on model-system lithium-ion battery electrodes to unravel the effect on the battery kinetics.
- Evaluate whether a good kinetic coating on a model-system electrode translates to similar performance enhancements on a more complex 3D-structured lithium-ion battery electrode.

Part iii will deal with the atomic layer deposition of manganese- and vanadium oxides for thin-film anodes and cathodes. Manganese-based electrodes were chosen as a candidate thin-film electrode, as manganese provides a more sustainable and cheaper alternative compared to cobalt- or nickel-based electrode chemistries. The focus is on an exact control of composition, crystalline nature and oxidation state of the films. This was done by developing several novel plasma-enhanced ALD processes for manganese oxide, allowing a control over the electrochemical nature of the ALD films by tuning the ALD process conditions, related to the exact nature of the plasma used during film deposition. Crystalline films in the range of MnO to MnO_2 (except Mn_2O_3) could be deposited, ranging from a conversion anode to an insertion cathode, respectively (Paper I). Further control over the phase transformations was demonstrated by post-ALD annealing, and the missing Mn_2O_3 phase could be obtained by the choice of annealing conditions and temperature. The water splitting properties of MnO_2 and Mn_2O_3 films were demonstrated in this chapter (Paper II).

ALD vanadium oxides were used as model systems to further study the effects of phase, oxidation state and crystalline nature of the films on the electrochemical properties. Vanadium oxides have been investigated since the initial lithium-ion battery research, but the main focus has always been on the V_2O_5-phase. Here, the ALD deposition of vanadium oxide resulted in amorphous VO_2 films. These could be annealed to phase-pure VO_2 (M1), VO_2 (B), V_6O_{13}, V_4O_9, V_3O_7 and V_2O_5. A careful interplay between initial film, temperature, substrate and ambient conditions on the crystallisation and phase formation was unravelled, as well as a clear influence of the process gasses used during the atomic layer deposition. Almost all of the vanadium oxides obtained show a clear electrochemical storage behaviour between 1.5 and 4V *vs* Li^+/Li, and capacities up to twice the capacity of commercial cathode compounds were obtained (Paper III).

Conventionally, crystalline compounds are used as battery cathodes. However, it has been shown that amorphous materials may show inter-

esting properties compared to their crystalline counterparts, thanks to the high diffusion coefficients (typically resulting in good battery kinetics) and lower densities (typically allowing for more lithium ion storage). The low-temperature nature of ALD enables the deposition of amorphous vanadium oxides, and their electrochemical performance were examined and benchmarked to their crystalline counterparts. A low-temperature variant of a plasma-enhanced V_2O_5 ALD process was developed to grow amorphous V_2O_5 films, which allowed not only the comparing study of amorphous *vs* crystalline vanadium oxide electrodes, but also the evaluation of VO_2 *vs* V_2O_5, as the latter is investigated most profoundly in literature. Amorphous VO_2 was found to exhibit a storage capacity more than three times higher compared to the reversible regime of crystalline V_2O_5, and similarly high capacities for amorphous V_2O_5 and crystalline VO_2. Furthermore, far better charge-discharge kinetics for the amorphous compounds were observed. To demonstrate the use of these films in 3D thin-film micro-batteries, amorphous VO_2, VO_2 (B) and crystalline V_2O_5 were deposited on a high aspect-ratio pillar structure, demonstrating a $>20\times$ footprint capacity increase, while maintaining the excellent kinetics inherited from the thin-film nature of the electrodes (Paper IV).

In part iv ALD for interface modifications was studied. The most-often used ALD interface modifier, ALD Al_2O_3, was examined and benchmarked to another interface modifier, amorphous ALD TiO_2. Simple, binary oxides using low-temperature ALD processes were selected to allow the results from this work to be potentially implementable in up-scaled battery production. Both ALD Al_2O_3 and ALD TiO_2 coatings were investigated on two thin-film model electrodes: anatase thin-film TiO_2 as a near-ideal electrode, and crystalline thin-film $LiMn_2O_4$ with known solvent oxidation issues. The ideal model system reveals that ALD Al_2O_3 is just a resistive coating with a very high resistivity towards lithium, and layers beyond 2 nm are completely capacitive and blocking. Amorphous ALD TiO_2 on the other hand never exhibits blocking features. Solvent oxidation on $LiMn_2O_4$ could be partially overcome by ALD Al_2O_3, but the kinetic barrier posed by the additional impedance is detrimental for the thin-film kinetics. ALD TiO_2 on the other hand can also overcome solvent oxidation, and does not pose a kinetic barrier, leading to surprisingly enhanced electrode kinetics (Paper V).

Finally, the 3D thin-film lithium-ion battery electrodes and ALD interface modifiers are brought together in Paper VI. Carbon nano-tubes are used as 3D template for surface enhancement, and are covered with ALD TiN as a current collector, V_2O_5 as a LIB cathode and amorphous ALD TiO_2 as an interface modifier. The good thin-film kinetics of ALD V_2O_5

are translated onto the 3D-structured template, but vanadium dissolution limits the cyclability of the cathodes. If a thin ALD TiO_2 coating is used to modify the surface, the cyclability is enhanced significantly. High-resolution tomography in combination with electrochemical methods are used to study and unravel the mechanism, and the ALD TiO_2 is shown not only to alleviate vanadium dissolution, but to aid in restructuring the V_2O_5 during cycling, resulting in enhanced thin-film kinetics.

1.6 SUMMARY OF THE CONTRIBUTIONS

This PhD thesis is paper-based, meaning that the research done is presented in the form of published or submitted peer-reviewed papers, preceded by introductory chapters. The papers included in this thesis are listed on the next page. Other publications besides the paper making up this PhD thesis and conference contributions are also listed.

1.6.1 *Publications related to this work*

Paper I **Deposition Of MnO Anode And MnO_2 Cathode Thin Films By Plasma Enhanced Atomic Layer Deposition Using The $Mn(thd)_3$ Precursor**
F. Mattelaer, P. M. Vereecken, J. Dendooven and C. Detavernier
Chemistry of Materials 27 (10), 36283635 (2015).

Paper II **Manganese Oxide Films With Controlled Oxidation State For Water Splitting Devices Through A Combination Of Atomic Layer Deposition And Post-deposition Annealing**
F. Mattelaer, T. Bosserez, J. Rongé, J. A. Martens, J. Dendooven and C. Detavernier
RSC Advances 6 (100), 98337-98343 (2016).

Paper III **Atomic Layer Deposition Of Vanadium Oxides For Thin-film Lithium-ion Battery Applications**
F. Mattelaer, K. Geryl, G. Rampelberg, T. Dobbelaere, J. Dendooven and C. Detavernier
RSC Advances 6 (115), 114658-114665 (2016).

Paper IV **Amorphous And Crystalline Vanadium Oxides As High-Energy And High-Power Cathodes For 3D Thin-Film Lithium Ion Batteries**
F. Mattelaer, K. Geryl, G. Rampelberg, J. Dendooven and C. Detavernier
ACS Applied Materials & Interfaces (2017).

Paper V **The Influence of Ultrathin Amorphous ALD Alumina and Titania On The Rate Capability of Anatase TiO_2 and $LiMn_2O_4$ Lithium Ion Battery Electrodes**
F. Mattelaer, P. M. Vereecken, J. Dendooven and C. Detavernier
Advanced Materials Interfaces (2017).

Paper VI **Heterogeneous TiO_2/V_2O_5/Carbon Nanotube Electrodes For Lithium-ion Batteries**
M. Kurttepeli, S. Deng, F. Mattelaer, D. J. Cott,
P. M. Vereecken, J. Dendooven, C. Detavernier, S. Bals
ACS Applied Materials & Interfaces (2017).

1.6.2 *Other publications*

- **Amorphous and perovskite $Li_{3x}La_{(2/3)x}TiO_3$ (thin) films via chemical solution deposition: solid electrolytes for all-solid-state Li-ion batteries**

  E. J. van den Ham, N. Peys, C. De Dobbelaere, J. D'Haen, F. Mattelaer, C. Detavernier, P. H. L. Notten, A. Hardy, and M. K. Van Bael

  J. Sol-Gel Sci. Technol. 73 (3), 536-543 (2015)

- **Plasma-Enhanced Atomic Layer Deposition of Iron Phosphate as a Positive Electrode for 3D Lithium-Ion Microbatteries**

  T. Dobbelaere, F. Mattelaer, J. Dendooven, P. M. Vereecken, and C. Detavernier

  Chem. Mater. 28 (10), 3435-3445 (2016)

- **Plasma-Enhanced Atomic Layer Deposition of Iron and Titanium Phosphates as Electrode Materials for 3D-Structured Lithium-Ion Microbatteries**

  T. Dobbelaere, F. Mattelaer, J. Dendooven, P. M. Vereecken, and C. Detavernier

  ECS Trans. 75 (6): 35-44 (2016)

- **Effect of Annealing Atmosphere on $LiMn_2O_4$ for Thin Film Li-Ion Batteries from Aqueous Chemical Solution Deposition**

  G. Maino, J. D'Haen, F. Mattelaer, C. Detavernier, A. Hardy, and M. K. Van Bael

  J. Mater. Chem. A, 4 (47), 18457-18469 (2016)

- **Molecular Layer Deposition of "titanicone", a Titanium-Based Hybrid Material, as an Electrode for Lithium-Ion Batteries**

  K. Van de Kerckhove, F. Mattelaer, D. Deduytsche, P. M. Vereecken, J. Dendooven, and C. Detavernier

  Dalton Transactions 45 (3), 1176-1184 (2016)

- **Electro-Precipitation via Oxygen Reduction: A New Technique for Thin Film Manganese Oxide Deposition**

  G. Vanhoutte, M. Wu, S. Schaltin, F. Mattelaer, C. Detavernier, P. M. Vereecken, K. Binnemans, and J. Fransaer

  J. Mat. Chem. A, 4 (35), 13555-13562 (2016)

- **Plasma-Enhanced Atomic Layer Deposition of Titanium Phosphate as an Electrode for Lithium-Ion Batteries**

  T. Dobbelaere, F. Mattelaer, A. K. Roy, P. M. Vereecken, and C. Detavernier

  J. Mat. Chem. A, 5 (1), 330–338 (2017)

- **Electrodeposition of Insulating Poly (Phenylene Oxide) Films with Variable Thickness**

  M. Y. Timmermans, F. Mattelaer, S. Moitzheim, N. Clerckx, A. Sepulveda, S. Deheryan, C. Detavernier, and P. M. Vereecken

  J. Appl. Polym. Sc., 134 (10), 44533 (2017)

- **Molecular Layer Deposition of Vanadicone, a Vanadium-based Hybrid Material, as an Electrode for Lithium-ion Batteries**

  K. Van de Kerckhove, F. Mattelaer, D. Deduytsche, P. M. Vereecken, J. Dendooven, and C. Detavernier

  Dalton Transactions (2017)

- **Electrochemical deposition of thick and adherent MnO_2 films for energy storage devices**

  M. Y. Timmermans, S. Deheryan, F. Mattelaer, N. Labyedh, S. Zankowksi, C. Detavernier, and P. M. Vereecken

  In writing (2017)

1.6.3 *Conference contributions*

- **Controlling the oxidation state of manganese during plasma enhanced atomic layer deposition using the $Mn(thd)_3$ precursor**

  F. Mattelaer, P. M. Vereecken, J. Dendooven and C. Detavernier

  12th International Baltic conference on Atomic Layer Deposition, Helsinki, Finland (2014) *Oral contribution*

- **Control of the oxidation state of manganese during plasma enhanced atomic layer deposition with the $Mn(thd)_3$ precursor**

  F. Mattelaer, P. M. Vereecken, J. Dendooven and C. Detavernier

  AVS Topical conference on Atomic Layer Deposition, Kyoto, Japan (2014) *Poster contribution*

- **Deposition of MnO Anode and MnO_2 Cathode Thin Films by PE-ALD Using $Mn(thd)_3$**

  F. Mattelaer, P. M. Vereecken, J. Dendooven and C. Detavernier

  Workshop - ALD for Batteries, Ghent, Belgium (2014) *Oral contribution*

- **Electropolymerization of Poly (phenylene oxide) Films with Variable Thickness**

  M. Y. Timmermans, S. Deheryan, F. Mattelaer, C. Detavernier, and P. M. Vereecken

  228th ECS Meeting, Phoenix, AZ, USA (2015) *Poster contribution*

- **Electrodeposition of Thick MnO2 Films on Restrictive Substrates**

  M. Y. Timmermans, S. Deheryan, F. Mattelaer, C. Detavernier, and P. M. Vereecken

  228th ECS Meeting, Phoenix, AZ, USA (2015) *Oral contribution*

- **Novel method for conformal $LiMn_2O_4$ thin films fabrication on planar and 3D microstructure substrates**

  N. Labyedh, M. Timmermans, F. Mattelaer, M. Mees, C. Detavernier, and P. M. Vereecken

  230th ECS Meeting: PRiME, Honolulu, HI USA (2016) *Oral contribution*

- **A new look on ALD vanadium oxides for 3D thin-film lithium ion batteries**

  F. Mattelaer, K. Geryl, T. Dobbelaere, G. Rampelberg, J. Dendooven, and C. Detavernier

  Joint EUROCVD 21- Baltic ALD 15, Linköping, Sweden (2017) *Poster contribution*

- **ALD Vanadium Oxides for 3D Thin-film Lithium Ion Batteries**

  F. Mattelaer, M. Kurttepeli, S. Deng, D. J. Cott, P. M. Vereecken, J. Dendooven, S. Bals, C. Detavernier

  AVS Topical conference on Atomic Layer Deposition, Denver, Co, USA (2017) *Oral contribution*

- **Unravelling The Role of ALD Al_2O_3 and TiO_2 Protective Coatings on Lithium-Ion Battery Electrodes**

  F. Mattelaer, K. Geryl, T. Dobbelaere, G. Rampelberg, J. Dendooven, and C. Detavernier

  AVS Topical conference on Atomic Layer Deposition, Denver, Co, USA (2017) *Oral contribution*

2

EXPERIMENTAL METHODS

This chapter briefly describes the experimental methods used throughout this work. It comprises the equipment and techniques used to deposit thin films (section 2.1), a brief explanation giving insight into the characterisation techniques used for the physical properties of the thin films (section 2.2) and electrochemical methods used to study them (section 2.3). Since this thesis is paper-based, the exact experimental details are found at the beginning of every paper, and this chapter is meant as a reference for those unfamiliar with some deposition- or measurement techniques.

2.1 THIN FILM DEPOSITION

Two deposition techniques were used in this work. Physical vapour deposition (PVD) was used as a workhorse to deposit films that functioned as a planar current collector, as an adhesion layer or as a planar electrode for electrochemical characterisation. The actual PVD technique used for this work was DC magnetron sputtering, but the abbreviation 'PVD' will be used throughout this work. The main advantage of PVD for these purposes is the ease of deposition and the high deposition rates usually associated with PVD. Magnetron sputtering will not be discussed here in detail, but the interested reader can find reviews detailing the principle and applications [89–91]. Atomic layer deposition (ALD) is the real backbone of this thesis. Processes were developed and used to deposit conformal current collectors, seed layers, adhesion layers, electrodes and interface coatings. The fundamental principles, advantages and limitations of atomic layer deposition were detailed in the introduction chapter (section 1.4.1). Here, some more practical items are explained, such as ALD process characteristics, precursors, substrates, reactor design and *in-situ* characterisation techniques.

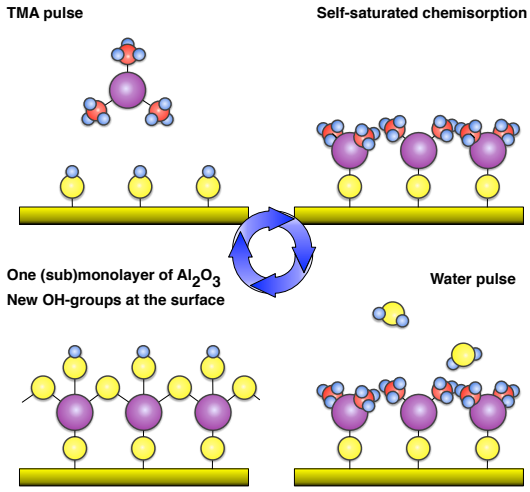

Figure 2.1: The four steps of the TMA-water ALD process: TMA exposure to the $-OH$ surface (top left), evacuation of the saturated $-Al(CH_3)_2$ surface (top right), H_2O pulse (bottom right) and evacuation of the freshly formed $-Al-OH$ surface (bottom left).

2.1.1 *Atomic layer deposition*

As was explained in chapter 1, an ALD process is based on self-limiting gas-surface reactions. A typical example is the TMA-H_2O ALD process depicted in figure 2.1. This process has been examined so often, it is considered a model system for atomic layer deposition [72]. The cycle is based on sequentially pulsing and removing TMA and water. ALD reactors are categorised based on how the precursor removal steps are performed. This can be done by purging away the remainder of reaction products and unreacted precursor molecules with an inert gas (purge-type reactor; flow-type or atmospheric ALD) or by pumping the ALD chamber to a low base pressure of typically 10^{-6} mbar to 10^{-7} mbar (pump-type reactor), effectively removing the reactive components (pump-type ALD) [69].

The reactor used for the work done in this thesis is a home-built high vacuum-type reactor [93–95]. The reactor is depicted schematically in figure 2.2. A high-vacuum pump is backed to 10^{-2} mbar by a rotation pump, and evacuates the stainless steel chamber (approx. 20cm in diameter) to a base pressure of 10^{-7} mbar through a gate valve. The chamber walls are heated to 150 °C to prevent precursor and water condensation. On top, a

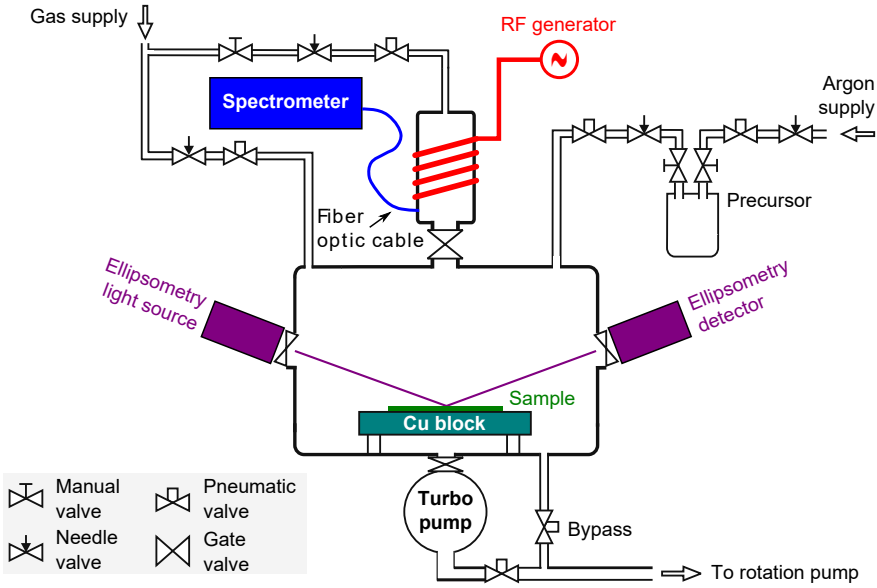

Figure 2.2: The high-vacuum ALD reactor used for the depositions in this work, equipped with the *in-situ* characterisation techniques used. Figure adapted from [92].

second gate valve connects the chamber to a glass column, in which gas can be ionized to a plasma by an inductively coupled radio frequency plasma generator (13.56 MHz). This attachment allows the use of this remote plasma as a reaction step during ALD (plasma-enhanced ALD or PE-ALD). Two *in-situ* measurement technique attachments, ellipsometry and optical emission spectrometry, are also depicted connected to the reactor, and will be explained in section 2.2. The whole system is controlled by in-house developed LabView-based software, rendering the setup extremely versatile.

Several gas and precursor inlets are connected to the chamber and plasma column through pneumatic valves. The materials grown in this work include Pt, Al_2O_3, TiO_2, TiN, VO_2, V_2O_5, MnO_2, MnO and Mn_3O_4. (PE-) ALD processes were readily available for the first five at the lab [94, 96–99]. ALD of MnO_2 was implemented based on an existing process [100, 101]. Novel PE-ALD processes were developed and published for the other manganese oxides [102]. The precursors used for these depositions are visualised in figure 2.3 and listed below:

- **(MeCp)PtMe$_3$**: (methylcyclopentadienyl)trimethylplatinum for Pt ALD (oxygen-based ALD)

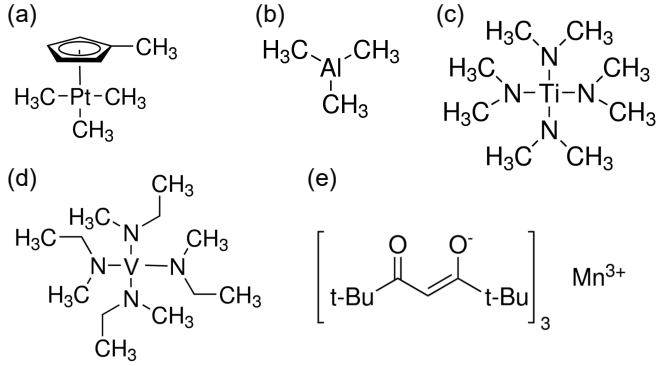

Figure 2.3: Structure of the precursors used in this thesis. (a) (MeCp)$PtMe_3$, (b) TMA, (c) TDMAT, (d) TEMAV and (e) $Mn(thd)_3$.

- **TMA**: trimethyl aluminum for Al_2O_3 (water-based ALD)
- **TDMAT**: tetrakis(dimethylamido) titanium for TiO_2 (water-based ALD) and TiN (NH_3 plasma-based PE-ALD)
- **TEMAV**: tetrakis(ethylmethylamido)vanadium for VO_2 (water- or ozone-based ALD) and V_2O_5 (oxygen-plasma PEALD)
- **$Mn(thd)_3$**: tris(2,2,6,6-tetramethyl-3,5-heptanedionato) manganese for the manganese oxides (ozone-based ALD and various plasma-based PE-ALD)

The samples are placed directly on a copper block (max. 5 cm × 5 cm) which can be heated up to ∼400 °C. The substrates used in this thesis are all silicon-based: either 100 nm thermal silicon oxide on silicon (SiO_2/Si), a current collector on top of silicon oxide (Pt/TiN/SiO_2/Si) or etched silicon micropillars. Other substrates are also within the realm of possibilities, for example, but not limited to, metal foils, polymers, textiles and powders can also be coated in this setup, but are beyond the scope of this PhD thesis.

2.1.2 *Characteristic properties of the ALD process*

As the ALD process is governed by the chemistry of the gas-surface reactions, the properties of these half-cycles determine the validity of the atomic layer deposition and the quality of the films. These properties are:

- **Growth per cycle (GPC)**. The growth per cycle is determined by the available surface groups that can be accessed by the precursor

molecules, and depends on energy (temperature, plasma energy) and steric hindrance (remaining ligands on the bound precursor molecule block nearby available surface sites).

- **Saturation**. As a pulse duration lengthens, an increasingly larger fraction of the surface is covered by the new surface groups. As the growth per cycle increases with increasing surface coverage, the former is dependant on the degree of surface coverage. When all available surface sites are consumed, increasing the pulse time further has no influence on the GPC. This phenomenon is called saturation, and is a critical condition not only for efficient precursor usage but also for conformality of the coating, as the surface sites deep within a complex substrate will be the last to be reached by the precursors. It is dependant on exposure time (how much molecules can interact with the surface) and sticking probability (a gas-surface interaction property).

- **Temperature window**. A limited temperature window exists where ideal ALD growth occurs. Four phenomena govern the upper and lower limits, as depicted in figure 2.4. The ALD reactions are energy-driven, i.e. an energetic barrier needs to be overcome to be able to form a chemical bond to the surface. This energy can be delivered thermally by heating the sample, or by the use of more energetic reactants (ozone, ions, radicals). Furthermore, at low temperatures, the heated precursor molecules can condensate onto the sample, leading to non-saturated growth conditions and increased growth rates. A certain temperature barrier has to be overcome to allow self-limiting gas-surface interaction without the possibility for precursor condensation. On the other hand, excessively high temperatures lead to precursor decomposition, causing incorporation of ligand fragments into the films (often giving rise to carbon contaminated films) and non-uniform film thicknesses. Too high temperature can also cause the gas-surface species to have too much energy, and detach from the surface during the evacuation step (desorption), which causes lowered growth rates. Between the two extrema, ideal ALD characteristics are valid (saturation, uniformity, non-contaminated films).

- **Film quality**. The half-reactions mostly occur according to either exchange or combustion mechanisms. This implies that the complete precursor ligands, i.e. everything but the metal, must be removed during the ALD cycle, rendering a metal oxide, metal nitride, metal sulfide or pure metal (depending on the specific ALD process), without contamination from the ligands, reflected in the film purity.

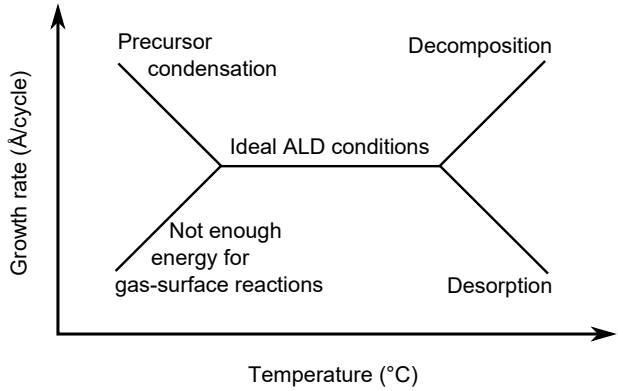

Figure 2.4: Schematic representation of the limitations to the ALD temperature window.

- **Conformality**. Finally, the self-limiting nature of the reactions accounts for the conformality of the films. This is readily evaluated by measuring the uniformity of the films on high-aspect ratio test structures.

These characteristic properties can be investigated *ex-situ* and *in-situ*. *Ex-situ* evaluation is done on films after they are deposited, and is comprised of evaluating the film composition, thickness, roughness and conformality of the deposited films. *In-situ* characterisation is performed during the ALD process by several *in-situ* examination techniques, as depicted in figure 2.2: *in-situ* ellipsometry and *in-situ* optical emission spectrometry. The reactors are equipped to also accommodate *in-situ* mass spectrometry and *in-situ* FTIR, but these were not used in this work and are not discussed here.

2.2 THIN FILM CHARACTERISATION

This section describes the measurement techniques and equipment used to characterize the physical properties of the deposited films. Three characterisation methods were used to determine film thickness in this thesis: X-ray reflectivity (XRR), spectroscopic ellipsometry (SE) and electron microscopy, used in scanning mode (SEM) or transmission mode (TEM). SEM and TEM are mainly used to evaluate surface morphology, for which Atomic Force Microscopy (AFM) was also used. Finally, SEM and TEM can also be used to evaluate composition using Energy-Dispersive X-ray (EDX) analysis, complementary to X-ray Fluorescence (XRF). A more thorough

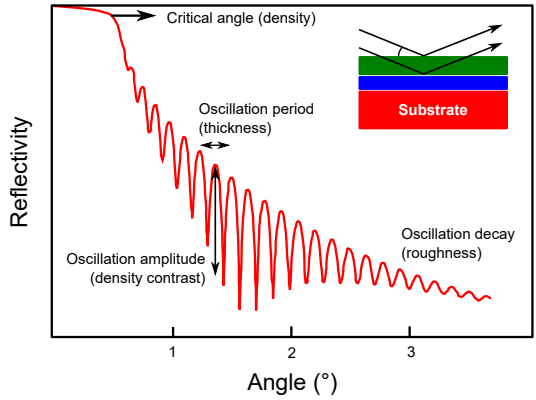

Figure 2.5: X-ray reflectivity interference profile, indicating which information can be extracted from the measurement. Figure adapted from [103].

understanding of the film composition and binding state was found from X-ray Photo-electron Spectroscopy (XPS). Finally, the crystalline nature was evaluated using X-ray Diffraction (XRD). This section will provide a brief introduction to the aforementioned techniques.

2.2.1 *Film thickness*

2.2.1.1 *X-ray reflectivity*

X-ray reflectivity is a non-destructive X-ray illumination technique, based on the interference between photons reflecting at interfaces of layers with different densities. It can be used to determine density, roughness and thicknesses in the 2 nm to 200 nm range with an accuracy down to the Å level [104]. A single-wavelength X-ray beam is used to illuminate the sample at a shallow angle (typically indicence angles from 0.3° to 3°). At low angles, the beam is reflected completely. At a critical angle (θ_c, which is a measure of the electron density of the top layer) a fraction of the beam will penetrate the surface, increasingly so with a rising incidence angle. Within the sample under study, a fraction of the penetrating X-rays reflects at every interface. If the X-ray path length from penetration to reflection is equal to half the X-ray wavelength, constructive interference occurs with directly reflected X-rays at the surface [105] as shown in figure 2.5, and an interference pattern can be recorded by varying the angle of incidence θ and recording the X-ray intensity at the same exit angle. By performing a fit to the measured spectrum, the film characteristics can be

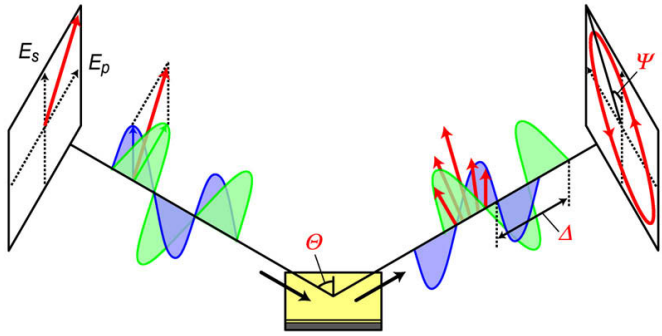

Figure 2.6: Principle of ellipsometry. Figure reprinted from [106].

extracted. The XRR patterns in this work were recorded in a Bruker D8 Discover using monochromatic Cu Kα radiation and a point detector.

2.2.1.2 *Spectroscopic ellipsometry*

Spectroscopic ellipsometry is a non-destructive method used to measure the optical properties and thickness of thin films in the range from sub-monolayers (Å) to thick films (μm, as long as the films are sufficiently optically transparent). SE makes use of the change in polarisation that occurs when visible and near infrared (NIR) light interacts with solid matter. Linearly polarised light illuminates the sample at a 70° angle, and the reflected beam is measured. The light is changed in polarisation to elliptically polarised light, with a change in amplitude $\tan\Psi$ and in phase $e^{i\Delta}$ (figure 2.6). These changes can be related to the wavelength-dependent complex optical properties n(λ) and k(λ) of the films as well as their thickness. The ellipsometer used in this PhD thesis is a J.A. Woolam M2000 with a wavelength range from 193 nm to 1700 nm, obtained from a Xenon arc light source.

Although SE can be used to measure film thickness and optical properties *ex-situ*, in this PhD thesis, it is mainly used *in-situ* to monitor the film thickness during ALD growth. This allows for a rapid evaluation of varying ALD conditions, such as pulse duration and temperature, on the growth per cycle. To this end, a film was first grown using optimal ALD conditions and measured *ex-situ* with both XRR and SE. The thickness obtained from XRR can then be used to construct an optical model using the SE measurement, which is then used to evaluate the data recorded *in-situ* during ALD. The *CompleteEASE* software package provided by Woollam was used to fit the optical models, using predefined optical models as initial guesses.

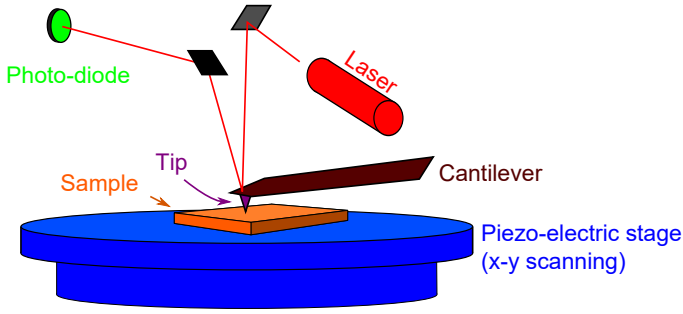

Figure 2.7: Principle of atomic force microscopy.

2.2.2 *Surface topology and morphology*

2.2.2.1 *Atomic Force Microscopy*

The atomic force microscope (AFM) is a non-destructive surface topology probing technique, designed to measure extremely local properties, such as height and friction, down to an Å-length scale. Figure 2.7 illustrates the principle. In AFM, an extremely sharp tip is moved across the surface under examination. The x-y movement is performed by a piezo-electric stage. Surface features will move the tip upwards and downwards. This motion deflects laser light focussed on the cantilever holding the AFM tip, which is then detected by a photodiode. The surface can be reconstructed to a three-dimensional topological map from the x-y-z information obtained, as is illustrated in figure 2.7.

In this work, the microscope used is a Bruker Dimension Edge AFM, used in tapping mode. Tapping mode is in-between contact and non-contact mode, as it samples the surface and moves the z-actuator of the sample stage accordingly with a feedback mechanism [107, 108].

2.2.2.2 *Electron Microscopy*

Another way of obtaining nano-scale (and below) morphological information is using electron microscopy. This is done by focussing and accelerating a mono-energetic beam of electrons towards the sample. To avoid scattering of the electrons, this needs to happen under ultra-high vacuum conditions (UHV). When an electron beam impacts on solid matter, various physical phenomena can occur, such as scattering (elastic-, back-, inelastic-), transmission and excitation. The latter phenomenon leads to generation of characteristic X-rays, secondary electrons and Auger electrons. All of

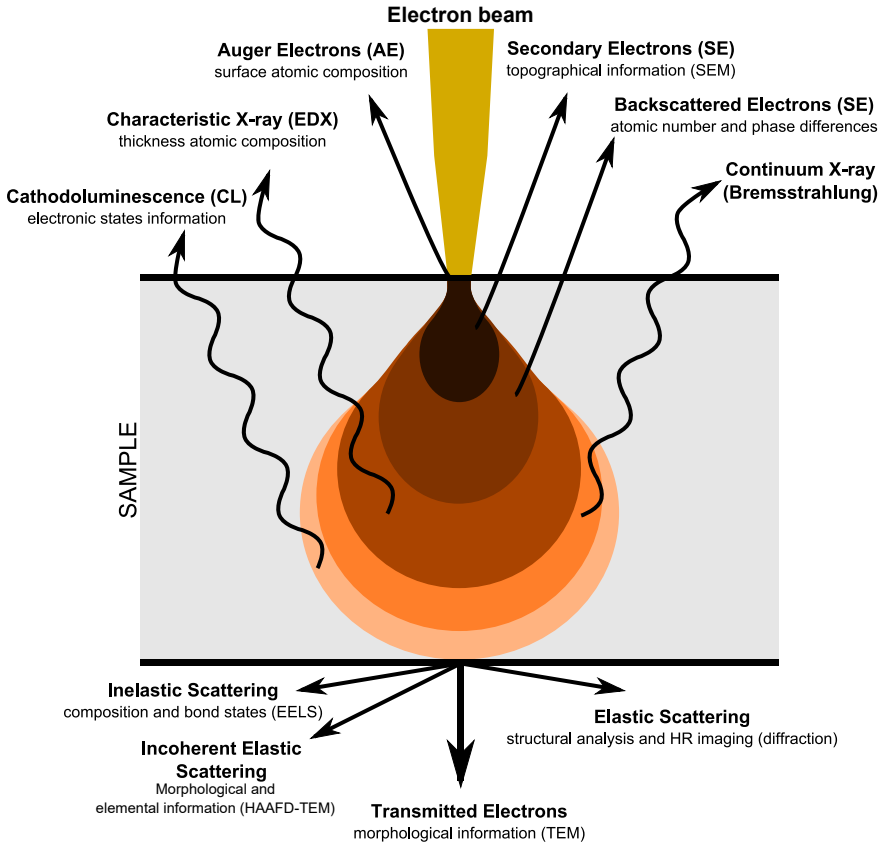

Figure 2.8: The phenomena resulting of the interaction of highly energetic electrons with matter. Figure edited from [109].

this can be detected to provide some information on the sample. The specific technique is determined by which output is detected.

Scanning electron microscopy (SEM) is done by moving a focussed electron beam across the sample, and recording the secondary electrons. The intensity of the secondary electrons at the detector depends on the surface morphology: more electrons will be able to escape from a protruding feature, and less from an indented feature. Scanning this intensity allows a 2D visualisation of the surface morphology with a resolution limited only by the focus of the electron beam on the surface. The SEM imaging in this work was carried out using an FEI Quanta 200F instrument with a focussing limit to approximately 10 nm features (200 000× magnification) under ideal conditions.

When very thin samples are used, high-energy electrons can penetrate through the sample, and the properties of the electrons are highly dependent on the properties of the transversed matter. By moving the focus of the converged electron beam across the sample surface, it can be used in scanning mode and is called Scanning Transmission Electron Microscopy (STEM). The position of electron detection at the back of the sample further defines the nature of the STEM imaging. The directly transmitted electrons contain mainly morphological information, but with a resolution far better than SEM; allowing the visualisation of single atoms. This High-Resolution TEM (HRTEM) was done in a FEI Osiris operated at 200kV at the university of Antwerp (EMAT).

In this work, High-Angle Annular Dark Field STEM (HAAFD-STEM) imaging is also used, which only collects incoherently scattered electrons (see figure 2.8). These electrons show little or no diffraction effects and are highly sensitive to variations in the atomic number of atoms, which allows to make the distinction between for example titanium (atomic number 22) and vanadium (atomic number 23) with an atomic resolution, by varying the tilt angle of the sample. This was done in an aberration corrected cubed FEI Titan operated at 200kV, at the University of Antwerp.

2.2.3 *Composition and chemical surrounding*

2.2.3.1 *Energy-dispersive X-ray spectroscopy*

The electron microscopy techniques from section 2.2.2.2 yield the possibility to examine the composition of the samples in a non-destructive manner. As figure 2.8 shows, interaction of the focussed electron beam with matter not only gives rise to secondary and transmitted electrons, used for SEM and STEM, respectively, but also generates characteristic X-rays. As an electron interacts with matter, a deep-level atom-bound electron can

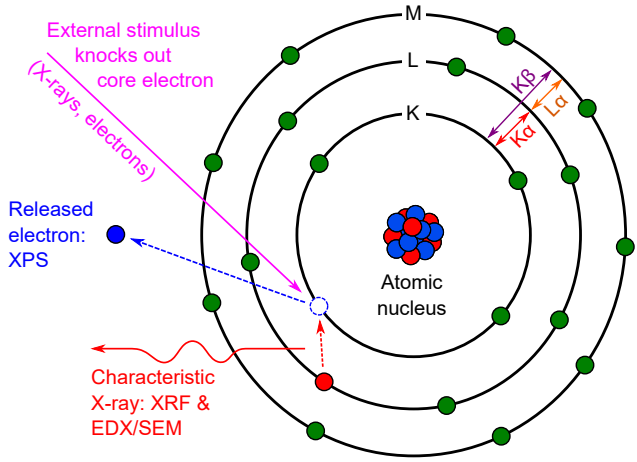

Figure 2.9: Interactions with electrons in the shell of the atom.

be kicked out of its shell (K-, L-, M-shell), ionizing or exciting the atom. Figure 2.9 illustrates that higher-shell electrons can recombine to fill these unstable vacancies with the emission of light at an energy corresponding to the energy difference between the two shells (fluorescent X-rays). The energy of the electron levels is element dependent:

$$E \sim \frac{Z^2}{n^2} \times 13.6eV \tag{2.1}$$

with Z the atomic number and n the n-th shell. This allows for elemental identification in the SEM/STEM devices described above by energy-dispersive analysis of the X-rays, as their energy is the difference between two electron binding levels [110]. This analysis is called Energy-Dispersive X-ray (EDX) spectroscopy. If the excitation or ionisation of the electrons is performed with a focussed electron beam, this is called EDX/SEM or EDX/STEM. As a result of the highly focussed nature of the electron beams and the small thickness of transversed matter in the case of EDX/STEM, elemental mapping can also be performed with a very high resolution.

2.2.3.2 *X-ray fluorescence*

Electrons can not only be excited/ionized by electrons, as described above, but also by X-rays, as shown in figure 2.9. If this is the case, the technique is called X-ray Fluorescence (XRF), which is another non-destructive variant of EDX and has the advantage that it does not require a UHV setup,

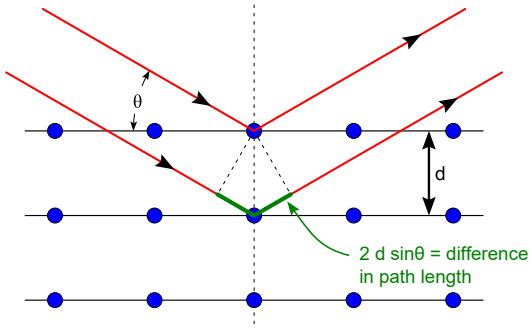

Figure 2.10: X-ray diffraction at lattice planes in a crystalline compound. Figure edited from [111].

as no electrons are to be injected into or detected from the samples. Also, elemental identification can be performed here from the characteristic fluorescent X-rays. As X-rays penetrate several micrometres through solid matter (depending on the elemental constitution and density) and the incident X-ray beam is mm-sized, the entire film can be evaluated in a single spectrum. In this work, XRF is performed using a Bruker Artax system consisting of a Mo X-ray source and a XFlash 5010 silicon drift detector.

2.2.3.3 *X-ray photo-electron spectroscopy*

The electrons released by ionisation with X-rays, as described above and in figure 2.9, can also be detected if the sample is placed in a UHV chamber. Since every electron bound to a nucleus has a specific binding energy (equation 2.1), detection of these photo-emitted electrons not only provides elemental information, but also information about the local bonding structure of the atoms (as this can modify the energy from equation 2.1). This technique is called X-ray Photo-electron Spectroscopy (XPS). The photo-electrons ejected from the samples have relatively low energies, which results in mean free path lengths of a couple of nm in solid matter, rendering XPS a surface-sensitive technique. In combination with sputtering to remove the top layers, it can also be used to measure depth profiles throughout films. In this work, XPS was performed on a Theta Probe system of Thermo Scientific using monochromatic Al Kα radiation (0.834 nm) under a take-off angle of 45° in an ultra-high vacuum chamber (2×10^{-9} mbar).

2.2.4 *Crystalline nature of the films*

X-ray diffraction (XRD) is a non-destructive measurement technique that uses X-ray scattering at lattice planes in crystalline materials to study lattice spacing. X-ray diffraction happens as depicted in figure 2.10. This diffraction only occurs at angle-wavelength couples that satisfy Bragg's law:

$$2d \sin\theta = n\lambda \tag{2.2}$$

where d is the spacing between crystal lattices, θ is the angle of the incident X-rays, λ the wavelength of the X-rays and n an integer ($n = 1, 2, 3, ...$). If a material has a crystalline nature and this condition is met, constructive interference between X-rays diffracting off two crystal planes occurs. In a crystalline structure, the lattice is constant (i.e. d is constant), and by using a single-wavelength X-ray source as well (λ is constant) and varying the angle of incidence, constructive interference results in a higher X-ray intensity detected at diffraction angle θ fulfilling the Bragg condition. Since d-spacings within a lattice are a fingerprint of a specific compound, databases of calculated and observed XRD patterns can be used to identify specific compounds and crystal structures based on their diffraction patterns.

In this thesis, XRD is used in two modes: *ex-situ* XRD and *in-situ* XRD. Both use the same measuring hardware, a Bruker D8 Discover equipped with a Cu Kα X-ray source and a position sensitive linear X-ray detector. The main difference between them is defined by the measurement conditions: *ex-situ* measurements are done to establish the crystalline nature of films as-is, while *in-situ* XRD is used to monitor crystallisation and phase changes during annealing. For this, a heating chamber was built by researchers of the CoCooN research group[1], in which the temperature and ambient can be varied, allowing to do controlled experiments while monitoring the crystalline state in a 20° 2θ window in a near-continuous manner.

2.3 EVALUATION OF THE ELECTROCHEMICAL ACTIVITY

As this PhD thesis discusses the use of ALD thin films for various applications in lithium-ion batteries, specific electrochemical measurement techniques to evaluate their activity were used and are discussed below. A specially designed Teflon body was clamped onto the samples using

1 The designing and building of the system used was spearheaded by dr. Werner Knaepen, dr. Geert Rampelberg and dr. Davy Deduytsche.

a Kalrez o-ring to provide a tight seal as depicted in figure 2.11, resulting in an exposed sample area of approx. 0.95 cm^2. Due to the air- and humidity sensitive nature of lithium and the electrolyte components, all measurements were carried out in an argon-filled glovebox with no detectable water and oxygen contamination present (H_2O, O_2 <1ppm). An Autolab potentiostat/galvanostat (PGSTAT702 and PGSTAT302) is used for the electrochemical scans, controlled by the NOVA software.

The films subjected to electrochemical testing were tested in a three-electrode setup. The current is measured between the sample, i.e. the Working Electrode/Sense electrode (WE/S) terminal, and a lithium metal strip as a source and drain for the lithium-ions, i.e. the Counter Electrode (CE). The area of the CE needs to be significantly larger than that of the sample (WE/S) to minimize IR-drop at the CE, and the lithium strips used here typically were $\sim$5 cm^2 partically submerged in a 1M $LiClO_4$ in PC electrolyte. The potential cannot be measured across the same terminals, as to avoid shifting of the measured potential as a consequence of overpotentials caused by Ohmic currents flowing between WE/S and CE. To this end, the potential is measured between the sample (WE/S) and a secondary lithium strip providing a Li^+/Li reference, submerged in a secondary electrolyte compartment, called the Reference Electrode (RE). The RE compartment is connected to the WE/CE compartment via a Luggin capillary approx. 3 mm above the sample. The total electrolyte volume amounts to approx. 10 ml to 15 ml.

Two general modes of electrochemical characterisation are possible: controlling the current and monitoring the potential (Galvanostatic mode) or applying a potential and monitoring the current response (Potentiostatic mode). In this PhD, three techniques are used: cyclic voltammetry, galvanostatic charge-discharge measurements and impedance spectroscopy. [112]

2.3.1 *Potentiostatic measurements*

Cyclic voltammetry (CV) is performed by varying the potential linearly from a zero-current potential to a potential at which oxidation or reduction occurs (i.e. $V(t) = V_0 \pm \nu \times t$ with ν the sweep rate [V/s]). After transversing one (or more) reduction or oxidation reactions, the sweep direction is reversed ($V(t) = V_{limit} \mp \nu \times t$) until the reversible reduction/oxidation reactions have occurred. By monitoring the electrochemical cell's current response, information can be obtained about the nature of the redox reactions in an easy and intuitive manner [113].

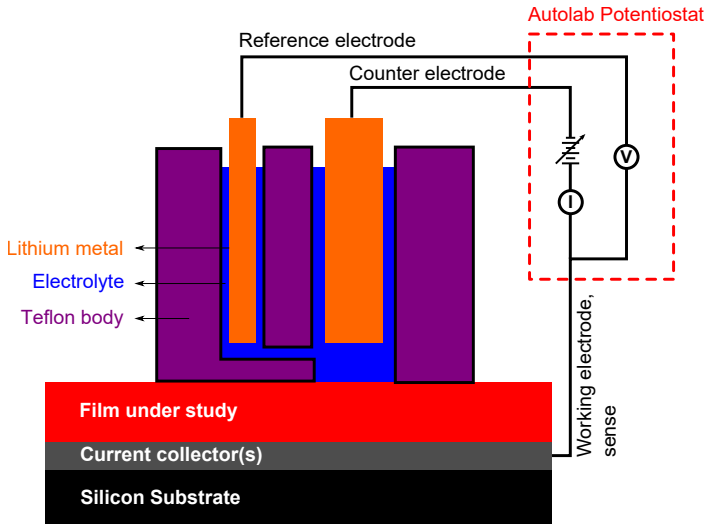

Figure 2.11: The three-electrode setup used in this thesis for all electrochemical evaluations.

An example of such a measurement can be seen in figure figure 2.12. A negative peak corresponds to a reduction reaction due to the acceptance of electrons in the working electrode. As figure 2.12 concerns the (de)lithiation of V_2O_5 to LiV_2O_5, both negative peaks correspond to the reduction of V^{5+} to V^{4+}. To balance the charge of the electrons, this is accompanied by insertion of lithium ions, resulting in $V_2O_5 + e^- + Li^+ \longrightarrow LiV_2O_5$. In this way, the measured electrons (current) are a direct measure for the amount of lithium ions shuffled (ionic current) into/from the sample. The double-peak nature of this spectrum reveals a different electrochemical potential for different lithium-ion sites in the V_2O_5 lattice, which is typically related to electrostatic surrounding of the lithium ion in the lattice. Several other properties can be measured using CV measurements:

- Peak potentials ($V_{positive}$ and $V_{negative}$) are an **electrochemical fingerprint** of the redox system under study [114]. Positive peaks correspond to lithium-ion extraction from the film, while negative peaks correspond to lithium-ion insertion. Their separation ΔV is a measure for the **internal resistance** of the cell, in other words, whether the rate constant for the charge-transfer reaction is fast or slow.

- Peak current ($i_{cathodic}$ and i_{anodic}) as a function of the applied scan rate provides information concerning the **charge storage mechanism**

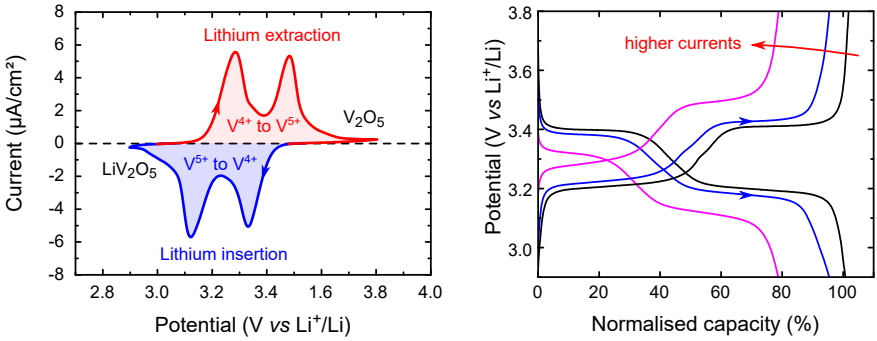

Figure 2.12: (left) Cyclic voltammogram and (right) charge-discharge profile of the lithium-ion insertion and extraction for a V_2O_5 film.

and its properties (for example, diffusion coefficient in a diffusion-limited mechanism) [112].

- By integrating the area under the CV-curves, **cathodic and anodic charge** gives an estimate for the capacity of the cations (lithium ions, in this case) that can be stored into the films, and of the **reversibility** of this storage, translating in a **Coulombic efficiency**.

Furthermore, the diffusion in the films can also be probed by the potentiostatic intermittent titration technique (PITT). When a potential is applied higher or lower than the equilibrium potential, current flows to obtain a new equilibrium. By monitoring this flow of current, lithium ion diffusion coefficients can be extracted from the decay of current when a new equilibrium situation is approached [115–117].

2.3.2 *Galvanostatic measurements*

For galvanostatic measurements a positive or negative current is applied. Charge neutrality dictates that for every electron forced through the external circuit, lithium ions are extracted from or inserted into the sample to compensate the electron movement[2]. This mode of charging-discharging corresponds most closely to actual use of the battery, as current will be drawn (discharge) or provided (charge) in approximately this manner during the battery's lifetime.

Since insertion or extraction of ions from the system change its electrochemical nature, the measured electrode potential varies. Here, an electro-

2 This is a simplified representation, as side reactions can occur, but for the sake of the explanation those will be omitted here.

chemical signature of the system is provided by plateaus in the charge-discharge profile in the case of crystalline materials, corresponding to distinct phase-transitions or crystal reorientations on critical lithium-loading thresholds, as seen on figure 2.12 for crystalline V_2O_5. No clear plateaus occur for amorphous materials, due to the solid-solution behaviour present for those compounds [118].[3] Three important electrode characteristics can be extracted from galvanostatic measurements: capacity, cyclability and kinetics.

The electrode capacity can be found by multiplying the current with the amount of time elapsed between cut-off potential thresholds:

$$Q[coulomb] = \int_{t1}^{t2} I(t)dt = I \times \Delta t \tag{2.3}$$

By varying the potential at a low current (i.e. low C-rate), the electrode can be fully charged and the maximal capacity can be found. The capacity retention (cyclability) and coulombic efficiency can be found by charging and discharging multiple times, and evaluating the evolution in capacity over cycling.

The usable potential obtained from the electrode will in reality be lowered by an overpotential, caused by a combination of charge-transfer overpotentials, concentration gradients and internal cell resistances [119]. While some of the energy provided to the system is lost in the form of heat, an increasingly larger fraction of the electrode just cannot be charged or discharged at higher currents due to mass-transport limitations before the cut-off potentials are reached, as is the case for figure 2.12.

2.3.3 *Electrochemical impedance spectroscopy*

The complex impedance is a measure of the opposition that a system presents to a current when a voltage is applied. In potentiostatic impedance measurements,[4] a small, time-dependent potential is applied, perturbing a fixed DC voltage (V_0),

$$V(t) = V_0 + \Delta V \sin \omega t \tag{2.4}$$

3 Although this is not exclusively valid for the crystalline and amorphous case, in general, (semi)plateaus are related to (crystal) phases, and jump between (semi)plateaus to phase transitions. This will be explained more in detail in chapter 8.

4 A galvanostatic perturbation can also be used. In that case, a sinusoidal current is applied and the potential response is measured

with ω the frequency of the perturbation (in this case 0.1 Hz$< \omega <$1 MHz) and ΔV the magnitude of perturbation (typically $\sim$10 mV). The current response is then represented by

$$i(t) = i_0 + \Delta i \sin(\omega t + \theta) \tag{2.5}$$

The resulting complex impedance can be written as

$$Z = \frac{V(t)}{i(t)} = \mid Z \mid e^{-j\theta} = Z' - jZ'' \tag{2.6}$$

with j the imaginary unit, Z and θ the magnitude and phase of the response, respectively, or Z' the real part, and Z" the imaginary part of the impedance [120]. It is a modified form of Ohm's law ($R = E/i$) that can be applied for not only time-independent circuit elements such as resistors ($Z = R$), but also for AC circuit elements such as capacitors and inductors.

Various electrochemical phenomena occur simultaneously in an electrode. Electronic current is provided in the form of electrons, collected at or provided by the current collector and conducted throughout the electrode. Ionic current is provided by mobile charged species in the electrolyte, which is dominated by the lithium ions here. Lithium ion migration in the electrolyte is typically very fast due to the high conductivity. The electrochemical potential of the electrode causes a build-up of ions at the electrolyte-electrode interface, resembling a capacitor element. Ionic diffusion through the electrode is much slower compared to the electrolyte. This diffusion is thus the equivalent of an ionic resistor. Phase transformations take place, grain boundary diffusion occurs, interfaces are formed, and so on. The interplay and combination of all of these phenomena gives the cell a very complex character, complicating the understanding of which phenomenon is responsible for which effect.

Luckily, the various electrochemical processes occurring in an electrode happen on their respective characteristic time-scales. By measuring the electrode's current response across a wide range of frequencies (hence the nomenclature *spectroscopy*), the separation and evaluation of these various electrochemical phenomena can be performed.

To deconstruct the frequency-dependent phase and amplitude responses, the complex electrode is modelled by a simplified *Equivalent Circuit*. In this circuit, every active electrochemical process is modelled by simple electronic components, such as resistors ($Z = R$, with R the resistance), capacitors ($Z(\omega) = -j/\omega C$, with C the capacitance) and in-between elements without real-life equivalents, such as constant-phase elements ($Z = 1/Q_0(j\omega)^n$ with $0 < n < 1$) [121] and Warburg impedance (CPE with $n = 0.5$) elements. The impedance data is collected using the cell construction as depicted in figure 2.11 connected to the impedance module of

the Autolab PGSTAT702 potentiostat/galvanostat in potentiostatic mode, controlled by the NOVA 1.10 software. A fit is made to the obtained measured data for every frequency using a software package called MEISP, developed specifically for this purpose by Barsoukov *et al.* [122].

Part III

ATOMIC LAYER DEPOSITION FOR THIN-FILM ELECTRODES

The world is changing very fast. Big will not beat small anymore. It will be the fast beating the slow.

– Rupert Murdoch

3

ATOMIC LAYER DEPOSITION OF MANGANESE OXIDES FOR ENERGY STORAGE AND CATALYSIS

In this first part of the PhD thesis, atomic layer deposition is used for the deposition of manganese oxide (this chapter) and vanadium oxide (chapter 8) thin films. The research on this culminated in four manuscripts, two for each materials system, detailing deposition, phase-control and applications as lithium-ion battery electrode (paper I, III and IV) or thin-film catalyst (paper II).

In this chapter, ALD of thin-film manganese oxides is discussed, and applications are found in thin-film lithium-ion battery electrodes and thin-film catalysts.

3.1 MANGANESE OXIDE PHASES

Manganese is a transition metal with five possible oxidation states: 0, +2, +3, +4 and +7. These are found in the five principal states of manganese: manganese metal, MnO, Mn_2O_3, MnO_2 and Mn_2O_7. The latter is a volatile unstable liquid, but the first four are stable solids at room temperature. Several mixed-oxidation state manganese oxides exist, such as Mn_3O_4 (+2,+3), Mn_5O_8 (+2,+4) and Mn_7O_{12} (+3,+4). Despite the wide range of phases and crystal structures, equilibrium phase transitions reveal only 4 thermodynamically stable states and crystal structures, and occur as

$$\alpha - MnO_2 \longrightarrow \beta - Mn_2O_3 \longleftrightarrow Mn_3O_4 \longleftrightarrow MnO \longleftrightarrow Mn \qquad (3.1)$$

with decreasing oxygen partial pressure and increasing temperature, from left to right [124, 125], as visible from the phase diagram in figure 3.1. The remaining phases and crystal states are metastable, and can only be observed in controlled environments, when doped to stabilize the structures or when bulk-thermodynamics are no longer valid, as is the case for thin films [126]. Re-oxidation to MnO_2 is thermodynamically possible, but requires oxygen pressures above 3000 bar to proceed. In practice, re-oxidation to MnO_2 does not occur under standard atmospheric pressure conditions [124].

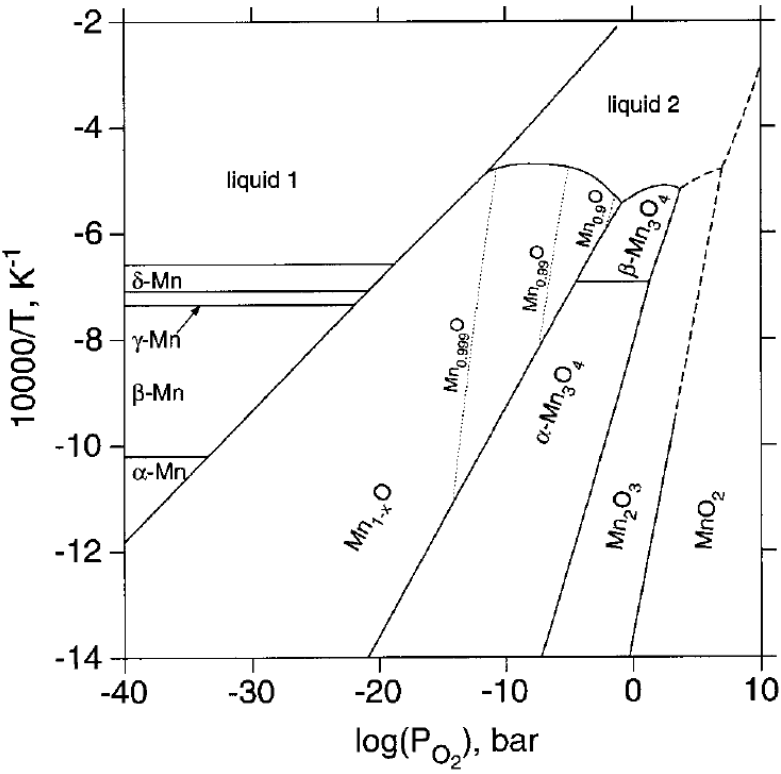

Figure 3.1: The manganese-oxygen phase diagram as constructed by Grundy *et al.* [123].

Manganese oxides have a wide range of applications, such as catalysis [127–137], energy storage (lithium-ion batteries [138, 139], dry-cell zinc-carbon [140, 141] and (pseudo-)capacitors [142–146]) and magnetoresistance applications [147]. Their low cost, low toxicity and the high abundance of manganese makes them attractive compounds for these applications [148].

Several manganese oxides have been of interest for energy storage applications in combination with lithium ions. In principle, manganese oxides can provide up to 5 V *vs* metallic lithium, but the cell voltage does not only depend on the formal valence state of the manganese ions, but also on the relative energy of the lithium ion sites in the wealth of various structures in which manganese oxides can exist. As the electrochemical potential of the positive electrode is that sensitive to the phase and oxidation state of the manganese in the compound, control over those properties is critical

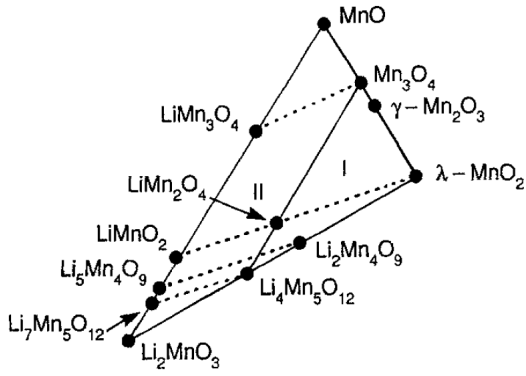

Figure 3.2: Section of the lithium-manganese-oxygen phase diagram, showing the spinel and rocksalt phases. Lithium ion insertion occurs according to the dotted lines. Figure reprinted from Thackeray *et al.* [150].

to determine the properties of the cells. A study of phase- and oxidation-state control is presented as the topic of Paper I (during ALD) and Paper II (post-ALD).

The main forms of manganese oxide studied for energy storage were reviewed by Thackeray [149], and the three main phases for energy storage are listed here:

- **MnO_2 for primary batteries**. Lithium/MnO_2 cells are most known as the 3V (see figure 3.3(b)), 225 mA h button-type non-rechargable batteries such as the CR2032 (see figure 3.3(a)) used in watches, calculators, computers, scales and small electronics. The manganese oxide in these is usually γ-MnO_2, which is an inter-growth between ramsdellite-MnO_2 and β-MnO_2 in which the oxygen ions are hexagonally close-packed. These manganese dioxides typically show a limited rechargability and poor lithium ion insertion properties [150]. However, nanoscaling of MnO_2 is believed to unlock higher storage capacities up to 320 mA h g^{-1} [154, 155]. Besides the use as electrode in lithium or lithium-ion batteries, MnO_2 is also considered as an electrode in electrochemical supercapacitors [156, 157].

- **Spinel $Li_xMn_2O_4$ (LMO)** is regarded as a promising intercalation cathode for lithium-ion batteries thanks to its low material cost, high natural abundance, low toxicity and good safety compared to $LiCoO_2$ [149]. Furthermore, the spinel structure provides three-dimensional interstitial space for Li^+ transport, and remains intact over a wide composition range as is shown in figure 3.2 ($Li_xMn_2O_4$ with $0 \leq$

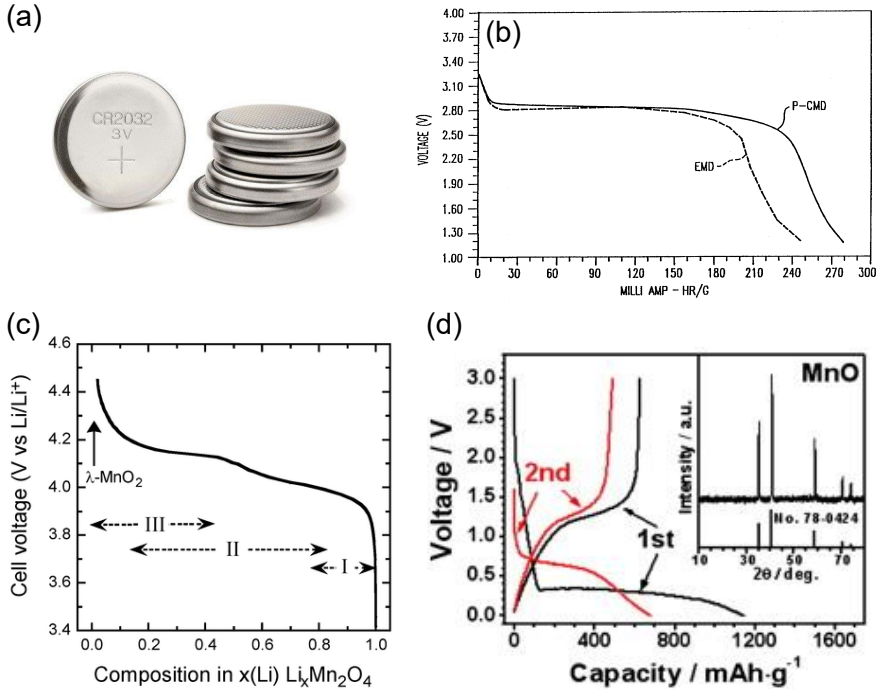

Figure 3.3: (a) Primary Li/MnO_2 CR2032 button cell. (b) Voltage profile of Li/MnO_2 cells at low currents (reprinted from [151]). (c) Voltage profile of the 4V-region of LiM_2O_4 (reprinted from [152]). (d) Voltage profile of MnO (reprinted from [153]).

$x \leq 2$) [150]. Two lithium ions can be intercalated per spinel host structure, one at 4 V *vs* Li^+/Li (theoretical capacity of 148 mA h g^{-1}, see figure 3.3(c)) and one at 3 V *vs* Li^+/Li, amounting to a total capacity of 285 mA h g^{-1}. Typically however, only the first region can be charged reversibly due to the lattice changes associated with the latter (up to 5 %), unless the electrodes are nanostructured to cope with these volume changes [158]. However, even in this limited range LMO suffers from capacity fading caused by an array of issues, such as Mn^{2+} dissolution, oxygen loss, Jahn-Teller lattice distortion at critical Mn^{3+} ion concentrations and electrolyte decomposition due to the catalytic nature of manganese oxides [159–161].

- **MnO as conversion anode.** Besides the use of high-valence manganese oxides as lithium-ion battery cathodes, the lower-valence oxides enable the use of manganese oxide as low-potential electrodes

(see figure 3.3(d)). The +2-valent manganese oxide (MnO) for example can be used to store lithium ions, and yields a very high capacity (theoretical capacity of 755 $mA\,h\,g^{-1}$) through a conversion storage mechanism, however, poor coulombic efficiency and high volume change limit practical applications so far [162, 163].

3.2 Literature overview of ALD of manganese oxides

MnO_x ($1 < x < 2$) thin films have mainly been deposited by means of electrodeposition [139, 155, 164, 165] (Electrolytic Manganese Dioxide or EMD), anodic deposition [144, 145] and chemical vapour deposition [166, 167]. At the start of this research, only two processes were available for atomic layer deposition of manganese oxide:

- Nilsen *et al.* developed a thermal process for the atomic layer deposition of MnO_2 in 2003, using the $Mn(thd)_3$ precursor and ozone. Unfortunatly, due to the catalytic properties of MnO_2 towards ozone, the deposition of uniform films proved challenging in their flow-type ALD reactor. Furthermore, the very large (thd)-ligands give rise to significant steric hinderance (the chemisorbed $Mn(thd)_2$-fragment spans an area of approx. 11.5 Å × 13 Å), blocking almost 20 surface sites [100]. This causes very low growth rates of only ∼0.2 Å/cycle. [100, 101, 168].

- In 2008 and 2009, a water-based ALD process with the $Mn(CpEt)_2$ precursor was reported by Lu *et al.* [169] and Burton *et al.* [170], respectively. As a merit of the much smaller ligands compared to the thd-ligands, growth rates up to ∼1.2 Å/cycle were found. Thanks to the liquid nature of the precursor and the higher reactivity, lower deposition temperatures were also possible. As a consequence of the pure ligands-exchange reaction mechanism with the water and the +2 oxidation state of the manganese in the precursors, MnO films were deposited using this process.

Amongst those precursors, the $Mn(CpEt)_2$ precursor was found to be too unstable to be used for longer periods of time. Since the start of this PhD research in 2012, several other studies were released detailing further development for these films, or novel processes. The three plasma-enhanced processes developed in the framework of this thesis were published [171]. Since then, two novel manganese precursors have surfaced: the zero-valent $Mn_2(CO)_{10}$ precursor [172] and the +1-valent $MeCpMn(CO)_3$ precursor [146]. Table 3.1 provides a complete overview of the reported (PE-)ALD processes for manganese oxides. ALD of more exotic manganese-containing

compounds, such as manganese borate [173], manganese fluoride [174] and manganese sulfide thin films [175], have also been demonstrated recently.

The manganese oxides are envisioned as positive electrodes. If they are deposited in their delithiated state this, in combination with the deposition of a lithiated negative electrode and an electrolyte, yields the deposition of a charged battery. However, several arguments can be made towards the incorporation of a lithiated positive in the battery stack. First, the deposition of a charged battery at the elevated temperatures at which ALD happens, would most likely result in a partial discharging the direct deposition of lithiated manganese oxides as potential leakage currents are temperature-dependant. Secondly, obtaining the desired phase in the delithiated state is not always possible. The low-density nature of the spinel structure of $LiMn_2O_4$ for example is very difficult to obtain without the stabilisation of the lithium cations present in the lattice. Indeed, the deposited MnO_2 films in table 3.1 are α-MnO_2, β-MnO_2 or ϵ-MnO_2, but no atomic layer deposition of lithium-free spinel γ-MnO_2 has ever been reported. If lithium is added to the ALD process cycle, as was done by Miikulainen et al. using Li(thd) or LiO^tBu as a lithium source, it is possible to obtain spinel $Li_xMn_2O_4$ using either lithium subcycles during the ALD growth or gas-phase lithiation of deposited MnO_2 films [176]. Another recently reported route is electrochemical conversion. Young *et al.* reported that by prolonged charging and discharging of ALD-deposited MnO in the presence of an aqueous electrolyte, ALD-deposited MnO eventually converts to spinel $LiMn_2O_4$ [177]. As a post-deposition conversion is possible according to the mechanisms presented above, the deposition of lithium-free films is examined in this work, since simple binary oxides tend to be much easier to deposit using ALD. In this work, the $Mn(thd)_3$ precursor is used as a manganese source due to its low cost and high stability.

3.3 OXIDATIONS STATES AND CRYSTALLINE PHASES

As mentioned above, the electrochemical properties of the manganese oxide are heavily influenced by the oxidation state of the manganese and the crystallographic state of the oxide. For lithium-ion batteries, the use of manganese oxide requires +4 valent manganese. For this valence state, potentials above 2.5 V *vs* Li^+/Li can be expected, justifying its use as a positive electrode in lithium-ion batteries. Lower valence manganese oxides also display lithium ion storage modes, but at lower electrode potentials. Mn_2O_3 for example (+3 valent manganese) can be charged to $LiMn_2O_3$,

Precursor		Reactant	Phase	Temperature window	Growth rate (Å/cycle)	Reference
$Mn(thd)_3$		O_3	MnO_2	138 °C to 230 °C	0.15 to 0.30	[100–102, 168, 171]
	*	H_2O plasma	Mn_3O_4	138 °C to 250 °C	0.2	[171]
	*	NH_3 plasma	Mn_3O_4/MnO	138 °C to 250 °C	0.2	[102, 171]
	*	H_2 plasma	MnO	138 °C to 250 °C	0.2	[171]
$Mn(CpEt)_2$		H_2O	MnO	150 °C to 300 °C	0.25 to 0.42	[169]
			MnO	100 °C to 250 °C	1.0 to 1.2	[170, 178, 179]
		O_3	Mn_5O_8	150 °C to 180 °C	>5	[126]
$Mn_2(CO)_{10}$		O_3	α-Mn_2O_3	80 °C to 100 °C	~1.2	[172]
			Mn_3O_4	100 °C to 200 °C	~1.2	[172]
$MeCpMn(CO)_3$		O_3	Mn_3O_4	100 °C to 275 °C	0.34 to 0.75	[146]

Table 3.1: Chronological table of reported ALD and PE-ALD processes for the deposition of thin-film manganese oxide up to January 2017.
$Mn(thd)_3$ = tris(2,2,6,6-tetramethyl-3,5-heptanedionato)manganese,
$Mn(CpEt)_2$ = bis(ethylcyclopentadienyl) manganese,
$Mn_2(CO)_3$ = dimanganese decacarbonyl,
$MeCpMn(CO)_3$ = methylcyclopentadienyl manganese tricarbonyl.
* = processes developed in this work.

but this only happens around 1.35 V *vs* Li^+/Li, a potential too low to be used as a positive electrode material [153]. One could envision the use of Mn_2O_3 as an negative electrode, but the capacity is rather low compared to conventional electrodes such as graphite. However, Mn_2O_3 does find its applications in for example catalysis, where it generally outperforms MnO_2 [129, 178, 180].

The next section briefly summarises the control of the oxidation state of ALD manganese oxides by careful selection of ALD process gas/plasma, or by post-ALD annealing in ambients with oxidizing, inert or reducing nature. These findings were published in two papers:

- **Paper I:** Deposition Of MnO Anode And MnO_2 Cathode Thin Films By Plasma Enhanced Atomic Layer Deposition Using The $Mn(thd)_3$ Precursor, published in *Chemistry of Materials* in 2015 [171].
- **Paper II:** Manganese Oxide Films With Controlled Oxidation State For Water Splitting Devices Through A Combination Of Atomic Layer Deposition And Post-deposition Annealing, published in *RSC Advances* in 2016 [102].

These two papers comprise the next two chapters, in which they are presented as they were published.

3.3.1 *Plasma-enhanced deposition of thin-film manganese oxides*

ALD with the $Mn(thd)_3$ precursor is the focus topic of the first paper. $Mn(thd)_3$ is a dark-brown solid at room temperature, and is extremely stable: the decomposition temperature is reported above 240 °C. The low cost and exceptional stability make this precursor highly interesting. Up to this work, researchers only investigated thermal ALD with ozone in flow-type reactor setups. Film uniformity was reported to be poor on 5 cm × 5 cm substrates due to the catalytic nature of manganese for ozone decomposition. In this work, the same process was implemented in a vacuum-type setup. Here, the influx of ozone was directional towards the sample surface, rather than ozone flowing across the sample surface in the flow-type F120-reactor used in the work of [100]. In contrast to that work, it was possible to yield uniform films on silicon substrates of comparable sizes, and saturation was possible with 5 second pulse times.

Plasma-enhanced processes were investigated using the same precursor. Five plasma processes were evaluated, and their properties are summarised in table 3.2. While O_2- and N_2-plasmas showed non-ideal ALD growth (non-uniformity and high C-content, respectively), H_2O-, H_2- and NH_3-plasmas yielded ideal ALD growth characteristics such as saturated

Reactant	Phase	Remarks
O_3	MnO_2	Poor uniformity in flow-type due to O_3 decomposition, resolved in vacuum-type setup
H_2O	-	No growth
O_2 plasma	-	No uniformity achieved
N_2 plasma	-	Saturated growth but incomplete ligand removal
H_2O plasma	Mn_3O_4	Saturated growth
H_2 plasma	Mn_3O_4/MnO	Saturated growth
NH_3 plasma	MnO	Saturated growth

Table 3.2: Properties of the (PE-)ALD processes investigated here using $Mn(thd)_3$ as a manganese source.

precursor- and plasma pulses, and complete ligand removal which was evident from the C-free nature of the deposited films.

Despite the uniform film growth on planar substrates, conformal depositions proved very challenging. The deposition of MnO_2 using the O_3-based ALD chemistry did not yield conformal films on silicon micro pillar structures. This can be explained from the ozone decomposition point of view, similar to the difficulties reported to grow uniform MnO_2 films in a flow-type reactor. A proof-of-concept was attempted for the conformal deposition of ALD MnO using the NH_3-plasma based chemistry. Using high exposures (up to 8 times the saturated pulse times) resulted in the deposition of manganese oxide along the pillar lengths (50 µm), but a gradient was observed with EDX/SEM. As these exposure times already ramped the cycle time up to almost 10 minutes per cycle, these attempts were further abandoned here.

All deposited films with the H_2O, H_2 and NH_3 PE-ALD processes and the thermal ozone-based ALD process were crystalline and with low carbon impurities. Their oxidation state was determined from XRD, and confirmed with XPS (see figure 3.4). Interestingly, it is found that the nature of the process gas or plasma, more specifically its oxidizing/reducing character, largely determines the oxidation state of the grown films. $Mn(thd)_3$ has manganese in the +3 oxidation state. The ozone combusts the (thd)-ligands and raises the manganese oxidation state to +4, resulting in MnO_2 films. Optical emission spectroscopy was used to study the active species in the H_2O, H_2, N_2 and NH_3 plasmas (see supplementary information to Paper I). The plasmas all contain the reductive $H\cdot$ radicals, causing a de-

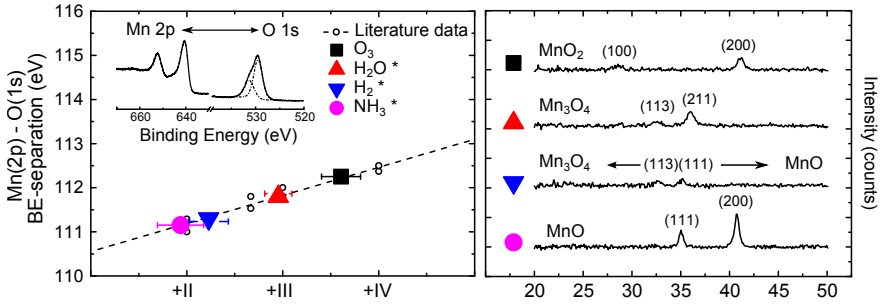

Figure 3.4: (left) Analysis of the XPS peak separation described in the text with literature data [165, 181–183], as shown in the inset for the NH_3* PE-ALD film. (right) XRD patterns measured on MnO_x films grown using 1000 (PE)ALD cycles with different reactants. The (h k l)-planes and corresponding phases are labelled in the figures.

crease in oxidation state to lower-valent manganese oxides. The severity of reduction depends on the presence of other active species (OH^- or $N_2 \cdot$ in the H_2O- and NH_3-plasma, respectively). A more in-depth discussion concerning this topic can be found in Paper I. By a careful choice of the oxidative/reductive nature of the process gas/plasma, the manganese oxide phase can be controlled in the MnO-MnO_2 range, as shown in figure 3.4.

3.3.2 *Influence of ambient and temperature on thin-film oxidation and reduction*

Due to the high stability of the $Mn(thd)_3$ precursor, a pure ligand-exchange reaction was not possible: reactants with higher reactivities such as ozone or plasma were required to enable film growth. As such, the +3-valence of the manganese in the $Mn(thd)_3$ did not translate into a +3-valent manganese oxide (Mn_2O_3) ALD film. Further post-ALD annealing was required to obtain this phase and complete the MnO-Mn_2O_3 sequence. Three types of annealing atmospheres were investigated; i.e. oxidizing (O_2), reducing (H_2/He) and inert (He) ambients, and the phase formation for temperatures up to 900 °C was studied with *in-situ* XRD. Figure 3.5 shows the *in-situ* X-ray diffraction patterns during annealing in these ambients for ALD MnO and MnO_2 films. Through oxidation (for MnO) and thermodynamic reduction (for MnO_2), three pathways were found to obtain thin-film Mn_2O_3, and it was even possible to obtain this at a relatively low temperature (∼400 °C) without the need for an oxidative ambient.

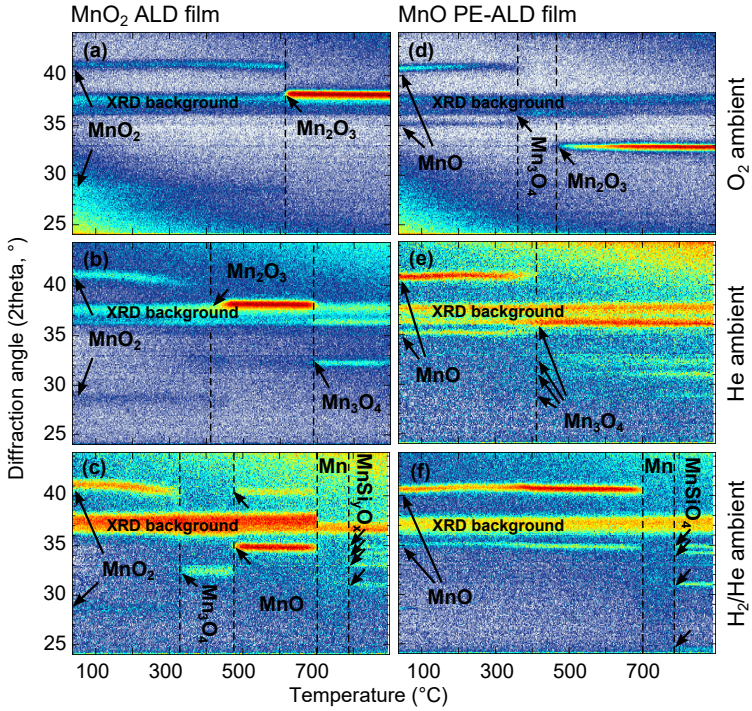

Figure 3.5: In-situ XRD measurements from room temperature to 900 °C at a heating rate of 0.25 °C s^{-1} in oxygen, helium and hydrogen ambient of the as-deposited MnO and MnO_2 films: MnO_2 in O_2 ambient (a), He ambient (b) and H_2/He ambient (c), and MnO in O_2 ambient (d), He ambient (e) and H_2/He ambient (f). Peak identification was performed using the JCPDS database: β-MnO_2 (81-2261), Mn_2O_3 (89-2809), Mn_3O_4 (24-0734), MnO (75-0625), α-Mn (32-0637), Mn_2SiO_4 (35-0747) and $MnSiO_3$ (89-2809).

Figure 3.6 summarises the ALD deposition and post-ALD heat treatments for the formation of thin-film manganese oxides from a single manganese source; i.e. the $Mn(thd)_3$ precursor. It highlights that the full range of manganese oxides can be achieved at relatively low temperature (deposition from 150 °C, reduction to Mn_2O_3 from 410 °C).

3.4 Applications of ALD thin-film manganese oxide

Two applications of atomic layer deposited manganese oxides were investigated. In Paper I, the as-deposited (PE-)ALD films are evaluated as thin-film lithium-ion battery electrodes. In Paper II, two of the films from

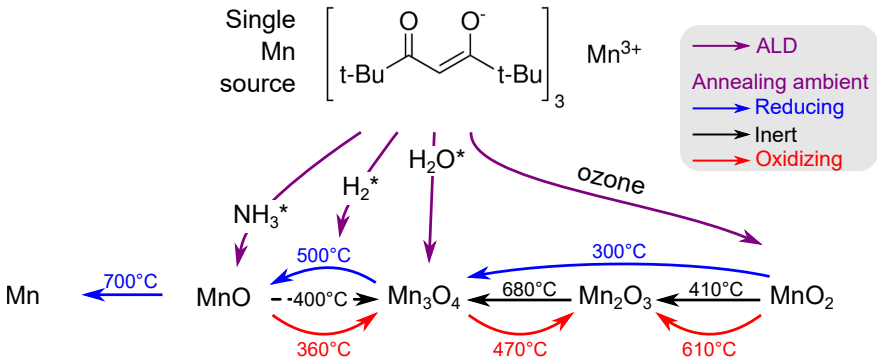

Figure 3.6: A summary of the formation of thin-film oxides from atomic layer deposition and post-deposition annealing. The star notation denotes a plasma rather than a gas.

figure 3.6 are benchmarked as transparent thin-film catalysts for water splitting applications. The details of both applications can be found in the next chapters. As the main topic of this PhD thesis is ALD for lithium-ion batteries, this application is highlighted below.

3.4.1 *Thin-film cathode and anodes for lithium-ion batteries*

The (PE-)ALD processes with the $Mn(thd)_3$ precursor yield several of the primary phases of thin-film manganese oxide, as discussed above: MnO, mixed-phase MnO/Mn_3O_4, Mn_3O_4 and MnO_2. All of these oxides can be used to store lithium ions: MnO_2 and Mn_3O_4 in a layered 2D-insertion mode at higher potentials, and MnO in a conversion mode at lower potentials. These are all tested in their respective potential ranges, of which the details can be found in Paper I and its supplementary information.

A remarkable observation can be made if the observed electrode potentials are compared to the oxidation states of the as-deposited films. A nearly linear relation exists between the former and the latter, as shown in figure 3.7. Since we have shown earlier that the oxidation state of the films can be controlled by a careful choice of the ALD process gas/plasma, the electrochemical properties of these films can, in effect, be tuned and grown into a film that can either be a Li-ion cathode (MnO_2) or anode (phase-pure MnO and mixed-phase MnO/Mn_3O_4), using a single manganese-source precursor chemistry.

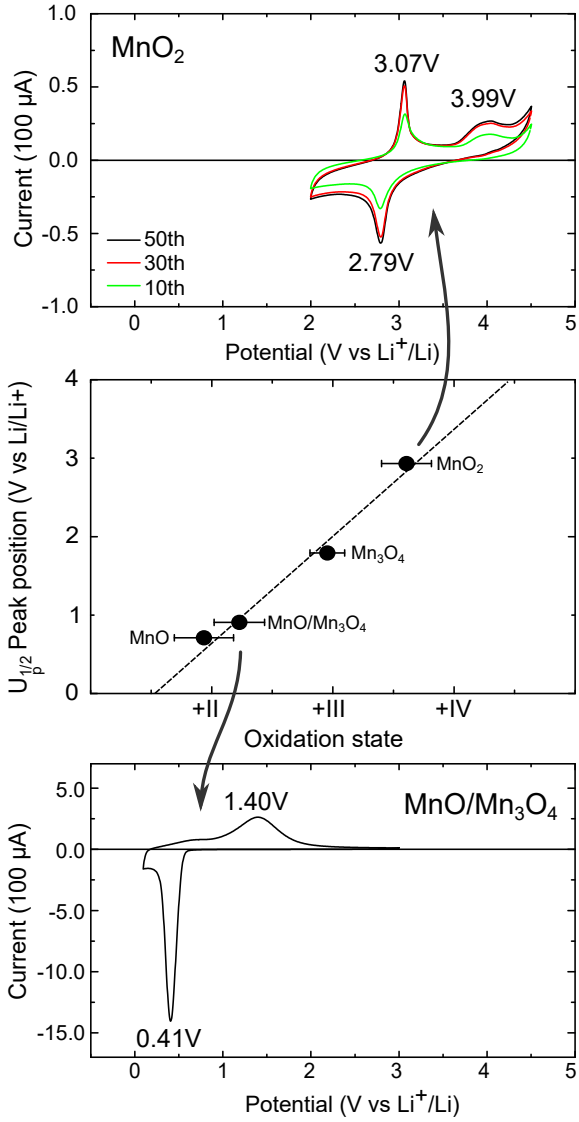

Figure 3.7: Relationship between measured as-deposited oxidation states (XPS, figure 3.4) and measured averaged peak potential ($U^p_{1/2} = 1/2 \times (U^p_{ox} + U^p_{red})$) from cyclic voltammetry (see Paper I).

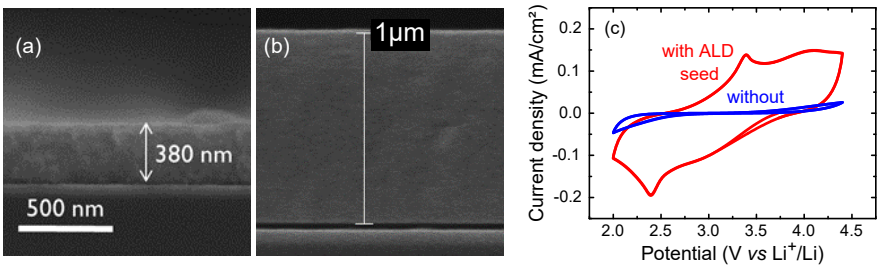

Figure 3.8: SEM images of EMD films deposited on (a) TiN and (b) TiN with a 1-2nm seed layer of ALD MnO_2. (c) Cyclic voltammetry of ~400 nm EMD films deposited on both substrates.

3.5 ALD MANGANESE OXIDES BEYOND THIN-FILM ELECTRODES

As is shown in this chapter, the growth rate of ALD manganese oxides is very slow, despite the improved growth rates using plasma-enhanced ALD. This limits the feasible film thickness with this process to around 30 nm. Combined with the limited conformality of these processes, thin-film electrodes and especially 3D thin-film electrodes appear out of range for this process chemistry. However, two applications are demonstrated here using ALD manganese oxides with a film thickness within the realm of possibilities: thin-film catalysts and seed layers.

In paper II, a MnO_2 film grown from 200 ALD cycles and a Mn_2O_3 film obtained by reducing the aforementioned MnO_2 film are benchmarked as thin-film catalysts. Both films displayed catalytic activity as was evident from oxygen evolution experiments in KOH. ALD-derived Mn_2O_3 showed a performance which was slightly poorer than the Pt-CB benchmark catalyst, while ALD MnO_2 performed better with an onset potential of 1.62 V *vs* RHE and on overpotential of 619 mV at currents of 10 mA cm^{-2}. Interestingly, both films were almost transparent to solar light, with solar light transmissions of 95.6 % and 98.8 % for Mn_2O_3 and MnO_2, respectively, which makes these films interesting for applications with buried photo-active light harvesters such as TiO_2.

Finally, high-quality manganese oxide thin films can also be used as a seed layer to enable another deposition technique. Electrodeposition of manganese oxides is an excellent way to deposit thick and conformal MnO_2 (EMD) films on a conductive substrate [155, 184]. This work was carried out at IMEC. There, it was found that for substrates as TiN, deposition in acidic environments oxidizes the current collector and disconnects the film electronically from the current collector, rendering inactive electrodes, as shown in figure 3.8(c). By depositing a very thin MnO_2 seed

layer with ALD, the current collector is protected from the acid bath. As a result, the deposited EMD films are now electrochemically accessible, enabling them as electrodes. Futhermore, the seed layer allows the deposition of much thicker films: on the bare TiN current collector the thickness is limited to $\sim$400 nm (fig. 3.8(a)), while the ALD-treated TiN accommodates films up to $\sim$1 µm (fig. 3.8(b)) [185].

4

PAPER I

DEPOSITION OF MnO ANODE AND MnO_2 CATHODE THIN FILMS BY PLASMA ENHANCED ATOMIC LAYER DEPOSITION USING THE $Mn(THD)_3$ PRECURSOR

Felix Mattelaer,[a] Philippe M Verreecken,[b,c] Jolien Dendooven,[a] and Christophe Detavernier[a]

Published in *Chemistry of materials* (2015). Doi: 10.1021/acs.chemmater.5b00255

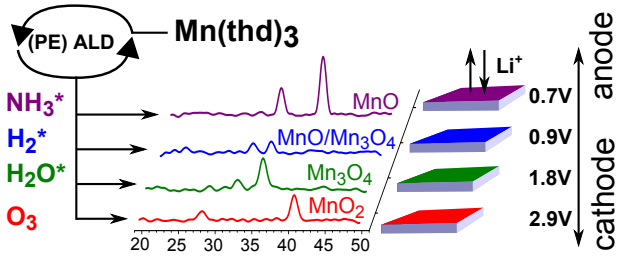

[a] *Department of Solid State Sciences, Ghent University, Krijgslaan 281 S1, 9000 Gent, Belgium,*
[b] *imec, Kapeldreef 75, 3001 Leuven, Belgium,*
[c] *Centre for surface chemistry and catalysis, KU-Leuven, 3001 Leuven, Belgium*

ABSTRACT

Atomic layer deposition (ALD) of a wide range of Mn oxides (MnO to MnO_2) is demonstrated by combining the $Mn(thd)_3$ precursor with different types of plasma activated reactant gases. Typical ALD behaviour is found with hydrogen, ammonia and water plasma, with a fully precursor controlled temperature window (from 140 °C to 250 °C) and constant growth rate (0.022 ± 0.001 nm/cycle). A purely ligand-exchange chemistry would predict Mn_2O_3 films with the transition metal in the +III state. However, it is found that the nature of the process gas or plasma, more specific its oxidizing/reducing character, largely determines the oxidation state of the grown films. Our approach provides an effective method for the deposition of MnO_2(+IV), Mn_3O_4(+II/+III) and MnO(+II) based on the $Mn(thd)_3$(+III) precursor. All as deposited films are found to be smooth (<1.2 nm rms roughness), crystalline and with $<6\%$ impurities. The resulting films are tested as lithium-ion battery electrodes, showing the MnO_2 and the MnO films as possible candidate thin-film cathode and anode, respectively.

INTRODUCTION

Rechargeable solid state thin-film batteries are emerging from the field of liquid battery research with applications in small autonomous devices, such as smart textiles, wearables, wireless sensors and medical implants. Since they lack the traditional liquid component, they are inherently safer than their standard liquid-battery counterparts, making them more suitable for these sensitive applications. The drawbacks of planar thin-film batteries are generally low-energy density, which can be overcome by going to novel battery architectures with high aspect ratios [28, 63, 64, 186, 187]. ALD typically deposits films in the 0.1 nm to 100 nm range, an order of magnitude lower than the typical electrode in a planar thin-film battery stack (1 µm) [188]. To overcome this gap, ALD builds on its inherently conformal nature. When working in high aspect ratio 3D architestures such as pillars or carbon nanosheets (CNS), an area enhancement of 10-100 can overcome and even surpass the planar thin-film battery stack equivalent thickness, leading to a much higher energy density while still having the advantage of thin-film kinetics [28, 63, 64, 81, 186, 187, 189]. This approach has been shown in literature on metal nanorods and -wires, graphene, CNT's and so on.

On the other hand, these same electrochemical active conformal films on a 3D architecture can work as supercapacitors (SC), more specifically,

pseudo-capacitors. Since a much thinner film is required for a pseudo-capacitor application, the cost of the ALD film will also be much lower. Here also very high surfaces are required by the conformal deposition since a (pseudo-)capacitor works on the surface, and not in the bulk of the material as is the case for the Li-ion electrodes in a battery. An demonstrated example of an ALD thin-film as a SC is V_2O_5 coated on carbon nanotubes [190].

Manganese oxides have recently attracted a lot of attention in industrial applications, with the main focus on their electrochemical properties as a cathode in lithium-ion batteries (with reversible lithiation to $LiMn_2O_4$ [138, 139]), as a component for dry-cell zinc-carbon batteries [140, 141], or as a candidate for thin-film capacitors [142–145]. A wide range of other applications can be found in the field of catalysis [127], namely in the oxidative dehydrogenation process [128], the oxygen reduction and water oxidation [129, 130], the oxidation and reduction of nitric oxide [131–134], and the decomposition of hydrogen peroxide [135], benzene [136] and ozone [137]. In the field of nano-electronics, manganese oxides have applications as a Cu-diffusion barrier [166].

So far, MnO_x ($1 < x < 2$) thin films have mainly been deposited by means of electrodeposition [139, 155, 164, 165] (Electrolytic manganese dioxide or EMD), anodic deposition [144, 145], chemical vapour deposition [166, 167], atomic layer deposition (ALD) [100, 101, 169, 170] and sol-gel methods [164]. ALD finds itself amongst the techniques delivering the highest conformality, inherent to the self-limiting surface-controlled nature of the gas-solid reactions [72]. Two precursors are reported in literature for thermal ALD: the $Mn(CpEt)_2$ (with H_2O as reactant) [169, 170] and $Mn(thd)_3$ (with O_3 as reactant) [100, 101], yielding MnO and MnO_2 respectively. A plasma enhanced ALD process (PE-ALD) for MnO_x has yet to be reported.

For many applications of transition metal oxides, control over the oxidation state in the deposited layer is a key requirement [99]. As ALD is often governed by ligand exchange type reactions, the oxidation state of the metal in the deposited compound is typically controlled by the oxidation state of the metal in the organometallic precursor molecule. Therefore the oxidation state in ALD layers is often determined by the chemical build of the precursor, and can only be modified by post-deposition annealing in an oxidative or reducing ambient [98]. However, for certain applications or substrates, the required annealing conditions may exceed the allowable thermal and chemical budgets. Controlling the oxidation state of the deposited layer during the ALD process itself is therefore of interest.

In this work, we investigate the PE-ALD of manganese oxides with the $Mn(thd)_3$ precursor. By varying the second ALD half cycle from the reported oxidative combustion chemistry with ozone [100] over mild to very reductive chemistries with water, hydrogen and ammonia plasmas, we show that we can effectively tune the oxidation state of the manganese in the deposited film, as well as maximize the growth rate within the temperature window. We finally test the electrochemical properties of the resulting films as lithium-ion battery electrodes.

EXPERIMENTAL

The manganese oxides were grown in an experimental high-vacuum ALD setup with a base pressure of 10^{-7} mbar [93–95]. The metal-organic precursor used for these experiments was $Mn(thd)_3$ (Tris(2,2,6,6-tetramethyl-3,5-heptanedionato)manganese (with manganese in oxidation state III) from Strem, 99%), held in a stainless steel container at 133 °C for optimal vapour pressure without decomposition. Since the vapour pressure at this temperature was still very low, argon carrier gas was applied to introduce sufficient precursor to the chamber. The precursor was pulsed at a pressure of 1 mbar by sealing the reactor from the pumps during the pulse. In between pulses, reaction products and remaining precursor or reactant gas were evacuated using a turbomolecular pump. As reactant gases, the previously reported O_3 [100] was tested, as well as H_2 (a mixture of 5%H_2 in Ar), H_2O, N_2, O_2 and NH_3 along with their respective plasmas (remote RF plasma at 300W). The ozone was produced with an OzoneLab^{TM} generator from a pure O_2 gas flow, resulting in a minimum concentration of 150 µg ml^{-1}. None of the non-activated gases were able to grow a film, likely due to the stable nature of the precursor, so only plasma and ozone results will be discussed below. The plasma activated gases will be indicated with the notation *gas**. The partial pressures of the ozone and reactant gases were 1 mbar and 1×10^{-2} mbar, respectively. The full ALD process consisted of 4 steps, each with a length of time t_i: t_1 is the precursor pulse time, t_2 is the pump time required to remove all the precursor gas, t_3 is the reagent pulse time and t_4 is the subsequent pump time. The full process is thus t_1-t_2-t_3-t_4. The films were grown on silicon covered with 100 nm thermal SiO_2 for the in-situ growth characterisation and on 60 nm PVD TiN for electrochemical characterisation.

For the O_3 -based process, in-situ spectroscopic ellipsometry (ISE) was used to monitor the film thickness during ALD. Ellipsometry was able to give a good estimate of the thickness, as verified by X-ray reflectivity (XRR), and could therefore be used to determine the saturation behavior

of the ALD half cycles in situ [191]. For each set of process parameters, 20 ALD cycles were performed and the growth per cycle (GPC) was determined by fitting a straight line to the ISE growth curve. The ellipsometer used was a J.A. Woollam M-2000 with a wavelength range of 245 nm to 1000 nm.

X-ray techniques were used to determine film thickness (XRR), crystallinity (X-ray diffraction or XRD) and film composition (X-ray photoelectron spectroscopy or XPS). XRR and XRD were done in a Bruker D8 Discover with a copper X-ray source (Cu Kα radiation at 0.154 nm). A point detector was used for the XRR, while the XRD was done using a linear detector to perform unlocked coupled scans with a 5° offset to avoid the Si substrate peak. XPS was performed using Al Kα radiation (0.834 nm) under a take-off angle of 45° in a high-vacuum chamber (2×10^{-9} mbar). A resolution of 0.108 eV was obtained.

The film morphology was probed using a Bruker Dimension Edge atomic force microscope (AFM) and film rms roughnesses were fitted to $1 \times 1\mu m$ AFM images.

Electrochemical measurements were done in an Ar-filled glove box (O_2 <1 ppm, H_2O <1 ppm) with a Metrohm Autolab PGSTAT302 connected to a three-electrode setup. Electrical contact to the TiN current collector was mady by contacting the side of the sample with silver paste to a Cu foil. Lithium ribbon (99.9 % , Sigma Aldrich) was used as counter- and reference electrodes, and 1M $LiClO_4$ in propylene carbonate (99 %, io-li-tec) was used as Li^+ electrolyte solution. Cyclic voltammetry (CV) measurements were performed at a 10 mV s^{-1} sweep rate between chosen potential boundaries, and galvanostatic charge/discharge was performed at positive and negative current densities of 10 µA cm^{-2}.

RESULTS AND DISCUSSION

First, the thermal ALD process with $Mn(thd)_3$ and ozone is compared to the PE-ALD processes. The thermal ALD process was developed and reported already by the group of Nilsen. [100, 101] In our case, a pump-type high vacuum ALD setup was used whereas a flow-type reactor was used in the work of Nilsen *et al.* [100]. In contrast to their results the films showed uniform deposition, as confirmed by XRF mapping on selected samples. This suggests that a high vacuum type ALD setup enables a more uniform ozone concentration over the sample surface, while the ozone concentration in flow type ALD reactors may be less uniform due to the laminar-flow geometry and the catalysing nature of the deposited manganese dioxide films towards ozone destruction [137]. For the

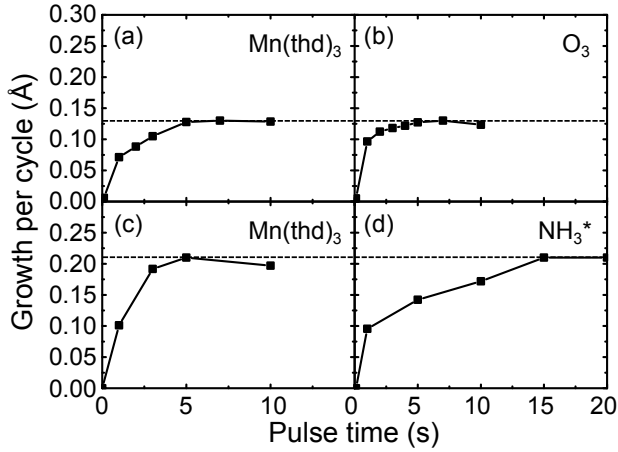

Figure 4.1: Growth per cycle curves showing the saturation of the surface reactions with $Mn(thd)_3$ precursor(a) and the O_3 reagent(b) for the thermal ALD process, and with $Mn(thd)_3$ precursor(c) and the NH_3* plasma(d) for the PE-ALD process. The saturation experiments were performed at 150 °C and the growth rates were monitored using ISE (top) or extracted from XRR (bottom). One pulse time was varied, while the other was kept at the highest value examined.

reported thermal ALD process, saturation of the half-reactions was examined using ISE (figure 4.1(a and b)). It was found that 5 s exposures at a pressure of 1 mbar were sufficient to saturate both ALD half-reactions. An increasing growth rate from 0.15 Å/cycle at 150 °C to 0.3 Å/cycle at 250 °C was confirmed within the ALD temperature window, and linearity was established (figure 4.2(top)). Nilsen *et al.* [100] attributed the low growth rate to the steric hindrance caused by precursor ligands during the first half-cycle. Since the precursor is the common factor throughout this paper, it can be expected that the GPC will also remain relatively low for the plasma processes under investigation.

The process using ammonia plasma (NH_3*) was examined in-depth. Saturation was investigated by growing 200-cycle films with different pulse times and extracting the GPC from the film thickness determined by XRR. The saturation curves are shown in figure 4.1 (c and d) and reveal a saturated exposure time of t_1=5 s at 1 mbar for the precursor and t_3=15 s at 1×10^{-2} mbar for the NH_3* plasma at 150 °C . The t_2=15 s and t_4=25 s pump times were chosen to allow the reactor to reach a pressure of ca. 10^{-6}mbar between each ALD half reaction. Figure 4.1 and figure 4.2 also show that the saturated GPC at 150 °C is almost twice as high for the NH_3* based process than for the O_3 based process.

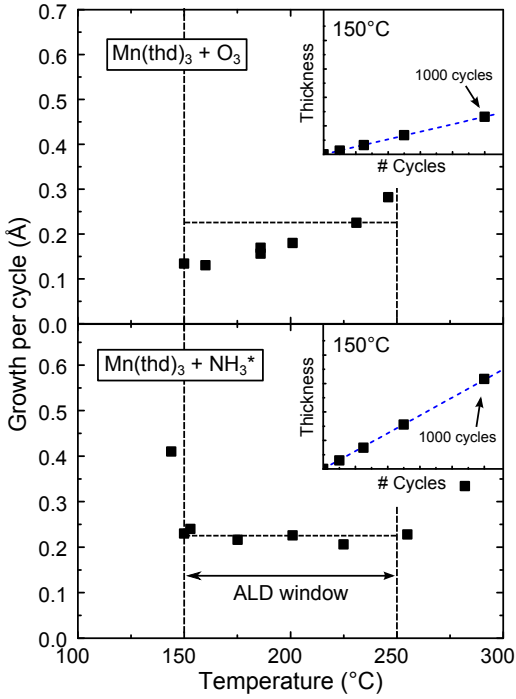

Figure 4.2: Temperature window for the $Mn(thd)_3 + O_3$ thermal ALD process (top), and the $Mn(thd)_3 + NH_3$* PE-ALD process(bottom). The GPC was determined by XRR. Insets demonstrate linearity at 150 °C up to 1000 cycles.

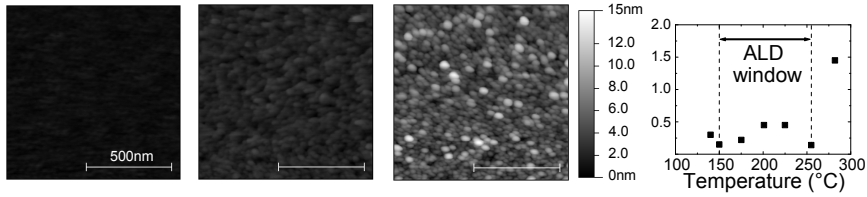

Figure 4.3: 1 µm × 1 µm AFM images of 500 cycles PE-ALD using the $Mn(thd)_3$ + NH_3* process. From left to right: deposited at 140 °C, 200 °C and 280 °C. The images are set on the same z-scale to allow for direct comparison. Right: rms roughness against the deposition temperature.

The temperature dependence of the NH_3* process was further investigated using XRR on 500 cycle films (figure 4.2(bottom)). Verification of the growth linearity ensured a constant GPC from the first ALD cycles, without any non-ideal initial growth behaviour (inset figure 4.2(bottom)). Contrary to the O_3 based process which shows a clear temperature dependence (figure 4.2(top)), the GPC in the NH_3* PE-ALD temperature window remains constant at a rate of 0.22±0.01 Å/cycle, i.e. near the highest observed GPC in the thermal ALD window.

The rise in GPC at temperatures below 150 °C is related to precursor condensation. Because precursor gas enters the chamber at 140 °C, condensation of the precursor vapour occurs at temperatures below 140 °C, causing CVD-like side reactions during the plasma pulse [192]. The increase in GPC at temperatures above 250 °C on the other hand, can be associated to thermal decomposition of the precursor which was reported by Nilsen *et al.* [193] between 240 °C and 260 °C, and is accompanied by a rise in the surface roughness as measured by AFM (figure 4.3). Within the ALD temperature window, as well as at lower temperatures in the CVD-like regime, smooth films with an average rms roughness of 0.3 nm were obtained.

Besides NH_3* plasma also O_2*, N_2* , H_2* and H_2O* plasmas were examined as ALD reactant for MnO_x growth at 180 °C. All plasmas resulted in film growth, however, for the O_2* plasma saturation could not be achieved. Pulse times up to 120 s were tested for O_2* but no uniform films could be obtained and this process was therefore not considered further.

The experiments with N_2* , H_2* and H_2O* plasmas were done under the saturated process parameters established for the NH_3* process. Saturation for these processes was conceptually checked by performing a deposition at double t_3 yielding similar growth rates of ∼0.2 Å/cycle in all cases.

Film impurities and oxygen content were determined using XPS (figure 4.4). While for the films grown from H_2*, H_2O* and NH_3* PE-ALD and

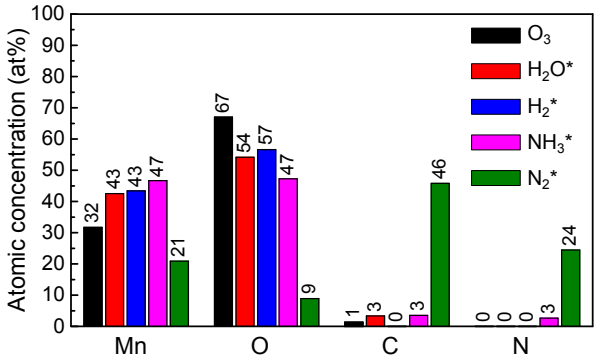

Figure 4.4: The atomic concentrations of Mn, O, C and N obtained from XPS for ALD-grown films with the $Mn(thd)_3$ and thermal (O_3 and PE reagents (H_2O*, H_2*, NH_3* and N_2*).

O_3 ALD processes the carbon and nitrogen impurities were very low, most of the N_2* grown films consisted of carbon (45.8%) and nitrogen (24.5%), pointing to a substantial build-in of the precursor ligands into the films. For this reason, the N_2* process cannot be considered an ALD process for a manganese oxide and was therefore not considered as a candidate Li-ion electrode material.

The rms roughness determined by AFM was 0.8, 1.2 and 1.5 nm for 20 nm films grown from H_2*, H_2O* and N_2* PE-ALD, respectively. Even though such rms values still indicate a smooth film for 20 nm films, the roughness is somewhat higher than that for the NH_3* process (0.3 nm), but comparable to the thermal O_3 process (0.8 nm).

The crystalline phases of O_3- , H_2*- , H_2O*- and NH_3*-based (PE)ALD films were investigated using XRD (figure 4.5). Film crystallinity only became apparent for films beyond 500 cycles ($\geq$10 nm), but it was unclear whether this arose as a growth effect or could be attributed to XRD sensitivity. The crystalline phases found were β-MnO_2, hausmannite Mn_3O_4, a mixed MnO/Mn_3O_4-phase and phase-pure MnO for the O_3 , H_2O*, H_2* and NH_3* processes respectively. The crystallinity was most pronounced for the NH_3*-grown MnO films, and weakest for the H_2*-grown mixed phase.

Although atomic concentrations as derived from XPS were used to estimate the impurity of the as-deposited layers, the Mn:O concentration ratio (figure 4.4) cannot be determined with sufficient accuracy to identify the oxidation state of Mn. In literature, alternative methods have been reported to obtain the Mn oxidation state from XPS data. A linear relation has been reported between the Mn oxidation state and the energy differ-

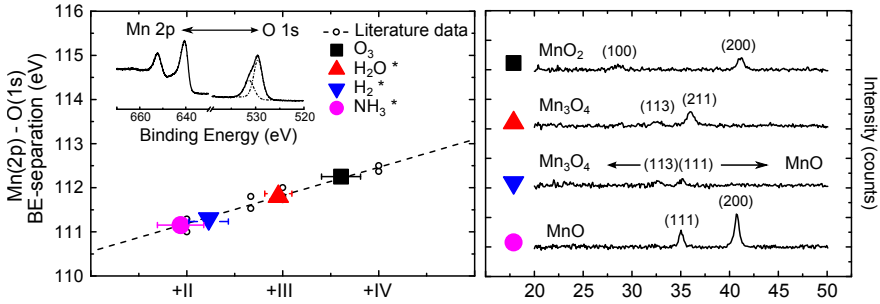

Figure 4.5: (left) Analysis of the XPS peak separation described in the text with literature data [165, 181–183], as shown in the inset for the NH_3* PE-ALD film. (right) XRD patterns measured on MnO_x films grown using 1000 (PE)ALD cycles with different reactants. The (h k l)-planes and corresponding phases are labelled in the figures.

	O:Mn	ratio	Crystallinity	Manganese oxidation state (XPS fit)
O_3	67.0 : 31.7	2.11	MnO_2	3.61 ± 0.21
H_2O*	54.2 : 42.5	1.27	Mn_3O_4	2.95 ± 0.15
H_2*	56.6 : 43.4	1.30	MnO/Mn_3O_4	2.23 ± 0.21
NH_3*	46.6 : 47.2	1.01	MnO	1.94 ± 0.25

Table 4.1: Film properties as determined by XPS (figure 4.4, 4.5) and XRD (figure 4.5), clearly illustrating the increase in reductivity from top to bottom.

ence between the Mn $2p^{3/2}$ maximum and the peak position of the lowest energy component of the O 1s spectrum (Mn-O-Mn bond) [165, 181–183]. This was used to estimate the oxidation state of Mn in the (PE-)ALD films. The results are depicted in figure 4.5 and summarised in table 4.1, and agree very well with the oxidation states predicted from crystal phase analysis.

The $Mn(thd)_3$ precursor has manganese in the +III state. If this was merely a ligand-exchange chemistry, the grown films would be Mn_2O_3, which has the same Mn oxidation state. However, none of the films do, as can be seen in table 4.1: with O_3 it goes to Mn(IV), NH_3* gives Mn(II), and both H_2* and H_2O* give a mix of Mn(II) and Mn(III), with more Mn(III) in the H_2O*-grown films than in the H_2*-grown films. The first half-reaction is assumed to be a simple ligand-exchange reaction with the surface-bound OH-groups (depicted as *−OH):

$$*-OH + Mn(R)_3 \longrightarrow *-O-Mn(R)_2 \qquad \text{(single surface bond)} \quad (4.1)$$

with R the 2,2,6,6-tetramethyl-3,5-heptanedionato ligands, leaving the +III oxidation state of the Mn intact. This reaction happens twice, as was found in the work of Nilsen. [100] The change of oxidation state from the precursor (+III) to different states (+IV, +II and +II/+III mixed state for the O_3 , NH_3* and H_2*/H_2O* resp.) can be attributed to the oxidizing or reducing nature of the reactant gas or plasma in the subsequent step. When an oxidizing atmosphere such as O_3 is used the film grows as MnO_2, raising the oxidation state from Mn(III) to Mn(IV). This is readily understood since Mn(IV)O_2 is the low-temperature most stable oxide of the series for MnO_x ($1 < x < 2$) [123, 194].

To explain the change in oxidation state from the precursor +III state to the +II and +II/+III mixed states for the NH_3* , H_2* and H_2O* processes, the active species in these plasmas were determined using OES (figure 5.1, supplementary information). In the NH_3* and H_2* plasmas, the H$\cdot$ radicals are likely responsible for the reduction of Mn(+III) to the lowest oxidation state oxide Mn(+II)O. The oxygen in these films does not originate from the reagent plasma, but is already bound to the Mn in the 2,2,6,6-tetramethyl-3,5-heptanedionato ligands. The H_2O* plasma is at an in-between state, having both oxidizing (OH^-) and reducing (H$\cdot$) radicals in its plasma. This in turn induces an in-between oxidation state in the films, namely a partly reduced +II/+III state for the Mn (Mn_3O_4). Some surface molecules will undergo a reduction reaction with the H$\cdot$ radicals, as is the case in the H_2* plasma, and some will undergo a second exchange-type reaction with the OH-groups, resulting in a mixed +II/+III oxidation state, in effect growing as Mn_3O_4. It is concluded that the oxidizing or reducing nature of the reactant gas or plasma determines the oxidation state of Mn in the ALD grown MnO_x layers, and it is found that the plasmas examined here can be arranged in order of increasing reductivity as H_2O* < H_2* < NH_3*.

Furthermore, it is worth mentioning that, while N_2* itself is not sufficient to avoid a significant build-in of precursor ligands, the presence of N_2 radicals in the plasma does seem to have an impact. The H_2* contained no activated nitrogen while the NH_3* does. It was shown in this work that the two plasmas lead to a different film in terms of impurities, crystallinity and as we will show later, electrochemical properties. However, the oxidation states are near each other, leading to believe that this is mainly caused by the H$\cdot$ radicals in both plasmas.

The four manganese oxide films that can be grown with the $Mn(thd)_3$ precursor (MnO_2, Mn_3O_4, MnO/Mn_3O_4 mixed state and phase-pure MnO) were tested as lithium-ion electrodes. The cyclic voltammograms of these films were investigated in their respective relevant potential ranges, as

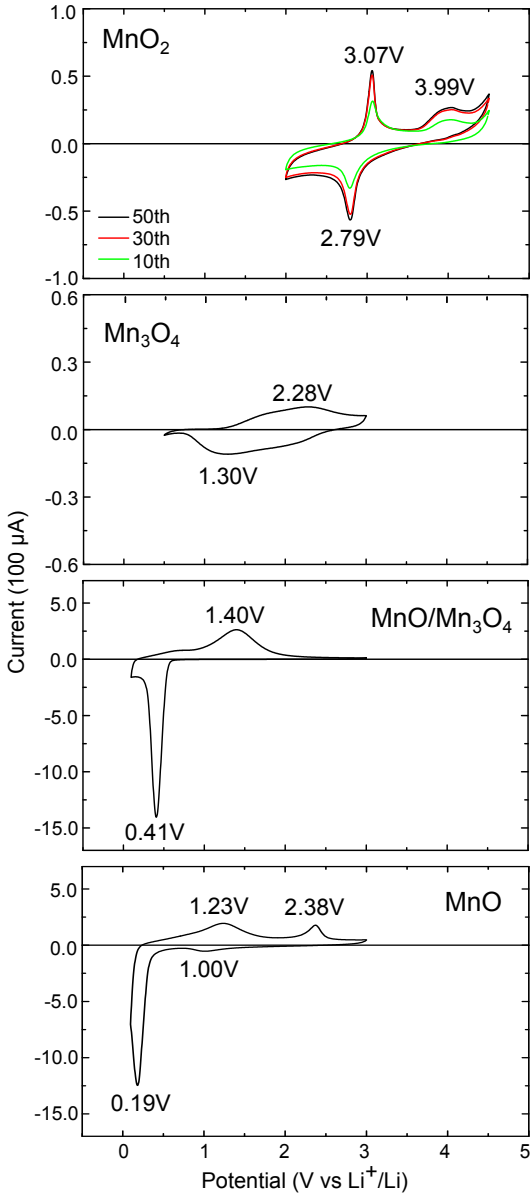

Figure 4.6: Cyclic voltammograms of the four selected films at 10 mV s^{-1}. From top to bottom: 18.3 nm MnO_2-film from the O_3 process cycled at 2.0-4.5V vs Li^+/Li, 20.0 nm Mn_3O_4-film from the H_2O* process cycled at 0.6-3.0V vs Li^+/Li, 26.3 nm MnO/Mn_3O_4-film from the H_2* process cycled at 0.1-3.0V vs Li^+/Li and 31.6 nm MnO-film from the NH_3* process cycled at 0.1-3.0V vs Li^+/Li.

shown in figure 4.6, from which the average peak potential was extracted as

$$U^p_{1/2} = \frac{U^p_{ox} + U^p_{red}}{2} \tag{4.2}$$

with U^p_{ox} the cathodic peak potential and U^p_{red} the anodic peak potential. The potential for the MnO_2 was examined between 2.0-4.5V vs Li^+/Li and shows reversible lithium insertion and extraction at 2.8V and 3.0V vs Li^+/Li , respectively. This gives an average peak potential of 2.9V for the reaction

$$MnO_2 + xLi^+ + xe^- \rightleftharpoons Li_xMnO_2 (0<x<1) \tag{4.3}$$

The as-deposited films showed electrochemical activity without the need for an additional post-deposition anneal step, in contrast to the reported Electrodeposited Manganese Dioxide (EMD) [155]. However, the same activation behaviour as observed on EMD was seen, meaning that more than 10 cycles were required to obtain a clear lithiation and delithiation behaviour around 2.9V vs Li^+/Li. This kind of evolution in cycling behaviour was ascribed in literature to restructuring, increased electronic conductivity, pore wall thinning or increased contact between film and liquid [155]. However, since the films investigated here are nonporous, the last two options can be omitted, leaving either restructuring due to re- or de-crystallisation, or/and increased electronic conductivity due to lithium doping as proposed explanations. Here, amorphisation was confirmed as no crystal structure could be found using XRD after the first lithiation.

The lithium undergoes a similar insertion mechanism into the Mn_3O_4 crystal lattice when lithiated to 1.0V vs Li^+/Li according to Fang *et al.* [153] and Thackeray *et al.* [150]:

$$Mn_3O_4 + xLi^+ + xe^- \rightleftharpoons LixMn_3O_4 (0<x<1) \tag{4.4}$$

and was cycled in the 0.5-3.0V vs Li^+/Li potential range to obtain this transition. A faint redox waveform was observed at $U^p_{1/2}$ = 1.79V vs Li^+/Li as shown in figure 4.6, but the capacity was very low, as will be shown further.

Lithiation into MnO happens according to a reversible conversion mechanism, where the oxide is reduced to a metal phase embedded into a Li_2O matrix [153]:

$$MnO + 2\,Li^+ + 2\,e^- \rightleftharpoons Mn + Li_2O \tag{4.5}$$

The films here were cycled between 0.1-3.0V vs Li^+/Li. Both as-deposited films showed electrochemical activity without the need for additional annealing (figure 4.6). Even though their as-deposited oxidation state and impurity content differed only slightly, very distinctive features in electrochemical performance were observed between the mixed-phase and

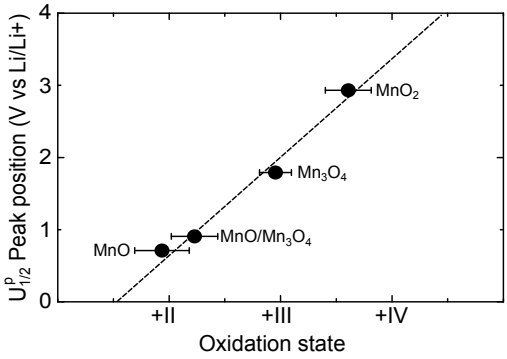

Figure 4.7: Relationship between measured as-deposited oxidation states (XPS, figure 4.5) and measured averaged peak potential ($U^p_{1/2} = 1/2 \times (U^p_{ox} + U^p_{red})$) from cyclic voltammetry (figure 4.6).

phase-pure films. The cyclic voltrammograms for the phase-pure MnO shows two reduction/oxidation waves: one at $U^p_{1/2}$ = 0.71V vs Li^+/Li, which is associated with the conversion reaction (reaction 4.5), and an additional couple at $U^p_{1/2}$ = 1.69V vs Li^+/Li, which is probably caused by film deterioration due to volume expansion and is thus a side reaction. The mixed-phase material has only one wave, at $U^p_{1/2}$ = 0.905V vs Li^+/Li.

Not taking into account the side-reaction wave, a nice result emerges when we also take into account the redox couples for the MnO_2 ($U^p_{1/2}$ = 2.93V vs Li^+/Li) and the Mn_3O_4 ($U^p_{1/2}$ = 1.79V vs Li^+/Li). In figure 4.7 the average peak potentials are related to the measured oxidation states and a linear relationship between the two is revealed. Since we have shown earlier that we can control the oxidation state by choosing the ALD process gas/plasma, we can in effect tune the electrochemical properties of these films, and grow a film that can either be a Li-ion cathode (MnO_2) or an anode (phase-pure MnO and mixed-phase MnO/Mn_3O_4), using the same precursor chemistry.

Electrode capacities were also investigated galvanostatically on fresh films, and charge-discharge curves can be found in supplementary to this paper for the first 20 cycles at $10\,\mu A\,cm^{-2}$ (figure 5.2), with potential boundaries chosen corresponding to the oxidation states. The MnO_2 films showed the same activation behaviour as observed in the CV-measurements. The reversible capacity grew from ∼15% of the theoretical capacity to ∼25% of theoretical capacity after 40 cycles at a C-rate of about 3.5. When the activated film was cycled at a current density of about ∼0.35C the measured reversible capacity rose to about 71% of the theoretical capacity.

Mn_3O_4 has a low theoretical capacity and an intermediate voltage, making it less attractive as an electrode material. Even with that, only 57% of the theoretical was obtained at ∼1C. Due to the loss of gravimetric capacity to irreversible storage of Li_2O when discharging to a lower voltage (reaction 4.6, results not shown here), this material can not compete with the MnO and MnO/Mn_3O_4 in terms of anodic capacity.

Finally, phase-pure MnO and mixed-phase MnO/Mn_3O_4 the anodes were compared in terms of capacity. The reversible capacities during the first cycle are 68% and 88% of the theoretical capacity for the mixed-phase and phase-pure samples, respectively. When a negative current is applied to the mixed-phase films, the Mn(III)-fraction is reduced to Mn(II) according to reaction 4.4 and further when lithiated to 0.4V vs Li^+/Li

$$LiMn_3O_4 + Li^+ + e^- \longrightarrow 3\,MnO + Li_2O \tag{4.6}$$

Since this last reaction is irreversible, this could explain the difference in initial reversible capacity between the phase-pure and mixed-phase films.

From the previous results the phase-pure film would seem the best candidate for the anode. However, when cycling this material 20 times between 0.1-3V vs Li^+/Li, a capacity loss of 25% was observed in the phase-pure MnO. The mixed-phase sample on the other hand lost only 4% of its capacity, which is a much better result. So, even though the phase-pure films have a much higher initial capacity, the mixed-phase films seem to be much more stable, as was also observed in cyclic voltrammetry as the lack of additional reduction/oxidation wave (figure 4.6). This could again be attributed to the build-in of Li_2O in these films. It was shown in other work on tin oxide that the addition of Li_2O in a conversion anode would accommodate some of the stress associated with volume changes in these films [195]. It is thus proposed that, similar to the tin oxide case, the irreversible incorporation of Li_2O in the mixed-phase films stabilises the MnO conversion reaction, allowing for improved cyclability.

CONCLUSIONS

The $Mn(thd)_3$-chemistry based ALD process was successfully extended to PE-ALD with 3 processes using ammonia, hydrogen and water plasma. The ALD parameters were investigated in detail for the ammonia plasma process, revealing a saturated growth rate of 0.2 Å/cycle in an ALD temperature window of 150 °C to 255 °C. Saturation was confirmed at 180 °C for the water and hydrogen plasma processes. All films showed low roughness (rms roughness <1.2 nm) and low carbon and nitrogen impurities. All as-deposited films with a thickness larger than 10 nm were crystalline

according to XRD. The combination of XRD and XPS peak separation analysis clearly showed that the oxidizing/reducing nature of the reactant gas or plasma is a determining factor for the oxidation state of manganese in the MnO_x films ($1<x<2$). The MnO, MnO/Mn_3O_4 and MnO_2-films (ALD-deposited using NH_3*, H_2* and O_3 as reactant resp.) showed as-deposited electrochemical activity at 0.71, 0.905 and 2.93V vs Li^+/Li respectively, yielding two conceptual li-ion anodes and one cathode. Further work towards thickness and effective surface area enhancement is required to provide a structure with sufficient energy density for a microstructured or so-called 3D thin-film battery. A linear relation between the as-deposited oxidation state and electrochemical properties was found, demonstrating that tuning the film properties (oxidation state) allows tuning the electrochemical properties. This work demonstrates an effective method for the controlled deposition of Mn(+IV)O_2, Mn(+II/+III)$_3O_4$ and Mn(+II)O based on the Mn(+III)$(thd)_3$ precursor.

5

SUPPLEMENTARY TO PAPER I

OPTICAL EMISSION SPECTROSCOPY

The plasmas investigated here were characterised by optical emission spectroscopy (OES) using an Ocean Optics QE65000 spectrometer with a wavelength range of 200 nm to 1000 nm. Acquisition times were chosen to allow the identification of individual emission lines by comparison with literature reports [196–198].

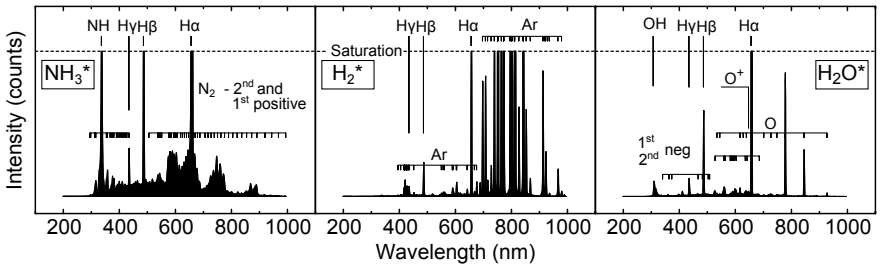

Figure 5.1: Emission lines of the plasmas under investigation: ammonia (left), hydrogen (center) and water (right).

GALVANOSTATIC EXPERIMENTS

Galvanostatic cycling of fresh films of all MnO_x films were performed to determine capacity and examine capacity evolution in the first 20 cycles. Results of these measurements are summarised in table 5.1 and shown in figure 5.2. The measurement for MnO_2 was performed between 2.0-4.0V vs Li^+/Li, as was also done in other work on thin film MnO_2 [155]. The galvanostatic measurements presented in figure 5.2 give an estimate of the capacity of the ALD-grown materials by comparing the measured values to the theoretical capacities. For an 18.3 nm MnO_2 film a maximum capacity density of 2.83 $\mu A\,h\,cm^{-2}$ is expected. Based on this calculated

theoretical capacity density, the C-rate of the galvanostatic cycling experiments at $10\,\mu A\,h\,cm^{-2}$ (figure 5.2) was about 3.5C. Under these conditions, the reversible capacity in the first cycle was only $0.42\,\mu A\,h\,cm^{-2}$ ($\sim$15% of theoretical capacity) but grew to $0.72\,\mu A\,h\,cm^{-2}$ ($\sim$25% of theoretical capacity) after 40 cycles, without halt in capacity increase. When the activated film was cycled galvanostatically at a current density of $1\,\mu A\,cm^{-2}$ ($\sim$0.35C) the measured reversible capacity (measurement not shown here) rose to $2.01\,\mu A\,h\,cm^{-2}$, about 71% of the theoretical capacity. An additional delithiation wave developed above 3.7V vs Li^+/Li during cycling, as was also revealed on the CV measurements. The peak potential was found at 3.99V vs Li^+/Li.

For a 20.0 nm Mn_3O_4 film the theoretical capacity was calculated to be $1.137\,\mu A\,h\,cm^{-2}$ from the gravimetric theoretical capacity $117\,mA\,h\,g^{-1}$ for the reaction

$$Mn_3O_4 + xLi^+ + xe^- \rightleftharpoons LixMn_3O_4(0<x<1) \tag{5.1}$$

while assuming a bulk density of $4.86\,g\,cm^{-3}$. However, the measured reversible capacity (table 5.1 and figure 5.2) was only a fraction of the theoretical value (22% and 28% in the first and 20th cycle, resp.). When cycling at $1\,\mu A\,cm^{-2}$ or $\sim$1C the capacity rose to $0.65\,\mu A\,h\,cm^{-2}$, about 57% of the theoretical value, but still not a very impressive value due to its already low theoretical capacity. Due to the loss of gravimetric capacity to irreversible storage of Li_2O when discharging to a lower voltage (as discussed elsewhere), this material can not compete with the MnO and MnO/Mn_3O_4 in terms of anodic capacity.

Finally, phase-pure MnO and mixed-phase MnO/Mn_3O_4 the anodes were compared in terms of capacity. The theoretical capacity density for the 26.3 nm-thick mixed-phase film is found to be $10.8\,\mu A\,h\,cm^{-2}$, calculated from theoretical gravimetric capacity of MnO ($756\,mA\,h\,g^{-1}$) and assuming bulk-MnO for the density ($5.43\,g\,cm^{-3}$). The measured initial reversible capacity at $10\,\mu A\,cm^{-2}$ ($\sim$1C) was $7.39\,\mu A\,h\,cm^{-2}$ during the first cycle, or 68% of the theoretical capacity. In comparison, the 31.3 nm-thick phase-pure MnO had a much higher initial reversible capacity: 11.24 $\mu A\,h\,cm^{-2}$ during the first cycle, i.e. 88 % of the theoretical capacity (12.8 $\mu A\,h\,cm^{-2}$).

Crystallinity (thickness in nm)	Mn Ox.St. (XPS fit)	Peak currents (V vs Li^+/Li) U^p_{ox}	U^p_{red}	$U^p_{1/2}$	Capacity ($\mu A\,h\,cm^{-2}$)[$A\,h\,cm^{-3}$] 1st lithiation	1st delithiation
					Reversible capacity after 20 cycles	
MnO_2 (18.3)	3.61 ± 0.21	3.07	2.79	**2.93**	0.923 [0.50]	0.417 [0.23]
		3.99	-	-	0.723 [0.40]	
Mn_3O_4 (20.0)	2.95 ± 0.15	2.28	1.30	**1.79**	2.21 [1.11]	0.249 [0.12]
					0.320 [0.16]	
MnO/Mn_3O_4 (26.3)	2.23 ± 0.21	1.40	0.41	**0.905**	15.46 [5.88]	7.39 [2.81]
					7.13 [2.71]	
MnO (31.3)	1.94 ± 0.25	1.23	0.19	**0.71**	21.27 [6.80]	11.24 [3.59]
		2.38	1.00	1.69	8.40 [2.68]	

Table 5.1: Overview of measured electrochemical properties of films. Cyclic voltammetry at $10\,mV\,s^{-1}$, galvanostatic charge/discharge at $10\,\mu A\,cm^{-2}$. Volumetric capacities (between square brackets) are calculated using the film thickness as measured by XRR on reference samples.

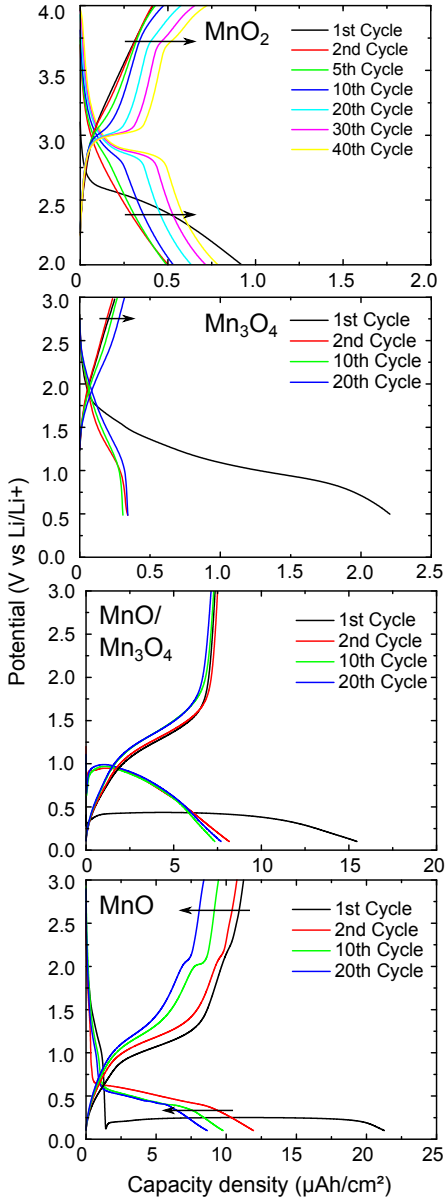

Figure 5.2: Charge-discharge voltage profiles of the four selected films at 10 µA cm^{-2}. From top to bottom: 18.3 nm MnO_2-film from the O_3 process cycled at 2.0-4.0V vs Li^+/Li, 20.0 nm Mn_3O_4-film from the H_2O* process cycled at 0.6-3.0V vs Li^+/Li, 26.3 nm MnO/Mn_3O_4-film from the H_2* process cycled at 0.1-3.0V vs Li^+/Li and 31.6 nm MnO-film from the NH_3* process cycled at 0.1-3.0V vs Li^+/Li.

6

PAPER II

MANGANESE OXIDE FILMS WITH CONTROLLED OXIDATION STATE FOR WATER SPLITTING DEVICES THROUGH A COMBINATION OF ATOMIC LAYER DEPOSITION AND POST-DEPOSITION ANNEALING

Felix Mattelaer,*[a] Tom Bosserez,[b] Jan Rongé,[b] Johan A. Martens,[b]
Jolien Dendooven,[a] and Christophe Detavernier[a]
Published in *RSC Advances* (2016). Doi: 10.1039/C6RA19188F

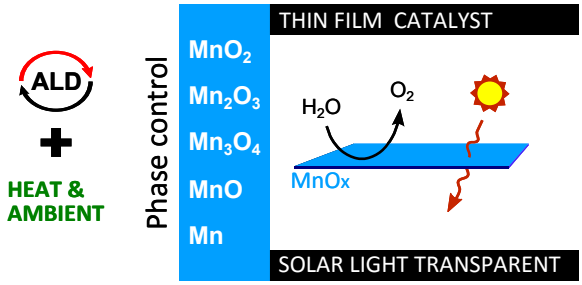

[a] *Department of Solid State Sciences, Ghent University, Krijgslaan 281 S1, 9000 Gent, Belgium,*
[b] *Centre for surface chemistry and catalysis, KU-Leuven, 3001 Leuven, Belgium.*

ABSTRACT

Solar hydrogen devices combine the power of photovoltaics and water electrolysis to produce hydrogen in a hybrid form of energy production. To engineer these into integrated devices (i.e. a water splitting catalyst on top of PV element), the need exists for thin film catalysts that are both transparent for solar light and efficient in water splitting. Manganese oxides have already been shown to exhibit good water splitting performance, which can be further enhanced by conformal coating on high surface-area structures. The latter can be achieved by atomic layer deposition. However, to optimize the catalytic and transparency properties of the water splitting layer, an excellent control over the oxidation state of the manganese in the film is required. So far MnO, Mn_3O_4 and MnO_2 ALD have been shown, while Mn_2O_3 is the most promising catalyst. Therefore, we investigated the post-deposition oxidation and reduction of MnO and MnO_2 ALD films, and derived strategies to achieve every phase in the MnO-MnO_2 range by tuning the ALD process and post-ALD annealing conditions. Thin film Mn_2O_3 is obtained by thermal reduction of ALD MnO_2, without the need for oxidative high temperature treatments. The obtained Mn_2O_3 is examined for solar water splitting devices, and compared to the as-deposited MnO_2. Both thin films show oxygen evolution activity and good solar light transmission.

INTRODUCTION

The rise of the internet of things (IoT) requires, besides sensors and energy storage, small and autonomous energy production. Integrated solar hydrogen devices consist of a photo-active material buried beneath a water splitting catalyst. The catalyst on top has to fulfil three requirements: (1) good water splitting performance, (2) excellent solar light transmission and (3) good stability. In order to minimize the local current density and improve criterion (1) and (3), thin films on high surface area 3D structures can be utilized. Atomic layer deposition (ALD) allows for conformal deposition of thin films of many metal oxides on very high aspect ratio structures [199], meeting the third requirement. Concerning the first two requirements, benchmark catalysts such as platinum suffer from high cost, low abundance and no solar light transmission. Other benchmark catalysts such as IrO_x may be more transparent, but iridium has an even lower abundance than platinum. Transparent, abundant and low cost oxides, such as manganese oxide, are more favourable in this respect. Thin film manganese oxides have been investigated as water oxidation cata-

lysts in many reported studies [129, 130, 178, 200–202]. In our previous work, we showed that the oxidation state of Mn can be controlled during ALD growth with the $Mn(thd)_3$ precursor by selecting the proper oxidative or reductive reactant gas or -plasma during the ALD process. Mn(+II)O, Mn_3(+II/+III)O_4 and Mn(+IV)O_2 are achievable by using ammonia plasma, water plasma and ozone, respectively [171]. $Mn(EtCp)_2$ was reported to grow the bivalent manganese oxide Mn(+II)O [170, 178]. Although Mn_2O_3 is reported as the most active catalyst for the oxygen evolution reaction (OER) thanks to the high activity of the Mn(+III) sites [129, 180], direct ALD of Mn_2(+III)O_3 thin films has not been reported so far [100, 101, 171, 199]. Pickrahn et al. evaluated an ALD-based Mn_2O_3 catalyst for OER by depositing MnO ALD and oxidizing it to Mn_2O_3 [178]. In that case, it was found that the oxidized Mn_2O_3 outperformed the as-deposited MnO. Li et al evaluated the influence of post-annealing of ALD-grown β-MnO_2 in oxidizing ambients up to 700 °C [203]. However, the oxidizing ambient used in those studies to increase the manganese oxidation state could have a detrimental effect on the surrounding and underlying materials in integrated materials. From the manganese phase diagram and earlier studies on bulk manganese oxides it is shown that re-oxidation of bulk manganese oxides up to Mn_2O_3 is possible, and reduction down to MnO and even manganese metal can be obtained by raising temperature and varying the oxygen partial pressures [124, 178, 182, 204]. Faster reduction can be achieved when introducing a hydrogen atmosphere to manganese oxides [204, 205].

In this work, we explore various annealing routes to control the oxidation state of ALD-grown manganese oxide thin films by tuning the ALD processing conditions and post-ALD anneal conditions. Starting from the two extrema in the manganese oxide spectrum, MnO and MnO_2, we used XPS and *in-situ* XRD to monitor the phase evolution in oxidizing, inert and reducing atmospheres from room temperature up to 900 °C. Since roughness is also a determining factor for catalytic performance, the surface topography of the oxidized and reduced thin films is systematically evaluated by atomic force microscopy. This paper reports a systematic study of possible pathways towards the full range of manganese oxides that can be obtained by tuning ALD process parameters and the post-ALD annealing conditions, such as temperature (20 °C to 900 °C) and ambient (oxidating, inert and reducing) as parameters. Our results show that thin film Mn_2O_3 can be obtained by heating ALD MnO_2 in an inert atmosphere. This enables a wider range of sensitive substrates. The MnO_2 and MnO_2-derived Mn_2O_3 were evaluated as water oxidation catalysts, and both perform well when compared to a known catalyst such as platinum,

with the added advantage of excellent solar light transmission coefficients and high abundance.

EXPERIMENTAL

The manganese oxides were grown in an experimental high-vacuum ALD setup with a base pressure of 10^{-7} mbar [93–95, 171]. The ALD processes are based on the $Mn(thd)_3$ precursor (Tris(2,2,6,6-tetramethyl-3,5- heptanedionato) manganese from Strem, 99%). In this work we examine the oxidation and reduction behaviour of MnO_2 and MnO thin films grown by thermal ALD ($Mn(thd)_3$ and O_3 ALD) and PE-ALD ($Mn(thd)_3$ and NH_3 plasma ALD) at 180 °C, respectively. ALD characteristics and growth conditions can be found in our earlier report [171]. MnO and MnO_2 films obtained from 1000 cycles of atomic layer deposition were grown on H-terminated Si (by stripping the native oxide by etching in a 5%HF solution for 1 min before deposition), 100 nm thermally grown SiO_2 on a Si substrate, resulting in a 37 nm and 20 nm film, respectively.

In-situ XRD was used to determine the crystal state during annealing, measuring with the X-ray source (Cu Kα radiation at 0.154 nm) and lineair detector in fixed positions at 20° and 35° respectively, resulting in a 24° to 44° window in 2θ with a 5° offset to avoid substrate peaks. Annealing was done in a stainless steel chamber, under a flow of $20\,l\,h^{-1}$ of oxygen (Praxair, 99.999 %), helium (Praxair, 99.999 %) or forming gas (helium + 5%H_2, Praxair, 99.999 %), at a heating rate of $0.25\,°C\,s^{-1}$ from room temperature to 900 °C [206, 207]. To verify the oxidation states derived from the crystal state found in XRD (and to confirm the absence of an amorphous fraction with a potentially different oxidation state) selected samples were investigated by XPS, which was performed using Al Kα radiation (0.834 nm) under a take-off angle of 45° in a high-vacuum chamber (2×10^{-9} mbar). A resolution of 0.108 eV was obtained. The Mn-O-Mn bond was investigated by evaluation of the binding energy difference between the Mn $2p^{3/2}$ and the O 1s signals (Mn-bond component) [165, 171, 181–183, 203].

The film morphology was probed on the as-deposited and quenched samples using a Bruker Dimension Edge atomic force microscope (AFM) and film rms roughness was determined from 1 µm × 1 µm AFM images. Film surface morphology was further examined using a high-vacuum electron microscope (FEI Quanta 200F).

MnO_2 and Mn_2O_3 are examined for their catalytic properties. To this end, 200 ALD cycles of MnO_2 (resulting in a 3 nm film) were deposited on Toray carbon paper as an electrical contact for the activity measurements, and MnO_2 films were deposited on glass substrates for the investigation

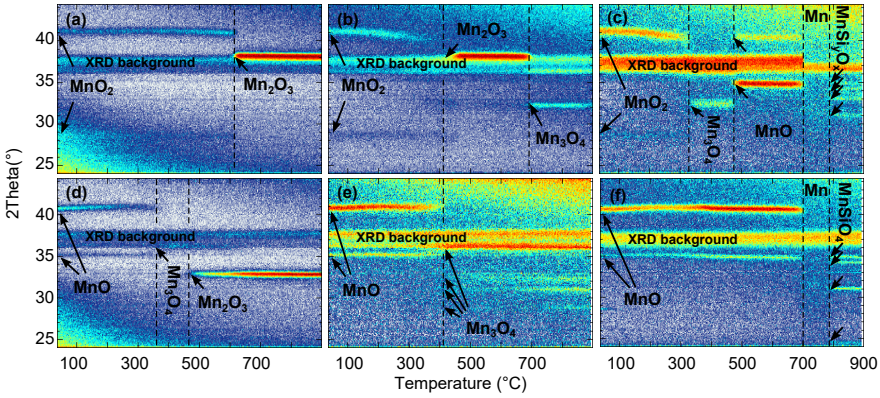

Figure 6.1: In-situ XRD measurements from room temperature to 900 °C at a heating rate of 0.25 °C s^{-1} in oxygen, helium and hydrogen ambient of the as-deposited MnO and MnO_2 films: MnO_2 in O_2 ambient (a), He ambient (b) and H_2/He ambient (c), and MnO in O_2 ambient (d), He ambient (e) and H_2/He ambient (f). Peak identification was performed using the JCPDS database: β-MnO_2 (81-2261), Mn_2O_3 (89-2809), Mn_3O_4 (24-0734), MnO (75-0625), α-Mn (32-0637), Mn_2SiO_4 (35-0747) and $MnSiO_3$ (89-2809).

of their optical properties. MnO_2 films were evaluated as such, and converted to $Mn_2O_3$by post-deposition annealing. Transmission UV-Vis spectroscopy of MnO_2 and Mn_2O_3 on glass substrates was carried out using an Infinite M200 Pro instrument (Tecan). Light absorbance ($A(\lambda)$) of the glass substrate and of the films deposited on the glass substrate was measured, and the former was subtracted from the latter to correct for the substrate. The absorbance, including components from both light absorption and reflection, was converted to a transmittance using $T(\lambda) = 10^{-A(\lambda)}$. Linear voltammetric sweeps in the anodic direction were performed on the as-prepared samples with a sweep rate of 2 mV s^{-1} (experimental details described in supplementary, figure 7.1).

RESULTS AND DISCUSSION

In-situ XRD and AFM results

In-situ XRD patterns measured on both films during annealing in oxidizing, inert and reducing ambient are shown in figure 6.1. The XRD peaks clearly reveal the oxidation and reduction behaviour of the manganese oxides thin films under study. A quench of every intermediate phase was taken to be examined separately. The oxidation state of the manganese

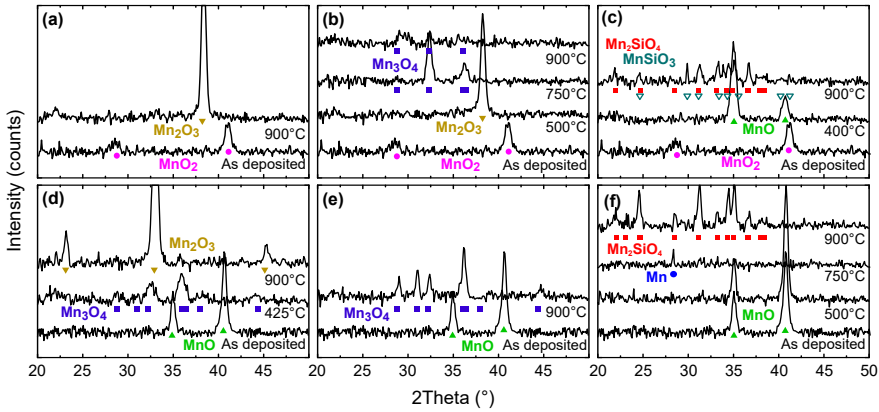

Figure 6.2: XRD spectra of selected quenches, starting from the ALD MnO_2 film (top) and from the ALD MnO film (bottom). From left to right: oxygen, helium and forming gas ambient, respectively. A background was subtracted from the measured spectra, and they are offset to allow better visualisation. Peak identification was performed using the JCPDS database (see figure 6.1), with reported peak positions shown on the graphs.

in selected samples was examined by XPS (supplementary information, figure 7.2) which matched the crystalline phase, indicating that no amorphous fraction was present with a different manganese oxidation state. The quenched samples all remained in the crystalline phase they were in at the time of the anneal, demonstrating that all these intermediate phase formations observed in in-situ XRD are stable when quenched (figure 6.2).

Next, we examined the roughness of the as deposited films and the selected quenches. Figure 6.3 shows AFM images of the as deposited samples, as well as the selected quenches. The as-deposited films are shown to be very smooth, with a roughness of only 0.40 nm and 0.86 nm for the MnO and MnO_2 films, respectively. Some quenches show little evolution, but most of the high-temperature quenches show severely changed morphology or increased roughness.

Discussion of the phase evolution

A summary of the phase formation and roughness evolution is presented in figure 6.4. This figure gives a systematic overview of different strategies that enable achieving a particular phase and resulting roughness. At low temperature and high oxygen ambient, the MnO_2 phase is the stable phase

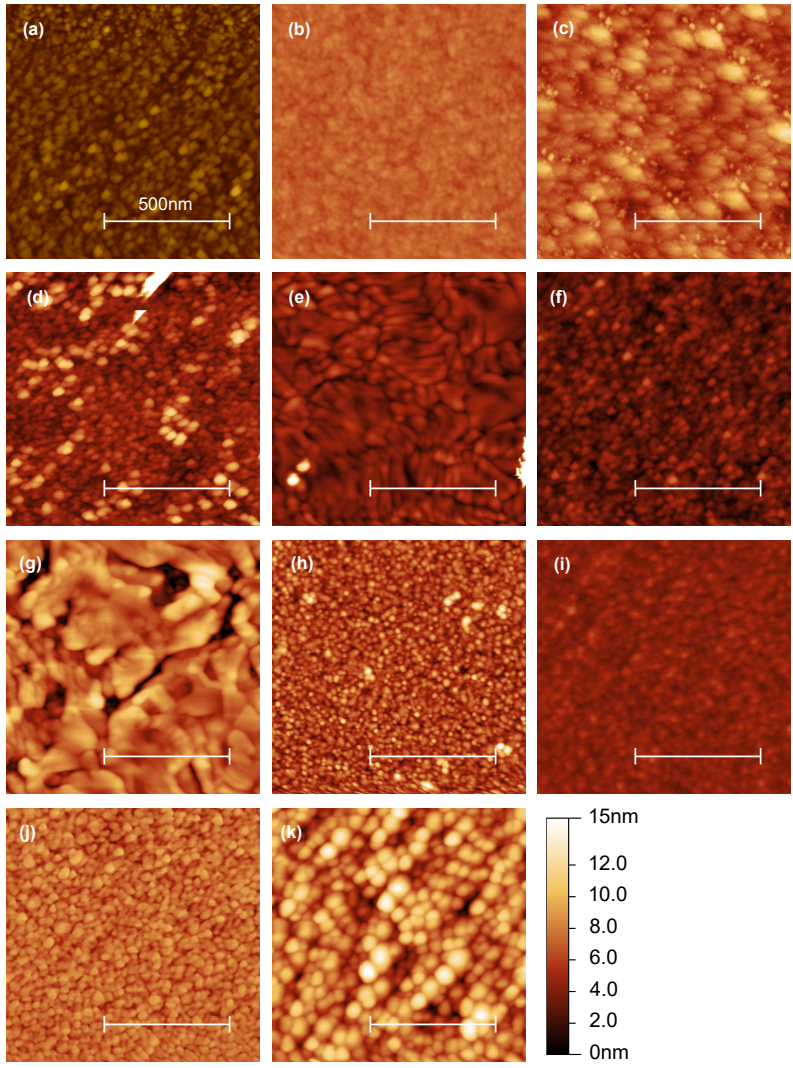

Figure 6.3: 1 by 1 µm AFM images of the as deposited MnO_2(a) and MnO(b) ALD films on the SiO_2 substrate. An AFM image of the H_2O PE-ALD film (c), resulting in a Mn_3O_4 film is added for completeness (process conditions according to earlier work [171]). AFM images of quenches are shown: MnO_2 annealed in oxygen to 900 °C(d), in helium to 500 °C(e), 750 °C(f) and 900 °C(g), and in He/H_2 to 500 °C(h), and MnO annealed in oxygen to 425 °C(i) and 900 °C(j) and helium to 900 °C(k). Images are set to the same 15 nm colour scale to allow direct comparison.

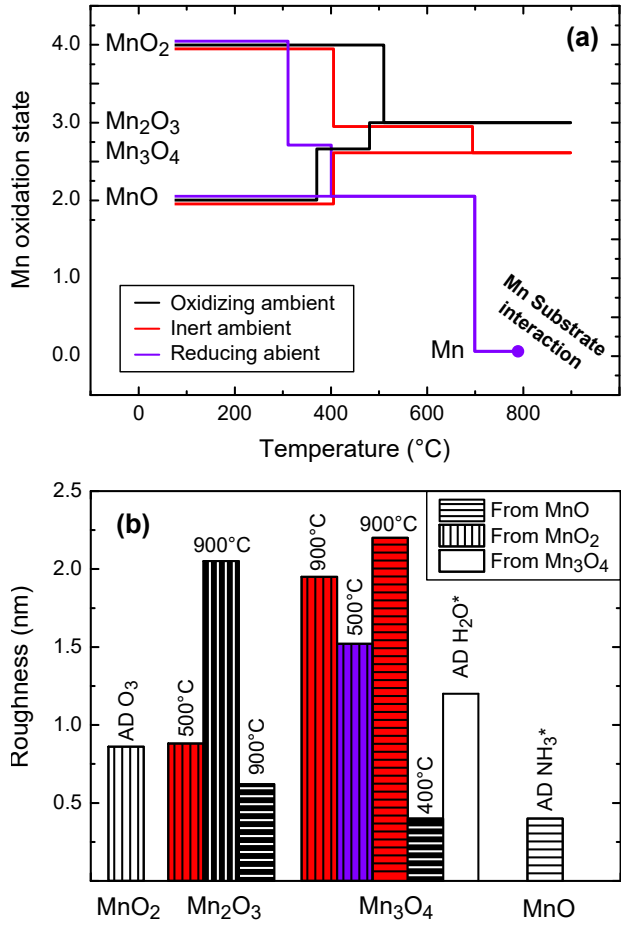

Figure 6.4: Summary of the manganese oxidation and reduction behaviour based on in-situ XRD results (figure 6.1) and AFM study (figure 6.3). (a) Thin film phase stability and (b) roughness evaluation for the as deposited (AD) and resulting films. The same colour mapping is used in both figures, and in the bottom figure horizontal or vertical lines indicate films that were originally MnO and MnO_2, respectively.

[123]. However, it is kinetically not possible to oxidize the MnO films to MnO_2 under standard atmospheric pressure conditions before entering the temperature regime where Mn_2O_3 becomes more stable, leaving only the as-deposited films grown using the ozone-based process with the Mn in the +IV oxidation state. Indeed, in an oxidizing ambient, the MnO films quickly transverse the Mn_3O_4 phase to end up in the Mn_2O_3 phase, as can be seen in figure 6.1(d). Even though these films undergo two phase transitions, this is still a smoother film than the Mn_2O_3 obtained from the MnO_2 films in oxidizing or inert ambient. This roughness has a two-fold origin. Firstly, the MnO_2 films themselves have a higher surface roughness than the MnO films. In the case of the anneal in inert atmosphere of the MnO_2 films, where the Mn_3O_4 is the high-temperature stable phase, the Mn_2O_3 can be formed at lower temperature, maintaining the surface roughness of the MnO_2. Secondly, when annealing the films in an oxygen ambient, the MnO_2 is stable for a broader temperature range and the Mn_2O_3 only forms at a higher temperature. This high temperature induces sharper features, as can be seen in figure 6.3(d), increasing the roughness. Besides the roughness, the Mn_2O_3 films originating from the MnO_2 and MnO process are also different in crystallinity. As we can readily see from the XRD spectra in figure 6.1 and figure 6.2, the films reduced from the MnO_2 phase show only one, albeit very strong, diffraction peak around a 2θ value of 38°, corresponding to the 400 reflection. This could indicate some form of preferential alignment of the crystal lattice. The film oxidized from the MnO on the other hand shows multiple diffraction peaks, indicating a more randomly oriented film. This corresponds well to the AFM image in figure 6.3(j), which shows small grains, while the films derived from an MnO_2 origin show much larger and more pronounced grains (e.g. figure 6.3(e)).

Mn_3O_4 thin films can be achieved in several ways. As was reported in our earlier work [171], this phase can be obtained without any additional processing steps when a H_2O plasma is used as a reagent during ALD, instead of the NH_3 plasma or ozone here that result in MnO and MnO_2, respectively. However, the films grown with the H_2O plasma process chemistry have a much higher surface roughness than the films obtained using the NH_3 plasma or ozone processes, as shown in figure 6.4. Indeed, three other pathways to obtain thin film Mn_3O_4 are shown here, where one of those has a significantly lower surface roughness than the as-deposited Mn_3O_4 obtained directly from the H_2O PE-ALD. This pathway is again the low-temperature method, by annealing the MnO films in oxygen above 360 °C. As was explained earlier the Mn_2O_3-phase is more stable at higher temperatures. This is also observed here: raising the tem-

perature of this film in an oxidizing ambient leads to further oxidation to a Mn_2O_3 film at a temperature of 470 °C. At high temperatures in an inert atmosphere, the MnO films also very gradually start to oxidise to Mn_3O_4, as can be seen in figure 6.1. This is likely related to oxygen impurities still left in the annealing chamber. Finally, the Mn_3O_4 phase can also be obtained by annealing a MnO_2 film in inert atmosphere, since this is the high-temperature stable phase in a low oxygen partial pressure ambient when sufficient oxygen is provided in the initial film. However, when closely observing the in-situ XRD spectrum at the highest temperatures (figure 6.1(b)), we see that the crystallinity fades near 900 °C. This also shows in the XRD spectrum of the quench on that point in figure 6.2, where barely any crystalline peaks remain visible. This change in the crystallinity translates into a severely increased roughness originating from a 'melt'-like surface topology, as shown in figure 6.3(g) and confirmed using SEM imaging (supplementary information, figure 7.4).

Since MnO is only thermodynamically favourable at high temperatures and low oxygen partial pressures, we also examined the effect of annealing in a reducing atmosphere. For this, a mixture of 5%H_2 in He was used as ambient in the annealing chamber. Here also, phase formation was monitored using in-situ XRD during annealing in the same temperature window as above. The resulting in-situ XRD figures are shown in figure 6.1. To allow for full phase identification, ex-situ quenches were made on selected temperatures and the diffraction patterns and identification is shown in figure 6.2.

The isXRD analysis in figure 6.1 shows that the introduction of a reducing ambient significantly influences the phase formation. Below 700 °C this is still the case, where the reducing ambient triggers rapid reduction of the manganese in the manganese oxide from MnO_2 over Mn_3O_4 to MnO in the case of a MnO_2 starting film. The as-deposited MnO film does not change phase below 700 °C, however, a strong increase in crystallinity is observed, associated with a peak shift to slightly lower 2θ-values. The MnO originating from the MnO_2 and MnO films are also not identical, since the ratios of diffraction peaks are inverse for both films. This again demonstrates that the initial film has some influence over the final film formation. Remarkably, the Mn_2O_3-phase is not observed here, and is seemingly 'skipped' when the MnO_2 films are first reduced.

Rather than simply remaining within the Mn-O phase system, the manganese oxides are fully reduced to metallic manganese above 700 °C. This, in turn, is able to react with the underlying SiO_2 substrate to form various forms of manganese silicate above 780 °C, as shown in figures 6.1 and 6.2. If the films are deposited on HF-cleaned silicon, a silicide is formed

instead of a silicate (not shown here). The nature of the silicate is again influenced by the initial film, even though both films are passing through the MnO phase before being fully reduced into metallic manganese. This difference in manganese silicate is seen in the presence of both $MnSiO_3$ and Mn_2SiO_4 in the film originating from the MnO_2 films, while the latter is found phase-pure in the films originating from MnO.

MnO_2 and Mn_2O_3 thin film water splitting catalysts

Generally, it is believed that the best manganese oxide for water splitting catalysis is the Mn_2O_3-phase, since the Mn(+III) sites show the highest catalytic activity [129, 180]. Above, we find that Mn_2O_3 can be obtained by spontaneous reduction at elevated temperatures of MnO_2 ALD films in inert atmosphere, since Mn_2O_3 is the high-temperature stable phase. In contrast to the MnO-route which was also investigated by Pickrahn et al [178], for the MnO_2 no oxidative atmosphere is required to transform to Mn_2O_3, opening a wider range of substrate compatibility. We investigated as-deposited MnO_2 and Mn_2O_3 (reduced from MnO_2) as water splitting catalysts. Linear voltammetry sweeps on these samples are shown in figure 6.5. As a reference, the Toray substrate, Pt on carbon black (PtCB, E-Tek 60 % platinum/carbon black powder, Umicore) on Toray substrate and sputtered IrO_2 on a silicon wafer are also shown. Surprisingly, ALD MnO_2 performs better than the derived Mn_2O_3: MnO_2 has an onset potential at 1.62 V *vs.* RHE (0.1 mA cm^{-2}) and an overpotential of 619 mV at 10 mA cm^{-2}. For Mn_2O_3 the onset potential was slightly higher at 1.63 V *vs.* RHE, but the overpotential at 10 mA cm^{-2} was much higher at 801 mV. Despite the similar onset of Mn_2O_3, it was less active compared to ALD MnO_2. This is clear from the different Tafel slopes of these materials (supplementary information, figure 7.3). These observations make ALD MnO_2 a very active OER catalyst with a higher activity compared to Pt-CB. However, both will still be outperformed by ruthenium oxide and iridium oxides that typically operate at an overpotential of 290 mV to 350 mV at the same current density, as shown in figure 6.5.

One important application of thin film catalysts would be integrated solar hydrogen devices, where electrocatalysts can be directly deposited on light absorbers [202]. For these applications, parasitic light absorption and reflection from catalyst layers needs to be minimized and therefore the transmittance of these films was investigated [208]. Figure 6.6 shows the transmittance of the ALD MnO_2 and derived Mn_2O_3 films deposited on glass in the range of 330-1000 nm. This shows a clearly higher transmittance for the Mn_2O_3, in agreement with the earlier study by Li et al

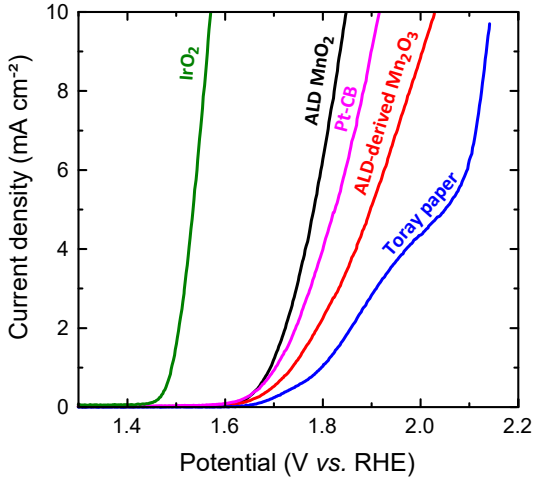

Figure 6.5: Anodic direction of linear voltammetry sweeps at 2 mV s^{-1} in 1 M KOH. Results for the as-deposited MnO_x films on Toray paper are shown, compared to Pt-CB, IrO_2 and Toray substrate reference samples.

[203]. For integration in a solar hydrogen device, the effect of the catalyst on light transmission integrated over the whole solar spectrum is particularly interesting and can be calculated as follows:

$$\eta = \frac{\int_{\lambda_{min}}^{\lambda_{max}} T_{film}(\lambda)\,\Phi(\lambda)\,\mathrm{d}\lambda}{\int_{\lambda_{min}}^{\lambda_{max}} \Phi(\lambda)\,\mathrm{d}\lambda} \tag{6.1}$$

where $T(\lambda)$ is the transmittance and $\Phi(\lambda)$ the photon flux in function of wavelength. Integrated over the solar flux, this yields an η_{solar} of 95.6 % and 98.8 % for ALD MnO_2 and derived Mn_2O_3 films, respectively. As can be seen from the light transmission in figure 6.1, the main difference in transmission is found in the ultra-violet wavelength region. This is critical to enable wide band gap semiconductors, such as TiO_2, as photoactive materials. So, even though the MnO_2 has a better catalytic activity, the derived Mn_2O_3 exhibits a better solar light transmission.

CONCLUSIONS

We present a study of transparent thin film manganese oxides, and report that every phase in the MnO-MnO_2 range can be synthesized in a controlled manner by well-chosen combination of ALD process and post-ALD annealing conditions. Due to the conformal nature of the ALD tech-

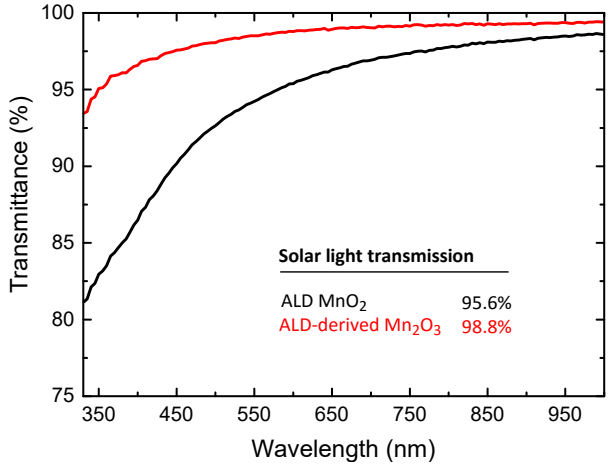

Figure 6.6: Light transmittance of the 3 nm ALD MnO_2 and derived Mn_2O_3 films from 330 nm to 1000 nm, corrected for the substrate. Integrated solar light transmission (η_{solar}) is calculated according to equation 6.1.

nique used to deposit these films, this allows the coating of complex structures with any required manganese oxide. We observed that the MnO films have a lower initial roughness than the MnO_2, likely due to the plasma-enhanced nature of the deposition of the former. The smoothest films of Mn_3O_4 and Mn_2O_3 are also found when using MnO as a start phase and when processing conditions allow a low-temperature anneal rather than a high temperature anneal. Re-oxidation to MnO_2 was never possible. When a reducing atmosphere is introduced instead of an oxidizing or inert atmosphere, all films reduce rapidly to MnO and reduce fully above 700 °C to metallic manganese. The latter can then interact with the substrate to form manganese silicate or silicide, depending on the nature of the substrate. We observe a large influence of the 'initial film' state (MnO_2 or MnO) on the crystalline states observed when reducing and oxidizing the manganese oxide thin films. The film resulting from 200 ALD cycles MnO_2 and the corresponding Mn_2O_3 reduced in inert atmosphere were both tested as catalysts for OER. The performance of ALD MnO_2 lies above that of a Pt-CB reference, but below top-end catalysts such as RuO_2 and IrO_x. The derived Mn_2O_3 does not outperform the Pt-CB reference, since it has a 182 mV higher overpotential than the ALD MnO_2 at 10 mA cm^{-2}. However, the Mn_2O_3 shows a higher solar light transmission coefficient than ALD MnO_2, 98.8 % and 95.6 %, respectively. Since the difference in transmission lies mostly in the UV region, this could have a large impact on buried wide band-gap photo-active materials. These re-

sults show that we are able to acquire MnO_2 and Mn_2O_3 OER catalysts for integrated solar hydrogen devices operating in alkaline conditions, without the requirement for a post-deposition oxidative atmosphere treatment, and show that control of the oxidation state of the thin film is critical to optimize the catalyst properties.

7

SUPPLEMENTARY TO PAPER II

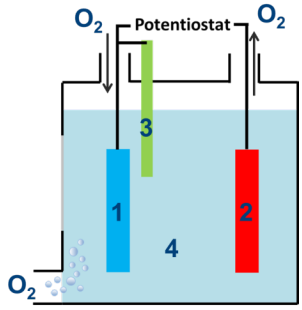

Figure 7.1: Schematic representation of electrochemical setup. 1 = working electrode (MnOx on Toray paper); 2 = counter electrode (Pt mesh); 3 = reference electrode (Ag/AgCl) and 4 = electrolyte (1M KOH).

EXPERIMENTAL DETAILS ON THE LINEAR SWEEP VOLTAMMETRY

An electrochemical setup as represented in figure 7.1 was used. 3-electrode electrochemical voltammetric experiments were performed using manganese oxides on carbon fiber Toray substrate served as the working electrode (WE), a Pt mesh as counter electrode (CE) and an Ag/AgCl (3M KCl, sat. AgCl, Radiometer Analytical) reference electrode. 1M KOH was used as electrolyte. The solution was vigorously stirred with a magnetic stirrer while bubbling a high oxygen flow through the solution for 10 minutes before every experiment. Additionally, oxygen was purged through the headspace of the container. During the experiments the O_2 purge and stirring was maintained. Linear voltammetric sweeps were performed on the as-prepared samples with a sweep rate of $2\,\mathrm{mV\,s^{-1}}$. As a control experiment, the Ag/AgCl (3M KCl) was referenced against a Hg/HgO electrode in 1M KOH. From this measurement we could conclude that the potential

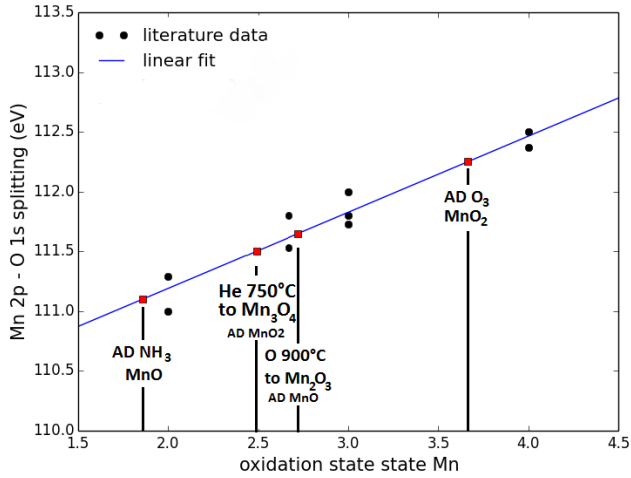

Figure 7.2: Relation between difference in binding energy of the Mn $2p^{3/2}$ maximum and the peak position of the lowest energy component of the O 1s spectrum (Mn-O-Mn bond) found from literature [165, 181–183], and the oxidation states of the reported films. The energy difference for selected ALD and annealed films are plotted on this graph to obtain the oxidation state, which matches to the oxidation state obtained from crystal phase analysis, save an offset to lower oxidations states.

of Ag/AgCl (3M KCl) in 1M KOH was +0.22V vs. RHE. This scale was used for analysis of voltammetric curves.

OXIDATION STATE CONFIRMATION BY XPS

XPS on four selected films was performed to confirm the oxidations state obtained by XRD. As was done in our earlier work [171], the linear relation between the Mn oxidation state and the energy difference between the Mn $2p^{3/2}$ maximum and the peak position of the lowest energy component of the O 1s spectrum (Mn-O-Mn bond) was used to estimate the oxidation state [165, 181–183]. Figure 7.2 shows the results of this analysis, alongside with the recipe to obtain these films and the manganese oxide state found from XRD. Besides an offset to lower oxidation states, likely caused by the spread in literature data, the trend in oxidation states is clearly visible, confirming that the XRD analysis is sufficient to obtain the oxidation state for these manganese oxide thin films.

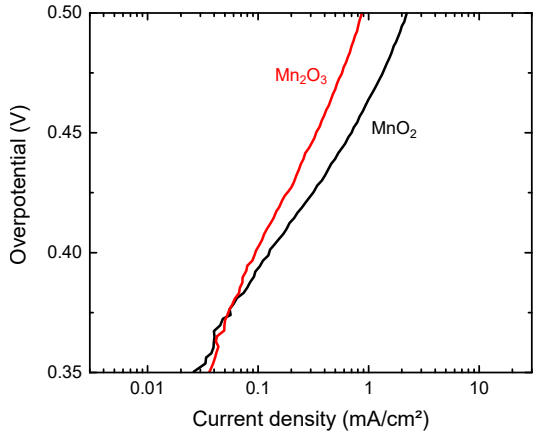

Figure 7.3: Tafel plot of the manganese oxides under investigation. Only the linear regime is shown to highlight the difference in activity.

TAFEL PLOT

To illustrate the difference in activity between the MnO_2 and derived Mn_2O_3 OER catalysts, a Tafel plot resulting from the linear sweep voltammogram is shown in figure 7.3. It can be seen that MnO_2 and Mn_2O_3 show similar onset potentials. However, the overpotential at $10\,mA\,cm^{-2}$ of both catalysts is very different and since the electrodes are operating in diffusion limitation regime during the linear sweep, this difference is best explained by a difference in Tafel slopes in figure 7.3. The derived Tafel slopes are $68\,mV\,dec^{-1}$ and $96\,mV\,dec^{-1}$ for MnO_2 and Mn_2O_3, respectively. Extrapolation of these results would result in overpotentials of 529 mV and 592 mV for MnO_2 and Mn_2O_3, respectively, indicating a higher activity for the MnO_2 films.

AFM CONFIRMATION BY SEM

Scanning electron microscopy was used to further study the surface topology. Similar surfaces were found to the surfaces obtained from AFM as shown in figure 7.4, confirming the validity of AFM even on the roughest films.

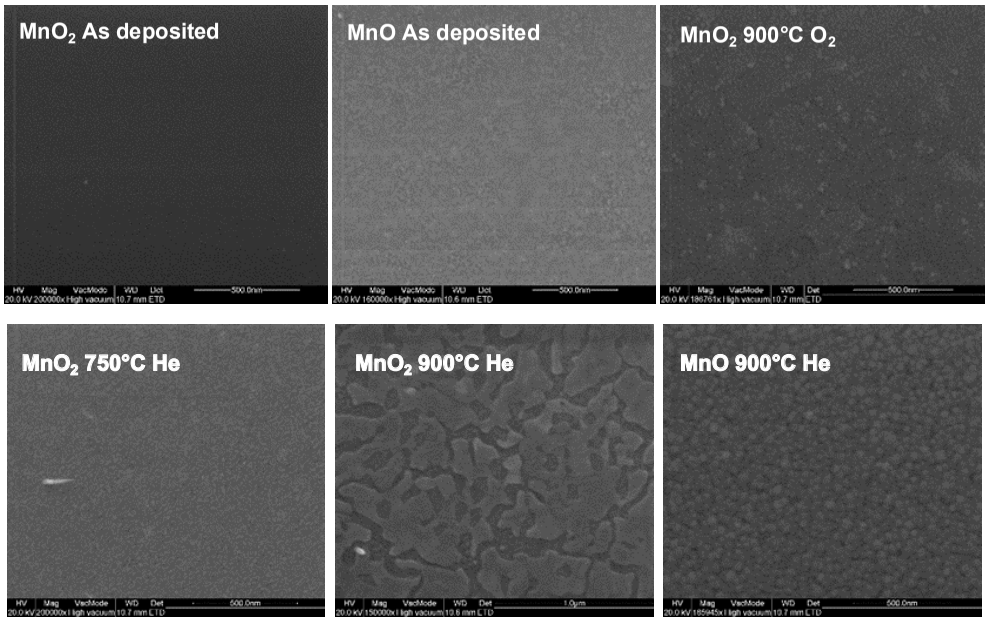

Figure 7.4: SEM imaging on selected samples to confirm the surface topology found from AFM.

8

ALD VANADIUM OXIDES FOR 3D THIN-FILM LITHIUM-ION BATTERIES

The previous chapter and papers discussed the deposition of ALD manganese oxide films, and their applications as thin-film lithium-ion battery electrodes and water splitting catalysts. This chapter details the research concerning ALD of vanadium oxide films, with a more in-depth view on three focus topics:

- The deposition of vanadium oxides from the TEMAV precursor and the post-ALD phase transformations in order to obtain all possible vanadium oxides in the Wadsley series. The excellent control over the properties of the as-deposited films that ALD offers allows the use of these films as model systems to study the influence of ALD process parameters, temperature, ambient and substrate on the phase transformations.
- The wide range of obtainable phase-pure vanadium oxide films from the previous bullet allows the use of ALD-deposited thin-film vanadium oxides as model systems to study and benchmark all these crystalline phases as thin-film lithium-ion electrodes.
- The low-temperature nature of the ALD processes using the TEMAV precursor unlocks the deposition of amorphous vanadium oxide films, not only VO_2 but also V_2O_5. The controlled composition inherited from ALD allows a direct comparison of the performance as lithium-ion battery electrodes. Amorphous vanadium oxide films are compared to crystalline films, and VO_2 films are compared to V_2O_5.

8.1 THE VANADIUM-OXYGEN PHASE DIAGRAM

As was the case with manganese and manganese oxides, a wide range of different vanadium oxide states exists, resulting in a rich phase diagram. Figure 8.1 shows the vanadium oxides in the VO_x system ($1 \leq x \leq 2.5$).

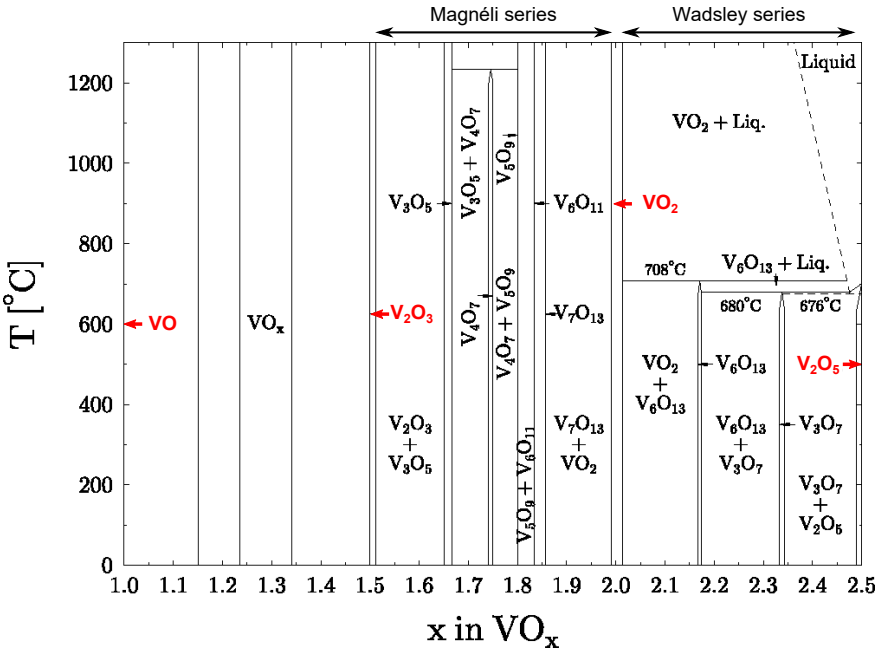

Figure 8.1: Experimental phase diagram of the vanadium oxygen system, with the principal vanadium oxides marked in red and the extent of the Mangéli and Wadsley series highlighted. Adapted from Katzke *et al.* [209].

Vanadium has five possible valence states, i.e. 0, +2 ,+3, +4 and +5, resulting in the metallic vanadium, VO, V_2O_3, VO_2 and V_2O_5 as principal base-states, respectively. Even more so than for the manganese oxides, many mixed-valence states give rise to a multitude of additional phases. These are categorised into two main sequences. The first sequence has a mixed +4/+3 oxidation state and is called the Magnéli series (V_nO_{2n-1} with $4 \leq n \leq 9$). The second sequence are the mixed +5/+4 vanadium oxides and is called the Wadsley series (V_nO_{2n+1} with $n = 3, 4, 6$). Vanadium oxide is found in many applications thanks to its many phases and valence states, and related to its specific properties and characteristics.

- The transition-metal nature of vanadium oxides makes them excellently suited as **catalysts** for propane dehydrogenation [210], oxidation of o-xylene [211, 212] and photocatalytic applications [213].
- The band structure of the vanadium oxides in the Magnéli series dictates they should behave like metals. However, at a critical temperature they undergo a remarkable temperature-driven reversible phase

transition that alters their conductivity by several orders of magnitude [214]. This **semiconductor-to-metal transition** is observed in VO, V_2O_3, VO_2 and many other vanadium oxides in that series, and the transition temperature is determined by the nature of the vanadium oxide [215]. The electronic properties of a compound influence its optical properties, so that the optical properties of these oxides are temperature-switched. The transition is most often considered temperature-driven, but can also be triggered by electrical, optical or pressure-related stimuli. Several applications have emerged from this phenomenon, such as optical and electrical switches, micro-electro-mechanical systems (MEMS) and smart windows [99, 215–217].

- The layered oxides (i.e. V_nO_{2n+1}, see figure 8.2) have been extenstively investigated for **energy applications** such as battery electrodes [218–227], supercapacitors [228] and pseudocapacitors. Application of thin-film vanadium oxides as lithium-ion battery electrodes is the topic of paper III and paper IV, and will be introduced and summarized below.

8.2 Vanadium oxides as lithium-ion battery electrodes

For insertion materials to be used as active electrodes for electrochemical storage, they must be able to accommodate a significant number of lithium ions. Therefore, the most suitable materials are most likely found among those with an open structure and a relatively low density [229]. One example of such compounds are the vanadium oxides in the Wadsley series. VO_2, V_6O_{13}, V_4O_9, V_3O_7 and V_2O_5 are also known as the *layered* vanadium oxides [213]. The oxides in this series are all closely related structures, and several formalisms have been put forward to explain this. Katzke et al proposed monoclinic VO_2 (B) as the metastable end compound of a series based on symmetry-breaking from the cubic VO structure [209]. Indeed, figure 8.2 shows calculated structures of the vanadium oxides in the Wadsley series. Derived from a hypothetical VO_3 with the ReO_3 structure [230], they are composed of distorted VO_6 octahedra or polyhedra. Strings are formed by edge-sharing amongst the polyhedra, and sheets of vanadium oxides are formed by corner-sharing, giving them their layered nature [231]. As can be seen on figure 8.2, the shear structure of VO_2(B) results in one-dimensional monotunnels into which lithium ions can be inserted, rather than a true layered structure. These available storage sites make these vanadium oxides particularly suited for the (reversible) intercalation of lithium ions, and provides the oxides in

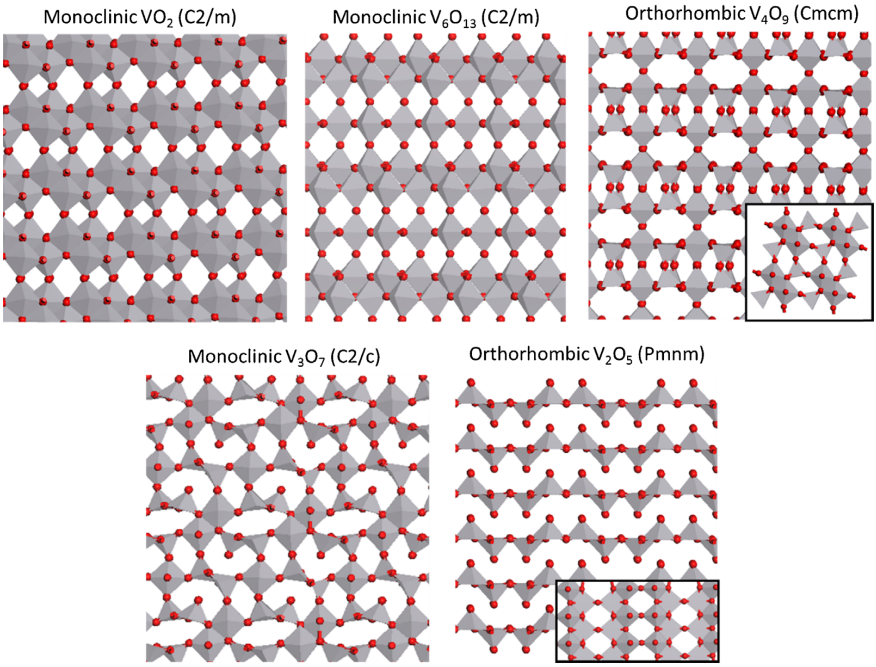

Figure 8.2: View along the a-axis of the lattice of the layered vanadium oxides; i.e. V_nO_{2n+1} ($n = \infty, 6, 4, 3, 2$). The insets provide an additional view along the c-axis. Their lattice structure is represented by VO_x polyhedra, with the oxygen atoms (red) on the corners. Figure reprinted from Bahlawane & Lenoble [213].

the Wadsley series with applications in energy conversion and storage. Some typical electrode potentials for lithium ion insertion into vanadium oxides are shown in figure 8.3. At the top-end of the Wadsley series, the single-valence +5 vanadium oxide is found. As the main topics of paper III and paper VI are related to V_2O_5, this will be discussed here in some depth.

Already in 1976, a first report was released by Whittingham [6] that lithium ions can be reversibly intercalated into the V_2O_5 lattice. Since that time, it has been heavily investigated as an insertion electrode for lithium-ion batteries [6, 219–221, 232–234]. As can be seen from figure 8.3, lithium ion insertion into V_2O_5 is accompanied by a series of voltage plateaus, corresponding to a series of phase transformations (the relation between voltage profile and phase transformations is explained briefly further). Five phase domains can be distinguished at room temperature, with increasing insertion of lithium ions [219–221]:

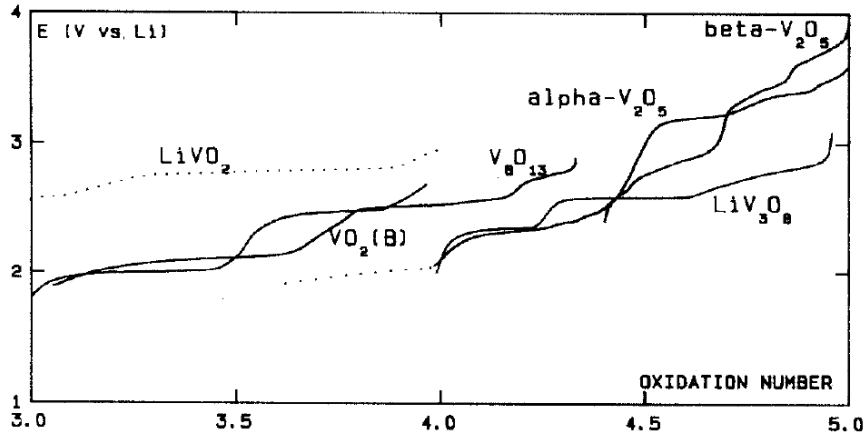

Figure 8.3: Experimental voltage profiles for several layered vanadium oxides as a function of the mean oxidation state of vanadium. In this figure, E is used to denote electrode potential. Figure reprinted from West *et al.* [229].

- α-$Li_xV_2O_5$, with $x \leq 0.01$
- ϵ-$Li_xV_2O_5$, with $0.35 \leq x \leq 0.70$
- δ-$Li_xV_2O_5$, with $0.70 \leq x \leq 1$
- γ-$Li_xV_2O_5$, with $1 \leq x \leq 2$
- ω-$Li_xV_2O_5$, with $2 \leq x \leq 3$

The reversibility of the lithium ion insertion into V_2O_5 is closely linked to the degree of lithium ion insertion. The lattice changes associated with the phase tranformations impose volume changes than can be detrimental for the cycle life, and irreversibly lock lithium ions into the lattice. Insertion of the first lithium ion into the V_2O_5 unit cell is accompanied by two phase transitions, i.e. $\alpha - Li_xV_2O_5 \longleftrightarrow \epsilon - Li_xV_2O_5$ (3.7 V *vs* Li^+/Li) and $\epsilon - Li_xV_2O_5 \longleftrightarrow \delta - Li_xV_2O_5$ (3.5 V *vs* Li^+/Li), with a theoretical capacity of $147\,mA\,h\,g^{-1}$. As is illustrated in figure 8.4, insertion of one lithium ion into the V_2O_5 lattice does not modify the structure much, save some change into the c-parameter of the lattice and puckering of the layers. Insertion of one lithium ion into V_2O_5 is known to be extremely reversible (more that 1000 cycles without significant capacity losses [235, 236]) and display excellent kinetics thanks to the high lithium ion conductivity in this range of insertion ($10^{-2}\,\Omega\,cm^{-1}$ to $10^{-1}\,\Omega\,cm^{-1}$) [229].

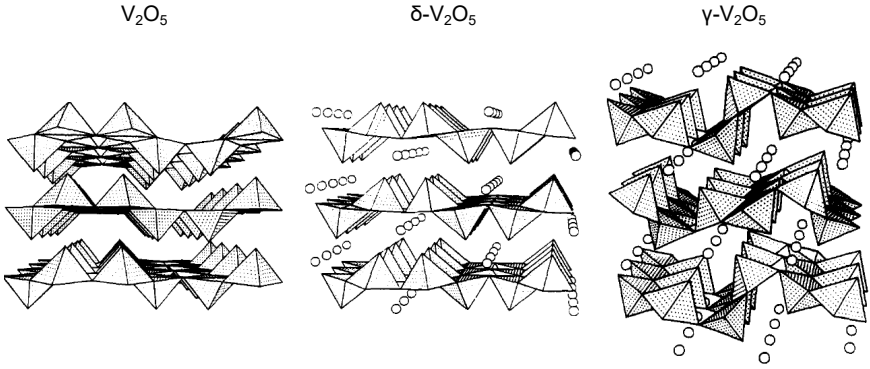

Figure 8.4: (left) Structure of V_2O_5 and (middle, right) deformation upon different degrees of lithium stoichiometry. Figure adapted from Delmas *et al.* [221].

Upon further lithium ion insertion into $Li_xV_2O_5$, a phase transformation to γ-$Li_xV_2O_5$ occurs at 2.4 V *vs* Li^+/Li. This transition is accompanied by an irreversible structural modification, as can be observed in figure 8.4. The up-up-down-down alternation of the VO_4-pyramids in the lattice structure is changed to an up-down-up-down alternation. A change in electrochemical performance is caused by this structural modification, amongst other observed in a higher cell voltage during the second lithiation cycle. It has been shown that lithium ion can be inserted reversibly into γ-$Li_xV_2O_5$ ($0 \leq x \leq 2$, with a theoretical capacity of 295 mA h g^{-1}), if γ-$Li_xV_2O_5$ is used as a starting material [221]. However, the gradual phase transformation from the V_2O_5-based structures to the γ-$Li_xV_2O_5$ structure, along with vanadium dissolution of the +3 and +4 soluble vanadium species, causes a significant capacity fade upon cycling [223].

Finally, insertion of a third lithium ion into the V_2O_5 host structure occurs at 2.1 V *vs* Li^+/Li, and has a promising theoretical capacity of 442 mA h g^{-1}. However, the phase transformation into the rock-salt ω-$Li_3V_2O_5$ is irreversible and severely changes the structure. This is evident from the discharge after the first charge, as shown in figure 8.5. Rather than discharging according to the same step-wise profile, ω-$Li_xV_2O_5$ behaves as a solid solution, with a very wide plateau centered around 2.85 V *vs* Li^+/Li. A large degree of irreversibility acompanies this transformation, as lithium ion insertion into ω-$Li_xV_2O_5$ is only found to be reversible for $0.4 \leq x \leq 2.65$. These significant lattice changes and large fraction of soluble +3-valent vanadium in the lithiated state give the deep lithiation of V_2O_5 a poor cyclability [223].

Despite the main spotlights being thoroughly fixed on V_2O_5, other crystalline vanadium oxides have also been evaluated as lithium-ion cathodes

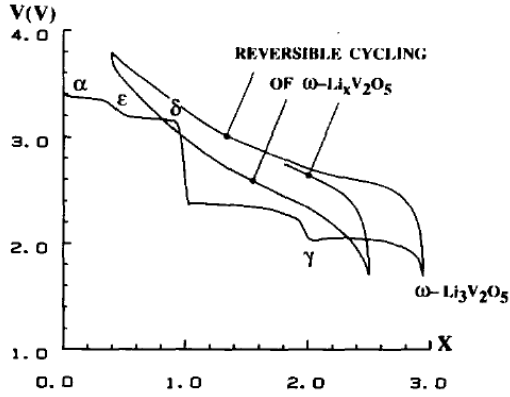

Figure 8.5: First cycles of a Li/V_2O_5 cell, showing the irreversible formation of the ω-$Li_3V_2O_5$ phase. Figure reprinted from Delmas *et al.* [221].

and anodes. The main focus so far has been on the orthorhombic VO_2(B) and V_6O_{13}, which will be not discussed here. More information detailing these oxides can be found in the following references: [237–241].

8.2.1 *Amorphous vanadium oxides*

A class of often-forgotten electrodes are the amorphous materials, also called 'glasses'. Rather than exhibiting a long-range order, as is the case for the layered oxides discussed above, only short-range order exists in these materials. This gives rise to distinctly different electrochemical properties, such as a completely different dependence of the electrode voltage on the state-of-charge of the compound, which can be explained nicely in the free-energy formalism [242].

As was derived in the introduction chapter (equations 1.5-1.14), the cell potential depends, amongst other things, on the chemical potential of the cell components (Nernst equation). As a reminder, the chemical potential is defined as the rate of change of a free energy of a thermodynamic system with respect to the change in the number of atoms or molecules of the species that are added to the system. Imagine a lithium compound as Li_xMA. MA is in this case a host structure, such as V_2O_5 or CoO_2. The lithium chemical potential for adding lithium to Li_xMA can then be defined as

$$\mu_{Li}^{Li_xMA} = \frac{\delta G}{\delta x} \tag{8.1}$$

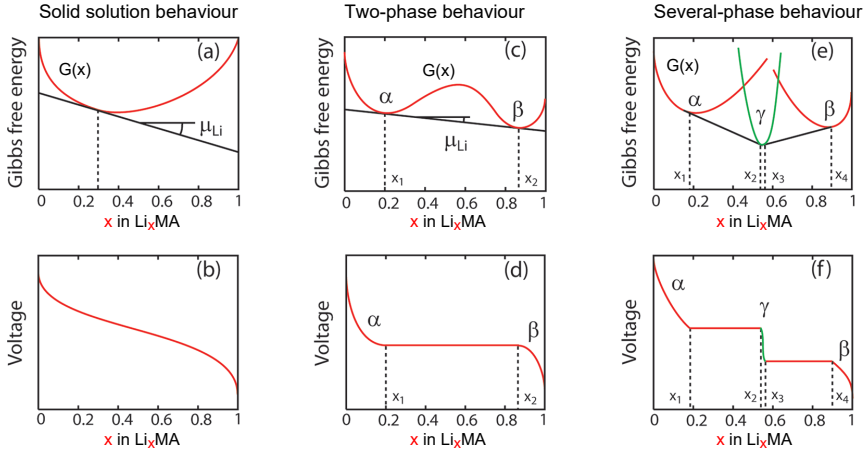

Figure 8.6: Relation between the potential profiles and the Gibbs free energy of the system. Figure adapted from Van der Ven *et al.* [242].

with x the stoichiometry of lithium in the host lattice. The Gibbs free energy term contains configurational contributions (entropy, -TΔS) and mixing (enthalpy, ΔH) contributions, is dependant on the phase and phase mixing of the system, which implies that the occurrence and nature of phase transformation will translate into measurable features on the voltage profiles. Three generalised cases exist, and are illustrated in figure 8.6.

- **Solid-solution behaviour** implies that no phase transformations occurs. A single minimum is found in the Gibbs free energy. This translates to a smooth sloping voltage profile as in figure 8.6 (a-b). Li_xTiS_2 is an example of such a compound. As amorphous compounds have no long-range order, the concept of a 'phase' is poorly defined in a glass, and they typically also behave in this manner.
- **Two-phase behaviour** is found in compounds that undergo a first-order phase transformation from a Li poor phase, α, to a Li rich phase, β. The free energy curve now has two distinct minima, as is the case in figure 8.6(c). The lithium chemical potential for compositions between the two minima is constant, as the free energy of the two-phase mixture resides on the common tangent to the free energy wells corresponding to α and β. Li_xFePO_4 and $Li_xTi_5O_{12}$ are examples of electrode that exhibit this type of behaviour.
- **Several phase transitions** give rise to several plateaus in the electrode potential. The multiple phase transitions in V_2O_5 for example

give rise to 4 plateaus during the first charging cycle, corresponding to 5 phases (see figure 8.5). This multi-phase situation is the case for most layered vanadium oxides (see figure 8.3).

For most applications, the two-phase behaviour is preferred, as this provides little variation in the cell's output voltage across most of the state-of-charge range of the cell (the change in electrode potential is preferably below 0.5V) [241, 243]. However, on-chip devices will usually require less than the 3 to 4V provided by common electrochemical cells. Typically, they also have built-in electronics to convert the provided potential to the required specifications of the chip. This makes the well-defined plateau, found in most crystalline materials, no longer a requirement for on-chip energy storage, enabling the use of amorphous materials for these applications.

The reseach on amorphous vanadium oxide glasses lagged behind crystalline vanadium oxides for almost a decade, due to the difficulty in synthesis of a pure V_2O_5 glass without glass formers like P_2O_5 and B_2O_3 from ordinary melt quenching techniques. Machida *et al.* succeeded in preparing pure V_2O_5 glasses for the first time from rapid quenching, and found diffusion coefficients for lithium ions 1-2 orders of magnitude higher than for crystalline $Li_xV_2O_5$ [244]. This fast lithium ion diffusion in glasses is caused by the lower density (increased free volume) and many sites for lithium-hopping [243, 245, 246], and gives rise to higher lithium ion conductivity in amorphous solid electrolytes [57, 87, 247] and better rate capabilities for amorphous electrodes [245, 248–251]. Furthermore, the lower density and numerous ill-defined vacant sites found in glasses provide more sites for storage of lithium-ions, translating into higher volumetric capacity densities [246, 252]. Finally, while the channels and planes in the crystalline layered vanadium oxides are not large enough to accommodate larger-than-lithium ions (such as sodium ions), amorphous vanadium oxides can reversibly store these ions, broadening the range of energy applications in which vanadium oxides find their use [250].

8.3 Atomic layer deposition of vanadium oxides

A great variety of thin-film growth techniques including sputtering [273–275], chemical vapour deposition [213, 276], pulsed laser deposition, electron beam evaporation, flash evaporation, solgel methods, and thermal evaporation have been used for the depositing vanadium oxide thin films on various substrates. A recent review on deposition processes for V_2O_5 films published by Beke [277] demonstrates the multitude of possible deposition techniques available. Atomic layer deposition is a gas-phase de-

Precursor	Reactant	Phase	Temperature window	Growth rate (Å/cycle)	Reference
TEMAV	O_3	a-VO_2	100 °C to 175 °C	0.3-2.9	[98, 99, 253–257]
	H_2O	a-VO_2	100 °C to 175 °C	0.45-0.8	[253, 255, 256, 258]
	O_2 plasma	a-V_2O_5, V_2O_5	80 °C to 175 °C	1.5	[99, 259]
VTOP	H_2O	a-VO_x	50 °C to 200 °C	0.1-0.3	[77, 260–267]
	H_2O plasma	a-VO_x	50 °C to 200 °C	0.7	[262, 263]
	O_2 plasma	V_2O_5	50 °C to 200 °C	0.5-0.6	[262, 263]
	O_3	V_2O_5	170 °C to 185 °C	0.280.3	[265, 267]
$VO(thd)_2$	O_3	a-VO_x, V_2O_5	162 °C to 235 °C	0.1-1	[235, 268]
$VO(acac)_2$	O_2	VO_2 (M1)	400 °C to 475 °C	2.4	[210, 269, 270]
$VOCl_3$	H_2O	V_2O_5 (impure)	490 °C	-	[271]
$VO(O^nPr)_3$	CH_3COOH	a-VO_2	200 °C	0.4	[272]
	H_2O	Mixed-phase	170 °C to 190 °C	1.0	[190]

Table 8.1: Overview of the reported ALD and PE-ALD processes for the deposition of thin-film vanadium oxides. a-VO_x represents the deposition of amorphous vanadium oxide without knowledge about the composition.
TEMAV = $V(NEtMe)_4$, VTOP = $VO(O^iPr)_3$, thd = 2,2,6,6-tetramethylhepta-3,5-dione, $VO(acac)_2$ = $VO(C_5H_7O_2)_2$.

position technique, that often inherits precursors from other gas-phase techniques, such as chemical vapour deposition (CVD). The earliest reports of CVD of vanadium oxides dates back the 1970s [278], and CVD of vanadium oxides is well established, as is evident from the recent review by Bahlawane & Lenoble [213]. As a consequence of the CVD research, a range of vanadium-bearing gas-phase precursors have been developed. So far, seven of those have made their way into atomic layer deposition. The first report on atomic layer deposition uses the $VO(O^iPr)_3$ precursor, and dates back to 2000 [77]. Since then, research has expanded to six different vanadium precursors. An overview of the ALD processes can be found in table 8.1, based on the following precursors: TEMAV, VTOP, $VO(thd)_2$, $VO(acac)_2$, $VOCl_3$ and $VO(O^nPr)_3$.

In this work, all depositions were done using the TEMAV precursor, based on three processes developed by Geert Rampelberg [257]. Here, the ozone-based and water-based ALD processes were used as reported, and the O_2-plasma PE-ALD process was examined at low temperature to deposit amorphous V_2O_5 thin films.

8.4 Oxidation-state tuning of thin-film vanadium oxide

As was clear from the previous chapters on manganese oxide, the electrochemical properties of thin-film transition metal oxides are heavily influenced not only by the formal oxidation state of the transition metals, but also by its crystal phase. Control of these two properties is thus essential, but often not straightforward as a consequence of the broad range of mixed oxidation-state crystal phases, as is evident from the previous sections. In this work, the influence of the (PE-)ALD deposition process, substrate, temperature and ambient on the oxidation state, crystallisation and oxidation/reduction behaviour of thin-film vanadium oxides was studied.

8.4.1 *Oxidation state tuning during ALD*

Three ALD processes using the TEMAV precursor for the deposition of vanadium oxides were examined in the course of this work: water-based ALD, ozone-based ALD and oxygen plasma PE-ALD. The TEMAV precursor has its vanadium in the +4 valence state. The simple ligand-exchange ALD process using water maintains this oxidation state, and thus deposits VO_2. The ozone-based ALD process combusts the ligands rather than performing a ligand exchange, but contrary to the manganese oxide depositions in the previous chapter, ozone also maintains the vanadium +4 oxidation state and also deposits VO_2, albeit a slightly different VO_2 film,

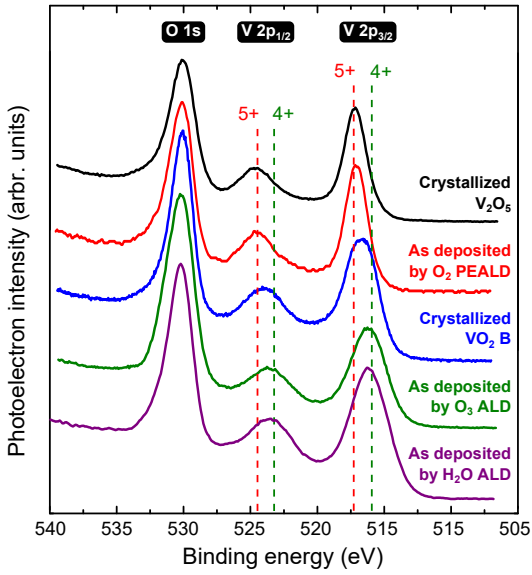

Figure 8.7: XPS O1s and V2p spectra of the vanadium oxides deposited from the three ALD processes using TEMAV, as well as crystallised V_2O_5 and VO_2(B).

as will be revealed further. The oxidation state of vanadium oxides can be determined by the shift in binding energy as was shown by Silversmit *et al.* [279]. Figure 8.7 demonstrates that the thermal ALD processes indeed maintain the +4 oxidation state for the vanadium. Using an oxygen plasma however, the vanadium shifts to the +5 valence state, and V_2O_5 is deposited.

Interestingly, the low-temperature nature of ALD often enables the deposition of amorphous films [199]. This empowers ALD to be used as a tool to study thin-film model systems of high-quality amorphous compounds, which are otherwise very difficult to obtain. Indeed, the two thermal ALD processes deposit amorphous films, as was also reported by Geert Rampelberg [257]. In his work, it was also reported that plasma-enhanced ALD with the same precursor raised the oxidation state from +4 to +5, and in most cases crystallised the films. However, low deposition temperatures (below 125 °C) or thin films (< 100 PE-ALD cycles) can accommodate the deposition of amorphous V_2O_5. Indeed, in paper IV the low-temperature boundary of the PE-ALD temperature window (100 °C) is examined and extended to 85 °C, for which saturated growth is demonstrated. Here, the pulse length of the plasma turned out to have a great influence on the order in the films. Saturated pulse times allowed

the deposition of C-free amorphous films, while longer pulse times resulted in *in-situ* crystallisation of the films to crystalline V_2O_5. The films grown from this process are amorphous, and have vanadium in the +5 oxidation state (see figure 8.7). The oxidation state of the as-deposited amorphous films can thus be controlled by the reagent used, while maintaining the deposition of amorphous films. In this section, crystallisation of these films into all the vanadium oxides in the Wadsley series will be demonstrated, with the influence of the reagent, ambient, temperature and substrate. This is summarized and published in **paper III**: *Atomic Layer Deposition Of Vanadium Oxides For Thin-film Lithium-ion Battery Applications*, which is presented as the next chapter. Finally, the simple one-precursor method to obtain both amorphous and crystalline films in +4 (VO_2) or +5 (V_2O_5) vanadium oxidation states, allows a systematic study of the effect of long-range order (crystalline or amorphous) and vanadium oxidation state (VO_2 or V_2O_5) on the electrochemical performance of these thin-film vanadium oxides as lithium-ion battery electrodes. This study is reported in **Paper IV**: *Amorphous And Crystalline Vanadium Oxides As High-Energy And High-Power Cathodes For 3D Thin-Film Lithium-Ion Batteries*, and briefly summarized below (section 8.6).

8.4.2 *Oxidation state tuning by post-ALD annealing*

Both thermal ALD processes can deposit amorphous VO_2 from the TEMAV precursor. Crystallisation of these films is monitored using *in-situ* XRD, as is shown in figure 9.4 of the next chapter for the SiO_2 substrate. Four parameters were varied for this crystallisation: as-deposited film, temperature, ambient and substrate. The crystallisation and phase formation of these thin-film vanadium oxides is summarized on phase-formation diagrams in figure 8.8. Their respective influences are discussed in-depth in paper III, but the conclusions are summarised here:

- **As-deposited film.** Both thermal ALD processes deposit amorphous VO_2 with the vanadium in the +4 state. However, it was found that the films deposited using the H_2O ALD process are more dense compared to the films deposited using the O_3 ALD process. This influences the initial crystallisation in VO_2. Crystalline VO_2 exists in two phases; the low-density orthorhombic phase labelled VO_2(B), belonging to the Wadsley series, and the higher density cubic structures labelled VO_2(M1) or VO_2(R), which are related to each other by a semiconductor-to-metal transition, and belong to the Mangéli series. Figure 8.8 shows that amorphous low-density VO_2, deposited by the O_3 process, crystallises into the low-density VO_2(B) phase,

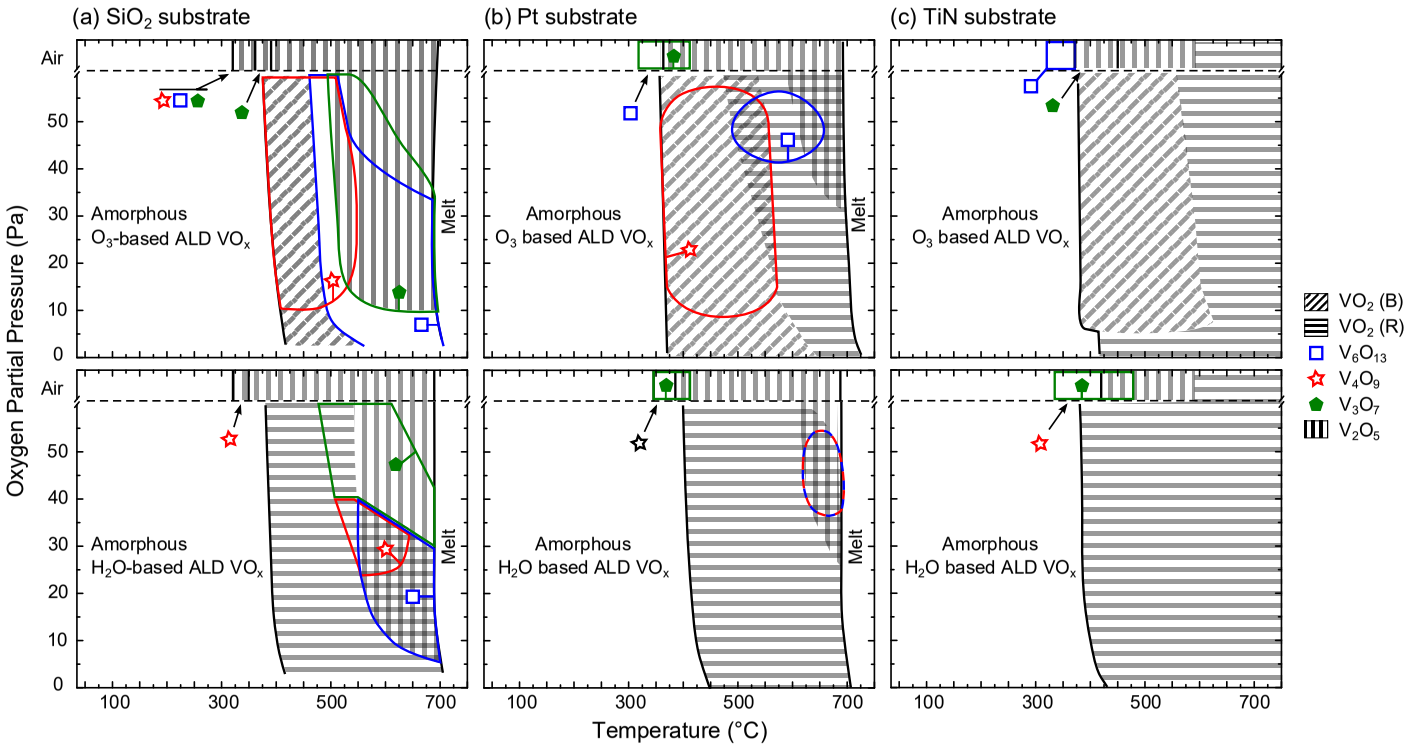

Figure 8.8: Phase formation diagrams for the formation of the VO_x crystal states ($2 \leq x \leq 2.5$) on (a) SiO_2, (b) Pt substrates and (c) TiN substrates, at 0.25 °C s^{-1} for He ambients with oxygen partial pressure of 3.7, 7.4, 14.8, 29.6 and 48.1Pa, and in ambient air. The absence of the melt-line on the right figure is related to the presence of rutile TiO_2 from the substrate, complicating the analysis of the VO_2 (R) phase on the TiN substrate at high temperatures.

while the amorphous high-density VO_2, deposited by the H_2O process, crystallises into the high-density cubic VO_2(R) phase. Furthermore, crystallisation to higher oxidation states happens faster for the O_3-deposited films, which could be related to either better oxygen diffusion through the lower-density films or incorporation of additional oxygen into the films due to a higher oxidant being used to deposit them.

- **Nature of the substrate.** A distinctively different phase-formation is observed on the three different substrates examined here: SiO_2, TiN and TiN/Pt. First, the phase-formation is much richer on the SiO_2 substrate than on the TiN or Pt substrates. Furthermore, oxidation of the vanadium to higher oxides occurs at lower temperatures on the SiO_2 substrate. This is caused by the presence of TiN in the other two substrates. TiN itself can be oxidized to TiO_2, which is also observed from the presence of TiO_2 rutile diffraction peaks in the XRD scans. the TiN substrate can thus act as an oxygen drain, even before the actual crystallisation to TiO_2 occurs. The Pt-substrate is an intermediate case, as TiN is buried beneath the 80 nm Pt layer: it can thus be regarded as a delayed oxygen drain, as oxygen can diffuse through the Pt layer to oxidize the TiN below.

- **Ambient.** The influence of the oxygen partial pressure in the annealing ambient is the most straightforward to interpret. From low to high oxygen partial pressure, we see that phases emerge and disappear in the order of increasing oxidation state: VO_2-V_6O_{13}-V_4O_9-V_3O_7-V_2O_5 with respective average oxidation states for the V of $4 - 4.33 - 4.5 - 4.67 - 5$.

- **Temperature.** Intuitively, one might expect thermodynamic arguments to determine the influence of temperature on the phase formation. However, the influence of temperature is not unilaterally explained solely by thermodynamic stability of the vanadium oxide phases. The diagrams in figure 8.8 are not thermodynamic phase diagrams, but rather phase formation diagrams. This implies they do not represent long-therm experiments on every temperature, but instead the sequence in which phases are formed and transformed at a certain linear ramp rate. As these phase formation diagrams are a dynamical representation of what happens during a ramp anneal at $0.25\,^{\circ}\mathrm{C\,s^{-1}}$, phase formation kinetics complicate the influence of temperature. However, it is still clear that in general with increasing temperature the average oxidation state rises to higher values, showing high-temperature stability for the higher oxides.

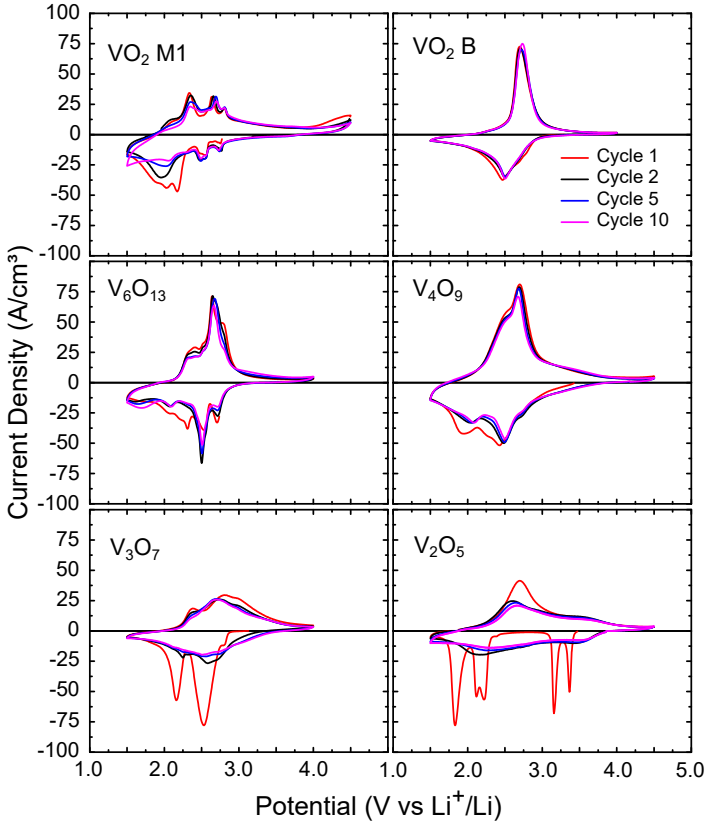

Figure 8.9: Cyclic voltammetry on the selected vanadium oxide thin films, performed at 10 mV s^{-1} in a 3-electrode setup with lithium as counter and reference electrodes, and 1M $LiClO_4$ in PC as electrolyte. Potential ranges were chosen according to the respective electrochemical activity window for each phase.

8.5 LAYERED VANADIUM OXIDES AS THIN-FILM ELECTRODES

The phase formation diagrams in figure 8.8 demonstrate that it is feasible to obtain every phase in the Wadsley series of vanadium oxide, starting from amorphous ALD-deposited thin-film vanadium oxides. Based on this information, an attempt was made to procure a phase-pure film of every phase, i.e. VO_2(B), VO_2 (M1), V_6O_{13}, V_4O_9, V_3O_7 and V_2O_5. The *in-situ* XRD figures in the supplementary information of paper III demonstrate that the phases formed during the phase formation could be quenched successfully, save for the V_3O_7, which contained a small fraction of V_2O_5.

	Potential (V vs Li^+/Li)	Capacity ($mA\,h\,cm^{-3}$)	Kinetics	Cyclability
VO_2 (B)	1.5-4.0	805	75 %	+
V_6O_{13}	1.5-4.0	894	75 %	-
V_4O_9	1.5-4.0	1380	78 %	-
V_3O_7	1.5-4.0	1255	49 %	-
V_2O_5 (1 Li)	2.9-3.5	488	93 %	+
V_2O_5 (2 Li)	2.9-3.5	1010	86 %	-
V_2O_5 (3 Li)	1.5-4.0	810	78 %	- -

Table 8.2: Summary of the electrochemical performance of the evaluated crystalline thin-film vanadium oxide thin films in the Wadsley series. The capacity at 1C is determined from extrapolation of the capacity at various C-rates to a C-rate of 1C. Kinetics were evaluated as the drop off from 1C to 10C. Cyclability was tested over 50 cycles at 2C

All these phases were tested electrochemically as lithium-ion insertion electrodes, as demonstrated in figure 8.9.

8.5.0.1 *Crystalline vanadium oxides*

It was found that all layered vanadium oxides, i.e. the vanadium oxides in the Wadsley series (VO_2(B), V_6O_{13}, V_4O_9, V_3O_7 and V_2O_5), were able to reversibly store lithium ions. The cyclic voltammograms in figure 8.9 also show some activity for VO_2 (M1), which is a phase from the Magnéli series, but further electrochemical testing revealed a very low capacity for this phase. As explained in section 8.2, lithium ion storage is possible in the layered oxides thanks to their low density and open channels (VO_2) or planes (V_nO_{2n+1} with $n = 6, 4, 3, 2$). The cubic VO_2(M1) has a higher density, i.e. $4.031\,g\,cm^{-3}$ and $4.67\,g\,cm^{-3}$ for VO_2(B) and VO_2(M1), respectively. The higher density translates into a lower availability of lithium ion storage sites, and thus a lower capacity.

The crystalline vanadium oxides in the Wadsley series all display lithium ion intercalation characteristics. They are discussed in some more detail in paper III and in the master thesis of Kobe Geryl [280]. 10 cyclic voltammetry sweeps were performed prior to the kinetics tests to ensure initial-cycling behaviour did not influence the capacity evaluations. Kinetics were tested by applying a range of currents, corresponding to C-rates in the range of 0.5-200C. The cyclability was evaluated on fresh films by charging and discharging 50 times at a current corresponding to ~2C. Their electrochemical properties are summarized in table 8.2.

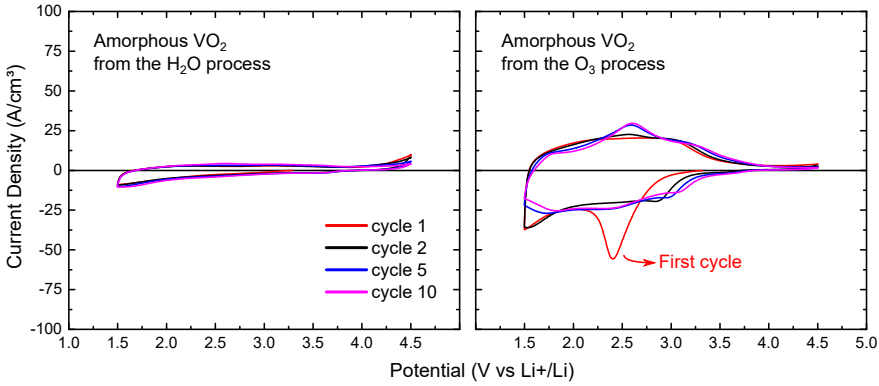

Figure 8.10: Cyclic voltammetry of the as-deposited amorphous VO_2 films from the water process (left) and the ozone process (right), performed at 10 mV s^{-1}.

From a kinetics and cyclability point of view, insertion of one lithium ion into V_2O_5 provides the best thin-film electrode. Almost 100 % of its capacity can be retained after 50 charge-discharge cycles, and excellent kinetics are observed. However, the capacity of this storage mode is very limited: 488 mA h cm^{-3} at 1C. Deeper lithiation of V_2O_5 increases the storage capacity, but is detrimental for the kinetics and cyclability of the thin-film electrodes. The capacity of V_2O_5 is little more than half of VO_2(B) (805 mA h cm^{-3} at 1C), and a third of V_4O_9 (1380 mA h cm^{-3} at 1C). The latter also displays good charge-discharge kinetics, but cyclability can still be improved significantly. Severe side reactions, likely related to dissolution of low-valent vanadium into the liquid electrolyte, should be tackled before this material could be considered a candidate electrode. VO_2(B) however has an excellent capacity retention over the 50 charge-discharge cycles examined. Despite the lower kinetic capacity retention (75 %, compared to 93 % for V_2O_5), the higher capacity of VO_2(B) enables it to store more charge up to 100C, compared to insertion of one lithium ion into V_2O_5.

8.5.0.2 *Amorphous VO_2*

As was mentioned above, VO_2(B) shows promising battery characteristics, while VO_2(M1) is almost incapable of storing lithium ions. Interestingly, this behaviour is already visible in the amorphous films. The water-grown

As a point of reference for the reader; note that the reversible capacity of $LiCoO_2$ is about ~550 mA h cm^{-3}, and that of commercial high-capacity cathodes such as $LiNi_{0.8}Co_{0.15}Al_{0.05}O_2$ only ~700 mA h cm^{-3}[16]. All vanadium oxides here, save V_2O_5, easily surpass those values.

and ozone-grown as-deposited films, i.e. amorphous vanadium dioxide, also have a different density, which translates into their formation into VO_2(R) (which settles to VO_2(M1) upon cooldown) and VO_2(B), respectively, as explained in the previous section. The poor capacity for the VO_2(M1) phase crystallised from the water-grown amorphous VO_2 is already clearly visible when comparing the electrochemical performance of both amorphous films in figure 8.10. The flat CV-profile reveals a far lower capacity for the water-grown film than for the ozone-grown films, while they are of comparable thickness ($\sim$20 nm).

A second remarkable observation that can be made from figure 8.10 is the presence of a peak in the cyclic voltammogram during the first cycle. As was explained above, a peak in the cyclic voltamogram (or a plateau on the voltage profile) is a signature of two minima in the Gibbs free energy, i.e. an abrupt phase transformation occurring at critical potentials (potentiostatic measurements) or state-of-charge (galvanostatic measurements), as can be seen for crystalline VO_2(B) on figure 8.9. However, amorphous compounds do not display long-range order, and typically a solid-solution behaviour is expected during their lithiation, translating into a sloped potential profile or a 'blob-like' cyclic voltammogram. The ozone-grown amorphous films however display a clear critical potential during the first lithiation in figure 8.10, that is furthermore remarkably similar to the peak potential of its crystallised form, VO_2(B), in figure 8.9. Despite the absence of observable crystallinity using X-ray diffraction, the O_3-grown amorphous VO_2 appears to be 'primed' into a state closely resembling VO_2(B). In the next section and in paper IV, they are benchmarked in more depth.

8.6 Benchmarking (PE-)ALD thin-film vanadium oxides

In the previous section, it was established that all vanadium oxides in the Wadsley series can intercalate lithium ions reversibly (to a certain extent). Crystalline VO_2(B) and V_2O_5 are the valence-pure end members of this series. In section 8.4, it was shown that these two vanadium oxides can also be established in their amorphous forms, a-VO_2 from O_3-based ALD process and a-V_2O_5 from a low-temperature variation on the O_2-plasma ALD process. The possibility to deposit both amorphous and crystalline film of both +4- and +5-valent vanadium oxides enables us to do a more in-depth study on the effect of (dis)order and valence on the performance

Amorphous VO_2 can also be grown from H_2O-based ALD, but cannot be used for lithium ion storage.

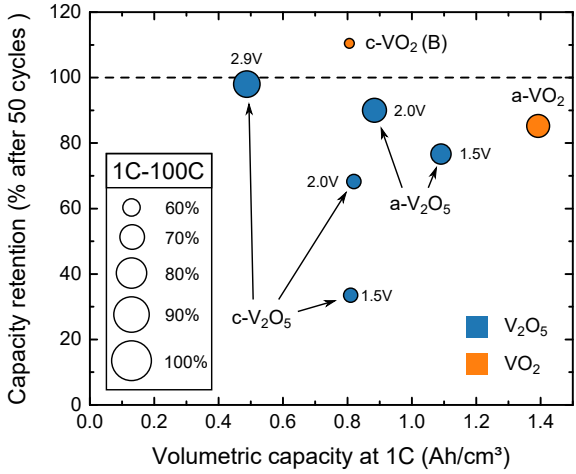

Figure 8.11: Summary of the electrochemical performance properties of the examined thin-film vanadium oxide cathodes. The size of the circles indicates the power capability according to the scale displayed in the inset, representing the kinetic capacity retention from 1C to 100C.

of the thin-film electrodes, and compare the results to some reported ALD-derived vanadium oxide electrodes.

8.6.1 *ALD vanadium oxides in this work*

The capacity, kinetics and cyclability of these four cases were evaluated as was done for the crystalline vanadium oxides in the previous section. As the depth-of-charge is a critical parameter in the electrochemical performance of V_2O_5, crystalline and amorphous V_2O_5 were evaluated up to several lower limits. The detailed characterisation can be found in paper IV. Figure 8.11 provides a summary graph of their reversible capacities, their kinetic performance and their capacity retention upon prolonged charge-discharging. Several conclusion can be drawn from this evaluation.

- VO_2 has a higher volumetric capacity than V_2O_5, both for the amorphous and the crystalline case. The highest capacity found was for a-VO_2, and was almost 1.4 A h cm^{-3}. This is related to the lower densities of the lower oxides. Gravimetrically, the capacities are much closer together, but since the vanadium oxides are envisioned for thin-film electrodes here, the volumetric capacity density is the relevant parameter. One has to take into account that the lower oxidation state of the +4-valent oxides also implies a lower electrode potential

(caused by a higher electrochemical potential), so the difference in energy density will also not be as explicit as the difference in volumetric capacity density.

- Generally, the capacity of the amorphous compound is higher than for their crystalline counterparts. This is related to the lower density and numerous ill-defined vacant sites found in an amorphous compound, that can provide more sites for storage of lithium-ions.
- The kinetics of the amorphous vanadium oxides outperform their crystalline counterparts in the same potential range. While most crystalline films have a kinetic loss of almost 40 % from 1C to 100C, the drop-off for amorphous films is closer to 20 %. This better performance is related to a diffusion coefficient that is quasi-independent of the state-of-charge, and thus higher than for the crystalline materials in the lithiated state.
- All examined vanadium oxides display better cycling behaviour than deep lithiation of crystalline V_2O_5. Especially, discharging of amorphous V_2O_5 to 2 V *vs* Li^+/Li retains 90 % of its initial capacity after 50 charge-discharge cycles, and the loss is very gradual, making it an interesting candidate. Crystalline VO_2(B) even increases in capacity after 50 cycles, which is likely related to gradual increase in electrode kinetics.

8.6.2 *Comparing ALD vanadium oxides electrodes to reported literature*

Figure 8.12 compares the rate capability and capacity of several of the above discussed ALD and ALD-derived vanadium oxides thin-film electrodes from this work, to some reported ALD and ALD-derived vanadium oxides thin-film electrodes. The bottom part of the graph contains V_2O_5 in its crystalline form with insertion up to LiV_2O_5, due to the low capacity of that storage mode. The reported capacities of the films are comparable at low C-rates to the capacity of the films in this work, as expected. However, it can be sees that the capacity retention of the c-V_2O_5 in this work outperforms the reported values, which could be related to its thin nature.

Secondly, Le Van reported the deposition of an amorphous V_2O_5 film with V^{4+} surfaces. This is thus a case in between amorphous V_2O_5 and amorphous VO_2, which are reported here. Indeed, the low C-rate capacity of the film reported by Le Van can be found between the values of a-VO_2 and a-V_2O_5 in this work. The kinetics are much poorer however, which is caused by a thicker film used in the work of Le Van ($\sim$200 nm) compared to the work here (30 nm to 40 nm).

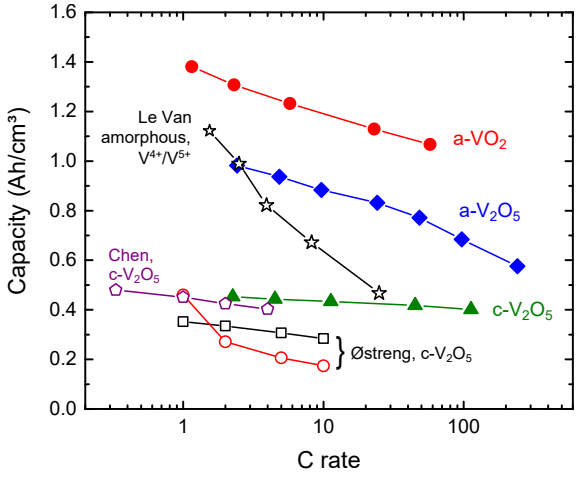

Figure 8.12: Comparing the kinetics of a-VO_2, a-V_2O_5 (1.5 V *vs* Li^+/Li) and c-V_2O_5 in the single lithium insertion region from this work to some reported ALD-derived vanadium oxides [235, 261, 267].

8.7 CONFORMAL VANADIUM OXIDES AS 3D THIN-FILM ELECTRODES

Finally, 3D thin-film electrodes were grown on a silicon scaffold. A silicon wafer was Bosch-etched to obtain silicon pillars with a diameter of 2 µm on a cubic lattice, with an center-to-center pillar spacing of 4 µm. The etch was continued until the pillars were 50 µm high. As a current collector, the pillars were coated with ALD TiN and ALD Pt. The ALD exposure doses were increased by sealing the pumps from the ALD chamber during precursor pulses, allowing ∼20 times higher pressures. For the O_2 PE-ALD process, it was found that raising the plasma exposure resulted in crystallisation of the films into crystalline V_2O_5. Thus, it was not possible to deposit conformal amorphous V_2O_5 on the pillar structures.

40 nm ALD films of a-VO_2 were deposited on the silicon micropillar structures. A 40 nm film of c-V_2O_5 and c-VO_2 (B) was obtained by depositing an a-VO_2 film and crystallizing the films as was discussed in section 8.4. The conformality was examined used SEM/EDX, as shown in figure 8.13. Line scans were made at equidistant spacings between the top and the bottom of the pillars. The detected vanadium content was independent of the position within the pillar substrates, indicating a uniform thickness of ALD vanadium oxide along the pillar walls.

Finally, these electrodes were also evaluated electrochemically. The real strength of atomic layer deposition for LIB electrodes emerges when thin

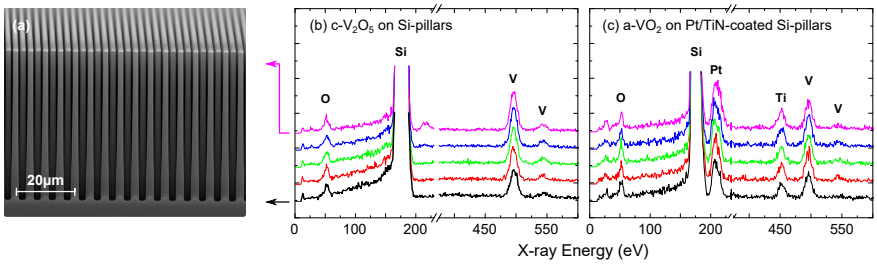

Figure 8.13: (a) Cross-sectional SEM image of the silicon micro pillar substrate used. EDX profiles resulting from line scans at equidistant lines between the top and bottom of 40 nm c-V_2O_5 film deposited on the bare Si micro pillar substrate, resulting from crystallizing a deposited a-VO_2 film (b) and a 40 nm a-VO_2 film deposited on the current collector-coated Si micro pillar substrate (c). The current collector is responsible for the presence of titanium and platinum characteristic X-rays.

films are able to be coated conformally on complex 3D substrates. This enhances the energy per footprint area by a factor of surface enhancement, while maintaining the excellent thin-film kinetics compared to the same energy electrodes in thicker films. In theory, the kinetics of the electrodes on the planar substrates should translate into the same kinetics on the surface-enhanced electrodes, since the current density and lithium ion diffusion is the same for both cases. The capacity per footprint area should be enhanced by a factor of surface enhancement of the substrate. The surface enhancement for this silicon micropillar substrate is 20.6 times that of the planar substrate.

Figure 8.14 shows the capacities of the planar electrodes and the 3D electrodes at various current densities, corresponding to C-rates between 0.1 C and 200 C. The capacities are indeed enhanced by deposition on the pillar substrates, and are even higher than the 20.6-factor expected from the 3D-structured substrate. The higher-exposure condition at which these films were grown could have resulted in slightly thicker films. The excellent thin-film kinetics observed for the planar electrodes is maintained when these are coated on the micro pillars, demonstrating the power of a conformal deposition technique in combination with micro- or nanostructuring of the electrodes. Compared to the benchmark crystalline V_2O_5, a 3.1-fold and 2.5-fold higher capacity is observed for the same thickness of amorphous VO_2 and crystalline VO_2(B) respectively, allowing either thinner films to obtain the same capacity, or a higher device storage with the same film thickness.

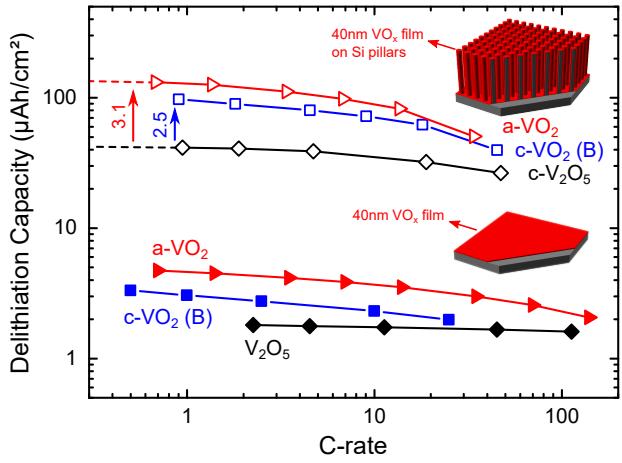

Figure 8.14: Illustration of the capacity enhancement from planar to micropillar electrodes, without loss of kinetics. Electrodes are constituted of 40 nm a-VO_2 (red), c-VO_2 (B) (blue) and c-V_2O_5 (black) films deposited on a planar Pt current collector (solid symbols) or on Pt-coated silicon micropillars (hollow symbols).

9

PAPER III

ATOMIC LAYER DEPOSITION OF VANADIUM OXIDES FOR THIN-FILM LITHIUM-ION BATTERY APPLICATIONS

Felix Mattelaer,*[a] Kobe Geryl,[a] Geert Rampelberg,[a] Thomas Dobbelaere,[a] Jolien Dendooven,[a] and Christophe Detavernier[a]

Published in *RSC Advances* (2016). Doi: 10.1039/c6ra25742a

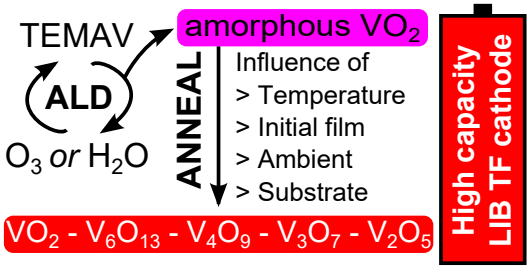

[a] *Department of Solid State Sciences, Ghent University, Krijgslaan 281 S1, 9000 Gent, Belgium,*

ABSTRACT

Amorphous VO_2 thin films are deposited by atomic layer deposition (ALD) using tetrakis [ethylmethylamino] vanadium (TEMAV) as vanadium precursor and water or ozone as oxygen source. The crystallisation and oxidation behaviour is investigated for different oxygen partial pressures between ambient air and 3.7 Pa, resulting in phase formation diagrams on SiO_2, TiN and Pt substrates demonstrating a series of stable vanadium oxide phases in the VO_2-V_2O_5 series. Most of the obtained phases exhibit lithium intercalation behaviour in the 1.5-4.5V vs Li^+/Li potential range, and demonstrate high volumetric capacities in the order of V_2O_5<VO_2 (B)<V_6O_{13}<V_3O_7<V_4O_9, with the latter at more than twice the capacity of the best commercial cathode materials.

INTRODUCTION

The development of an 'internet of things' requires both wireless sensor networks and autonomous micro systems [59, 60]. While the electronics, sensors and wireless communication systems abide Moore's law, the energy storage devices lag behind [3, 59]. To advance from traditional secondary batteries to energy storage systems tuned for these micro-devices, all-solid state thin-film batteries can provide the answer [54]. While the lack of liquid component in an all-solid state battery provides a huge advancement in battery safety and bio-compatibility [281], the thin-film approach provides integrability to on-chip devices as well as improved charge-discharge kinetics.

Due to the transition metal nature of vanadium oxides and the high number of vanadium-oxygen ratio compositions, vanadium oxides are heavily investigated materials for applications such as catalysis [210], optical switching [99] and thin-film batteries [218–227]. Although V_2O_5 and VO_2(B) are the most investigated cathode materials in lithium ion battery research [218–227], all vanadium oxides in the Wadsley series (V_nO_{2n+1}) are related to one another [282] and show promising electrochemical properties [219, 241]. Even though vanadium oxides have a high theoretical energy density, they suffer from poor charge-discharge kinetics due to their moderate electronic conductivity and intrinsically low ionic diffusion [283].

By going from a typical thin-film battery (1 µm to 10 µm thick electrodes) to truly thin-film electrodes (10 nm to 100 nm), the resistance for electronic current drops orders of magnitude, and interface intercalation dominates over the bulk diffusion [284]. However, the thin-film nature

of these batteries inherently leads to a low energy density. This problem can be overcome by depositing these thin-films on complex battery architectures leading to significant enhancements in effective surface area and thus in energy density per footprint area [28, 64, 80, 186, 187]. Many deposition techniques have been used to deposit a variety of vanadium oxides such as PVD [285, 286], sol-gel [286] and CVD [213], however, only few techniques have the high step-coverage of atomic layer deposition (ALD) required to coat the high-aspect-ratio structures required in 3D thin-film batteries [95]. Several ALD processes exist for vanadium oxides [77, 94, 98, 99, 253, 254, 270, 272].

In this work, we will investigate the formation of vanadium oxide thin films in the VO_2-V_2O_5 series, based on the atomic layer deposition of amorphous VO_2. We will show that we can obtain all vanadium oxide phases in the series by changing the post-deposition annealing conditions, and demonstrate electrochemical activity of different phases.

EXPERIMENTAL

The vanadium oxides were grown in an experimental high-vacuum ALD setup with a base pressure of 10^{-7} mbar with walls heated at 95 °C [93–95]. The ALD process used here was characterised earlier by Rampelberg et al [98, 99, 253, 254, 287], and is based on tetrakis[ethylmethylamino]vanadium ($V(NC_2H_5CH_3)_4$, or TEMAV) in combination with H_2O and ozone. The precursor was held in a stainless steel container at 70 °C with argon as a carrier gas. TEMAV and argon were pulsed at a pressure of 6×10^{-3} mbar. As reactant gases H_2O and O_3 were applied, pulsed at 7.5×10^{-3} mbar and 2×10^{-1} mbar respectively. The ozone was produced with an Ozone-Lab^{TM} generator from a pure O_2 gas flow, resulting in a minimal concentration of 150 µg ml^{-1}. In between pulses, reaction products and remaining precursor or reactant gas were evacuated using a turbomolecular pump to a pressure of $<2.0 \times 10^{-6}$ mbar. The films were grown on silicon substrates covered with 100 nm thermal SiO_2, 60 nm PVD TiN and 80 nm PVD Pt. Two thermal ALD processes were used here: the TEMAV-H_2O process and the TEMAV-O_3 process. To ensure similar conditions both processes were performed at a substrate temperature of 150 °C with saturated process parameters, as determined by earlier experiments [98, 99]. Pulse times for the TEMAV precursor were 5 s and 4 s in the water and ozone processes. Water and ozone pulse times were 5 s on the SiO_2 substrate. The Pt substrate influenced the growth, as was also reported by Premkumar *et al.* [254], so higher ozone pulse times (8 s) were required to ensure uniform films. The growth rate for the water process was 0.67 Å/cycle. The

growth rate for the ozone process was 1.05 Å/cycle, a higher value than reported by Rampelberg *et al.* [99], but still lower than the reported value by Premkumar *et al.* [254].

X-ray techniques were used to determine film thickness (X-ray reflectivity or XRR), crystallinity (X-ray diffraction or XRD) and film composition and oxidation state (X-ray photo-electron spectroscopy or XPS). XRR and XRD were performed in a Bruker D8 Discover using a copper X-ray source (Cu Kα radiation at 0.154 nm) and a point detector (for XRR) or a linear detector (for XRD). To determine the film crystallinity during annealing in a controlled ambient, *in-situ* XRD was performed using a linear detector and a controlled ambient/temperature system. XPS was performed using Al Kα radiation (0.834 nm) under a take-off angle of 45° in a high-vacuum chamber (2×10^{-9} mbar). A resolution of 0.108 eV was obtained.

The film morphology was probed using a Bruker Dimension Edge atomic force microscope (AFM) and film rms roughnesses were determined from 1 µm × 1 µm AFM images.

Electrochemical measurements were performed in an Ar-filled glove box (O_2 <1 ppm, H_2O <1 ppm) with a Metrohm Autolab PGSTAT302 connected to a three-electrode setup. Electrical contact to the TiN or Pt current collector was mady by contacting the side of the sample with silver paste to a Cu foil. Lithium ribbon (99.9 % , Sigma Aldrich) was used as counter- and reference electrodes, and 1M $LiClO_4$ in propylene carbonate (99 %, io-li-tec) was used as Li^+ electrolyte solution. Cyclic voltammetry (CV) measurements were performed at a 10 mV s^{-1} sweep rate between 1.5 and 4.5V vs Li^+/Li, or relevant potential boundaries. Galvanostatic charge-discharge measurements were performed to examine the capacity and thin film kinetics at varying current densities.

RESULTS AND DISCUSSION

VO_x thin film deposition by thermal ALD

First, the properties of the as-deposited amorphous films were investigated. The rms roughness of the as-deposited films on a Pt substrate, as measured by AFM, was 1.95 and 1.77nm for the H_2O- and O_3-based films, respectively. The Pt substrate was also measured, and showed a roughness of 1.75nm, so the deposition of a 10nm film on the substrate barely increases the roughness, indicating smooth films. The surface morphology was investigated using SEM, and images are shown in figure 9.1 for both films on the Pt substrate. A very similar granular morphology is observed

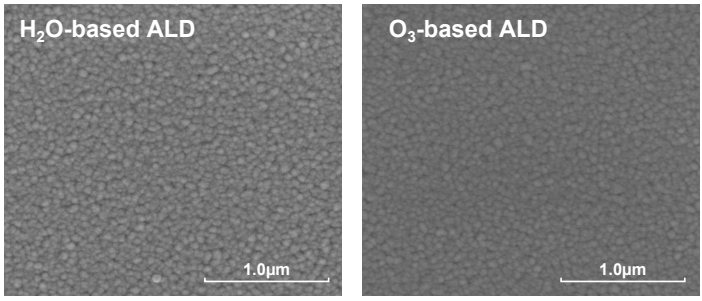

Figure 9.1: Morphology of the as-deposited VO_x films on the Pt substrate as measured by SEM, showing the H_2O-based (left) and O_3-based (right) ALD films.

for both processes. These results imply that the choice of process barely influences the as-deposited film morphology and topology.

Next, the film composition was investigated using XPS. Since vanadium oxides are reported to be very sensitive to the preferential sputtering of oxygen during depth profiling with XPS, only the surface spectra are evaluated to determine the composition and the oxidation state [279]. The measured spectra were calibrated to the O1s signals at 530.0 eV, since calibrating using the C1s peak is not ideal for vanadium oxides [288]. As the V2p core level binding energy depends strongly on its oxidation state [99, 279], fitting can be used to determine the oxidation state of the as-deposited films. Furthermore, the separation of the $V2p_{3/2}$ peak from the O1s VO_x-component at 530.0 eV was also used to compare the two as-deposited ALD films [279]. Figure 9.2 shows the results of this analysis, alongside a V_2O_5 reference, using the reported binding energies for the V2p components: 515.8eV and 523.2eV for the $V2p_{3/2}$ and $V2p_{1/2}$, and 517.2eV and 524.5eV for the $V2p_{3/2}$ and $V2p_{1/2}$ for the V^{4+} and V^{5+} components, respectively. Both as-deposited films clearly have vanadium in the 4^+ oxidation state.

Even though the morphology and oxidation state of the as-deposited films are shown to be quite similar, a difference in film density was found by evaluating the V XRF counts, normalised to the Si-substrate XRF counts to account for surface and distance factors. When these values are compared to the film thicknesses measured by XRR, it is clear from figure 9.3 that there is more vanadium per unit thickness in the H_2O-deposited films than in the O_3-deposited film, a direct proof that the films grown by utilizing the water process are denser when compared to those grown from the ozone process, as is consistent with XRR and XRF measurements performed in earlier work.

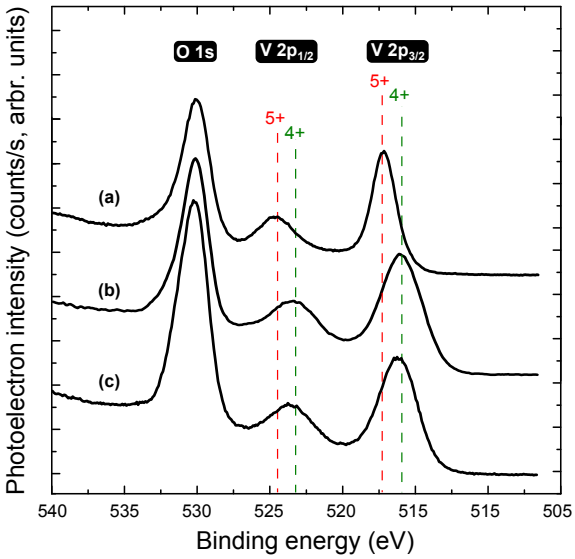

Figure 9.2: XPS spectra for the VO_x film surface: (a) a crystalline V_2O_5 reference film, (b) as-deposited film using the water-based ALD process and (c) as-deposited film using the ozone-based ALD process. The binding energies are referenced to O1s calibrated at 530.0eV [288].

VO_x crystallisation and oxidation state control for $2 \leq x \leq 2.5$

The as-deposited films using the TEMAV ALD processes are found to be amorphous by XRD with vanadium in a 4^+ oxidation state. By post-ALD annealing in ambients with carefully controlled oxygen partial pressures, vanadium oxides in the V_nO_{2n+1} series could be reached. The crystallisation was monitored using *in-situ* XRD and the oxidation states were in accordance to the crystal state, as was confirmed by XPS on selected quenches (not shown here). Ex-situ XRD on selected quenches confirmed the crystal states at intermediate temperatures. The crystallisation of the thin films was investigated on three substrates: SiO_2, Pt and TiN.

First, we will discuss the results on the SiO_2 substrate. The systematic study of the crystallisation behaviour of the ALD VO_x on the SiO_2 substrate is presented in figures 9.4(a) and 9.4(b) for the H_2O- and O_3-ALD deposited films, respectively. As an example, the phase evolution of the ozone-grown film during annealing in a 3.7 Pa oxygen partial pressure is discussed here (top section of figure 9.4(b)). One can observe that the film is initially amorphous by the lack of diffraction peaks. When heating in

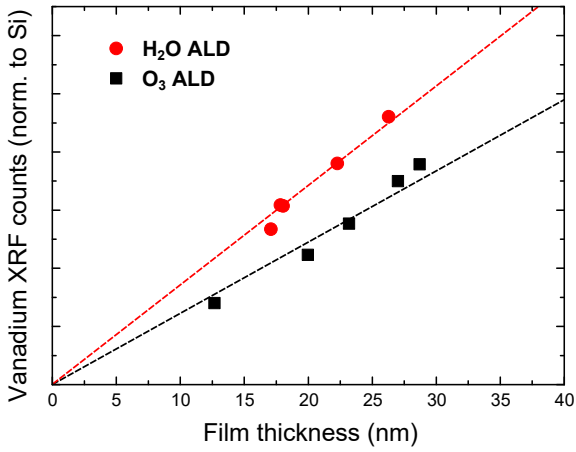

Figure 9.3: Relation between the XRF vanadium counts (normalised to the Si signal) and the measured film thickness (XRR) for different film thicknesses for both processes. The higher values for the H_2O-based ALD films indicate a higher VO_x density for these films. The dashed lines are a guide to the eye to illustrate this.

a controlled ambient, the film crystallises into VO_2 (B) just above 400 °C, and finally oxidizes between 500 °C and 600 °C to V_6O_{13}.

The results of the in-situ XRD measurements are summarized in 'phase formation diagrams', as shown in figure 9.5 for the crystallisation and oxidation on a SiO_2 substrate. These should not be interpreted as thermodynamic phase diagrams, since no constant-temperature steps were made to allow film stabilisation to the equilibrium state, but as phase formation diagrams displaying the kinetic path the films go through while being heated at 0.25 °C s^{-1} in the ambients under study (He with oxygen partial pressure of 3.7, 7.4, 14.8, 29.6 and 48.1Pa, and ambient air).

The in-situ XRD data provides a wealth of information on the often quite complex phase formation sequence. On SiO_2 substrates, phase-pure regions were only observed for the VO_2, V_6O_{13} and V_2O_5 phases. A clear trend emerges when examining the influence of the oxygen partial pressure. When going through both formation diagrams in figure 9.5 from low to high oxygen partial pressure, we see that phases emerge and disappear in the order of increasing oxidation state: VO_2-V_6O_{13}-V_4O_9-V_3O_7-V_2O_5 with respective average oxidation states for the V of $4 - 4.33 - 4.5 - 4.67 - 5$. The influence of the temperature is more complex since the phases have no time to settle to an equilibrium state at each temperature, so thin-film kinetics will complicate this behaviour. However, we can see that in gen-

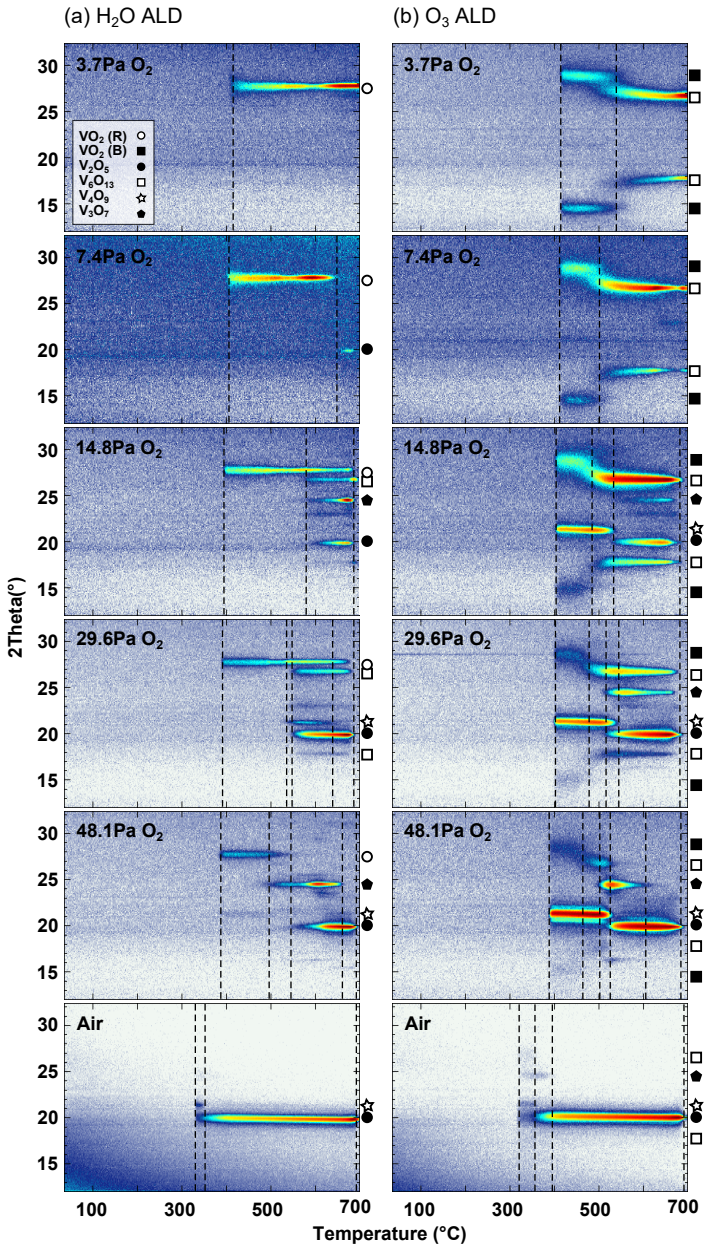

Figure 9.4: Crystallisation of the as-deposited VO_x thin films on the SiO_2 substrate, as studied by *in-situ* XRD in varying oxygen partial pressure at a heating rate of $0.25\,^{\circ}\mathrm{C\,s^{-1}}$. Symbols indicate VO_x crystal states ($2 \leq x \leq 2.5$), as shown in the legend (top left).

eral with increasing temperature the average oxidation state rises to higher values, showing high-temperature stability for the higher oxides.

Futhermore, we can see the remarkable influence of the as-deposited film on the initial crystallisation of the amorphous layers. Since all parameters are equal except for the ALD process gas during the ALD process (ozone or water), this translates to an influence of the latter on the initial crystallisation. The ozone-based ALD crystallizes into the VO_2(B)-phase, while the water-based process crystallizes into the high-temperature stable (>68 °C) VO_2(R)-state (which settles to the VO_2(M1) state when quenched in that phase). Both these phases are based on a bcc lattice with vanadium on the octahedral sites. The difference lies in the mutual orientation of the fourfold axis of the oxygen octahedra, being aligned or perpendicular for the VO_2(B) and VO_2(R), respectively [289]. This translates into a difference in structure as well as in density: VO_2(R) has a higher density (4.67 g cm^{-3}) than VO_2(B) (4.03 g cm^{-3}) [289]. Earlier, we showed that the water-based process grows a higher density amorphous VO_x layer than the ozone process. The high density amorphous layer deposited using the H_2O-based ALD proces crystallizes into the high density VO_2 (R) phase, while the lower density amorphous layer deposited using the ozone process crystallizes initially into the lower density VO_2 (B) phase. So, by choice of ALD process, we can choose to crystallise the film to either the VO_2(B) or VO_2(M1) phase for electrochemical testing.

We hypothesize that the use of ozone in the ALD process also has an influence on the oxidation behaviour. Even though XPS shows that these films have the same oxidation state for the vanadium (4+), we observe a lower temperature for the introduction of higher oxidation state vanadium oxides for the ozone grown films. For the lowest oxygen partial pressure we obtain phase-pure VO_2 for both films. For higher oxygen partial pressures, we see the presence of V_4O_9 upon crystallisation of the ozone grown films, having a higher oxidation state. For the water-grown films this was not the case, and we could obtain phase-pure VO_2 for all oxygen partial pressures examined (except for air), before further oxidation occurred. Even though the oxidation state is the same, a stronger oxidant is used during the ozone-based ALD process, which could incorporate more oxygen into the films. Another hypothesis is based on the fact that the films are less dense when using the ozone process. This could allow faster oxygen diffusion into these films, enhancing the oxidation kinetics during post-ALD annealing.

The crystallisation of the films on the Pt and TiN substrates was examined next, since a current collector is required to test the vanadium oxides as LIB electrode materials. The results are shown in figure 9.6. Similar

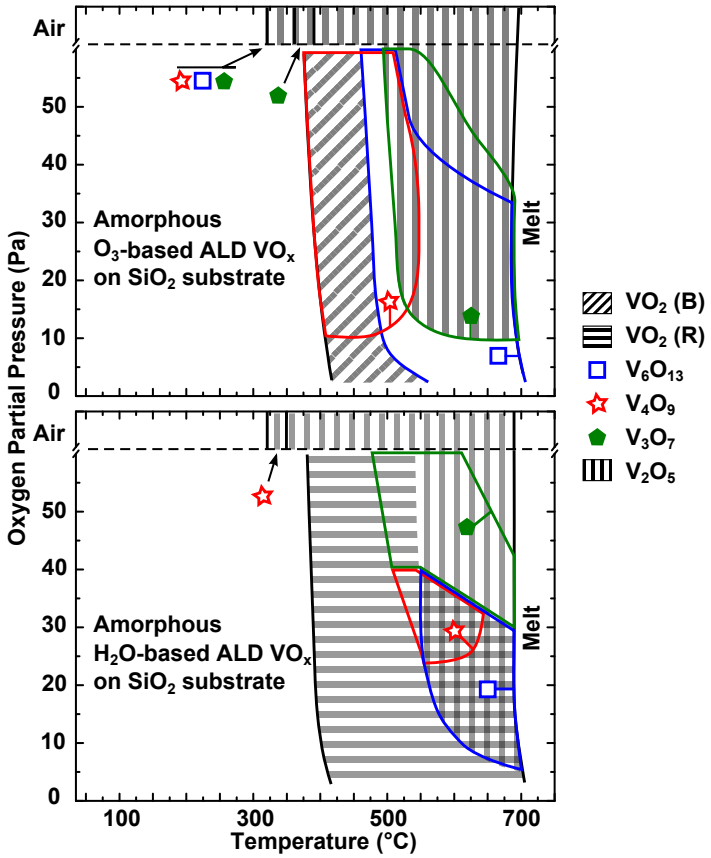

Figure 9.5: Phase formation diagrams for the formation of crystalline VO_x phases ($2 \leq x \leq 2.5$), based on the isXRD measurements (figure 9.4) at $0.25\,^{\circ}\mathrm{C\,s^{-1}}$ for He ambients with oxygen partial pressures of 3.7, 7.4, 14.8, 29.6 and 48.1Pa, and in ambient air. The same set of symbols is used as in figure 9.4 except for the extrema, namely VO_2 and V_2O_5 states, since these dominate the phase formation diagrams to a large extent.

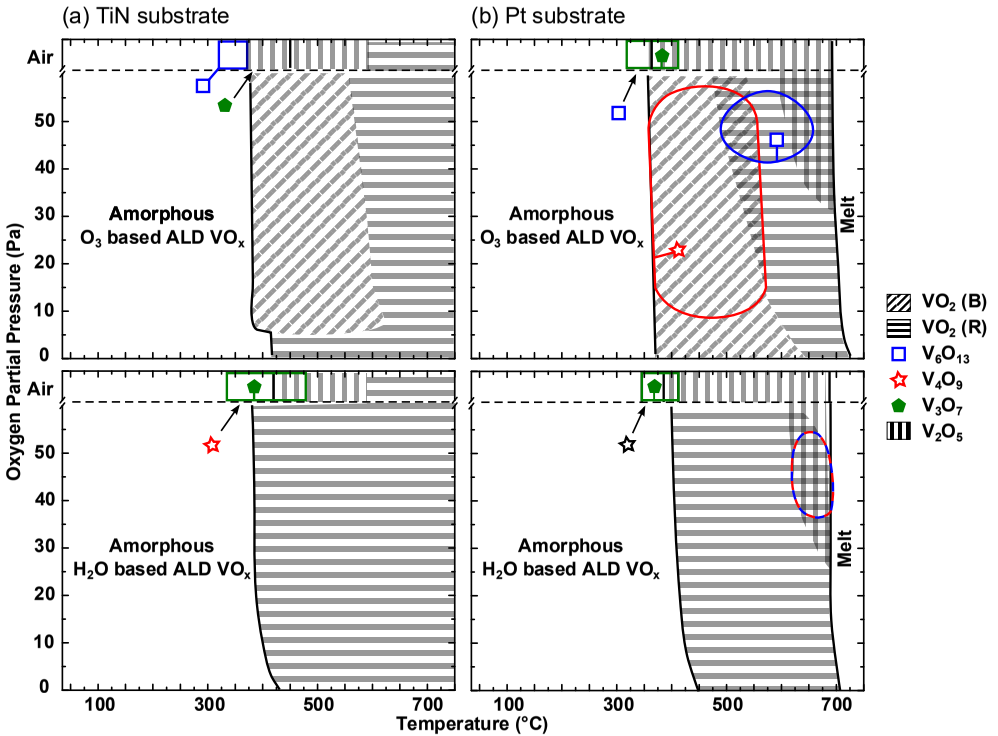

Figure 9.6: Phase formation diagrams for the formation of the VO_x crystal states ($2 \leq x \leq 2.5$) on TiN substrates (left) and on Pt substrates (right), at $0.25\,^{\circ}\mathrm{C\,s^{-1}}$ for He ambients with oxygen partial pressure of 3.7, 7.4, 14.8, 29.6 and 48.1Pa, and in ambient air. The absence of the melt-line on the left figure is related to the presence of rutile TiO_2 from the substrate, complicating the analysis of the VO_2 (R) phase on the TiN substrate at high temperatures.

Phase	ALD reactant	Ambient	Temperature (°C)
VO_2 (B)	O_3	He + 3.7 Pa O_2	420
VO_2 (M1)	H_2O	He + 18 Pa O_2	450
V_6O_{13}	O_3	He + 3.7 Pa O_2	550
V_4O_9	H_2O	Ambient air	356
V_3O_7	O_3	He + 48 Pa O_2	560
V_2O_5	H_2O or O_3	Ambient air	500

Table 9.1: Conversion paths from the as-deposited films to their crystallised and oxidized forms, on the Pt-substrate.

trends were observed, with again formation of the VO_2(B) or VO_2(M1) as first phases for the ozone and water-based ALD, respectively, and the V_2O_5 phase occurring at high-temperature and/or high oxygen ambients. However, one can note two main differences when comparing these phase formation diagrams to those on SiO_2. Firstly, the SiO_2 formation diagrams are much richer in phase zones than their counterparts on Pt and TiN. Furthermore, we observed that on SiO_2 the transformation to higher oxidation state vanadium oxides happens at lower temperatures than on the other investigated substrates. In the case of a TiN substrate, the vanadium oxide phases with the highest oxidation states appear at the highest temperatures, or not at all, when compared to SiO_2 and Pt. The Pt case lies in between both other cases. Here, we see the influence of the TiN in the substrate. We hypothesise that the TiN-substrate acts as an oxygen drain, extracting oxygen from the film, and thus preventing further oxidation of the vanadium oxides, as was also observed by the presence of TiO_2 rutile diffraction peaks in the XRD scans taken after the oxidation experiments. The SiO_2 is completely oxidized already, so it does not act as an oxygen drain, lowering the oxygen pressure and temperatures required to oxidise the vanadium oxides. The Pt substrate has a TiN layer underneath. Since oxygen can diffuse through the Pt layer, the underlying TiN can still get oxidized, as was confirmed by XRD. However, this oxidation is delayed by the presence of the Pt layer. This causes both observed differences: the phase-richness in the formation diagrams likely also occurs for TiN or Pt substrates, but at higher oxygen partial pressures than examined here, when the supply of oxygen is higher than the harvesting effect of the TiN.

Electrochemical characterisation of the possible VO_x phases ($2 \leq x \leq 2.5$)

All of the obtained crystalline vanadium oxides (VO_2 (B), VO_2 (M1), V_6O_{13}, V_4O_9, V_3O_7 and V_2O_5) were tested as LIB electrodes on Pt substrates. Film crystallisation was monitored by in-situ XRD to ensure corresponding phase formations and oxidations (supplementary information, figures 10.1 to 10.6), and summarised in table 9.1. Only V_3O_7 was not obtainable in a phase-pure form on the Pt substrate, but the oxidation path indicated in table 9.1 shows only a small fraction of the V_3O_7 film crystallised to V_2O_5, as was confirmed by XRD and XPS. This makes the V_3O_7 almost phase-pure, and will be denoted further just as V_3O_7. The path to V_6O_{13} does not match the phase formation diagram, since phase-pure V_6O_{13} was obtained by performing a ramp slower than the one used for the formation diagrams. Cyclic voltammetry at $10\,mV\,s^{-1}$ was performed down to 1.5V vs Li^+/Li to examine the electrochemical intercalation behaviour of the different vanadium oxides. As can be seen in figure 9.7, all phases show a clear lithiation and delithiation behaviour. However, even though the VO_2 (M1) appeared to show activity, initial galvanostatic charge-discharge tests showed only very low electrochemical storage capacity. Furthermore, some peaks of the cyclic voltammogram appear closely related to the electrochemical activity of the Pt substrate, as shown in supplementary (figure 10.7). Due to the absence of storage of lithium into these films, VO_2 (M1) was not examined in-depth further. All other films showed a clear lithium insertion/extraction behaviour, indicating lithium can be stored in these films reversibly.

Galvanostatic charging and discharging was performed on the films to determine the available storage capacity and compare it to V_2O_5, which is the most investigated form of vanadium oxide and is generally considered to be the most promising phase. The films were cycled at varying current densities between 0.1C and 100C, and the capacity was extrapolated to the 1C capacity to allow direct comparison between the different VO_x phases, as shown in figure 9.8. Extrapolation was performed by fitting a linear relation to the logarithm of the capacity plotted to the logarithm of the C-rate, which provided fits with $R^2 > 0.98$, demonstrating the validity of this approach. Table 9.2 summarizes the extrapolated capacities at 1C. Both table 9.2 and figure 9.8 clearly demonstrate that, although V_2O_5 is the most investigated vanadium oxide for LIB cathodes, the capacity of the stable region (which corresponds to insertion of one lithium into V_2O_5), has a limited volumetric capacity. This is related to the low density of this V_2O_5 ($3.36\,g\,cm^{-3}$) compared to that of commercial lithium-ion cathodes such as $LiCoO_2$ ($4.9\,g\,cm^{-3}$) [16]. All of the other investigated vana-

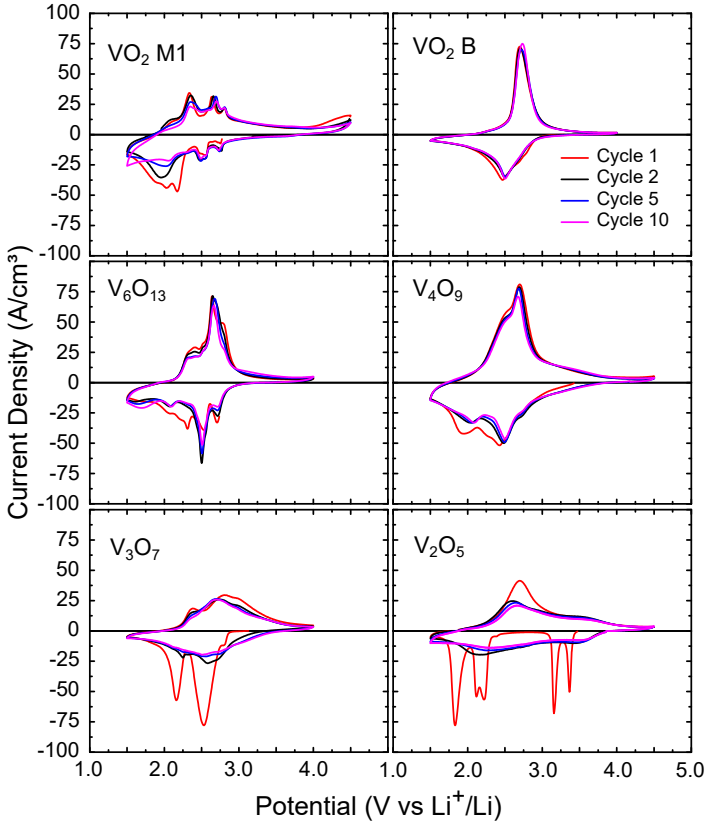

Figure 9.7: Cyclic voltammetry on the selected vanadium oxide thin films, performed at 10 mV s^{-1} in a 3-electrode setup with lithium as counter and reference electrodes, and 1M $LiClO_4$ in PC as electrolyte. Potential ranges were chosen according to activity.

dium oxide phases have capacities well above the commercial cathodes, which is spearheaded by $LiNi_{0.33}Mn_{0.33}Co_{0.33}O_2$ (NMC) with a capacity of 600 mA h cm^{-3}. The higher capacity for other vanadium oxides has an origin in material density and insertion range. First, the densities of the lower oxidation state vanadium oxides are higher than that of V_2O_5, leading to a higher volumetric capacity density. V_3O_7, V_4O_9, V_6O_{13} and the VO_2 (B) films have a density of 3.61 g cm^{-3}, 3.78 g cm^{-3}, 3.91 g cm^{-3} and 4.0 g cm^{-3}, respectively. Second, while V_2O_5 can only be used in the narrow range that leads to LiV_2O_5, i.e. reduction of vanadium from V^{5+} to an average oxidation state of $V^{4.5+}$, the vanadium in the series of vanadium oxides tested here changes its oxidation state much more, ranging

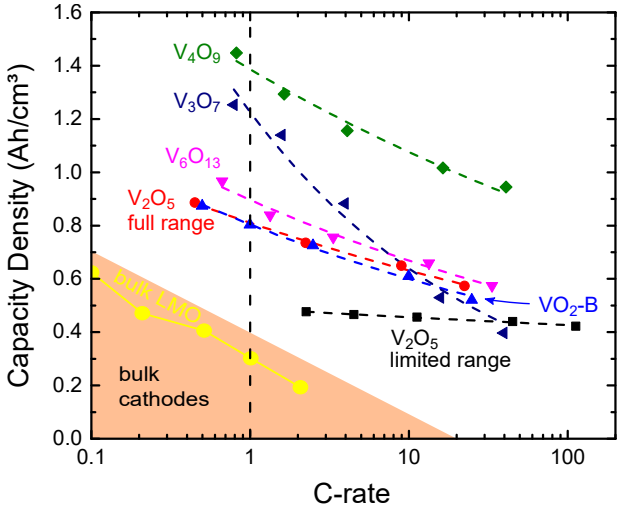

Figure 9.8: Measured delithiation capacity of the examined films on a logarithmic-linear scale (solid symbols). The data was extrapolated (dashed lines) resulting in a good match to the data ($R^2 > 0.98$). Micron-sized LMO is shown as a model bulk cathode,(red circles) [290] and more general bulk cathodes (shaded left corner) [16] from literature are shown for comparison.

from a change in average oxidation state of 0.62 for VO_2 (B) to almost 1.2 for V_4O_9. So, while V_2O_5 and VO_2 (B) are generally considered the most promising cathode materials, vanadium oxides in between them exhibit higher volumetric capacities.

CONCLUSIONS

We demonstrated the deposition of two different forms of amorphous VO_2 using two different ALD chemistries based on the same TEMAV precursor. Films were shown to be similar in morphology and as-deposited oxidation state of vanadium, but differ in density. By annealing these films in controlled ambients with varying oxygen partial pressures, we demonstrated that all crystalline phases between VO_2 and V_2O_5 could be obtained. the substrate was found to influence the oxidation and crystallisation behaviour, with TiN acting as an oxygen drain delaying the oxidation. All obtained crystalline phases were characterised electrochemically, and showed activity as lithium-ion electrodes. We demonstrated that, while V_2O_5 is the most widely investigated vanadium-based cathode material, also VO_2 (B), V_6O_{13}, V_4O_9 and V_3O_7 can be used as cathodes, with capaci-

	Potential (V vs Li^+/Li)	Volumetric capacity ($mA\,h\,cm^{-3}$)
this work		
VO_2 (M1)	1.5-4.0	*no activity*
VO_2 (B)	1.5-4.0	805 (1C)
V_6O_{13}	1.5-4.0	894 (1C)
V_4O_9	1.5-4.0	1380 (1C)
V_3O_7	1.5-4.0	1255 (1C)
V_2O_5 ($\rightarrow LiV_2O_5$)	2.9-3.5	488 (1C)
V_2O_5 ($\rightarrow Li_3V_2O_5$)	1.5-4.0	810 (1C)
Commercial cathode materials		
$LiCoO_2$	3.8	550
$LiMn_2O_4$	4.1	596
$LiFePO_4$	3.4	589
$LiNi_{0.33}Mn_{0.33}Co_{0.33}O_2$	3.7	600
$LiNi_{0.8}Co_{0.15}Al_{0.05}O_2$	3.8	700

Table 9.2: Delithiation capacities for the examined thin films, calculated by charging and discharging the films at varying current density over several orders of magnitude and extrapolating the measured capacity to 1C (fig. 9.8), which corresponds to the current necessary to reach the theoretical capacity in 1 hour. Volumetric capacities of commercial cathode materials are included for comparison [16].

ties up to $1380\,mA\,h\,cm^{-3}$ (V_4O_9), more than twice the volumetric capacity for commercial cathode materials such as NMC.

10

SUPPLEMENTARY TO PAPER III

IN-SITU XRD

To demonstrate the formation of the phases that are examined electrochemically, in-situ X-ray diffraction is done during the formation of the phases. Table 10.1 shows an overview of the atmosphere, temperature and initial film conditions used to obtain all phases between VO_2 and V_2O_5. Figures 10.1 to 10.6 show the resulting isXRD plots on the current collector substrate, demonstrating the successful phase formation.

Phase	ALD Reactant	Ambient	Temperature
VO_2 (B)	O_3	He + 3.7 Pa O_2	420
VO_2 (M1)	H_2O	He + 18 Pa O_2	450
V_6O_{13}	O_3	He + 3.7 Pa O_2	550
V_4O_9	H_2O	Ambient air	356
V_3O_7	O_3	He + 48 Pa O_2	560
V_2O_5	H_2O or O_3	Ambient air	500

Table 10.1: Conversion paths from the as-deposited films to their crystallised and oxidized forms, on the Pt-substrate.

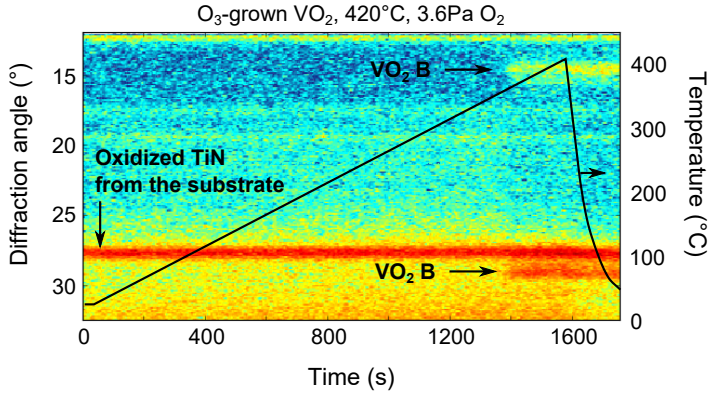

Figure 10.1: In-situ XRD during the oxidation of ozone-grown amorphous VO_2 to crystalline VO_2 B on the Pt substrate. The temperature was ramped linearly to 420 °C in an ambient consisting of He + 3.6Pa O_2.

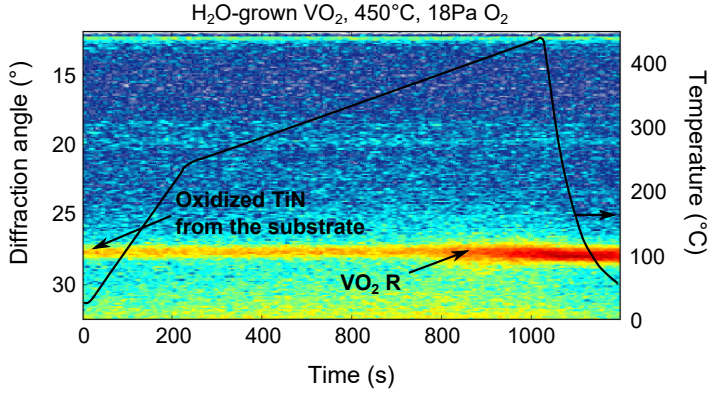

Figure 10.2: In-situ XRD during the oxidation of water-grown amorphous VO_2 to crystalline VO_2 M1 on the Pt substrate. The temperature was ramped to 450 °C in an ambient consisting of He + 18Pa O_2.

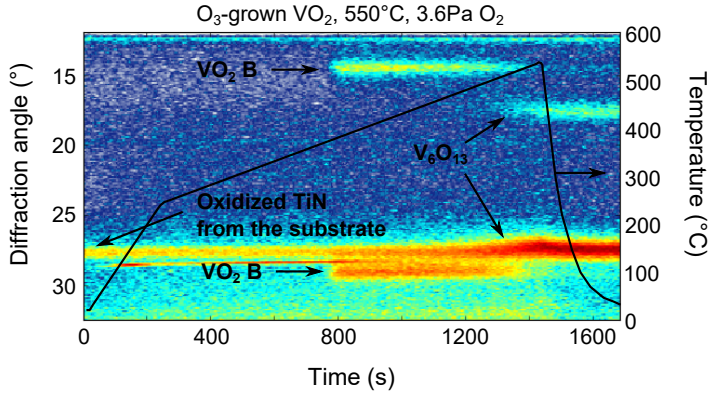

Figure 10.3: In-situ XRD during the oxidation of ozone-grown amorphous VO_2 to crystalline V_6O_{13} on the Pt substrate. The temperature was ramped to 550 °C in an ambient consisting of He + 3.6Pa O_2.

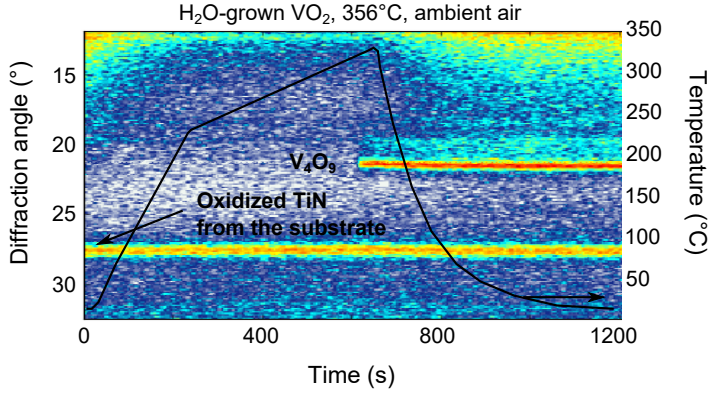

Figure 10.4: In-situ XRD during the oxidation of water-grown amorphous VO_2 to crystalline V_4O_9 on the Pt substrate. The temperature was ramped to 356 °C in ambient air.

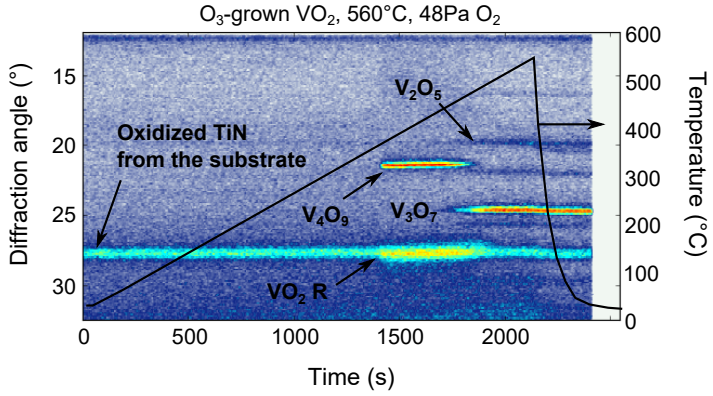

Figure 10.5: In-situ XRD during the oxidation of ozone-grown amorphous VO_2 to crystalline V_3O_7 on the Pt substrate. The temperature was ramped to 560 °C in He + 48Pa O_2.

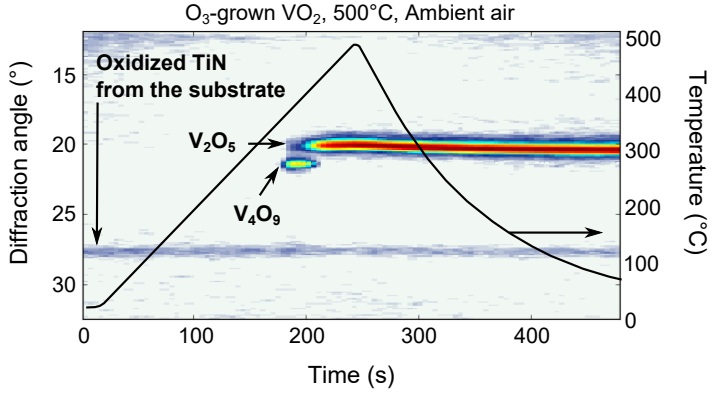

Figure 10.6: In-situ XRD during the oxidation of ozone-grown amorphous VO_2 to crystalline V_2O_5 on the Pt substrate. The temperature was ramped linearly to 500 °C in ambient air.

CYCLIC VOLTAMMETRY ON THE PT SUBSTRATE AND THE VO_2 M1 PHASE

Figure 10.7 shows the cyclic voltammograms of the VO_2 M1 film and of the uncoated Pt substrate. Some similarities can be seen between the peak positions of both cyclic voltammograms. Furthermore, galvanostatic charge-discharging showed the film displayed almost no storage capacity, indicating almost no bulk energy storage, and thus mostly surface-related electrochemical activity is present for these films.

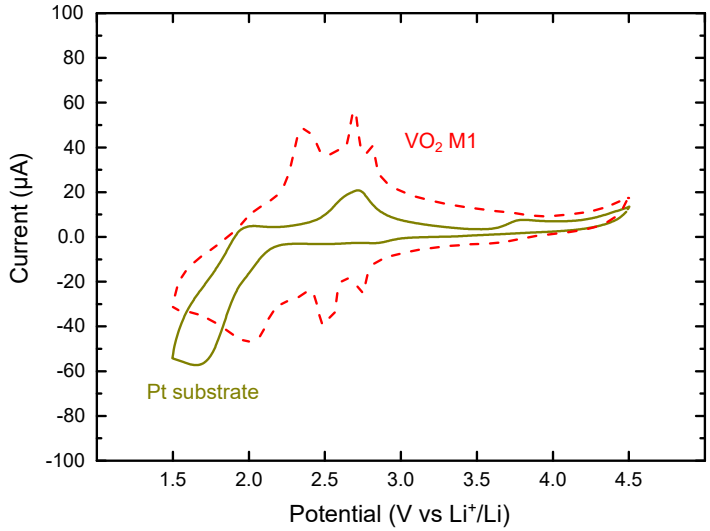

Figure 10.7: Cyclic voltammetry on the Pt substrate and VO_2 M1 thin film, performed at $10\,mV\,s^{-1}$ in a 3-electrode setup with lithium as counter and reference electrodes, and 1M $LiClO_4$ in PC as electrolyte.

11

PAPER IV

AMORPHOUS AND CRYSTALLINE VANADIUM OXIDES AS HIGH-ENERGY AND HIGH-POWER CATHODES FOR 3D THIN-FILM LITHIUM ION BATTERIES

Felix Mattelaer,*[a] Kobe Geryl,[a] Geert Rampelberg,[a] Jolien Dendooven,[a] and Christophe Detavernier[a]

Published in *ACS Applied Materials & Interfaces* (2017). Doi: 10.1021/acsami.6b16473.

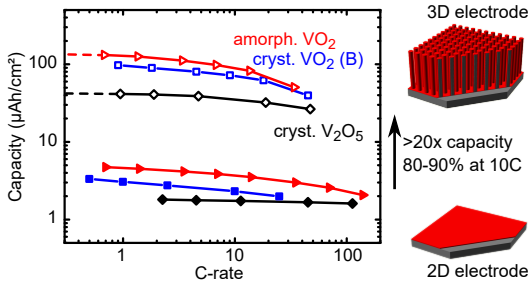

[a] *Department of Solid State Sciences, Ghent University, Krijgslaan 281 S1, 9000 Gent, Belgium,*

ABSTRACT

Flexible wearable electronics and on-chip energy storage for wireless sensors drive rechargeable batteries towards thin-film lithium ion batteries. To enable more charge storage on a given surface, higher energy density materials are required, while faster energy storage and release can be obtained by going to thinner films. Vanadium oxides have been examined as cathode in classical and thin-film lithium ion batteries for decades, but amorphous vanadium oxide thin films have been mostly discarded. Here, we investigate the use of atomic layer deposition, which enables electrode deposition on complex 3D battery architectures, to obtain both amorphous and crystalline VO_2 and V_2O_5, and we evaluate their thin-film cathode performance. Very high volumetric capacities are found, alongside excellent kinetics and good cycling stability. Better kinetics and higher volumetric capacities were observed for the amorphous vanadium oxides compared to their crystalline counterparts. The conformal deposition of these vanadium oxides on silicon micropillar structures is demonstrated. This study shows the promising potential of these atomic layer deposited vanadium oxides as cathode for 3D all-solid-state thin-film lithium ion batteries.

INTRODUCTION

Lithium ion batteries (LIBs) are currently the energy storage system that offers the highest specific power and energy, almost double that of NiMH batteries. This explains why LIBs have gradually taken over the market since their first introduction by Sony in 1991. Their market share for electric vehicles for example is expected to increase from 56.4 % in 2011 to 91.8 % in 2020 [291]. This position is consolidated further by the wide range of applications that call for energy storage. The LIB is able to provide energy for MWh applications such as grid storage, kWh applications such as electric vehicles (EV) and hybrid electric vehicles (HEV), down to Wh energy storage in consumer electronics and μWh energy storage for on-chip devices such as sensors. This wide range of applicability makes LIBs indispensable in current day society.

In a classical battery, such as the LIB for EV/HEV applications, the main focus of research lies in further advancing the available energy and power density. For the μWh range batteries, energy and power density advancements are also relevant, but many other factors become equally important. For on-chip devices, integrability and processability are paramount to enable the combination with an integrated circuit design. Thin film batteries enable this combination of energy storage with microdevices [54]. Safety

and biocompatability become critical when considering implantable sensors, which is one of the main motivators to go to all-solid-state LIBs [281]. If the energy storage is combined with a microscale energy harvester, such as a photovoltaic element, power density also becomes an important factor to enable fast charging of the battery while energy is being harvested, and fast and safe release of the stored energy when the sensor requires it, are key to the good operation of an autonomous sensor system. Thin-film all-solid state LIBs are the energy storage device of choice for this range of applications.

Going from traditional thin-film batteries with 1 µm to 100 µm electrodes to truly thin-film electrodes in the 10 nm to 100 nm regime reduces the impact of the slow diffusion in the bulk of the material, allowing batteries to be (dis)charged at far higher rates [158, 284], an effect also observed for nanoscaling of electrode powders [1]. The downside is that the transition from micro- to nano-electrodes limits the available energy. This can be overcome by moving from traditional planar thin-film batteries to thin-film batteries deposited on complex 3D architectures, such as silicon nanopillars [292, 293] or carbon-based nanostructures [294–296]. This maintains the excellent power capability of thin film nano-scaled electrodes, while at the same time elevates the energy density per footprint area, the relevant parameter for an on-chip battery [28, 54, 64, 80, 186, 187].

Another way to obtain a higher power capability in lithium ion batteries is moving from crystalline to amorphous electrodes. In typical crystalline cathode materials, a transition metal superlattice offers a periodic lattice with sites for lithium storage and pathways for lithium conduction [241, 297], and research has shown that a higher degree of order generally enhances the energy and power densities of the electrode material [298–301], causing what is known as the 'ordering paradigm' [245, 302]. However, amorphous electrodes can offer several potential advantages over their crystalline counterparts [243, 303]. Since most amorphous materials have a lower density than crystalline and numerous ill-defined vacant sites exist, more storage is available [246, 252]. Due to the lack of long-range order, no preferred ion diffusion channels exist, causing isotropic lithium diffusion [243]. Furthermore, a lower density and many lithium-hopping sites enable higher lithium diffusion coefficients [243, 245, 246], reported to be several order of magnitude higher than in crystalline electrodes. This is expressed in the high conductivity found in lithium phosphate glasses used as electrolytes [57, 87, 247], but also in the excellent power capability often found in amorphous electrodes [245, 248–251].

Vanadium oxides have been heavily investigated as possible electrode materials starting from the early beginning of the lithium ion battery in

the 1970's [237, 239]. The excellent stability of the V_2O_5 to LiV_2O_5 cycling made it an excellent cathode candidate, but it was never commercialized on a large scale due to the relatively low capacity of this intercalation compound compared to commercial cathodes such as $LiCoO_2$ and $LiMn_2O_4$ [6, 219–221]. While deeper lithiation of V_2O_5 would increase the capacity, it unfortunately leads to poor cyclability due to vanadium dissolution and structural instability [221, 223]. Therefore, other vanadium oxides such as V_6O_{13} [237–239, 304] and VO_2 [237, 239, 305–309] have been studied. Even though they have a lower oxidation state for the vanadium, resulting in a lower electrochemical potential, far higher theoretical capacities and decent electrochemical performance can be obtained. Amorphous vanadium oxides have also been studied with the main focus on amorphous V_2O_5 or V_2O_5-based glasses as cathodes [29, 243, 244, 246, 250–252, 261, 310–313] or lower valent a-VO_x based bronzes as anodes [314, 315].

Various 3D-structured electrode concepts based on vanadium oxides have been proposed in literature, such as core-shell structures or nanobelt arrays. To enable vanadium oxides for the complex structures required for 3D thin-film all-solid-state LIBs, a conformal deposition technique is needed. Atomic Layer Deposition is unmatched in its ability to conformally cover high aspect ratio structures, due to the self-limiting gas-surface reactions of the precursors [69, 72, 95]. Furthermore, the low deposition temperature typically required for ALD often enables the deposition of amorphous films rather than crystalline, which is the case for the high temperatures typically required in for example sol-gel depositions [199]. Several processes have been developed for the ALD and post-ALD annealing of vanadium oxides [77, 98, 253, 254, 270], and ALD vanadium oxides have been demonstrated as 3D thin film cathode [235, 261, 267].

The main part of the literature details either crystalline V_2O_5, crystalline V_6O_{13} or crystalline VO_2. In this work, we perform a systematic study comparing amorphous and crystalline forms of thin-film VO_2 and V_2O_5, and evaluate the electrochemical performance of the two amorphous vanadium oxides thin films (a-VO_2 and a-V_2O_5) and their crystalline counterparts (c-VO_2 (B) and c-V_2O_5) as thin-film LIB cathodes. We report high energy density and exceptional power capability for all amorphous films. While the cyclability of the amorphous films is better for V_2O_5, c-VO_2 has a much longer cycle life than a-VO_2, at a volumetric capacity still beating the best available commercial cathode materials. Finally, we report the deposition of several ALD vanadium oxides on a 3D silicon micropillar structure, demonstrating a $>$20-fold enhancement of the capacity per footprint area, while maintaining the excellent thin film kinetics.

EXPERIMENTAL

Amorphous vanadium oxide thin films were grown in a home-built ultra-high vacuum ALD setup [93–95]. The setup has a base pressure of 10^{-7} mbar. To avoid precursor condensation on the reactor walls, the entire system is heated to 95 °C. The vanadium-bearing ALD precursor used here was tetrakis[ethylmethylamino]vanadium ($V(NC_2H_5CH_3)_4$, or TEMAV). Ozone or oxygen plasma were used as oxidants. For the VO_2 ALD, process conditions were reported in earlier work by Rampelberg et al [98, 99, 253, 254, 287], and a substrate temperature of 150 °C was chosen. For the deposition of amorphous V_2O_5 (a-V_2O_5), the substrate temperature was 85 °C, and the RF plasma pulse time (200W) was optimized to be as short as possible. The substrates used were silicon covered with native oxide for process characterisation, and 80 nm PVD Pt on 60 nm PVD TiN on SiO_2 as current collector substrate for the electrochemical characterisation. A silicon micropillar array was etched into a silicon substrate, yielding 50 µm high pillars with a diameter of 2 µm, spaced 2 µm apart. To use these as a substrate for the electrode, they were coated with 20 nm ALD TiN and 5 nm Pt.

To characterize the film thickness, X-ray Reflectivity was used. Crystallinity of the films was evaluated by X-ray Diffraction (XRD), and monitored during annealing by *in-situ* X-ray diffraction (isXRD) in a controlled ambient/temperature system [206, 207] using a copper X-ray source (Cu Kα radiation at 0.154 nm) and a point detector (for XRR) or a linear detector (for XRD). X-ray photo-electron spectroscopy (XPS) was used to determine the oxidation state of the vanadium in the deposited films from the $V2p_{3/2}$ and $V2p_{1/2}$ binding energies [99, 279, 288]. XPS was performed using Al Kα radiation (0.834 nm) under a take-off angle of 45° in an ultra-high vacuum chamber (2×10^{-9} mbar). A resolution of 0.108 eV was obtained.

The film surface morphology was examined using a high-vacuum electron microscope at a magnification of 100000x (FEI Quanta 200F).

Electrochemical measurements were performed on thin-film electrodes ($\sim$50 nm) in an Ar-filled glove box (O_2 <1 ppm, H_2O <1 ppm) with a Metrohm Autolab PGSTAT302 connected to a three-electrode setup. Electrical contact to the TiN/Pt current collector was established by contacting the side of the sample with silver paste to a Cu foil. Lithium ribbon (99.9 %, Sigma Aldrich) was used as counter- and reference electrodes, and 1M $LiClO_4$ in propylene carbonate (99 %, io-li-tec) was used as Li^+ electrolyte solution. Cyclic voltammetry (CV) measurements were performed at a 10 mV s^{-1} (planar electrodes) or 1 mV s^{-1} (micropillar elec-

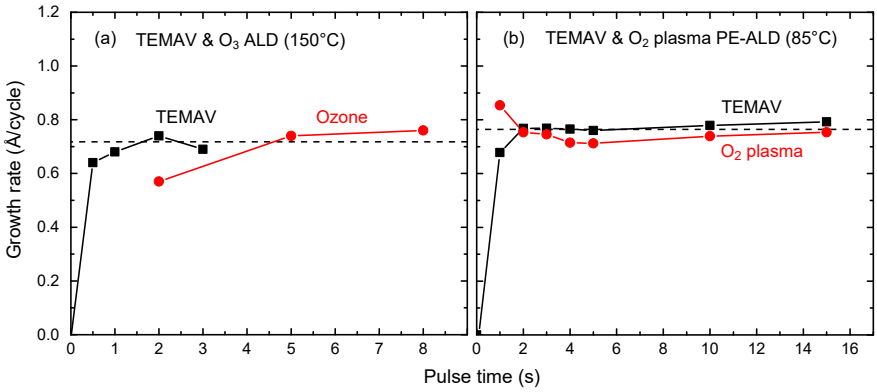

Figure 11.1: Saturation curves of the pulse times during (a) the TEMAV and ozone ALD process (150 °C) and (b) the TEMAV and oxygen PE-ALD process (85 °C). The data for the ozone process has been reported elsewhere, and is reproduced with permission.

trodes) sweep rate between relevant potential boundaries. Galvanostatic charge-discharge measurements were performed to examine the capacity evolution and thin film kinetics at varying current densities. All capacities and currents in this work are expressed volumetrically ($A\,h\,cm^{-3}$) or per footprint area ($A\,h\,cm^{-2}$), as thin-film devices are envisioned. To accommodate a comparison to reported gravimetric capacities ($A\,h\,g^{-1}$), a table with the densities of the examined films is placed in the supplementary information (table 12.1). The potentiostatic intermittent titration technique (PITT) was performed as described in supplementary information.

RESULTS AND DISCUSSION

Deposition and physical properties of the vanadium oxide films

Amorphous VO_2 (a-VO_2) was deposited using TEMAV and ozone, according to saturated process conditions. Saturation is demonstrated in figure 11.1 (a). To the best of our knowledge, no process was previously reported to deposit a-V_2O_5 using the TEMAV precursor and an oxygen plasma in a plasma-enhanced ALD (PE-ALD) process. The deposition of V_2O_5 using TEMAV was reported to grow crystalline V_2O_5 (c-V_2O_5) [99]. However, the work of Rampelberg et al indicated that extrapolating the known oxygen plasma based process to short plasma exposures and to low temperatures could lead to amorphous films. Therefore, we investigated the low-temperature border of the temperature window, which was already

explored to a lower limit of 100 °C, and extend it by reporting ideal ALD behaviour at temperatures down to 85 °C (saturation shown in figure 11.1 (b)). Here, we find a lower growth rate at 85 °C, which is in line with the reported decrease in growth rate with decreasing temperature from the work of Rampelberg et al. No carbon content could be detected in the films from XPS measurements, indicating that a complete ligand removal takes place even at this relatively low temperature.

First, the crystallinity of both layers was examined. XRD measurements indicated that both the layer grown from the ozone process at 150 °C and the layer grown from the oxygen plasma process grown at 85 °C were amorphous at saturation conditions, as shown in figure 11.2 (a). To crystallize the films, the samples were ramp annealed under well-chosen ambients in a home-built *in-situ* monitoring chamber. Annealing conditions for these films have been thoroughly investigated in previous work. To obtain crystalline V_2O_5, a ramp anneal was performed on the a-V_2O_5 in ambient air to allow a high oxygen partial pressure to the films. To obtain crystalline VO_2, the oxygen partial pressure and temperature are critical, and a slow ramp (0.25 °C s^{-1}) up to 425 °C on the a-VO_2 sample was done in a helium ambient, mixed with 20 Pa partial pressure of oxygen. Results on the SiO_2 substrates are shown in figure 11.2 (b) and (c), demonstrating that (1) the films are initially amorphous, (2) can be converted to a crystalline VO_2 or V_2O_5 state which (3) remains stable during and after cooldown. The film morphology of the as-deposited amorphous films and their crystalline counterparts was examined, and can be found in figure 12.1 in supplementary information. The amorphous films are smooth and closed films. The crystallisation of VO_2 to VO_2(B) largely retained the morphology of the original films, but induced some pinholes into the films. Crystallisation of amorphous V_2O_5 to crystalline V_2O_5 drastically changed the morphology from a smooth, closed film to a non-closed film constituted of interconnected V_2O_5 crystallites with sizes around 100 nm.

To confirm the oxidation state of the as-deposited amorphous films, and their crystallized counterparts, the binding energy of the vanadium was investigated. It is well known that the position of the V2p peaks relate to the oxidation state of the vanadium oxide [279, 288]. X-ray photo-electron spectroscopy measurements in figure 11.3 show that the as-deposited films had their vanadium oxidation in the 4+ and 5+ state for the ozone and oxygen plasma process, respectively. Crystallisation had little effect on the oxidation state of the V_2O_5 films, but shifted the vanadium peaks to slightly higher binding energy for the c-VO_2 (B), indicating a rise in oxidation state. However, the film composition matched that of VO_2, and the XRD clearly confirmed the c-VO_2 (B) state.

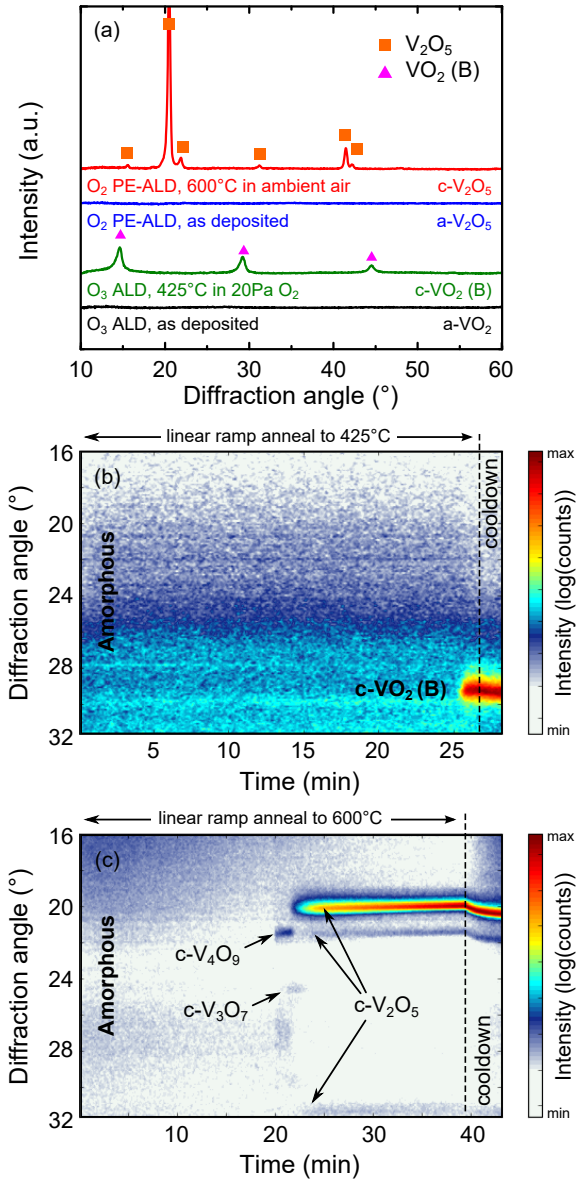

Figure 11.2: (a) XRD patterns recorded before and after the crystallisation of the films. *In-situ* XRD measurements during the crystallisation of the VO_2 (b) and V_2O_5 (c) films by controlled ramping at 0.25 °C s^{-1}.

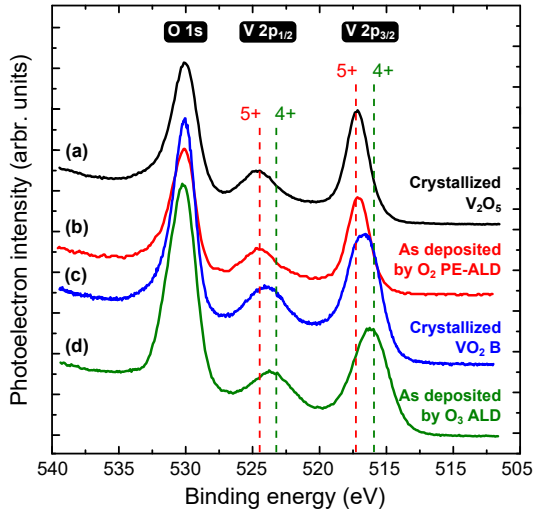

Figure 11.3: XPS O1s and V2p spectra of the amorphous (b and d) and crystallized (a and c) VO_2 and V_2O_5 films.

Electrochemical performance evaluation of amorphous and crystalline vanadium oxides

Crystalline compounds, such as the c-VO_2 (B) and c-V_2O_5 films here, are in a well-defined crystalline phase. This phase changes abruptly as the compound moves across the (lithium)-(metal oxide) phase diagram, when a critical lithium concentration enables the sudden phase transformation to another minima in the Gibbs free energy [242]. These abrupt changes in crystalline phase at certain critical lithium contents of the electrode give rise to abrupt shifts in electrochemical potential, which in turn cause distinct peaks in the cyclic voltammograms (CV, potential driven measurement), or plateaus in the charge-discharge profiles (current driven measurements, corresponding to the lithium-content in the electrode). Amorphous electrodes typically have a CV-profile without sharply defined peaks, resulting from the lack of distinct phase-transformations during the (de)lithiation of amorphous materials [243]. This is reminiscent of capacitive storage, which also happens without peaks, but does not have the same origin: capacity storage happens at an interface, while lithium storage in amorphous materials originates from bulk-storage into a solid-solution type compound without phase changes, due to the presence of only one minimum in Gibbs free energy [242], as is also the case for ω-V_2O_5, as will be explained below. While the well-defined potential

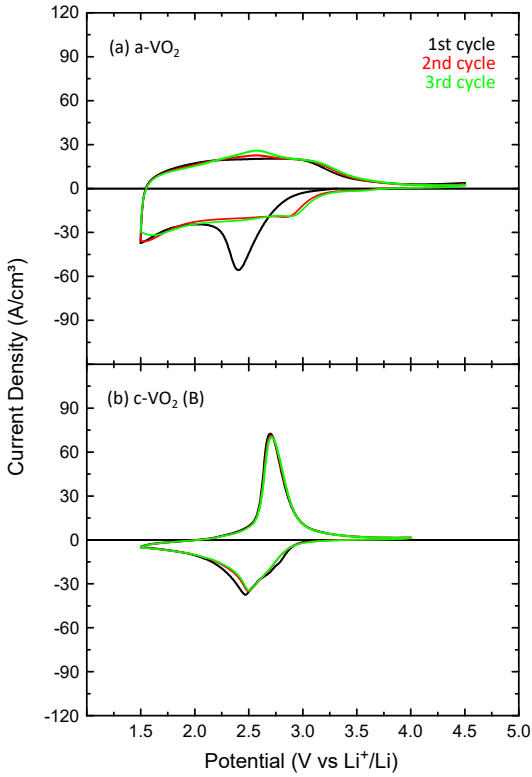

Figure 11.4: Cyclic voltammetry sweeps during the first three cycles of (a) ozone-grown a-VO_2 and (b) c-VO_2 (B), formed by crystallizing the ozone-grown VO_2 at 20 Pa oxygen partial pressure.

plateau is a critical factor for use of a battery in Wh-range applications and above (consumer electronics to EV/HEV), on-chip devices will usually require less than the 3-4V provided, and have built-on electronic conversion of the provided potential to the required specifications. This makes the well-defined plateau, found in most crystalline materials, no longer a requirement for on-chip energy storage, enabling the use of amorphous materials for these applications.

The cyclic voltammograms (CV) for the first three charge-discharge cycles of the VO_2 films are shown in figure 11.4. Indeed, the c-VO_2 (B) films display clearly defined lithium insertion and extraction peaks during the first cycle at 2.47 and 2.70 V vs Li^+/Li, respectively, in agreement with the crystalline nature of the electrode. This electrochemical behaviour is retained over the first three cycles. For the a-VO_2, that is not the case.

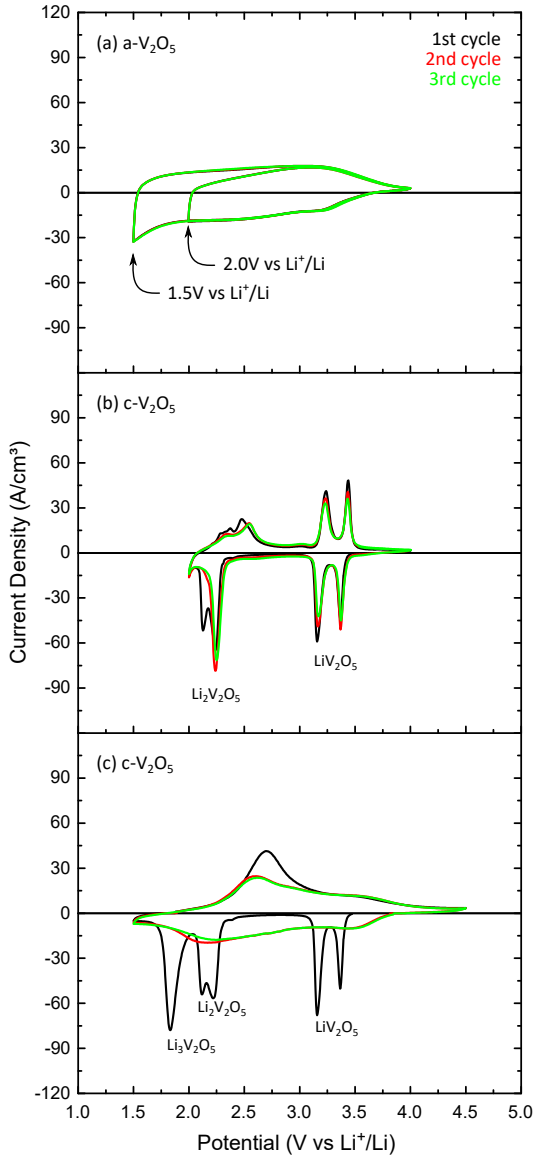

Figure 11.5: Cyclic voltammetry sweeps during the first three cycles of (a) oxygen plasma-grown a-V_2O_5 (top) and (b,c) c-V_2O_5 films in two potential ranges.

During the first lithiation (negative current range of the CV), an insertion peak is visible at 2.41 V *vs* Li^+/Li, superimposed on a more continuous current. While the peak typically corresponds to a crystalline material, no crystallinity is found on these films using XRD. This suggests some short-range order present in the a-VO_2 films in the as-deposited state. The similarity of the insertion peak to those that were found for the c-VO_2 (B) points to a similar short-range order as the latter. However, during the first delithiation (positive current range of the CV), no recurring peak is found, indicating that the initially present short-range order is converted to a film with a higher degree of disorder during the first lithiation. Only the continuous quasi potential-independent current is left, resulting in blob-like features in the CV, signifying the earlier mentioned homogeneous single-phase state of the amorphous film. Besides the change in the first cycle for a-VO_2, not much evolution is visible during the first three CV cycles of both a-VO_2 and c-VO_2 (B), indicating good initial cycling stability.

Crystalline V_2O_5 is known to have three ranges of insertion, corresponding to $x = 1, 2, 3$ in $Li_xV_2O_5$. The $x = 1$ region is known to be very stable, since the V_2O_5 lattice undergoes no significant changes, and the potential range is far above the V-dissolution boundary. $x = 2$ and $x = 3$ have higher theoretical capacities, but are less stable over charge-discharge cycles, due to the irreversible structural modifications observed for $x = 2$ and the transformation to a solid solution rather than a crystalline structure for $x = 3$ [221]. Indeed, in the cyclic voltammograms of c-V_2O_5 in figure 11.5 (middle and bottom figure), the insertion and extraction peaks decrease even over the first few cycles for insertion of two lithium into the c-V_2O_5, and disappear completely if three lithium ions are inserted into the c-V_2O_5, indicating a poor cyclability for these films. The a-V_2O_5 on the other hand (figure 11.5, top) displays excellent cyclability in the same potential range, as indicated by an almost perfect overlap of the 3 CV sweeps, regardless of the potential range. Contrary to the a-VO_2, no peaks are observed on these voltammograms, indicating no as-deposited short-range order. A second significant difference is present between the VO_2 and V_2O_5 films. Due to the higher oxidation states in the latter, electrochemical activity is observed above 3.0 V *vs* Li^+/Li. For the VO_2 films on the other hand, almost no lithiation is seen above that potential, resulting in a lower available energy of the cathode.

To investigate the obtainable capacity and the rate capability, the thin films are lithiated and delithiated at varying current densities, as shown in figure 11.6 on films of approximately the same thickness (~ 50 nm). The obtainable capacities are compared by extrapolating the obtained capacities to a C-rate of 1C, i.e. corresponding to a full charge or discharge of

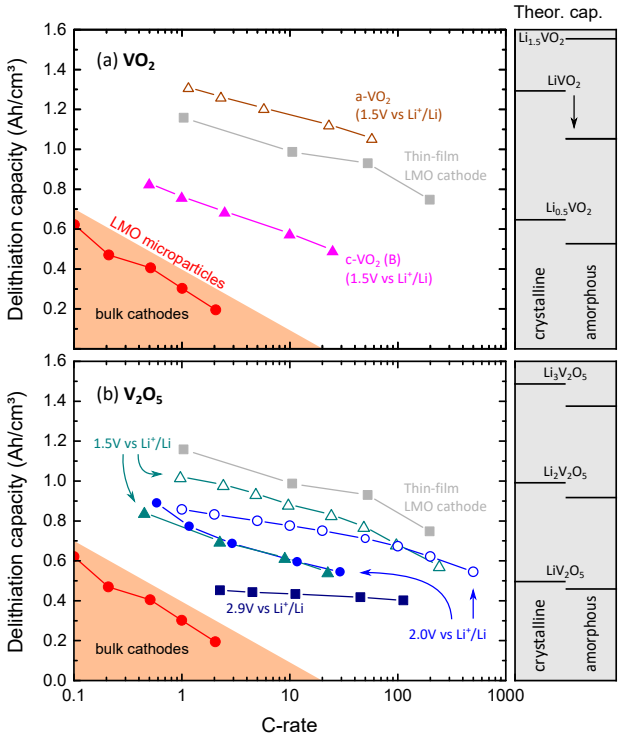

Figure 11.6: Evaluation of the capacity and capacity fading upon fast charging of the amorphous (hollow symbols) and crystalline (solid symbols) vanadium oxides: (a) VO_2 and (b) V_2O_5. Theoretical capacities (right bars) are calculated taking into account the measured effective density of the films, and are thus different for amorphous and crystalline films. Literature data for $LiMn_2O_4$ thin-film (gray squares) [158], micron-sized $LiMn_2O_4$ (red circles) [290] and commercial bulk cathodes (shaded left corner) [16] is included.

the theoretical capacity of the film in one hour. The rate capability is evaluated by extrapolating the same data to a C-rate of 100C, i.e. charging or discharging in 36 seconds, and comparing that value to the 1C value. The extrapolated capacities and kinetic drop-off from 1C to 100C are summarized in table 11.1.

Several observations can be made from these experiments. First, the c-V_2O_5 shows excellent kinetics in the 1-lithium range (2.9 V to 4.0 V *vs* Li^+/Li). However, as explained below, the capacity of this range is rather low at only 488 mA h cm^{-3}. This capacity lies below that of commercial cathode materials such as $LiCoO_2$, $LiMn_2O_4$ and $LiMn_{0.3}Ni_{0.3}Co_{0.3}O_2$, typically in the range of 550 mA h cm^{-3} to 700 mA h cm^{-3} [16]. All of the other investigated vanadium oxides here show better capacity than the 1-lithium range of c-V_2O_5, and even better than the commercial range. The downside to the high available potential is that c-V_2O_5 in the 2- and 3-lithium range and c-VO_2 (B) have poorer kinetics (close to 40 % dropoff, i.e. almost four times poorer than the 12.6 % of the crystalline V_2O_5 in the 1-lithium range). The reader should note that the 'poorer' kinetics reported here are still quite reasonable due to the thin-film nature of these electrodes. A second note that has to be made is that, even though these materials have poorer kinetics than the limited-range c-V_2O_5, all of them still have a comparable capacity to the latter at high C-rates, due to the far higher volumetric capacities available. The amorphous films on the other hand (a-VO_2 and a-V_2O_5) display both good capacity and kinetics, with the best kinetics for a-V_2O_5 in the 2.0 V to 4.0 V *vs* Li^+/Li range (only 19.4 % dropoff), and the best capacity for a-VO_2 (1393 mA h cm^{-3} at 1C, double the capacity of commercial cathodes and well above other thin-film cathodes like LMO [158]). This makes the amorphous vanadium oxides very interesting thin-film cathode candidates.

From the previous paragraph, figure 11.6 and table 11.1, it is clear that the amorphous films outperform the crystalline films on rate capbility. Typically, amorphous electrodes are reported to have much higher lithium diffusion coefficients than their crystalline counterparts [243, 245, 246]. To investigate this for the vanadium oxide films here, the lithium diffusion coefficients were measured using PITT measurements across the examined potential range [115–117]. The diffusion coefficients for the amorphous anodes are almost independent of state-of-charge in the entire potential range investigated, as shown in supplementary information (figure S4), with average diffusion coefficients of 1.4×10^{-13} cm^2 s^{-1} and 1.9×10^{-13} cm^2 s^{-1} for a-VO_2 and a-V_2O_5, respectively. The diffusion coefficients for the cyrstalline vanadium oxides are much more potential- or state-of-charge-sensitive, as was also reported in literature [316]. While

	Voltage range (V *vs* Li^+/Li)	Capacity at 1C ($A\,h\,cm^{-3}$)	Kinetic drop from 1 to 100C (%)	x in Li_xVO_y at 1C
a-VO_2	1.5-4.0	1.393	22.1	1.33
c-VO_2 (B)	1.5-4.0	0.806	44.9	0.62
a-V_2O_5	2.0-4.0	0.884	19.4	0.94
	1.5-4.0	1.091	28.2	1.18
c-V_2O_5	2.9-4.0	0.488	12.6	0.49
	2.0-4.0	0.820	39.1	0.82
	1.5-4.0	0.810	39.3	0.82

Table 11.1: Summary of the volumetric capacity and kinetic performance of the vanadium oxide thin films.

the crystalline films have higher diffusion coefficients just below the measured OCP ($7 \times 10^{-13}\,cm^2\,s^{-1}$ and $1 \times 10^{-12}\,cm^2\,s^{-1}$ for c-V_2O_5 and c-VO_2(B), respectively), the diffusion coefficient drops two orders of magnitude when the films are lithiated, with minima at $8 \times 10^{-15}\,cm^2\,s^{-1}$ and $6 \times 10^{-15}\,cm^2\,s^{-1}$ for c-V_2O_5 and c-VO_2(B), respectively. These low diffusion coefficients at high state-of-charge can explain the poorer kinetics observed for the crystalline vanadium oxides, compared to their amorphous counterparts.

Finally, the cyclability was examined by charging and discharging the films for 50 times at a current density corresponding to 2C. The delithiaton capacity of the films is shown in figure 11.7, and the results summarized in table 11.2. Again, the crystalline V_2O_5 performs excellent in the 1 lithium range, but at a lower capacity than all other vanadium oxides. However, deeper charging of the c-V_2O_5 has a detrimental effect on the cyclability, as the capacity retention drops to only 68.2 % or even 33.5 % for charging two or three lithium into the c-V_2O_5 respectively. This is caused by irreversible lattice changes upon overcharging and vanadium dissolution upon deep discharging of the crystalline V_2O_5 close to 1.5 V *vs* Li^+/Li, as can be seen from the additional inflection point below 1.8 V *vs* Li^+/Li on the potential profiles in figure 12.2 (a) in the supplementary information of this paper. Indeed, if the amorphous vanadium oxide is charged to the same potential, vanadium dissolution is also observed, as is visible from the rapid loss of delithiation capacity in figure 11.7 (b). Observing the potential profile in figure 12.2 (c), an inflection point can be seen below 1.8 V *vs* Li^+/Li (visible from the decrease of the slope of the first lithiations), indicating the vanadium dissolution, observed in the same potential region as the vanadium dissolution on c-V_2O_5. This conclusion is further supported by

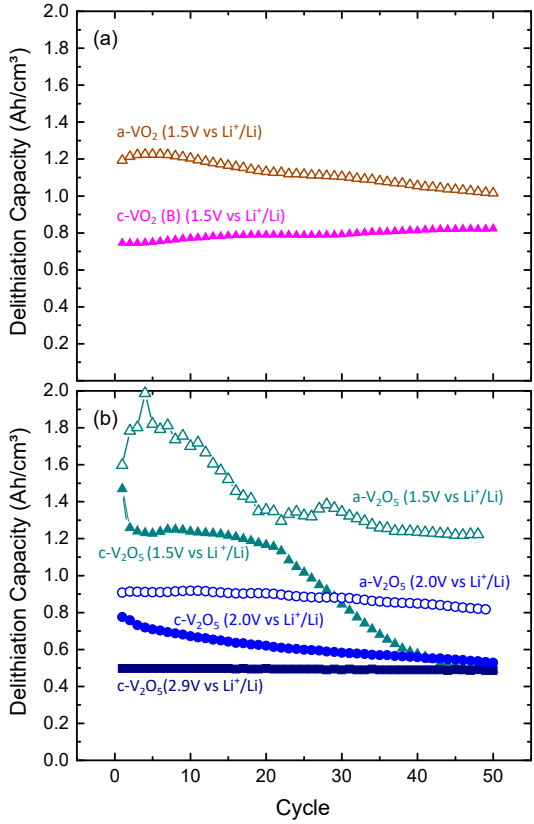

Figure 11.7: Cyclability of the examined amorphous (hollow symbols) and crystalline (solid symbols) vanadium oxides: (a) VO_2 and (b) V_2O_5. Cyclability experiments were performed at current densities corresponding to 2C for the respective films.

the uncontrolled electrolyte-electrode interface reaction observed above 3.5 V *vs* Li^+/Li, indicating a destabilized interface region related to vanadium dissolution. This causes an apparent capacity increase during the first cycles, but should be disregarded, as this capacity is not related to lithium storage in the films. However, if the a-V_2O_5 is kept above 1.8 V vs Li^+/Li, no vanadium dissolution occurs (figure 12.2(b)), and a fairly stable capacity is observed (figure 11.7(b). Taking into account the better kinetics and slightly higher capacity, the a-V_2O_5 in the 2.0 V to 4.0 V *vs* Li^+/Li range can be considered the best V_2O_5 candidate thin film electrode. The a-VO_2, having the highest capacity and kinetics similar to that of a-V_2O_5, displays a similar capacity fading (figure 12.3(a)), also related to the same

	Voltage range (V *vs* Li^+/Li)	Delithiation capacity ($A\,h\,cm^{-3}$) *Initial - Final*	Retention after 50 cycles (%)
a-VO_2	1.5-4.0	1.19 - 1.02	85.2
c-VO_2 (B)	1.5-4.0	0.75 - 0.82	110.4
a-V_2O_5	2.0-4.0	0.91 - 0.82	90.0
	1.5-4.0	1.60 - 1.22	76.3
c-V_2O_5	2.9-4.0	0.50 - 0.49	98.0
	2.0-4.0	0.78 - 0.53	68.2
	1.5-4.0	1.47 - 0.49	33.5

Table 11.2: Summary of the results from the cyclability evaluation of the vanadium oxide thin films (figure 11.7).

vanadium dissolution close to 1.5 V *vs* Li^+/Li. Further investigation into the region between 1.5 and 2.0 V *vs* Li^+/Li region could find an ideal optimum trade-off between capacity and cyclability for the amorphous V_2O_5 films. Since most capacity fading is likely related to vanadium dissolution, a protective coating could also mitigate the capacity fading problem while retaining the high capacity and good kinetics related to the amorphous vanadium oxide, as was demonstrated recently by Xie et al [310]. Remarkably, c-VO_2 (B) does not suffer from the vanadium dissolution issue, as is evident from the stable storage capacity and the lack of an electrochemical dissolution signal of vanadium dissolution at low potentials. Figure 12.3 (b) shows a clean potential profile, displaying only a single inflection point at 2.5 V *vs* Li^+/Li. The capacity even slightly increases over time. This can be explained by a kinetics mechanism. The c-VO_2 (B) has the poorest kinetics of all investigated vanadium oxides, as shown in table 11.1. The cyclability experiments in figure 11.7 are performed at a C-rate of 2C. This has as a consequence that not all VO_2 in the c-VO_2 (B) films can be reached during the first cycles. However, upon cycling the iR-drop decreases: the (quasi)-plateaus corresponding to the insertion and extraction of lithium in c-VO_2 (B) are much closer together for the 50th cycle than for the 2nd cycle (fig. 12.3 (b)). This implies that by cycling the c-VO_2 (B) its kinetics are enhanced, and an increasingly larger fraction of the film becomes available for storing lithium. This kinetic enhancement upon cycling gives the impression that the capacity rises. The c-VO_2 (B) is the most stable vanadium oxide, not in the least due to the absence of vanadium dissolution.

Figure 11.8 provides a combined summary of the electrochemical properties of the investigated vanadium oxides. Most of the vanadium oxides show some degree of capacity fading. However, since most of the capacity fading is related to vanadium dissolution close to 1.5 V *vs* Li^+/Li, this issue could be overcome by (a) a careful choice of the lower potential boundary or (b) a protective coating to mitigate this dissolution. The amorphous layers always have a higher capacity than the crystalline counterparts, with a-VO_2 displaying the highest capacity at 1393 A h cm^{-3}. The a-V_2O_5 films have a capacity close to that (1091 A h cm^{-3}) but display electrochemical activity above 3.5 V *vs* Li^+/Li, making the energy of both amorphous films almost equal. The amorphous films do not only have high capacity, but also excellent charge-discharge kinetics, making them excellent candidates for high energy and high power applications. Finally, the c-VO_2 (B) films have a capacity comparable to V_2O_5, but a much better cycling stability due to the lack of vanadium dissolution and the very stable 2.5 V *vs* Li^+/Li potential window. Figure 12.5 shows the absolute volumetric capacities upon cycling (a) and high-rate charge-discharing (b). Here, it can be seen that, although c-VO_2 (B) has a relatively low initial capacity compared to the other tested films, the far better capacity retention leads to comparable capacities after 50 cycles. While kinetic capacity retention is best for the crystalline V_2O_5 in the 1-lithium range, all other tested films outperform it at 100C, with the highest capacity retention for a-VO_2 due to the high initial capacity and excellent retention.

The real strength of atomic layer deposition for LIB electrodes emerges when thin films are able to be coated conformally on complex 3D substrates. This enhances the energy per footprint area by a factor of surface enhancement, while maintaining the excellent thin-film kinetics compared to the same energy electrodes in thicker films. To test this, vanadium oxide films were coated on silicon micro pillar substrates. To obtain a conformal coating in these structures, higher precursor exposure were required to allow precursors to penetrate into the 50 µm-deep pillar structures. This was obtained by closing the valve to the turbo molecular pump, essentially raising the precursor pulse pressure to 1 mbar. Due to the very sensitive nature of the amorphous V_2O_5 PE-ALD process to the plasma exposure, we were not able to coat amorphous V_2O_5 in the pillars. Crystallisation was always found, caused by the highly reactive nature of the plasma step. Alternative set-ups, using a capacitively coupled plasma applied directly to the sample, rather than an inductively coupled plasma remote from the sample, could be envisioned to attempt the conformal deposition of amorphous V_2O_5 in high aspect-ratio structures, but this goes beyond the scope of this report.

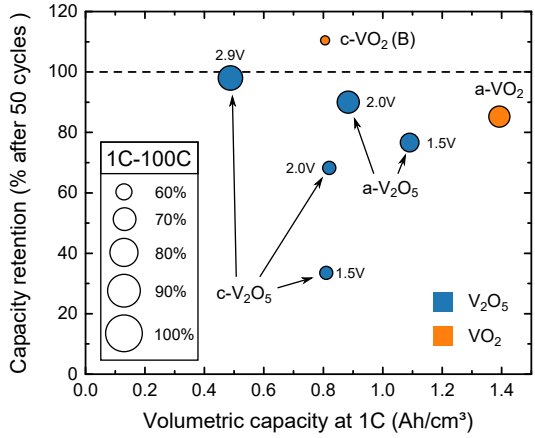

Figure 11.8: Summary of the electrochemical performance properties of the examined thin-film vanadium oxide cathodes. The size of the circles indicates the power capability according to the scale displayed in the inset, representing the kinetic capacity retention from 1C to 100C.

40 nm ALD films of a-VO_2 were deposited on the silicon micropillar structures. A 40 nm film of c-V_2O_5 and c-VO_2 (B) was obtained by depositing an a-VO_2 film and crystallizing the films using the same conditions as for the planar films: to c-V_2O_5 in air, and to c-VO_2 (B) in a 20 Pa ambient of oxygen. Cross-sectional electron microscopy was used to visualize the silicon micropillar forest, as shown in figure 11.9(a). Using EDX line-scans along different depths within the pillar structure, the conformal nature of the depositions was verified. Figure 11.9(b) shows the crystallized c-V_2O_5 film on a bare silicon micro pillar substrate, and figure 11.9(c) shows the a-VO_2 film on a substrate already covered with the aforementioned current collector layers. In 11.9(b) and (c), the V-peaks around 500 keV and 550 keV are almost independent of the position on the pillars, indicative of a conformal deposition along the pillars. The same can be said for the current collector related peaks in figure 11.9(c), indicating that the latter is also conformally coated.

The electrochemical activity and performance of the surface-enhanced electrodes was characterised. Cyclic voltammetry was performed at a slow scan rate (1 mV s^{-1}) to examine the electrochemical activity. The potential range for the a-VO_2 and c-VO_2 (B) on pillars was chosen the same as for the planar electrode, i.e. 1.5 V to 4.0 V vs Li^+/Li. For the c-V_2O_5 on pillars, the reversible potential range was chosen, i.e. 2.9 V to 3.8 V vs Li^+/Li, due to the poor kinetics and cycle life observed for the further lithiation of

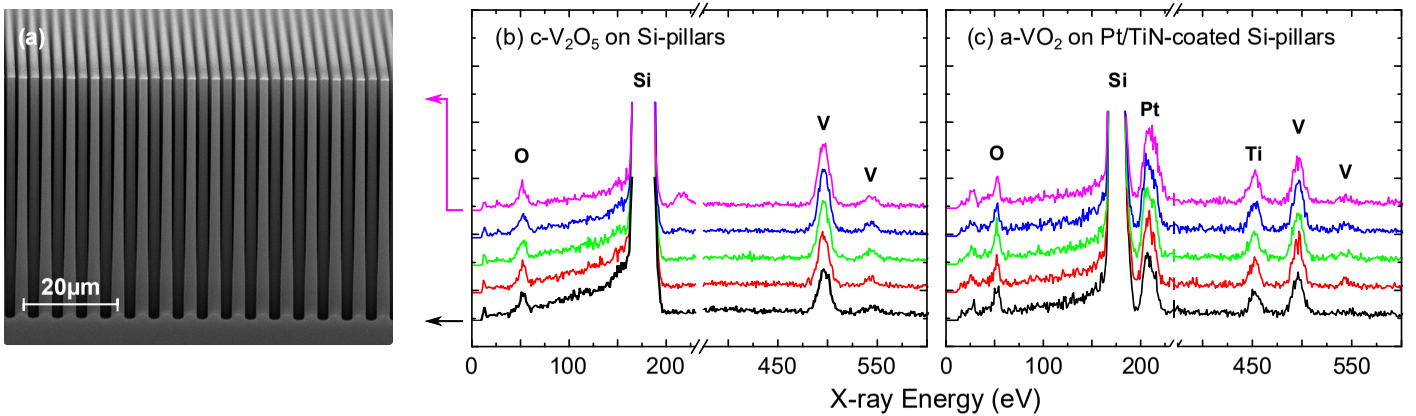

Figure 11.9: (a) Cross-sectional SEM image of the silicon micro pillar substrate used. EDX profiles resulting from line scans at equidistant lines between the top and bottom of 40 nm c-V_2O_5 film deposited on the bare Si micro pillar substrate, resulting from crystallizing a deposited a-VO_2 film (b) and a 40 nm a-VO_2 film deposited on the current collector-coated Si micro pillar substrate (c). The current collector is responsible for the presence of titanium and platinum characteristic X-rays.

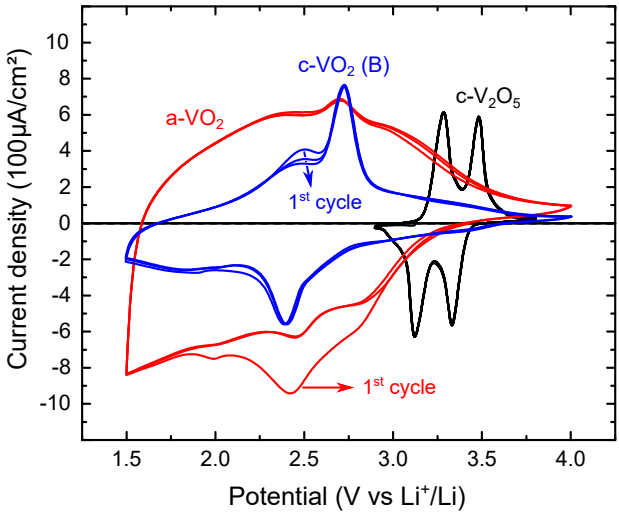

Figure 11.10: Cyclic voltammograms of 40 nm c-V_2O_5 (black), a-VO_2 (red) and c-VO_2 (B) (blue) films, coated on the silicon micro pillar substrates. The potential was varied at 1 mV s^{-1}.

c-V_2O_5. The cyclic voltammograms in figure 11.10 show a clear lithium insertion and extraction behaviour for the surface-enhanced electrodes.

Finally, the capacity per footprint area and rate capability of the surface-enhanced electrodes was examined, and compared to 40 nm films of a-VO_2, c-VO_2 (B) and c-V_2O_5 on planar substrates. In theory, the kinetics of the electrodes on the planar substrates should translate into the same kinetics on the surface-enhanced electrodes, since the current density and lithium diffusion is the same for both cases. The capacity per footprint area should be enhanced by a factor of surface enhancement of the substrate. The silicon micro pillar substrate used here is made by etching silicon pillars in a silicon substrate, at a pillar width and pillar-to-pillar spacing of 2 µm and a pillar height of 50 µm. This results in a surface enhancement of 20.6. The C-rates of the surface-enhanced electrodes were calculated using the theoretical capacity of a 40 nm film, and the theoretical surface enhancement factor. Remarkably, the Peukert plot in figure 11.11 shows capacity enhancement factors that are consistently higher than 20.6. This could be caused by thicker films deposited using the process conditions required for the conformal coating of these micro pillar structures. Nevertheless, the films are coated conformally, as is clear from figure 11.9. As figure 11.11 shows, the excellent thin-film kinetics observed for the planar electrodes is maintained when these are coated on the micro pillars,

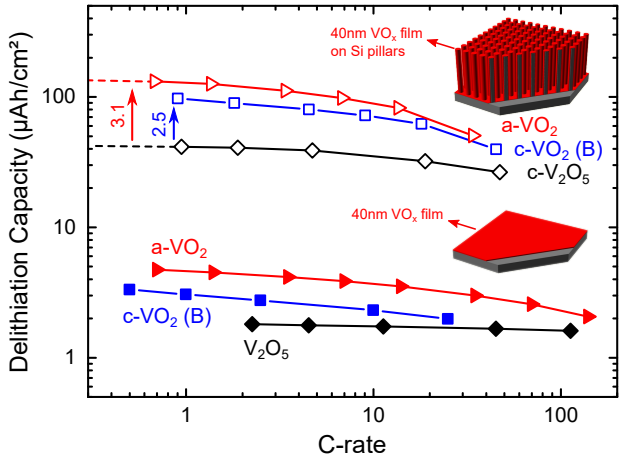

Figure 11.11: Rate capability for planar and micropillar electrodes of 40 nm a-VO_2 (red), c-VO_2 (B) (blue) and c-V_2O_5 (black).

demonstrating the power of a conformal deposition technique in combination with micro- or nanostructuring of the electrodes. At high C-rates, the kinetics are not maintained any longer. This is most likely caused by the 20 times higher currents required to cycle the surface-enhanced electrodes at these C-rates, and the thinner nature of the current collectors (20 nm TiN and 5 nm Pt) compared to the planar case (60 nm TiN and 80 nm Pt), causing an iR drop which is more severe. Finally, we see that the surface enhanced a-VO_2 is able to deliver a capacity above 130 µA h cm^{-2}, 3.1 times higher than the same film thickness of c-V_2O_5 on the micropillars. The c-VO_2 (B) film also delivers almost 100 µA h cm^{-2}, beating the c-V_2O_5 with a factor of 2.5. From a device engineering point of view, this implies that a 3.1 or 2.5 times thinner film can be used to obtain the same capacity, or the same film thickness in a lower aspect ratio 3D structure. The latter not only implied a lower production cost for the 3D structures, but also lower precursor cost and higher ease of deposition from a deposition point of view [317, 318]. This demonstrates that, even though the cyclability of amorphous VO_2 or the kinetics of crystalline VO_2 (B) are not as excellent as is the case for crystalline V_2O_5, a significant amount of capacity can be gained through the use of VO_2, especially for amorphous VO_2. This illustrates that amorphous ALD electrodes are very promising for 3D thin film lithium ion batteries.

CONCLUSIONS

Thin film vanadium oxide cathodes were synthesized and characterised. a-VO_2 was deposited using a reported TEMAV and ozone process. c-VO_2 (B) was obtained upon careful annealing in a well-controlled ambient, which was monitored using *in-situ* XRD. a-V_2O_5 was deposited by low-temperature (85 °C) and PE-ALD using TEMAV and oxygen plasma (200W), and crystalline V_2O_5 films were obtained by annealing these films in ambient air. The oxidation state of the vanadium in the amorphous films was examined using XPS, and was confirmed to be 4+ and 5+ for the a-VO_2 and V_2O_5 films, respectively. The four thin-film vanadium oxides were characterised electrochemically as lithium-ion cathodes. It was found that all other vanadium oxides outperform crystalline V_2O_5, even though the latter is the most investigated vanadium oxide cathode. Amorphous vanadium oxides show excellent kinetics, which is likely related to a higher diffusion coefficient in those films, but also good capacity retention and volumetric capacities which are close to double that of commercial cathode materials. c-VO_2 (B) shows a lower capacity but remarkably does not suffer from vanadium dissolution issues, making it an extremely stable 2.5 V *vs* Li^+/Li cathode. We demonstrate the conformal coating of a-VO_2, c-VO_2 (B) and c-V_2O_5 on silicon micropillar substrates to enhance the capacity per footprint area. The excellent thin-film kinetics found on the planar substrates is maintained, while the capacity per footprint area is significantly enhanced. A micropillar electrode of 40 nm of a-VO_2 or c-VO_2 (B) is able to deliver a capacity above 130 µA h cm^{-2} or 100 µA h cm^{-2} respectively, which is 3.1 or 2.5 times higher than the same film thickness of c-V_2O_5 on the micropillars. These results shed new light on the use of vanadium oxides in thin-film batteries, and highlight the potential of the often-forgotten class of amorphous cathodes as high-power and high-energy electrode.

12

SUPPLEMENTARY TO PAPER IV

SURFACE MORPHOLOGY OF THE VANADIUM OXIDES FILMS

The surface morphology of the vanadium oxide films is evaluated using scanning electron microscopy. Figure 12.1 shows the surface under a 100000x magnification. The amorphous films are closed and appear smooth. While a-VO_2 still displays some surface features, the a-V_2O_5 is completely featureless. The SEM was focussed on surface contaminations near the image area to ensure a good focus, but still no features could be distinguished. The crystalline VO_2(B) film shows a very similar morphology to its amorphous counterpart, although some pinholes are present in the films. The morphology of c-V_2O_5 on the other hand is clearly different from that of amorphous a-V_2O_5: the film has transformed into interconnected V_2O_5 flakes with crystallite sizes around 100 nm.

GALVANOSTATIC CHARGE-DISCHARGING

The paper discusses the cyclability of the amorphous (a-) and crystalline (c-) forms of thin films VO_2 and V_2O_5. To better understand the capacity evolution, the potential profiles during charging and discharging of the films are shown in figures 12.2 (V_2O_5) and 12.3 (VO_2) for the initial cycles (1-2), steady state cycles (5,10) and the last cycle (50). The theoretical capacities for each respective film is denoted on the graphs.

The reader can note that the capacities here are expressed volumetrically ($A\,h\,cm^{-3}$), rather than gravimetrically ($A\,h\,g^{-1}$), as is customary in battery research. This notation stems from the fact that thin-film electrodes are discussed. In this paper specifically, 3D thin-film lithium-ion batteries are envisioned, with applications such as on-chip energy storage. For those applications, the mass of the electrode is a less critical parameter than the volume and the footprint area. Hence, all capacities are volumetric ($A\,h\,cm^{-3}$) or normalized on footprint area ($A\,h\,cm^{-2}$). However, to allow the reader to compare these results to values reported gravimetri-

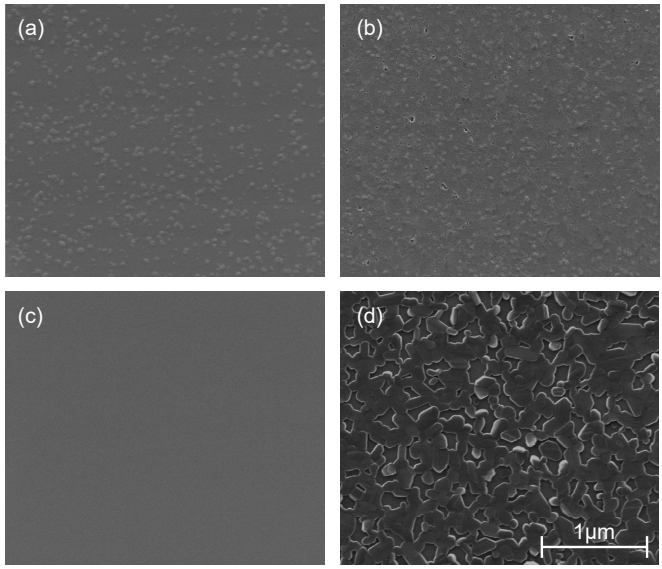

Figure 12.1: Surface morphology at a 100000x magnification of 30 nm amorphous VO_2 (a) and amorphous V_2O_5 (c) films, and their crystallized counterparts; i.e. c-VO_2 (B) (b) and c-V_2O_5 (d).

cally, the density of these compounds can be used as a conversion factor. Table 12.1 summarizes the measured and reported densities that can be utilized to perform a conversion.

POTENTIOSTATIC INTERMITTENT TITRATION

To study the lithium diffusion in the vanadium oxide films, the widely used potentiostatic intermittent titration was used [115–117]. By applying small potential steps below the equilibrium potential, information can be obtained from the decay of current over time. In the initial stage of re-equilibration ($t \ll L^2/D$, with D the diffusion coefficient and L the characteristic length of the electrode, which was chosen as the film thickness here) the diffusion coefficient can be obtained from the linearity between current and the square root of time, and for longer equalisation times ($t \gg L^2/D$) from the linearity between ln(I(t)) and time, as discussed by Wen *et al.* [115]. Here, we use the latter method. 50 mV potential steps are applied, and the current is measured until one of three cut-offs occurs: the measuring time has exceeded 1800 seconds, the current has decreased to 2 % of its initial value or has dropped below 1×10^{-7} nA. The linear

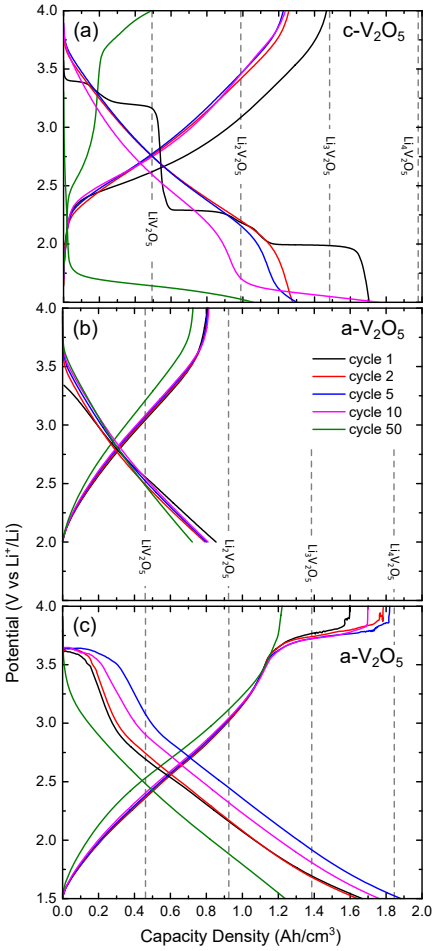

Figure 12.2: Potential profiles of the crystalline V_2O_5 (a) and a-V_2O_5 (b and c) during the cyclability experiments.

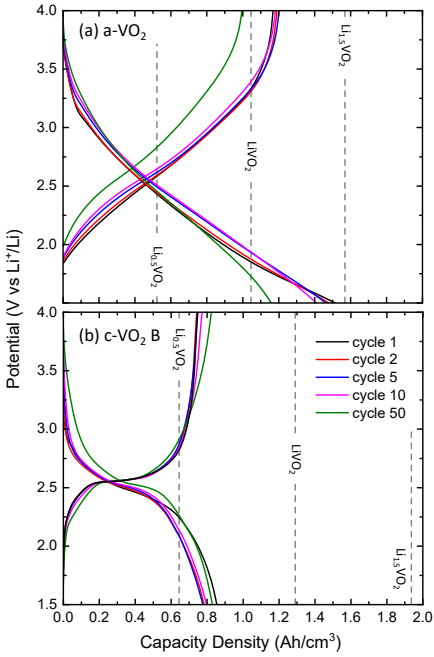

Figure 12.3: Potential profiles of the a-VO_2 (a) and c-VO_2 (B) (b) during the cyclability experiments.

Phase	Deposition temperature	Density ($g\,cm^{-3}$)
a-VO_2	150 °C	3.24
c-VO_2(B)	150 °C + anneal	4.00
a-V_2O_5	85 °C	3.05
c-V_2O_5	85 °C + anneal	3.35

Table 12.1: Densities of the amorphous and crystalline films. The densities were measured b XRR for the amorphous films, and are reprinted from the crystalligrapic datasheets for the crystalline films (VO_2(B) 01-081-2392, V_2O_5 00-041-1426).

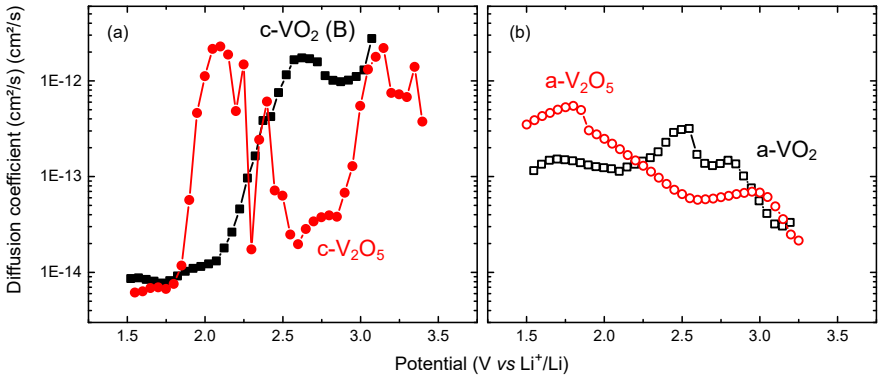

Figure 12.4: Diffusion coefficients as obtained from potentiostatic intermittent titration for the (a) crystalline and (b) amorphous vanadium oxides.

region of the relation between the logarithm of the current and time was evaluated, and the slope was fitted using linear regression. The diffusion coefficient for these conditions were then obtained from

$$D = \frac{dln(I(t))}{dt}\frac{4L^2}{\pi^2} \tag{12.1}$$

and L was chosen to the film thickness of the measured films. Figure 12.4 shows the obtained diffusion coefficients, which are discussed in the manuscript.

SUMMARY OF THE ELECTROCHEMICAL PROPERTIES OF THE FILMS

Figure 11.8 the relative performance of the different vanadium oxide films. However, the information about the actual capacity is lost visually by summarizing all these properties into a single figure. Figure 12.5 summarizes

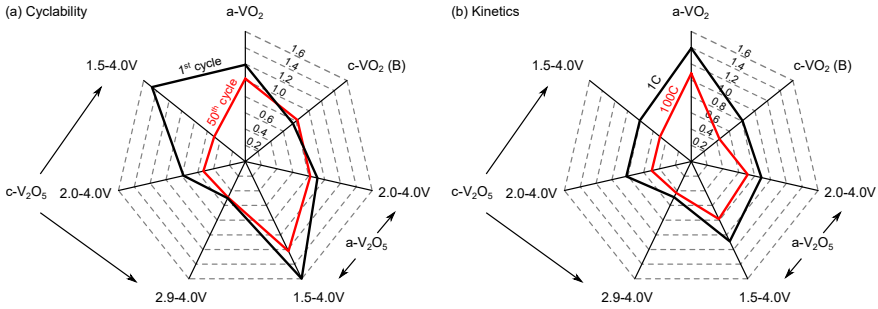

Figure 12.5: Summary of the absolute values of the volumetric (delithiation) capacity ($A\,h\,cm^{-3}$) from the (a) cyclability and (b) kinetics experiments performed on the thin-film vanadium oxide cathodes.

the volumetric capacities of all films for comparison, before and after the cyclability experiment (figure 12.5(a)) and the capacity evolution from 1C-100C (figure 12.5(b)).

Part IV

INTERFACE MODIFICATION IN LITHIUM-ION BATTERIES

Great things are done by a series of small things brought together.
– Vincent Van Gogh

13

ATOMIC LAYER DEPOSITION AND THE LITHIUM-ION BATTERY INTERFACES

In this chapter, the role of ALD-deposited thin films is examined as interface modifier for lithium-ion battery electrodes. First, the issues related to electrode-electrolyte interfaces are briefly discussed. Next, a literature overview of ALD surface modifiers for lithium-ion batteries is presented. Finally, the work done in the context of this PhD thesis is briefly summarized, and presented in the form of two submitted papers: paper V, which discusses the role of ALD Al_2O_3 and ALD TiO_2 coatings on two model thin-film electrodes, and paper VI in which the role of an ALD TiO_2 coating on nanostructured electrodes composed of ALD V_2O_5 on a carbon nanosheet scaffold is examined.

13.1 INTRODUCTION

In section 1.4 of the introduction chapter, the different application areas for atomic layer deposition in the lithium-ion battery were introduced. Part iii discussed ALD for electrodes, more specifically vanadium-based and manganese-based lithium-ion cathodes and anodes. ALD is very suited when nano-structured electrodes are envisioned. Three main concepts have been proposed for nanostructured electrodes in lithium-ion batteries [79]:

- **Nanoparticle-based electrodes**: common electrodes are mostly comprised of μm-sized particles of active material. The particle dimensions can be reduced to accommodate greater lithium ion diffusion into the electrodes, enabled by shortened diffusion lengths and greater electrode-electrolyte contact area.
- **3D-structured electrodes** are especially engineered for short diffusion lengths. Rather than maintaining the particle-based electrode structure, electrodes are composed of specifically designed 3D architectures that allow for easy transport of the electrons and the ions.

The nanostructuring of these electrodes arises from a structured scaffold, such as anodised aluminium oxide (AAO) or the silicon micropillars used in part iii of this thesis. The 3D-structuring can also arise from a 3D-structured current collector scaffold, such as metal nanowires, carbon nanosheets (CNS) or carbon nanotubes (CNTs) [294].

- **3D all-solid-state microbatteries** come into view when scaling energy storage to small devices, as packaging methods for liquid electrolytes do not scale down well. The challenge here is to achieve high energy densities for very small sizes. They can be considered as either a solid-state version of the above 3D-structured battery, or as a 3D version of the all-solid-state thin-film microbattery.

In part iii, planar thin-film electrodes were developed and extended to 3D-structured electrodes on a passive scaffold, i.e. silicon micropillars, where a thin metal film provided the current collection. Unfortunately, the use of ALD for 3D-structured electrodes is limited by the slow growth of films. Only on very high aspect ratio structures, where no other deposition techniques can conformally deposit layers, the use of ALD for the electrodes can be justified, but the cost of the electrode will be very high.

However, the shift towards nano-structured electrodes highlights another field of application for atomic layer deposition in lithium-ion batteries: interface modification. Even without nanostructured electrodes, the interfaces in a lithium-ion battery are already very important. A great deal of the ageing mechanisms of the lithium-ion battery are associated with interface- or surface-related effects both at the anode and at the cathode [319]. For batteries with nanostructured components, the interface-to-bulk fraction becomes increasingly larger with the degree of downsizing of the components. Electrode performance can be typically enhanced by a larger electrolyte-electrode contact area (faster lithium ion injection into the electrode), downsizing of the electrode particles or films (shorter diffusion paths for lithium ions, short electronic pathways in the electrode) and a larger electrode-current collector contact (better current collection). However, since ageing mechanisms are often also associated with the surface area, these are also amplified.

13.2 AGEING OF LITHIUM-ION BATTERIES

Today, more than 25 years after the commercialisation of the first lithium-ion battery, counteracting of battery ageing is still one of the holy grails of battery research. Stabilizing a battery for 100 to 1000 cycles has been

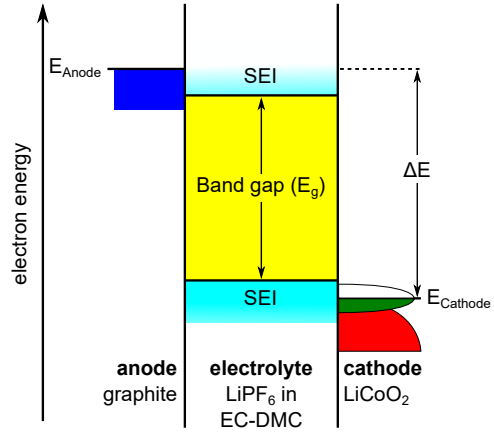

Figure 13.1: Electronic band diagram of a graphite and $LiCoO_2$ Li-ion battery, illustrating the electronic stabilisation effect of the SEI layer. This stabilisation is paramount when the E_{anode} or $E_{cathode}$ energy levels lie above or below the electrolyte band gap, respectively. Figure adapted from Julien *et al.* [327].

demonstrated extensively, but to access the next orders of magnitude (e.g. 10 000 cycles to 100 000 cycles) an extremely stable chemistry is paramount. To obtain this performance, an excellent understanding of battery ageing mechanisms is crucial, as is evident from the several reviews that have been published over the last decade [319–326]. Several ageing mechanisms are related to structural or morphological changes in the electrodes, such as irreversible phase changes or volume changes, but the true devil lives at the interfaces.

13.2.1 *Anode stability and the solid electrolyte interphase*

Lithium-ion battery anodes can be classified into low- and high-volume change anodes. The low-volume change anodes such as carbonaceous compounds have been heavily investigated, and graphite is still mainly used in lithium-ion batteries today. Ageing of these electrodes is mostly related to the low electrode potential at which they operate. Graphite has an average electrode potential below 0.5 V *vs* Li^+/Li, while reductive solvent decomposition typically takes place in the 0.4-0.9V *vs* Li^+/Li potential window [18]. This reductive solvent decomposition can be readily understood from the band diagram in figure 13.1: the low electrode potential corresponds to a high fermi level energy (or electron electrochemical potential), allowing electron flow from the electrode to the electrolyte. This initiates reductive solvent decomposition, forming an SEI on the anode

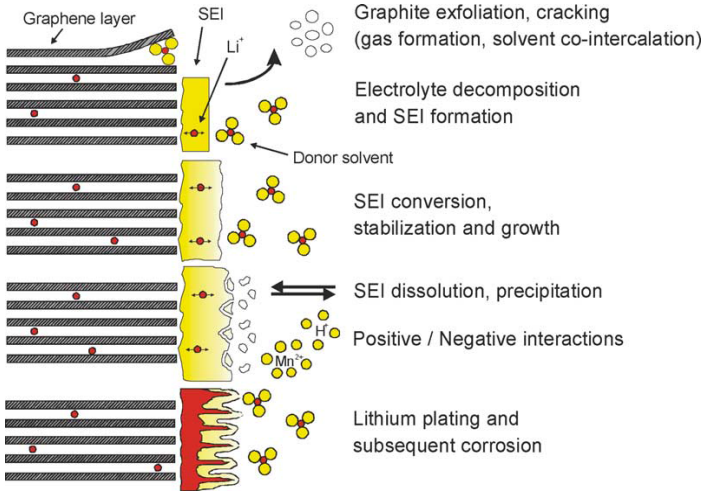

Figure 13.2: Schematic representation of the ageing phenomena associated with graphite and the solid electrolyte interphase. Reproduced from Vetter *et al.* [319].

which imposes an energy barrier at the interface, preventing further electron flow. Similarily, a decomposition film is also formed on the cathode if the electrode potential lies outside of the stability window of the electrolyte [328]. This decomposition can be considered both advantageous and disadvantageous. Primarily, the solid electrolyte interphase (SEI) that is formed during the first cycle(s) acts as a 'protective coating' during the remainder of the battery lifetime, as it is almost impenetrable for both electrons and electrolyte components, preventing further reductive decomposition and stabilizing the anode-electrolyte interface [329], as illustrated in figure 13.1. However, the beneficial SEI layer suffers from several pitfalls, as shown schematically in figure 13.2:

- Lithium ions are irreversibly consumed when the SEI is formed.
- SEI formation is accompanied by release of gaseous electrolyte decomposition products.
- The SEI layer is not a perfect solid electrolyte, as the transference number for lithium ions is not unity, i.e. some current is still carried by other charges such as electrons.
- The SEI layers are not thermally stable. At elevated temperatures, SEI degradation takes place, which can in turn give rise to restructuring or re-precipitation of dissolved SEI products.

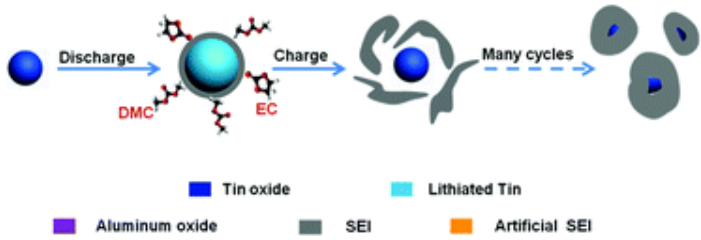

Figure 13.3: Schematic representation showing SEI formation on SnO_2 particles upon cycling. Figure adapted from Wang *et al.* [330].

- Solvents or impurities can also still be transported through the electrolyte. Thus, the SEI layer does not completely stabilize the interface, as electrolyte decomposition is still ongoing throughout the entire anode lifetime.

High volume change anodes typically face the same issues. Silicon for example has an electrode potential that also lies outside of the stability window of the electrolyte. However, the substantial morphological strain associated with the high volume changes (up to 320 % for silicon) causes additional impedance-increasing and capacity-fading effects, such as cracking, delamination and electrode-current collector contact loss [331, 332]. Furthermore, particle swelling causes the formed SEI layers to open up, and the freshly exposed surface caused by this phenomenon and the particle pulverisation can promote further irreversible capacity loss by re-initiated SEI formation, as shown in figure 13.3.

13.2.2 *The complex nature of ageing at the cathode*

As is clear from the previous section, ageing of the anode and the formation of the SEI layer have an unmistakable influence on the battery performance. However, the performance and cycle life are still mainly determined by the cathode material. Moving from the expensive $LiCoO_2$ cathode to alternatives such as $LiNiO_2$ and $LiMn_2O_4$ is hindered by the rapid deterioration of cathode performance for those compound. Understanding the ageing mechanisms in novel cathode materials is thus of paramount importance. Here, some concepts will be introduced, but the full extent of ageing mechanisms is not yet fully understood, and is still the topic of active investigation.

Figure 13.4 provides an overview of the cathode-related phenomena influencing the long-term performance of lithium-ion batteries. In general,

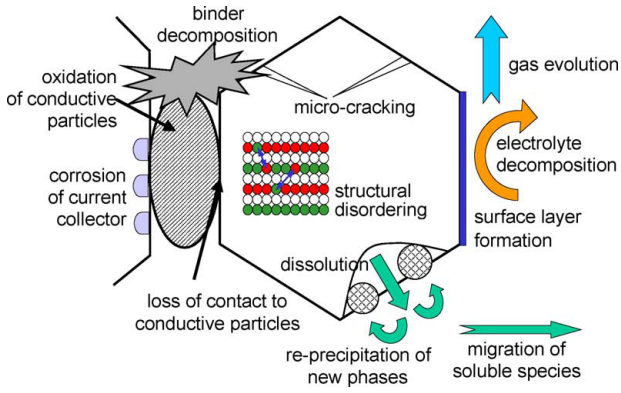

Figure 13.4: Schematic overview of the ageing phenomena for lithium-ion battery metal oxide cathodes. Reproduced from Vetter *et al.* [319].

capacity fading and impedance rising in cathode materials can be ascribed to two main classes of phenomena; i.e.

- **Structural changes** during cycling such as conductive agent contact loss and particle cracking are mostly related to volume changes at different degrees of lithiation. Structural disordering within the bulk of the electrode particles is an inherent compound property.
- **Chemical decomposition** and **chemical dissolution** occurs both at the cathode interface (electrolyte decomposition, SEI formation, metal dissolution) and at the surface of the non-active components (binder decomposition, corrosion of the current collector, oxidation of conductive particles). The dissolution of soluble species gives rise to additional unwanted side reactions, as these can precipitate on the cathode particles to form new (inactive) phases, or migrate towards the anode. Metal deposition at the anode results in severe side reactions, such as lithium plating and accelerated solvent decomposition reactions.

While structural changes are material-specific and mostly related to bulk phenomena, the latter class of chemical decomposition and dissolution reactions primarily occurs at the interfaces with the liquid electrolyte. To accommodate long-term stability, interface stabilisation is paramount, both at the cathode and anode interfaces.

The occurence of ageing phenomena related to the interfaces in lithium-ion batteries can be mediated by clever interface engineering, which has been the topic of many studies over the past decades [45, 46, 50, 327, 333].

The decoration of the surface with many coatings has been studied. Carbon is the focus of many studies due to its excellent electronic properties, which not only enables the alleviation of ageing effects, but also betters the performance of the battery materials. $LiFePO_4$ (LFP), for example, has a lower electrode potential, corresponding to energy levels within the band gap of most electrolytes, which eludes electrolyte oxidation on this compound. However, the specific crystal structure of olivine LFP in essence makes it an electronic insulator. Highly electronically conductive coatings are needed to establish an electronic network throughout the LFP-based cathodes. Hence, LFP is almost never used without the presence of a carbon coating [11, 327].

Of course, not only carbon has been investigated as an electrode coating. The review paper by Li *et al.* [50] regarding surface coatings on cathode materials demonstrates the broadness of coated materials:

- Simple oxides as Al_2O_3, MgO, ZnO, ZrO_2 and CoO.
- Complex oxides as $AlPO_4$, $MgAl_2O_4$ and $ZrTiO_4$.
- Lithium-containing compounds, such as solid electrolytes (e.g. Li_2CO_3, $Li_2O{-}2\,B_2O_3$ glass) or with another electrode material (e.g. $LiCoO_2$, $LiMn_2O_4$, $LiMnCoO_x$)
- Conductive coatings such as carbon, TiN, silver, gold or acetylene black.

A broad range of deposition techniques has been investigated the past decades for lithium-ion battery surface coatings, such as co-precipitation, sol-gel deposition, dry coating, melting impregnation, pulsed laser deposition, intermixing nanoparticles into the electrode slurry preparation or deposition of films by chemical vapour deposition. Generally, a beneficial effect of the coating is reported, typically attributed to a reduced electrolyte-electrode contact, an improvement of the structural stability or the suppression of unwanted phase formations. Remarkably, the performance of the coating particles varies significantly from one coating technique to another, implying that the film quality and the deposition conditions themselves have a great influence on the sensitive surface chemistries. For example, cathode materials with a high nickel are known to be extremely sensitive to water, so a co-precipitation technique could be detrimental for the surface of the cathode compound [334].

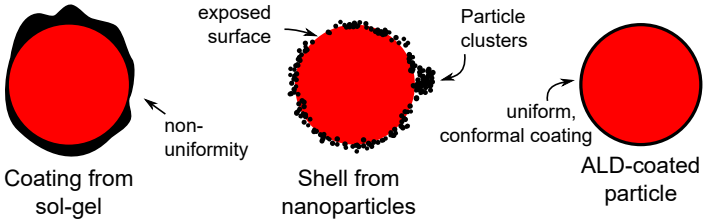

Figure 13.5: Illustration of the different surface modifications from different coating techniques.

13.3 ALD COATINGS FOR INTERFACE MODIFICATIONS

Atomic layer deposition itself has been used for various applications, from high-k oxides and barrier layers in semiconductor devices to thin-film catalysis, but ALD has also been a rising star in lithium-ion battery interface modification. Since initial research on this topic started in 2010, an interest has been sparked onto ALD for surface coatings, as is evident from the many published research papers and the reviews on this topic [79–82, 335]. Most of the work deals with ALD Al_2O_3 coatings of various thickness on electrode powders [47, 138, 336–347], the composite electrode [47, 49, 88, 138, 330, 336, 343, 347–360] or even the separator[88]. Not only ALD Al_2O_3 has been investigated: other compounds such as TiN [39, 361], ZrO_2 [345, 347, 356, 362–365], HfO_2 [335, 366], TiO_2 [39, 310, 344, 349, 355, 356, 367–369], ZnO [48, 345, 347, 370, 371], hybrid metal-organic films [352, 372], fluorides [342, 373], phosphates [374] and ALD solid electrolytes [87, 375–377] were also evaluated. In this section, some of these coatings will be discussed to highlight the advantages and pitfalls of ALD coatings for electrodes.

13.3.1 *Coating the electrode particles or coating the composite electrodes*

Most of the above-mentioned deposition techniques deposit the coating directly on electrode particles, which are then mixed into a slurry to be fabricated into a composite electrode. ALD deposition has also been investigated on the electrode particles prior to electrode composition. One of the main differences between ALD and other deposition techniques is the excellent conformality and uniformity of the films that are deposited. The particles coated with ALD can be considered as core-shell particles with an excellent, closed shell, depending on the number of ALD cycles deposited. Other deposition techniques, such as deposition from a solution of nanoparticles, can also deposit a shell on the electrode particles,

but the quality of the shell is typically less uniform due to the nature of the deposition technique, as is schematically illustrated in figure 13.5. Furthermore, ALD operates at a much lower temperature than is required for solvent evaporation in sol-gel based deposition for example, and can deposit much thinner coatings (down to 1 Å) compared to conventional coating techniques (typically 50 nm to 100 nm), accommodating a minimal gravimetric capacity loss due to particle mass loading.

13.3.1.1 *ALD coating on the electrode particles*

Suprisingly, these 'ideal' coatings not always match the performance benefits observed for non-ALD coated electrodes, and often performance degradation is even observed for ALD-coated powders. Anodes assembled from graphite powder coated with just 2 or 5 cycles of ALD Al_2O_3 have been reported to display a larger overpotential and decreased cycling stability [336]. Similarly, 4 cycles of ALD Al_2O_3 on MoO_3 particles yielded an inferiour rate performance compared to the uncoated particles, and even an accelerated capacity fading [47, 378]. This poor performance of direct particle coating is related to the electronic network between the active particles and the current collector.

On cathodes, where battery ageing is often mostly related to metal dissolution and oxygen release rather than to SEI-related phenomena, coating the battery particles yielded beneficial results on the cyclability, but increased the impedance of the electrode, reducing electrode performance. Just a few cycles of ALD Al_2O_3 on high-voltage cathodes such as LMNO or NMC indeed enhanced the cycle life of the electrodes by reducing SEI formation, acting as an HF scavenger or suppressing metal dissolution, but at the cost of an increased overpotential, which resulted in reduced rate capabilities [340, 343, 345, 346].

The aforementioned examples all use ALD Al_2O_3 as a surface modifier, as does the bulk of ALD literature. Al_2O_3 is a well-known electronic insulator with a bulk resistivity around $10^{14}\,\Omega\,\mathrm{cm}$. A conformal coating of this oxide can shield the electrode particles electronically from the electronic network formed by the current collector and the conductive agent particles, as illustrated in figure 13.6(a). This intuitively results in degraded electrode performance. The Al_2O_3 deposited from other coating techniques is believed to be less uniform or non-closed due to the high-temperature nature often related to these deposition techniques (see figure 13.5). In those cases, the non-closed nature of the coatings actually still allows for reasonable battery performance, while the coated surface is stabilized towards the ageing phenomena related to the exposed electrode surfaces.

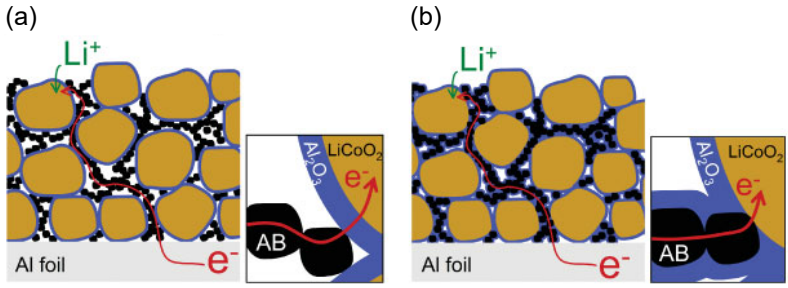

Figure 13.6: Electronic considerations for (a) ALD-coated electrode particles or (b) ALD-coated electrode. The "AB" in the figure stands for "acetylene black"Figure adapted from Jung *et al.* [336].

It is clear from figure 13.6(a) that the electronic network is not disturbed, and perhaps even enhanced, if the coating applied to the electrode particles is electronically transparent or even conductive. ZrO_2 coatings, for example, have been shown to enable enhanced cycle life and kinetics on cathode particles, especially at high temperature when ZrO_2 becomes more conductive [345, 363]. The deposion of amorphous TiO_2 on V_2O_5-based electrodes enabled improvements in the cyclability, without compromising the kinetics of the electrodes [310]. However, the use of an electronically conductive protective coating has the downside that electrolyte decomposition, which is an electronically driven phenomenon, is not completely suppressed. An ALD ZnO coating on $Li_{1.2}Mn_{0.54}Ni_{0.13}Co_{0.13}O_2$ particles for example was able to reduce the oxygen loss, but an SEI layer was still formed due to the high electrode potential of this cathode and the conductive nature of this coating [371].

13.3.1.2 *ALD coatings on composite electrodes*

When the coating is applied directly on the assembled or 'composite' electrode, as is shown in figure 13.6(b), the electronic network is not influenced by the surface modification. To achieve these coatings uniformly in the porous high aspect-ratio and high surface-area structure that is the composite electrode, a conformal coating technique is required with excellent thickness control, which is where ALD excels. The same argument is valid for 3D-structured electrodes or thin-film electrodes. As the coating is only applied as the final step of the electrode assembly, it does not directly influence the current collector-electrode network. Interestingly, this makes thin-film electrodes ideal model systems to study the electrode-electrolyte surface interactions. Below and in paper V, thin-film TiO_2 will be used to

evaluate the effect of ALD coatings on the kinetics of a lithium-ion battery electrode.

Indeed, an evaluation of the available literature shows that research is either on conductive coatings, both on the electrode particles or composite electrodes, or non-conductive coatings, but mostly on the composite electrodes. Jung *et al* for example compared ALD Al_2O_3-coated graphite when the coating was applied either on the particles directly, or on the composite anode. The latter showed improved cyclability, while the former only decreased the performance [88, 336].

13.3.2 *Lithium ion transfer through ALD coatings*

The paragraphs above only consider the transport of electrons into the electrode particles. Using an electronically conductive ALD coating, or coating the composite electrode rather than the electrode particles, has been shown to deliver better battery performance than coating of the insulating ALD Al_2O_3 directly on electrode particles. However, a battery does not rely on electrons alone, and lithium ion diffusion through the applied coatings needs to be considered as well. Independent of whether the coating is applied onto electrode particles, composite electrodes or nanostructured electrodes, without transfer of lithium ions the battery can not function, so the coatings need to be (at least) transparent towards lithium ions or (preferably) lithium-ion conducting to some degree.

Taking these and the previous considerations into account, ALD coatings can be classified into four categories according to their ionic and electronic conductivities:

- blocking coatings (σ_{e^-} and σ_{Li^+} low)
- electronically conductive coatings (σ_{e^-} high and σ_{Li^+} low)
- solid electrolytes (σ_{e^-} low and σ_{Li^+} high)
- dual or 'mixed' conductors (σ_{e^-} and σ_{Li^+} high) [379]

One should note the thickness of the coatings here. ALD coatings typically scale from 1 Å to 100 nm, but surface modifications are typically below 10 nm. This puts 'low' and 'high' conductivities in perspective: while a solid electrolyte in a thin-film battery has a low conductivity towards lithium ions if $\sigma < 10^{-6}\,\mathrm{S\,cm^{-1}}$, ALD electrolytes are typically two orders of magnitude thinner, so $10^{-7}\,\mathrm{S\,cm^{-1}}$ is an excellent conductivity.

Intuitively, one can envision a range of applicability for coatings according to their conductivity. As lithium ions need to pass through the

coatings, good lithium ion conductivity is always required. For coatings directly on the electrode particles, electronic conductivity is an additional requirement, so particle coating needs to be done with dual conductor coatings. For a coating on the composite electrode, electronic conductivity is not a requirement. Solid electrolyte coatings have the advantage that the ageing processes involving electronic contact with the liquid electrolyte (SEI formation, metal dissolution, ...) are also suppressed. Indeed, a good solid ALD solid electrolyte can be considered as the 'holy grail' of ALD for lithium-ion battery applications, and is being researched intensely. A non-exhaustive list of ALD lithium-ion electrolytes contains lithium aluminates, lithium silicates, lithium aluminium silicates, lithium tantalates, lithium phosphates and lithium aluminium sulphides [87, 357, 375–377, 380–389]. However, from the above list it is clear that the lithium-ion electrolytes are almost exclusively ternary or even quaternary compounds. Furthermore, several of them require higher deposition temperatures (typically 200-300 °C) and many are air sensitive, especially the sulphides. This makes the deposition of these films much more challenging than simple binary oxides with a far easier process chemistry, such as Al_2O_3 or TiO_2.

Blocking coatings without lithium ion conductivity, such as Al_2O_3 and $AlPO_4$ for example, or coatings with only electronic conductivity, such as TiN, are rather counter-intuitive in the framework of this simplified image, and should not find their application into this field. Nevertheless, ALD Al_2O_3 is still the most investigated coating for surface modifications. The strength of ALD for non-conductive coatings such as ALD Al_2O_3 is the ultimate thickness control: by scaling the coating down to only a few monolayers, the small nature of the lithium ions still allows them to be transferred through the inactive coating and enables the beneficial properties of these coatings to still be applicable and even to be commercialized [390].

13.4 INFLUENCE OF THE ALD COATING ON THE LITHIUM ION KINETICS

Despite the fact that non-conductive ALD coatings can in principle be used as surface modifiers in lithium-ion batteries, the poor lithium-ion conducting properties of for example Al_2O_3 raise the question of the influence of such coatings on the rate capability of the battery electrode whose surface it is meant to stabilize. The rate performance of Al_2O_3-coated electrodes is often omitted in literature, and the few reports where rate information is being mentioned indeed confirm a very sensitive balance. A sufficiently thick ALD Al_2O_3 needs to be present to stabilize the

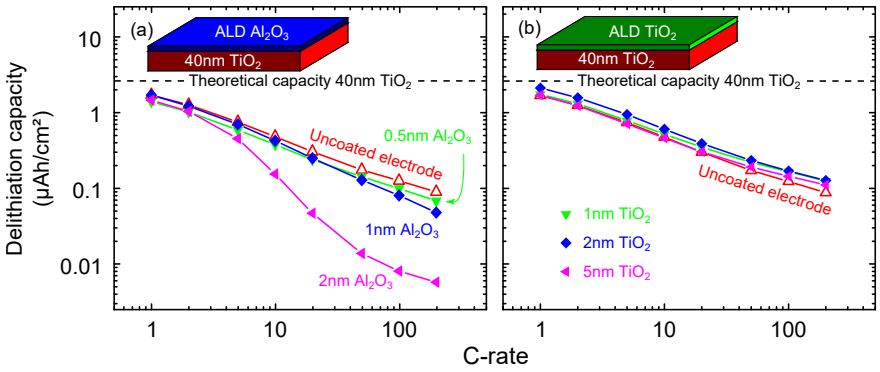

Figure 13.7: Rate performance of the (a) ALD Al_2O_3 coated and (b) ALD TiO_2 coated thin-film electrodes.

electrode, but the coatings need to be sufficiently thin to avoid introducing a kinetic bottleneck on the electrochemical performance of the electrode [330, 337, 391]. The question can be posed whether better options are available which can provide the beneficial effects a high-quality coating such as ALD Al_2O_3 has to offer, without raising the impedance of the cell.

In paper V, planar thin-film electrodes are used to study the effect of amorphous ALD Al_2O_3 and ALD TiO_2 coatings on the rate performance of LIB electrodes. The benefit of using a thin-film system lies in the separation of the electron source and drain (current collector | electrode) from the lithium ion source and drain (electrode | electrolyte), which are 1-dimensionally and spatially separated, which is not the case for the complex 3-dimensional nature of lithium ion and electron transport in a particle-based LIB electrode. Furthermore, the planar thin film geometry is very easy to cover with atomic layer deposition, so additional effects related to coating imperfections at corners or particle-particle interfaces can also be excluded.

In this case, two thin-film electrode systems are used: a 40 nm anatase TiO_2 film and a 100 nm $LiMn_2O_4$ (LMO) film. The former can be considered as a model for an ideal electrode, as TiO_2 has an electrode potential well within the stability window of the electrode, and is not known to suffer severely from metal dissolution or dramatic volume changes. Thus, any effect of the coating on the performance of the electrode is purely related to kinetic transfer of lithium ions across the modified electrode interfaces. The latter electrode, i.e. the LMO film, does suffer from a range of issues such as metal dissolution and electrolyte oxidation, and can thus be used as a model system for electrode ageing.

ALD coatings with thicknesses in the range of 0.5 nm to 5 nm were deposited on the anatase TiO_2 electrode. The rate performance was evaluated, as shown in figure 13.7. Al_2O_3 is considered a non-conductive compound for lithium-ions. As expected, a decrease in rate performance can already be observed for extremely thin films (0.5 nm) in figure 13.7(a). For thicker coatings the effect becomes increasingly dramatic: a 1 nm Al_2O_3 reduces the 200C capacity to half the available 200C capacity for the uncoated TiO_2 electrode, and with a 2 nm Al_2O_3 coating only 7 % remains. Films beyond 2 nm no longer accommodate the transfer of lithium ions across the modified interface.

As a second case, amorphous ALD TiO_2 was evaluated. TiO_2 itself is also an electrode material: its crystalline form is used as thin-film electrode here. This implies that it is a conductor for lithium ions. From figure 13.7(b), it can be seen that a coating of up to 5 nm has no performance degrading effect on the electrode, and the kinetics of the underlying thin-film electrode are completely preserved.

The blocking nature of ALD Al_2O_3 is a rather surprising result as it is easily the most investigated coating in literature. To further clarify its blocking nature, cyclic voltammetry and electrochemical impedance spectroscopy were used to study the different aspects of the resistive nature of these coatings. Cyclic voltammetry revealed that the lithium ion transfer through ALD Al_2O_3 is surprisingly asymmetrical; the coating poses a greater kinetic barrier for lithium ion insertion from the liquid electrolyte to the electrode than vice versa. Electrochemical impedance spectroscopy was performed at OCP for a film thickness of 0.5 nm to 3.0 nm of ALD Al_2O_3 coated on the TiO_2 electrode. A fit was performed according an R-RQ-RQ-Q equivalent circuit, with Q representing a constant phase element. The latter RQ-element is not present for the uncoated TiO_2 electrode, and is thus related to the additional surface coating imposed by the ALD Al_2O_3 film. Figure 13.8 shows that an increasingly larger semicircle is present for increasing thickness of the coating. An almost linear relation can be found between the two, which can be fitted to a room temperature conductivity of $\sigma_{Li^+} = 6.7 \times 10^{-13}\,\mathrm{S\,cm^{-1}}$. A coating of 3 nm ALD Al_2O_3 appeared to be completely shielding the electrode from lithium ion insertion, as is evident from the lack of a distinguishable semi-circle. As a point of note here, the reader has to take into account that a semicircle could still be present, but the magnitude may be too large, which places it outside of our measuring range. Furthermore, the constant phase element evolved from a non-ideal capacitor to an ideal capacitor for 0.5 nm to 3 nm of ALD Al_2O_3, respectively. Thus, a coating of 3 nm of ALD Al_2O_3 appears to act

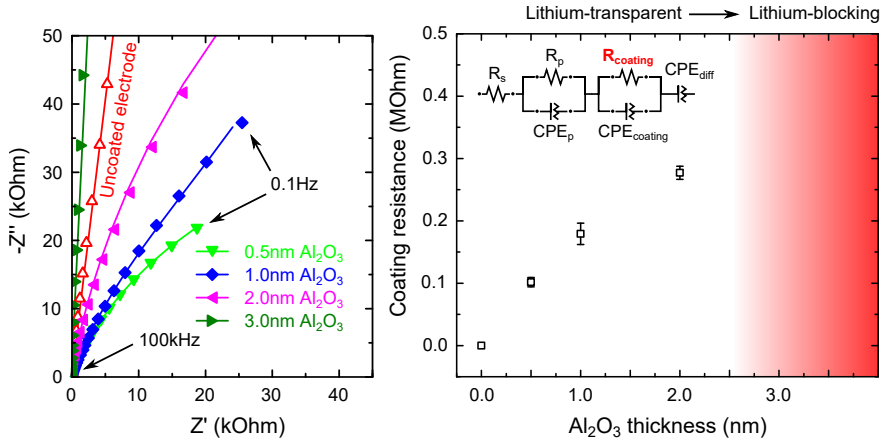

Figure 13.8: (left) Electrochemical impedance spectroscopy measurement of the ALD Al_2O_3 coated thin-film electrode as depicted in figure 13.7(a). The solid lines are fitted spectra according to the equivalent circuit shown. (right) The fitted interface resistance imposed by the ALD Al_2O_3 coating, indicating the boundary where the ALD Al_2O_3 coating becomes blocking towards lithium ions.

as an impenetrable capacitor for lithium ions, rather than a lithium-ion transferring resistor for thinner coatings.

In conclusion, it appears that to reap the benefits of an ALD Al_2O_3 coating, a sacrifice will have to be made towards rate performance. Other coatings, such as ALD TiO_2, have also been reported to yield improved battery performance [39, 310, 344, 349, 355, 356, 367–369]. These coatings can be a wiser choice if rate performance is critical, as is often the case in nano-structured batteries.

13.5 Case studies for improvement of battery performance by interface engineering

With the effects of the ALD Al_2O_3 unravelled in the previous section on an ideal system, less ideal model systems need to be explored to investigate whether non-blocking coatings such as ALD TiO_2 can indeed be both beneficial and at the same time maintain the rate performance. In paper V, a thin-film LMO film is examined in the overcharged region (3.5 V to 4.5 V *vs* Li^+/Li) to study the effect of these coatings on the solvent oxidation at those potentials. Finally, in paper VI one of the electrodes from the previous chapter, i.e. crystalline V_2O_5 from ALD vanadium oxide, is revisited on a 3D-structured current collector scaffold provided by a forest

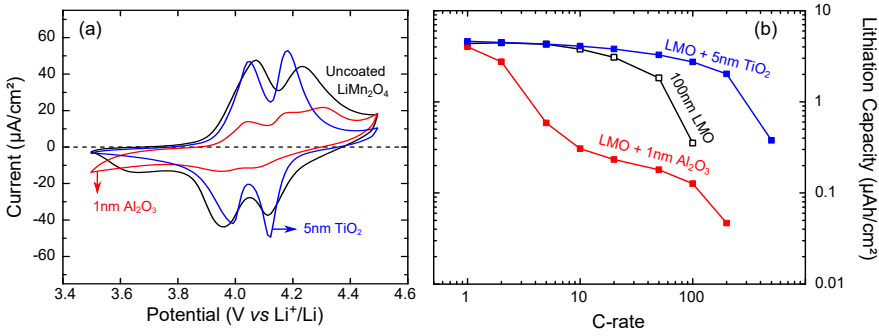

Figure 13.9: (a) Cyclic voltammogram (at $1\,\mathrm{mV\,s^{-1}}$) and (b) rate performance of 100 nm $LiMn_2O_4$ films, either uncoated (black) or coated with 1 nm ALD Al_2O_3 or 5 nm ALD TiO_2 (blue).

of carbon nanotubes (CNTs). By deep lithiation of the V_2O_5, this nanostructured electrode suffers from metal dissolution, and can be considered a model system for this ageing phenomenon. The effect of an ALD TiO_2 coating on these electrodes is evaluated.

13.5.1 *Lithium manganese oxide and the electrolyte oxidation*

$LiMn_2O_4$ or LMO is a material that is heavily investigated as a candidate cathode to replace $LiCoO_2$ because of its low cost and high safety (high flash point). However, it is known to suffer from a range of issues causing accelerated ageing, such as undesirable lattice distortions, metal dissolution and solvent oxidation due to the highly oxidative nature of Mn^{4+}. The solvent of the electrolyte used in this work, propylene carbonate, is reported to decompose on noble metal substrates above 4.0 V *vs* Li^+/Li [392]. Here, we will intentionally drive LMO outside of the stability window of the electrolyte by performing a delithiation step up to 4.5 V *vs* Li^+/Li. The influence of the two ALD coatings, i.e. ALD Al_2O_3 and ALD TiO_2, is studied on this decomposition behaviour and how this translates to the rate capability of the thin-film electrodes.

First, the electrodes are 'strained': several CV sweeps are performed in the 3.5 V to 4.5 V *vs* Li^+/Li range, which corresponds to (dis)charging the $Li_xMn_2O_4$ spinel for $0 > x > 0.5$. In the completely discharged state, i.e. above ~4.2 V *vs* Li^+/Li, no lithium is left in the film, meaning that all the manganese has a 4+ oxidation state. By further raising the potential, the propylene carbonate electrolyte is oxidized and deposited on the electrodes, forming a solid-electrolyte interphase.

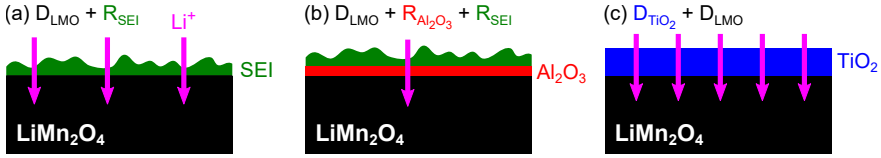

Figure 13.10: Charge transfer resistances for the uncoated LMO (left), ALD Al_2O_3-coated LMO (middle) and ALD TiO_2-coated LMO (right). R represents a charge transfer resistance, while D represents bulk diffusion.

Two amorphous ALD coatings are examined to prevent this ageing mechanism from occurring: ALD Al_2O_3 and ALD TiO_2. Based on the previous results, thick ALD Al_2O_3 coatings are too resistive towards lithium ions, and thus a 1 nm ALD Al_2O_3 film was chosen as the first coating. Since ALD TiO_2 poses no kinetic bottleneck whatsoever, the maximal investigated coating thickness (5 nm) was used for this film. Figure 13.9(a) shows the cyclic voltamograms during straining of the electrodes. Two observations can be made straight away from these measurements:

- Although an ultrathin ALD Al_2O_3 coating was chosen, i.e. only 1 nm, the two peak couples related to lithium ion insertion and extraction from the LMO are still severely suppressed for the Al_2O_3-coated LMO. The TiO_2-coated LMO does not suffer from peak suppression, rather, the insertion and extraction peaks are sharper and closer together, indicative of a lower internal resistance.
- A third cathodic feature can be observed above 4.3 V *vs* Li^+/Li, which is linked to solvent oxidation. This feature is not suppressed for the Al_2O_3-coated LMO, but a clear reduction of solvent oxidation is readily observable for the TiO_2-coated LMO electrode.

Figure 13.9(b) shows the rate capability after the straining of the electrodes for several cycles. For the lowest C-rates, the capacity for the three electrodes coincides. The rate capability of the Al_2O_3-coated LMO is inferior to the uncoated LMO, and drops dramatically for higher C-rates. This was to be expected, based on the previous discussion of the nature of the ALD Al_2O_3 coating, alongside the observation that the solvent oxidation is not suppressed. For this electrode, a double kinetic bottleneck thus exists, one formed by the solid electrolyte interphase (R_{SEI}), and one posed by the deposited ALD Al_2O_3 coating ($R_{Al_2O_3}$), resulting in very poor rate performance.

The rate capability of the ALD TiO_2-coated LMO is surprisingly much better than the uncoated LMO. Here, the hypothesis is that this is caused by a deteriorated rate performance of the LMO itself, i.e. diffusion through

the solid-electrolyte interphase layer (D_{SEI}) formed on the LMO. As is clear from figure 13.9(a), the PC solvent oxidizes when the potential is swept to 4.5 V *vs* Li^+/Li. Figure 13.10 shows that a solid electrolyte interphase is thus present on the electrode surface, imposing a charge transfer impedance for the lithium ions to be inserted or extracted from the electrode. The ALD TiO_2 in itself does not pose a significant charge transfer impedance as the diffusion through amorphous ALD TiO_2 is reported to be very fast [393]. So, suppression of the solvent oxidation and thus the formation of the SEI impedance allows the kinetics for this electrode to surpass that of the uncoated electrode. In conclusion, for this case an ALD TiO_2 surface modifier is a superior choice compared to ALD Al_2O_3.

13.5.2 *3D Vanadium pentoxide and metal dissolution*

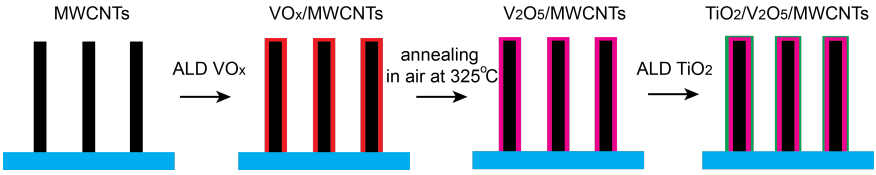

Figure 13.11: The synthesis route towards TiO_2/V_2O_5/MWCNTs electrodes.

With the excellent performance of ALD TiO_2 as a stabilizing layer in mind, its functionality on a far more complex system is investigated. The synthesis of these electrodes is summarized in figure 13.11. A 3D-structured electrode is devised by coating amorphous ALD VO_x on a ~5 µm thick, highly porous current collector, i.e. a dense forest of carbon nanotubes (CNTs). The VO_x is crystallized by a careful anneal in air to V_2O_5, in order to leave the CNTs and TiN current collector unchanged. As was shown in part iii of this thesis, crystalline V_2O_5 films suffer from serious capacity fading when lithiated to $Li_2V_2O_5$, i.e. to a potential of 2.0 V *vs* Li^+/Li. From the previous section, it is clear that ALD TiO_2 can act as a retardant for the solvent oxidation at high potentials, without imposing a bottleneck on the battery kinetics. Here, the ageing mechanism of V_2O_5 is shown to be related to the dissolution of vanadium into the liquid electrolyte. An amorphous ALD TiO_2 was deposited on the V_2O_5/CNTs electrodes to investigate whether this coating could also act as a metal dissolution barrier, and improve the cycle life of the high capacity V_2O_5/CNTs electrodes.

As the topology of this electrode is much more complex than the thin-film systems described above, the quality of the coatings needed to be evaluated. Advanced electron microscopy measurements were performed

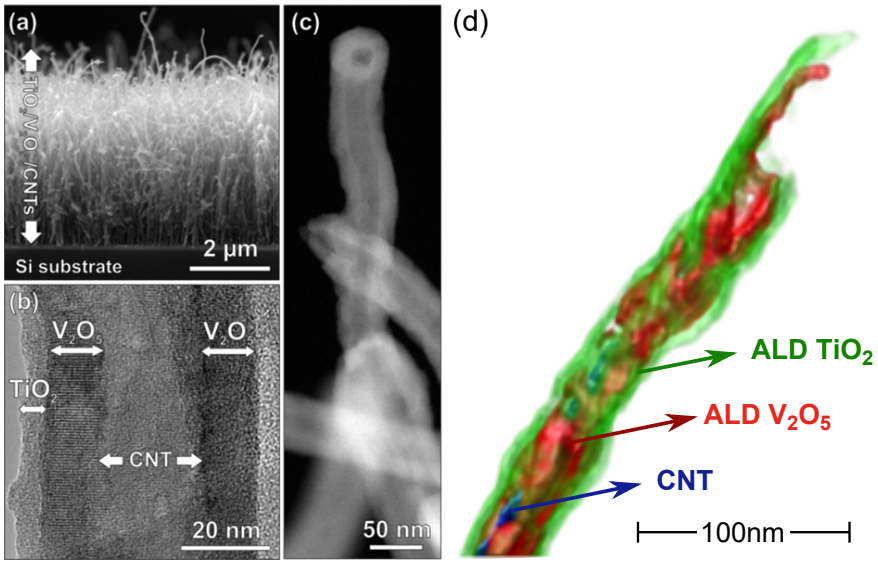

Figure 13.12: (a) Cross-sectional SEM, (b) HRTEM and (a) HAAFD-STEM image of the 25 cycles coated V_2O_5/CNTs electrodes. (d) A superposition of 3D-reconstructed elemental distributions of C, V and Ti of a V_2O_5/CNTs electrode coated with 25 cycles of amorphous ALD TiO_2, from EDX-STEM.

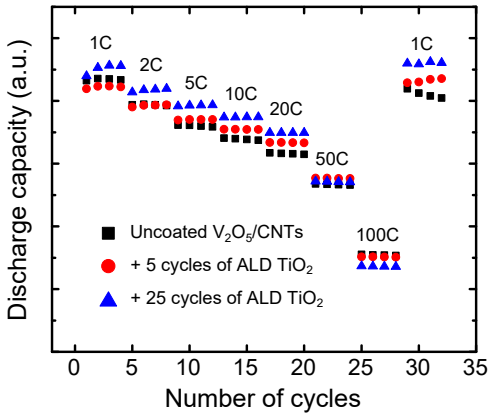

Figure 13.13: Rate performance of the uncoated V_2O_5/CNTs (black squares), and V_2O_5/CNTs coated with 5 (red circles) or 25 (blue triangles) ALD cycles of TiO_2. The capacities are normalised to the amount of vanadium in the electrodes.

at the EMAT electron microscopy centre in Antwerp. Figure 13.12(a) is a cross-section of the CNTs as measured by SEM. A dense forest of interlinked CNTs is visible, with a substantial degree of porosity in between. Coating these substrates with ALD vanadium and titanium oxides did not change the morphology on this scale. However, HRTEM revealed the coatings deposited on a single CNT. The crystalline nature of the V_2O_5 is clear from the periodic spacing of the individual atoms in this layer. No such periodicity was observed for the ALD TiO_2 layer, indicating an amorphous film. An HAADF-STEM image of individual coated CNTs is shown in figure 13.12(c). By varying the measurement angles, a tomographical reconstruction could be made from the individual CNTs. Furthermore, by combining this with EDX, a 3D elemental map could be reconstructed, as shown in figure 13.12(d). The reader is invited to view a short movie of this HAAFD-STEM and EDX-STEM reconstruction at this link.

Finally, the performances of the uncoated and ALD-coated V_2O_5/CNTs electrode are evaluated in figure 13.13 and 13.14. To allow for direct comparison between the samples, the capacities had to be normalised, as the CNT density was not equal for every sample. The actual capacities are presented in the supplementary of paper VI. To give the reader a point of reference; the footprint capacities measured at 1C are in a range from 70 $\mu A\,h\,cm^{-2}$ to 90 $\mu A\,h\,cm^{-2}$.

As was expected from the previous sections, the addition of an ALD TiO_2 coating did not impede the rate capability, except for very high C-

cocoon.ugent.be/sites/default/files//M1.mpg

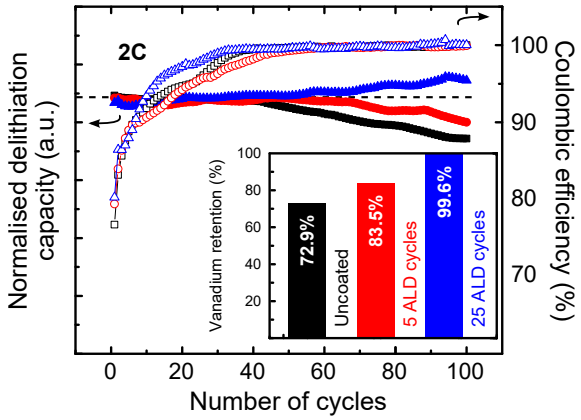

Figure 13.14: Cyclability of the uncoated V_2O_5/CNTs (black squares), and V_2O_5/CNTs coated with 5 (red circles) or 25 (blue triangles) ALD cycles of TiO_2. The capacities are normalised to the amount of vanadium in the electrodes. The inset shows the amount of vanadium retained on the electrode after 100 charge-discharge cycles, compared to the respective pristine electrodes.

rates, where the electrode coated with 25 cycles of TiO_2 performs marginally poorer than the other two electrodes. The cyclability of these electrodes on the other hand changed significantly by the coating. The uncoated V_2O_5/CNTs age rapidly: close to 17 % of the initial capacity is lost over 100 charge-discharge cycles. This capacity fade is delayed by coating the electrode with 5 cycles of ALD TiO_2; capacity fading for those electrodes is only observed after the 65th cycle, and a larger fraction of the capacity remains available after 100 cycles. Coating the V_2O_5/CNTs electrodes with 25 cycles of ALD TiO_2 on the other hand completely impedes their ageing. As can be seen from the inset in figure 13.14, this ageing corresponds very well to a fraction of the vanadium oxide dissolving from the surface of the electrodes into the electrolyte. A coating of 5 ALD cycles of TiO_2 appears to be insufficient to completely halt this dissolution, but for 25 ALD cycles of TiO_2 on the other hand almost all of the V_2O_5 is still present after 100 cycles.

Moreover, for the V_2O_5/CNTs electrodes coated with 25 cycles of ALD TiO_2 an increase in capacity is observed, which is linked to the gradual amorphisation of the V_2O_5 films. In the previous part, it was shown that amorphous films of V_2O_5 have a better rate performance compared to their crystalline counterpart, and it is thus hypothesized that this increase in capacity is related to an increasing fraction of amorphous vanadium oxide in the electrode.

To conclude, despite the fact that ALD Al_2O_3 is attributed beneficial properties in literature, the same beneficial properties are found here for ALD TiO_2 coatings, while much better kinetics can be maintained. In electrode engineering, Al_2O_3 should not be considered as the only option, and perhaps not even as the ideal coating, and especially coatings with better lithium ion conducting properties are by definition a better choice.

14

PAPER IV

THE INFLUENCE OF ULTRATHIN AMORPHOUS ALD ALUMINA AND TITANIA ON THE RATE CAPABILITY OF ANATASE TiO_2 AND $LiMn_2O_4$ LITHIUM ION BATTERY ELECTRODES

Felix Mattelaer,*[a], Philippe M. Vereecken,[b,c] Jolien Dendooven,[a] and Christophe Detavernier[a]

Published in *Advanced Materials Interfaces* (2017). Doi: 10.1002/admi.201601237

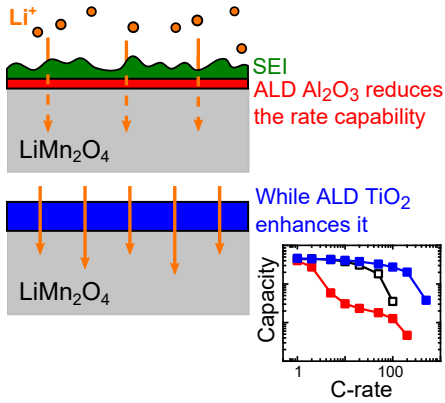

[a] *Department of Solid State Sciences, Ghent University, Krijgslaan 281 S1, 9000 Gent, Belgium,*
[b] *imec, Kapeldreef 75, 3001 Leuven, Belgium,*
[c] *Centre for surface chemistry and catalysis, KU-Leuven, 3001 Leuven, Belgium*

ABSTRACT

Interface modification is a heavily investigated method of extending the lifetime of lithium ion batteries. While many studies have explored the effect interface coating on the lifetime, the rate capability is often overlooked. In this study, we investigated the influence of ultrathin (<10nm) ALD coatings of amorphous Al_2O_3 and amorphous TiO_2. It was found that, on thin-film anatase TiO_2, the rate capability is unaffected by an amorphous TiO_2 coating since it does not pose an additional impedance on the system, while Al_2O_3 coatings are detrimental for the rate performance due to the $1.5 \times 10^{12}\,\Omega\,\mathrm{cm}$ resistivity towards lithium ions. A thicker than 2nm ALD Al_2O_3 film was found to block lithium transfer completely, resulting in a purely capacitive film. Solvent oxidation was studied on thin-film $LiMn_2O_4$. We demonstrated that both coatings can partially solve the solvent decomposition. However, the kinetic bottleneck posed by 1 nm Al_2O_3 was still greater than the uncoated $LiMn_2O_4$, leading to worsened rate capability. ALD TiO_2 on the other hand could prevent most of the solvent decomposition, resulting in smoother electrodes. The absence of the decomposition layer and lithium conducting properties of the ALD TiO_2 films result in an improved rate capability for the ALD TiO_2 coated electrode.

INTRODUCTION

Autonomy comes in all shapes and sizes, ranging from electric vehicles requiring a sufficient reach and acceleration, to small chip devices requiring local energy storage and production. No matter the size of the application, modern day technology could not be where it was, and where it's going, without energy storage. Lithium ion batteries (LIBs) are nowadays storage medium of choice, due to the superior storage capacity and power density compared to other mature battery types. However, industry is still pushing to further improve the power capability and lifetime of the battery, which is constantly being out-paced by the demands of new applications [62].

To obtain such advances in LIBs, two routes are under investigation. On the one hand, novel material chemistries are being investigated, for example moving from the classical graphite anode to high capacity composites of graphite including silicon, and moving from the original cathode $LiCoO_2$ to cheaper and safer high-power cathodes such as spinel $LiMn_2O_4$ (LMO), and higher energy compounds such as $LiMn_{1.5}Ni_{0.5}O_4$ (LMNO) [16]. On the other hand, the classical lithium ion battery can still be im-

proved to some extent, by nanoscaling the electrodes [26, 158, 393], moving to complex 3D battery architectures [63, 187], Carbon nanotube or carbon nanosheet based electrodes [394], and interface engineering [355, 395–397].

Interface engineering in particular has received much attention, since many of both the lifetime and power density degradation effects are related to what happens at the interface. On the negative electrode side, the potential is often too low for the electrolyte's solvents, causing them to reduce during the first charge of the battery and forming an organic layer called the Solid-Electrolyte Interface (SEI). While this layer is in itself a protective layer against further SEI formation, several downsides are found because of it, amongst which are irreversible lithium loss, reduced lithium diffusion coefficient, temperature instability and incontrollability of the critical solid-liquid interface. On the positive electrode side, many battery lifetime killer phenomena are also related to direct electrode-electrolyte contact, such as metal dissolution, which is particularly troublesome for manganese-containing cathodes [241, 397], or solvent oxidation, causing an SEI on the cathode side [328, 392].

Electrode surface coatings can be applied to mediate these effects. Many coatings techniques are used to improve battery lifetime; but the best results are obtained using atomic layer deposition (ALD) because of its conformal nature, allowing direct coating on the composite electrode in stead of coating on the electrode particles, and because of the extremely uniform nature of the films, causing no pinholes or thickness variations along the coating [69, 72]. Jung *et al* for example compared an ALD Al_2O_3 film coated on graphite particles and on a composite graphite anode. The latter showed improved cyclability, while the performance of the former was decreased [88, 336]. Many materials have been investigated since research on ALD coatings for lithium-ion batteries started in 2010 [81, 83–85], most of the work dealing with ALD Al_2O_3 coating of various thickness on electrode powders [47, 138, 336–347], composite electrode [47, 49, 88, 138, 330, 336, 343, 347–360] or even the separator [88]. These coatings can suppress SEI formation, act as an artificial SEI, strengthen the electronic network by knitting the electrode together, act as an HF scavenger, help maintain particle morphology, prevent unwanted phase tranformations and block metal dissolution. The net result of these coatings is generally an extended lifetime. However, alumina has a very low lithium diffusion coefficient, typically even lower than the naturally formed SEI. So, while the result of coating with simple non-conductive oxides is a longer lifetime, this can pose a kinetic bottleneck, as pointed out by some researchers. For example, Wang & Wang [349] found that only 10 ALD cycles of alumina reduces the

Sometimes also called 'solid electrolyte interphase'.

diffusion coefficient of lithium in a graphite anode. Furthermore, Li *et al.* [356] found that even a coating of 2 ALD cycles of Al_2O_3 introduces a significant voltage hysteresis, which results in a worsened rate capability. Other ALD coatings are also investigated, such as TiN [39, 361], ZrO_2 [345, 347, 356, 362–365], HfO_2 [335, 366], TiO_2 [39, 310, 344, 349, 355, 356, 367–369], ZnO [48, 345, 347, 370, 371], hybrid metal-organic films [352, 372] and ALD solid electrolytes [87, 375–377]. While the focus of the investigation is mostly to improve the lifetime of the electrodes, the kinetics are an often-overlooked and very important battery characteristic.

Here, we use two ideal model systems to investigate amorphous coatings of alumina and titania, and unravel their influence on the kinetics of the electrode. Planar thin film electrodes were chosen to simplify the electronic and ionic flow, from three-dimensional in electrode particles to one-dimensional in thin-film electrodes. Anatase TiO_2 was selected as model system, since this is a very low volume change material with an electrochemical potential above solvent reduction potentials (TiO_2 shuffles lithium around 1.8V vs Li^+/Li) and no metal dissolution is known for TiO_2. So, contrary to many performed studies, here, we examine an already close-to-ideal system to separate the influence of the coating from the issues, and examine it as such. Finally, we apply the coatings under study to a model system which does suffer from known issues, which is thin film $LiMn_2O_4$. By overcharging it well beyond electrolyte solvent stability, we induce a solvent oxidation layer (SEI) on the $LiMn_2O_4$, and study the influence of the kinetics with this effect present. We find that, while Al_2O_3 is the most investigated buffer layer, it imposes a kinetic bottleneck on the battery, degrading power capability of the electrodes. Non-blocking alternatives providing similar protection to known issues exist, such as TiO_2.

EXPERIMENTAL

Ultra-thin films were deposited in a home-built high-vacuum ALD reactor [93–95] with a base pressure of 10^{-7} mbar. The reactor walls are heated to 95 °C to avoid precursor condensation. Trimethyl aluminium (TMA) and water were used to deposit amorphous Al_2O_3, and Tetrakis (dimethylamido)titanium (TDMAT) and water were used to deposit amorphous TiO_2, at substrate temperatures of 100 °C and 150 °C, respectively. 5 second precursor pulses of 5×10^{-3} mbar were alternated with pump times allowing the pressure to drop to 10^{-6} mbar. Films were deposited

SEI is mostly used to describe the layer formed on the anode, but for simplicity, we will call the solvent oxidation layer here by the same denominator.

on 100 nm thermal SiO_2 on Si to monitor the thickness. As electrodes, TiO_2 and $LiMn_2O_4$ thin films were used. The TiO_2 electrode constituted a stack of 20 nm SiO_2 - 40 nm PVD TiN - 40 nm anatase TiO_2 acting as an adhesion layer, current collector and thin-film electrode, respectively. The $LiMn_2O_4$ electrode constituted a stack of 60 nm PVD TiN - 80 nm PVD Pt - 100 nm PVD $LiMn_2O_4$ as current collectors and thin-film electrode, respectively.

Film thickness on the SiO_2 substrate was characterised by X-ray reflectivity (XRR) measurements using a copper X-ray source (Cu Kα radiation at 0.154 nm) and a point detector. XRR was not possible for the films on the electrode substrate due to the substrate complexity, so alternative thickness characterisation was used. For the ALD Al_2O_3 films, spectroscopic ellipsometry (SE) was performed for the films on the SiO_2 substrate and on the electrode substrate. The ALD Al_2O_3 film thickness was fitted using a Cauchy model, resulting in a good match of the thickness to the XRR-measured values. The ellipsometer used was a J.A. Woollam M-2000 with a wavelength range of 245 nm to 1000 nm. X-ray fluorescence was used to evaluate the amount of titanium deposited on the substrates. A Mo K_α X-ray source was used for these measurements.

Electrochemical characterisation was carried out in an Ar-filled glove box (O_2 <1 ppm, H_2O <1 ppm) with a Metrohm Autolab PGSTAT702 potentiostat/galvanostat connected to a three-electrode cell. Electrical contact of the working electrode was established by contacting the thin-film current collectors exposed at the side of the samples to a copper foil, using a silver paste. Lithium ribbon (99.9 %, Sigma Aldrich) was used as counter- and reference electrodes, and 1M $LiClO_4$ in propylene carbonate (99 %, io-li-tec) was used as Li^+ electrolyte solution. Impedance spectroscopy was performed using an Autolab PGSTAT702 potentiostat equipped with an impedance module. The frequency ω of the applied modulation was varied between 100 kHz and 0.1 Hz. A sinusoidal perturbation of 10 mV was applied around the measured open circuit potential. From the phase shift (ϕ) and amplitude of the current response of the system, the complex impedance was determined for every frequency as $Z(\omega) = |Z(\omega)|e^{-j\phi(\omega)} = Z'(\omega) - jZ''(\omega)$.

Cross-sectional Scanning Electron Microscopy (cross-SEM) was used to evaluate the film surface morphology, using a FEI Quanta 200F high-vacuum electron microscope.

RESULTS AND DISCUSSION

The aim of this study is to examine the effect of an ultra-thin coating on TiO_2 and $LiMn_2O_4$ thin film electrodes. The coatings envisioned here

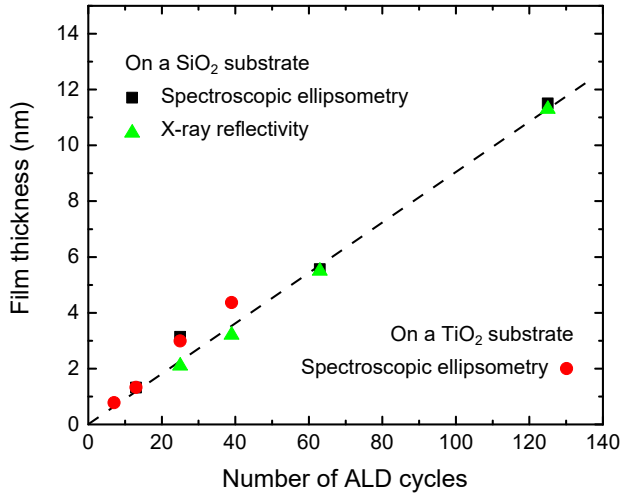

Figure 14.1: Thickness of the ALD Al_2O_3 film, deposited on SiO_2 substrates as a reference and on the TiO_2 electrode for electrochemical characterisation. Thickness measurements on the formed possible using x-ray reflectivity and spectroscopic ellipsometry, while the latter substrate only allowed spectroscopic ellipsometry.

are 0.5 nm, 1 nm, 2 nm and 3 nm of amorphous Al_2O_3, and 1 nm, 2 nm and 5 nm of amorphous TiO_2. Both are deposited using thermal ALD at 150 °C, using water as an oxygen precursor and TMA or TDMAT as a metal precursor for the alumina or titania, respectively. The number of ALD cycles was adapted to the growth rates of the respective ALD processes, which were found from the linear dependence of thickness on number of ALD cycles measured on a SiO_2 monitor substrate which was added to every deposition, as measured using XRR (figure 14.1 and figure 14.2(a)). XRR was not possible for the coated electrodes due to the complexity of the stack. To confirm the Al_2O_3 thickness, the films were measured using spectroscopic ellipsometry (SE), and a good agreement was found between the thickness measured by SE and XRR on both substrates. For the ALD TiO_2 coating, ellipsometry was not straightforward due to the ambiguity of the fitting, caused by the similar optical nature of the ALD TiO_2 and the TiO_2 in the electrode substrate. To overcome this, a relation was studied between the titanium XRF counts and the film thickness. Figure 14.2(a) shows a clear linear relation between the XRF counts and the film thickness. The titanium XRF counts of the ALD TiO_2-coated electrodes in figure 14.2(b) clearly show a similar trend, allowing us to conclude that the films are the same thickness on both the SiO_2 and the electrode substrates, as is expected for atomic layer deposition.

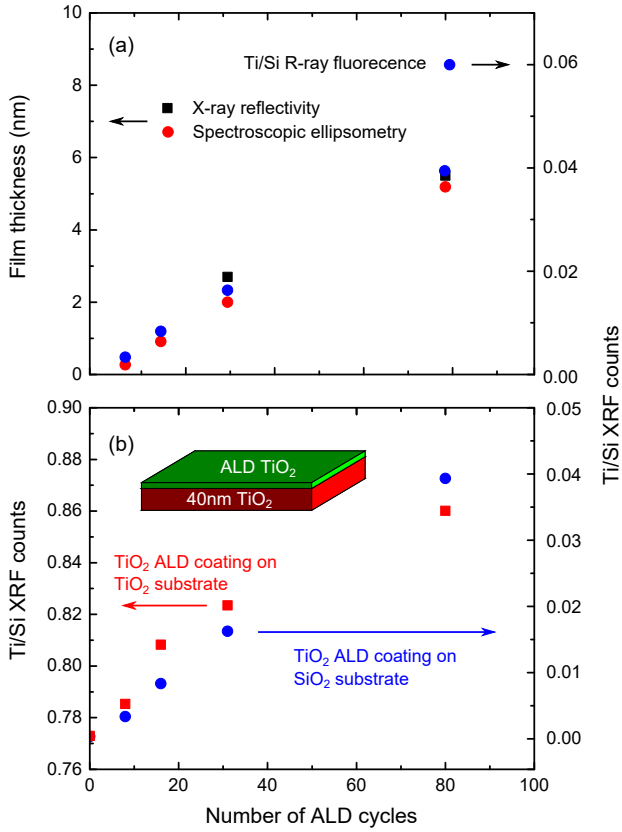

Figure 14.2: (a) Thickness of the ALD TiO_2 films deposited on a SiO_2 substrate, as measured by XRR and SE (left axis) and titanium XRF counts for the same films, scaled to the silicon XRF signal to account for measurement variations (right axis). (b) Titanium to silicon XRF signal ratio for the ALD TiO_2 films on the SiO_2 monitor substrate and on the TiO_2 electrode substrate.

Thin film TiO_2 as an ideal electrode model system

The coatings were deposited on 40 nm of anatase TiO_2. Since this is a near-zero volume expansion material with the active potential well above solvent reduction potential, very little intrinsic problems exist, making it an ideal model material. First, the kinetics of the electrode are tested by varying the current density from 1C to 200C, which corresponds to current densities equivalent to charging the theoretical capacity of the electrode in 1 hour and 18 seconds, respectively. The capacity retained at high C-rates gives information concerning the rate-limiting step of the charge-storage process, which is mostly related to charge transfer over the interface with a thin-film electrode. By modifying the interface with the ALD coatings, we can examine the effect of the coating on the kinetics. Figure 14.3 shows the results for the alumina- and titania-coated electrodes on two Peukert plots, ranging between 1C and 200C. The applied current densities for every C-rate were calculated from the theoretical capacity for TiO_2 (168 mA h g^{-1}), the density for bulk anatase TiO_2 (3.78 g cm^{-3}), the film thickness (40 nm) and the cell surface (0.9503 cm^2), resulting in a theoretical capacity of the electrodes of 2.4 µA h. The applied currents thus ranged from 2.4 µA (1C, (dis)charging in 1 hour) to 480 µA (200C, (dis)charging in 18 seconds).

From figure 14.3 (a) it is immediately apparent that an alumina coating has a detrimental effect on the kinetics. Even a coating as thin as 0.5 nm Al_2O_3 already shows a slow-down of the kinetics. A 1 nm Al_2O_3 reduces the 200C capacity to half the available 200C capacity for the uncoated TiO_2 electrode, and with a 2 nm Al_2O_3 coating only 7 % remains. A thicker layer, such as 3 nm Al_2O_3, no longer allows lithium storage in the underlying TiO_2 electrode. Thus, only ultra-thin layers of alumina can be used as a coating, and will be examined further. The TiO_2 coating on the other hand shows completely different behaviour. Rather than reducing the kinetics of the buried TiO_2 electrode, the excellent kinetics of the latter are maintained, and even slightly improved for very high C-rates. The latter effect could be caused by the ability of the coated amorphous TiO_2 to store lithium in the same potential range as the burried anatase TiO_2 layer. Since amorphous electrodes are known to exhibit excellent kinetics, a better capacity retention can be expected for the coating than the buried crystalline electrode affecting the charge/discharge kinetics at high C-rates. We realise that applying an amorphous TiO_2 coating onto the anatase TiO_2 electrode adds active material, as the amorphous TiO_2 lithiates in the same potential range as the anatase TiO_2. However, even for the 5 nm coating, the buried TiO_2 still makes up more than 85 % of the

electrode, so we argue that the lithiation capacity will still be dominated by the anatase TiO_2.

To unravel the mechanism behind the blocking nature of the Al_2O_3 coating, the coated electrodes were studied using cyclic voltammetry at varying sweep rates as well as using impedance spectroscopy. Figure 14.4 shows the cyclic voltammograms for a sweep rate of $1\,mV\,s^{-1}$. Generally, the peak current (I_p) of cyclic voltammetry experiments can be determined from

$$I_p = \alpha v^x \tag{14.1}$$

where v is the scan rate (in $V\,s^{-1}$). In this equation, the interpretation of α is dependant of the charge transfer mechanism, defined by the exponent x. For example, if $x = 0.5$ the charge transfer mechanism is an infinite diffusion length mechanism, and the ruling equation simplifies to the Randles-Sevcik equation, where α is related to diffusion. For higher values of x, the diffusion region becomes smaller than the system itself, which in the ultimate case results in a capacitor for $x = 1$. In general, α is thus related to both diffusion and kinetic components. By varying the scan rate from $1\,mV\,s^{-1}$ to $100\,mV\,s^{-1}$ for the uncoated and coated electrodes and extracting the peak currents for each scan rate, as is shown in figure 14.5 for the uncoated TiO_2 electrode, α and x can be determined from the fit between peak current I_p and the scan rate v. The fits according to equation 14.1 for every electrode are shown in figure 14.6, and indicate an excellent agreement between data and fit.

Figure 14.7(a) shows the resulting α-parameters for lithiation and delithiation of the coated thin-film electrodes, scaled to the parameter for lithium extraction from the uncoated electrode (α_0). Several observations can be made from these data. First, it is clear that the alumina coating has a very negative effect on the insertion and extraction of lithium into the electrode, as α is reduced significantly even for a coating of only 0.5 nm of ALD Al_2O_3. Thicker coatings cause an ever bigger decrease: for 2 nm ALD Al_2O_3 α/α_0 is reduced to 65 % for the lithium insertion, and almost one orders of magnitude for lithium extraction from the electrode. ALD Al_2O_3 layers above 2 nm are no longer transparent for lithium, and render the buried electrode inaccessible for ion storage. For the ALD TiO_2 coating, α is practically constant, almost independent of coating thickness. For thin TiO_2 coatings, a slight improvement could even be observed. These observations further solidify the blocking nature of the ALD Al_2O_3 coatings, and conductive nature of the TiO_2 coating. Futhermore, figure 14.7(b) shows the power x of equation 14.1. For the uncoated electrode, the power lies just above 0.5, indicating finite length diffusion as the predominant rate limiting step. While the TiO_2 ALD coating barely modifies this value,

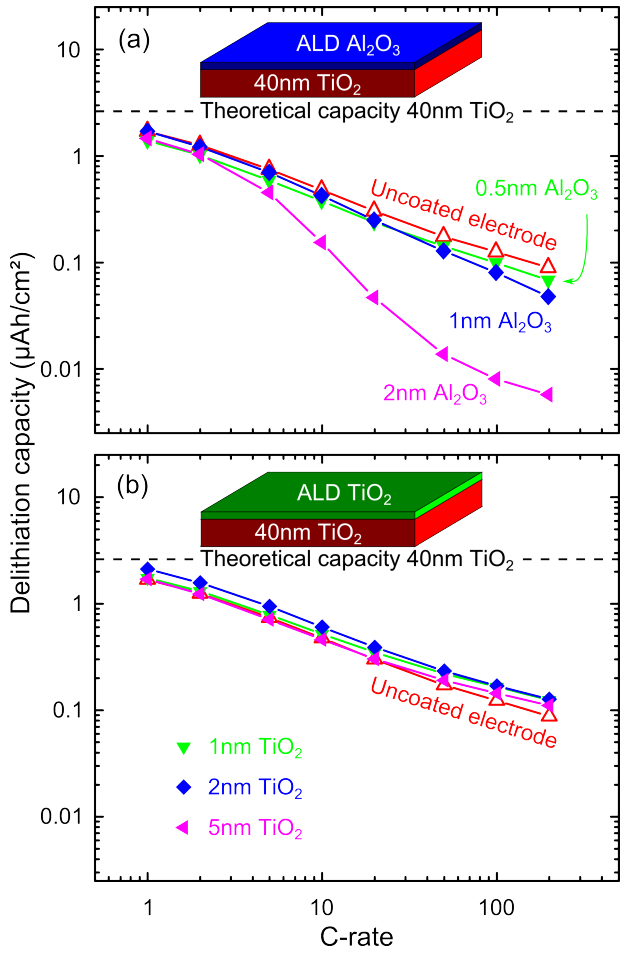

Figure 14.3: Peukert plot, showing the delithiation capacity of the electrodes under study, measured by charging and discharging the films at current densities varying from 1C to 200C between 1.0 V and 3.0 V *vs* Li^+/Li.

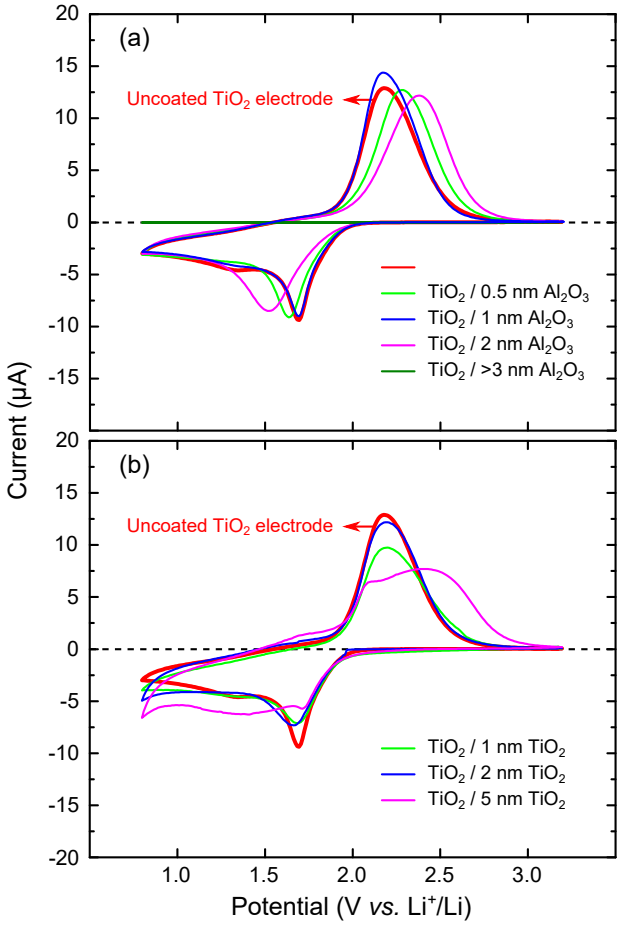

Figure 14.4: Cyclic voltammetry of the 40 nm thin film anatase TiO_2 electrodes, coated with ALD Al_2O_3 (top) and ALD TiO_2 (bottom). The potential was varied at 1 mV s^{-1} between 0.8 V and 3.2 V *vs* Li^+/Li.

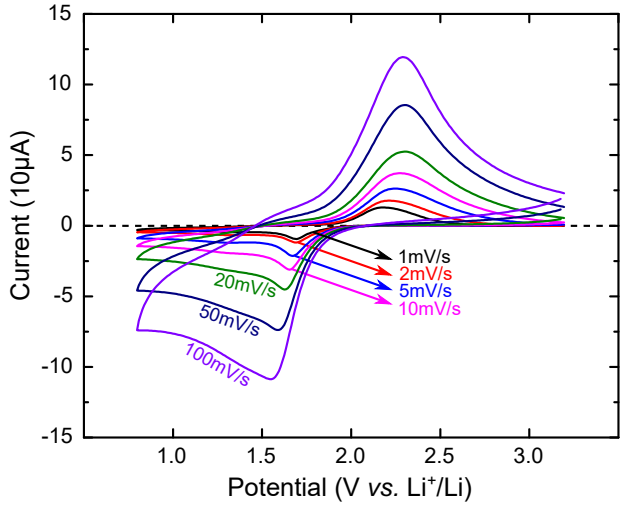

Figure 14.5: Cyclic voltammetry of the uncoated 40 nm TiO_2 electrode at scan rates from 1 mV s^{-1} to 100 mV s^{-1} in the 0.8 V to 3.2 V *vs* Li^+/Li range.

the Al_2O_3 ALD coating lowers the value significantly. This is indicative of a severe iR drop (Ohmic drop), as this modifies the electrode potentials and thus makes the measurements hard to interpret without iR corrections, as this also influences the applied scan rate.

A second observation than can be made from figure 14.7 (a), is the difference in diffusion parameter between lithium insertion and lithium extraction. For the uncoated sample, the α parameter is almost equal for lithiation and delithiation, with the former found at 99 % of the latter. The α-values are almost unmodified by the TiO_2 coatings and are all between 1.01-1.50, i.e. very close to the value for the uncoated electrode. For ALD Al_2O_3 coatings on the other hand, the ratio rapidly decreases with increasing coating thickness: the $\alpha_{extraction}$ to $\alpha_{insertion}$ ratio varies from 80.0 %, 71.6 % to 25.3 % for 0.5 nm, 1.0 nm and 2.0 nm of ALD AlO_3, respectively. This indicates that lithium liquid-to-solid transfer of lithium ions across the Al_2O_3 interface is much easier than the solid-to-liquid transfer. The slow-down of the kinetics will thus be mainly attributed to slow delithiation, rather than slow lithiation. Although currently not completely understood, we hypothesize that this may be related to coulombic repulsion effect, as the Al_2O_3 layer will be a signification potential barrier to overcome to be insertion or extracted from the TiO_2. Depending on the insertion or extraction nature, this barrier may be higher or lower, and while a barrier

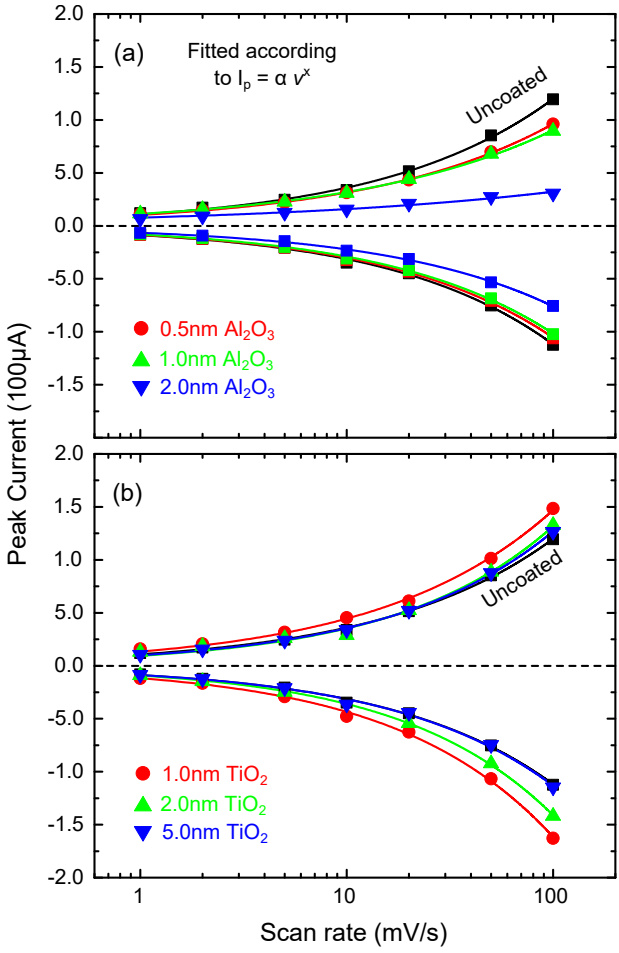

Figure 14.6: Electrochemical lithiation (negative) and delithiation (positive) peak current of the cyclic voltammograms measured for the TiO_2 electrodes, coated with with ALD Al_2O_3 (top) and ALD TiO_2 (bottom). The scan rate is varied between 1 mV s^{-1} to 100 mV s^{-1} in the 0.8 V to 3.2 V *vs* Li^+/Li potential window. The solid lines are fitted to the experimental data according to equation 14.1.

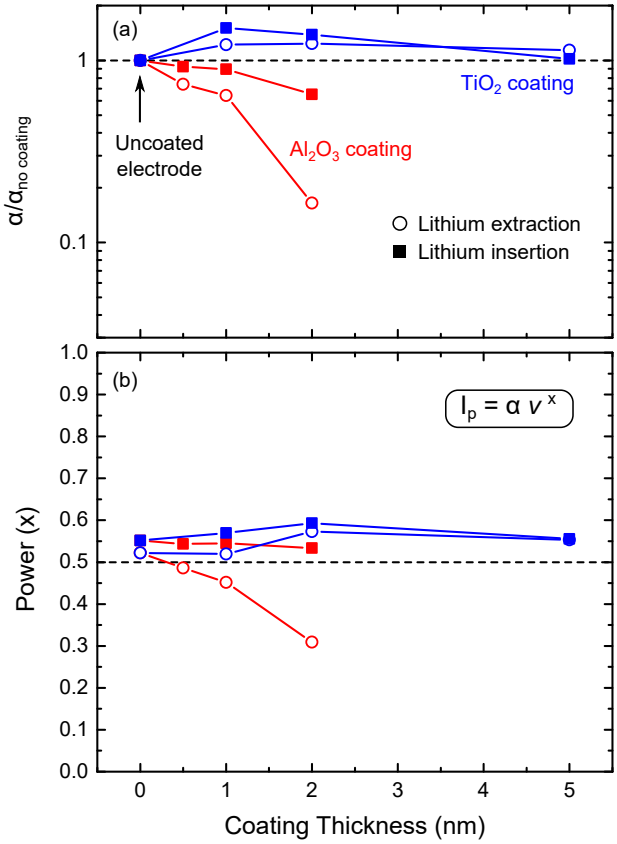

Figure 14.7: Diffusion-related parameter α, extracted from cyclic voltammetry experiments at varying scan rates and relating the observed peak currents to the scan rate as $I_p = \alpha\sqrt{v}$ (figure 14.6). α is normalised to the lithium extraction of the uncoated TiO_2 electrode, marked as α_0.

is imposed for both, it will be harder to overcome in one direction, which appears to be the extraction direction.

Besides peak current I_p, the peak potential V_p of the electrochemical lithiation and delithiation can also be extracted from the cyclic voltammetry experiments. An additional analysis based on Ohmic arguments can be found in supplementary (figures 15.1 and 15.2), which corroborates the conclusions above; i.e. the resistance for lithium goes up dramatically for the ALD Al_2O_3 coating with thickness, while the ALD TiO_2 layer barely modifies the lithium transfer resistance.

To truly unravel the blocking nature of the ALD Al_2O_3 coating, impedance spectroscopy was performed at open circuit potentials for the coated but uncharged electrodes. Plotting the imaginary part of the impedance $-Z''(\omega)$ as a function of the real part $Z'(\omega)$ for every frequency results in Nyquist plots, which are shown in figure 14.8 up to 50 kΩ. A figure displaying the lowest examined frequencies is shown in supplementary (figure 15.3). To analyse these spectra, a fit was made using the MEISP package developed by Barsoukov *et al.* [122]. The equivalent circuit used is shown in supplementary information (fig 15.3, and is made up of four parts, from high to low frequency elements:

1. a series resistance representing the electronic contacts and sheet resistance of the current collector (R_s)
2. an R-C circuit corresponding to charge transfer into the TiO_2 electrode modelled by a resistor (R_{ct}) and the accompanying double layer capacitance modelled by a constant phase element (CPE_{dl})
3. a second R-C circuit corresponding to charge transfer across the coating layer ($R_{coating}$ and $CPE_{coating}$)
4. a constant phase element corresponding to diffusion of lithium into the 'bulk' of the electrode (CPE_d)

The uncoated electrode was fitted without the second R-C circuit, as no coating was present on the samples (and no second half-circle was observed). The first R-C circuit has a rather high frequency response and produces a fairly small semi-circle which is not visible on figure 14.8. As a reference, a thicker film of 3 nm ALD Al_2O_3 on the electrode was also measured. For that system, no lithium could diffuse into the system, so the fit did no longer require the $R_{coating}$ (which became infinite) and CPE_d, since no lithium diffusion was present.

In an ideal system, the CPE_{dl} and $CPE_{coating}$ would be modelled by capacitors instead of a constant phase element. The latter corresponds to something between a capacitor and a resistor ($Z_{CPE} = 1/Y_0(j\omega^n)$).

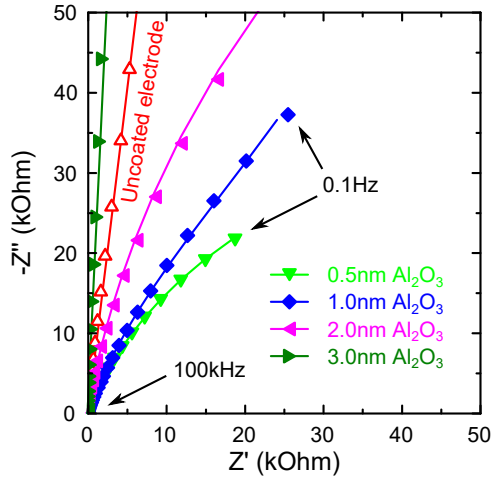

Figure 14.8: Electrochemical impedance spectra of the ALD Al_2O_3-coated electrodes between 100 kHz and 0.1 Hz, using a 10 mV perturbation around the open circuit potentials of the uncharged films. The top figure shows the experimental data (symbols) and the fits, made according to the equivalent circuit shown as inset in the bottom figure. The bottom figure shows the fitted data in a larger impedance range, demonstrating the lack of secondary half-circles for the uncoated and 3 nm-coated electrodes.

The solid lines on figure 14.8 are the obtained fits applying the equivalent circuit. These are good fits across the entire frequency spectrum, using the two modifications for the uncoated and 3 nm-coated samples, as described above. The coating-related R-C circuit's parameters, i.e. the coating charge-transfer resistance $R_{coating}$, and the double layer capacitance modelled by a constant phase element $CPE_{coating}$, are shown in figure 14.9. The resistance for lithium is shown in figure 14.9(a), and increases almost linearly from zero for the uncoated TiO_2, up to 0.3 MΩ for 2 nm of ALD Al_2O_3, corresponding to a resistivity of $1.5 \times 10^{12}\,\Omega\,cm$ for lithium transfer through ALD Al_2O_3. These high values of resistance for lithium transfer across the interface certainly explain the difficulty to insert lithium at high C-rates, corresponding to high currents, as the higher currents associated with the higher C-rates will cause considerable iR-drops across this interface, making lithiation virtually impossible. Furthermore, the double layer capacitance $CPE_{coating}$, modelled by a constant phase element, behaves more and more as an ideal capacitor: as the coating approaches 3 nm thickness, corresponding to a lithium-blocking film, the n-factor approaches 1. The n-factor of the CPE is a measure of the degree of deviation from an ideal capacitor or resistor: $n = 1$ corresponds to an ideal capacitor,

while $n = 0$ corresponds to a resistor. Upon increasing coating thickness, the film becomes less and less transparent for lithium, as is apparent from the increasing coating resistance, and behaves more and more as an ideal capacitor. At the blocking limit, a 3 nm coating behaves as an ideal capacitor, as lithium is stored on the one interface, and electrons on the other, and no lithium transfer and storage in the bulk of the TiO_2 film.

Thin film $LiMn_2O_4$ as model system for solvent oxidation

Since the TiO_2 electrode in the previous section is a near-ideal model system, no improvement is expected when a coating is used. Indeed, the kinetics of the anatase TiO_2 electrode are maintained by the best coating, i.e. the amorphous ALD TiO_2 coatings, but not improved, since they are already excellent and not degrading. Keeping in mind that this coating does not aggravate the kinetics in ideal situations, we can examine if it can also mediate certain known issues, and in that way improve the intrinsic kinetics. To that end, thin film $LiMn_2O_4$ is used as a model system. Several issues are present for $LiMn_2O_4$ as a cathode, mainly related to manganese dissolution related to Mn^{3+} (~ 3 V *vs.* Li^+/Li) and solvent oxidation related to the high oxidative nature of Mn^{4+} (> 4 V *vs.* Li^+/Li). The latter is a serious issue on overcharging. When the 4.0 V *vs* Li^+/Li range is exceeded, solvent oxidation can occur. Here, we artificially overcharge $LiMn_2O_4$ up to 4.5 V *vs* Li^+/Li to examine solvent oxidation, and the effect on cathode kinetics. By only using the 4 V *vs.* Li^+/Li range of the $LiMn_2O_4$, we don't encounter the metal dissolution issue, which is not the aim of this report. From the study above we know ALD Al_2O_3 is already a non-ideal coating, due to the resistive nature of the layer. However, for ultra-thin films (<2 nm), lithium can still pass reasonably well through the films. Therefore, a 1 nm of ALD Al_2O_3 is examined. For the ALD TiO_2, we have shown that the bulk of the layer does not impose a kinetic barrier, only the interface. Considering this, we examine a 5 nm of ALD TiO_2 on the $LiMn_2O_4$ cathode.

First, the electrodes were 'strained' by slowly charging and discharging between 3.5 V and 4.5 V *vs* Li^+/Li. Figure 14.10 shows the cyclic voltammogram of the 4.0 V *vs* Li^+/Li region of $LiMn_2O_4$ after 'straining' the electrode. The electrochemical signature of $LiMn_2O_4$, i.e. the 4.0 V *vs* Li^+/Li peak pair, is observed for both the uncoated $LiMn_2O_4$ and the $LiMn_2O_4$ covered with the ALD coatings. It is already apparent that the $LiMn_2O_4$ coated with 5 nm of ALD TiO_2 displays better kinetics, which is visible from the sharper and less separated peaks. The ultra-thin ALD Al_2O_3

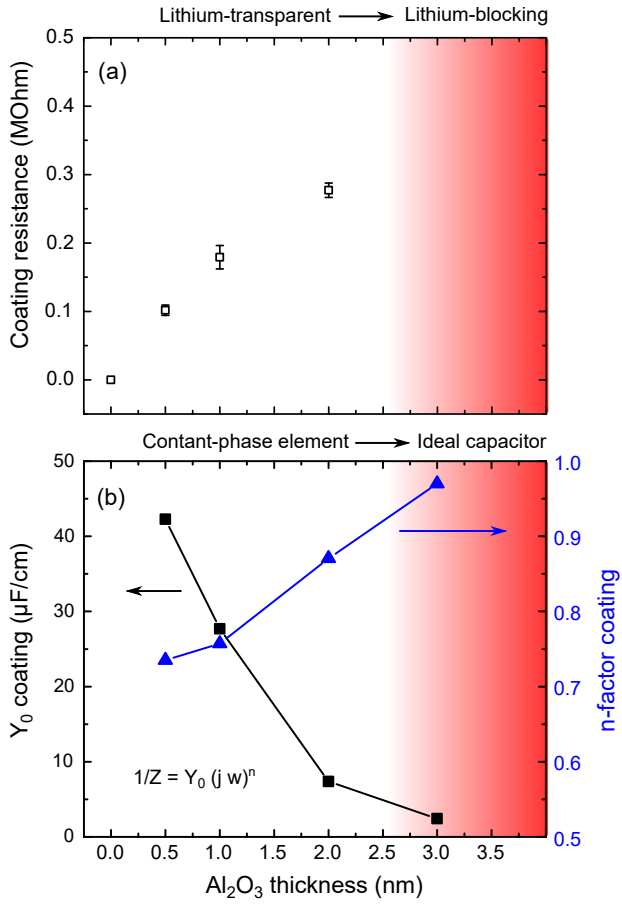

Figure 14.9: Electrochemical impedance spectra of the ALD Al_2O_3-coated electrodes between 100 kHz and 0.1 Hz, using a 10 mV perturbation around the open circuit potentials of the uncharged films. The figure shows the experimental data (symbols) and the fits, made according to the equivalent circuit shown supplementary.

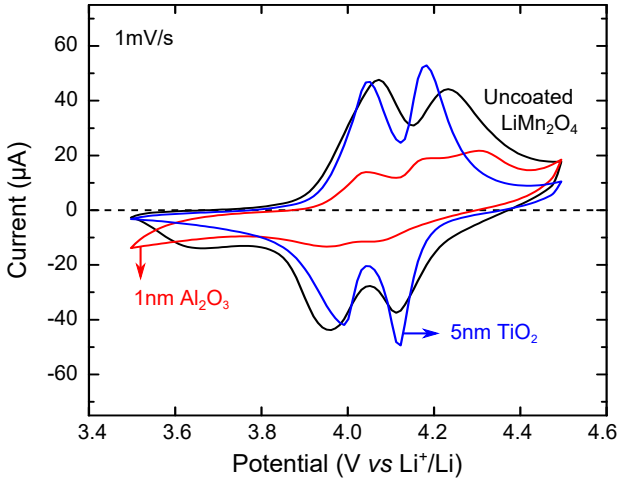

Figure 14.10: Cyclic voltammetry of the uncoated 100 nm thin film $LiMn_2O_4$ electrodes (black line), as well as the same film coated with either 1 nm of ALD Al_2O_3 (red line) or 5 nm of ALD TiO_2 (blue line). The potential was varied at 1 mV s^{-1} between 3.5 V and 4.5 V *vs* Li^+/Li.

coating on the other hand shows a strong supression of the peaks, which is caused by the blocking nature of these films.

The kinetics of the three 'strained' cathodes were studied. The Peukert plot (figure 14.11) shows the resulting capacities. C-rates were determined based on the theoretical capacity of $LiMn_2O_4$ in the 4V region (630 mA h cm^{-3}), film thickness (100 nm) and cell surface (0.9503 cm^2), resulting in a theoretical capacity of 6.0 µA h. At a current density of 6.3 µA h cm^{-2}, corresponding to a C-rate of 1C, the capacity is almost identical for both coated and uncoated films, and close to the theoretical capacity of $LiMn_2O_4$. At higher current densities, the capacity for the Al_2O_3-coated film drops dramatically. This is expected, and can be related to the resistive nature of the Al_2O_3 coating. Up to current densities corresponding to 5C, the capacity of the uncoated $LiMn_2O_4$ and the TiO_2-coated film is only decreasing slowly, and almost no effect of the coating is observed. However, beyond 5C the capacity of the uncoated $LiMn_2O_4$ film drops rapidly. The best kinetics are clearly attributed to the $LiMn_2O_4$ film coated with 5 nm of ALD TiO_2, far surpassing that of the uncoated $LiMn_2O_4$.

To examine the cause of these improved capacity retention at high C-rates, the 'straining' cycles of the three cathodes are examined. This activation is performed by charging and discharging the films at 3 µA, corresponding to a C-rate of 0.5C. The films are delithiated, lithiated and

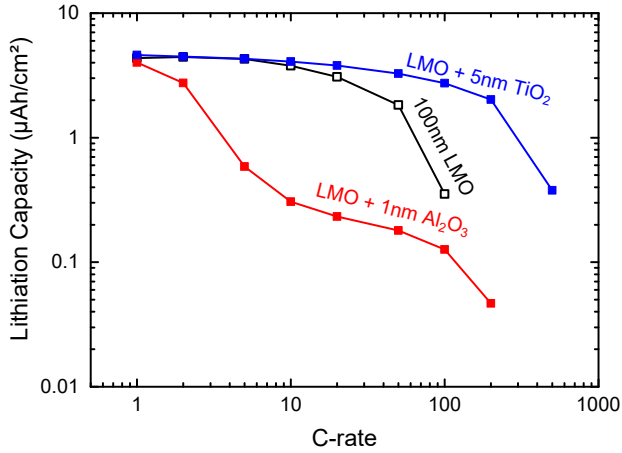

Figure 14.11: Delithiation capacity of the uncoated and coated $LiMn_2O_4$ electrodes under study, measured by charging and discharging the films at current densities between 3.5 V and 4.5 V *vs* Li^+/Li.

delithiated again between 3.5 V and 4.5 V *vs* Li^+/Li. Figure 14.12 shows the resulting potential profiles for uncoated and coated $LiMn_2O_4$, and the corresponding derivative charge profiles (dQ/dV) as a function of potential. The latter often reveal plateaus which are barely visible in the normal potential profiles. For the uncoated sample, overcharging the $LiMn_2O_4$ results in a capacity far larger than the theoretical capacity. The characteristic 4V $LiMn_2O_4$ features are clearly present as two plateaus just above 4.0 V *vs.* Li^+/Li and 4.2 V *vs.* Li^+/Li. However, as soon as the potential exceeds 4.3 V *vs.* Li^+/Li, the dQ/dV jumps up to a contant value, corresponding to an increasingly thick film growing on top of the $LiMn_2O_4$. Aurbach et al showed that the oxidation of the PC solvent can occur above 4.0 V *vs.* Li^+/Li on noble metal electrodes [392]. Due to the highly oxidative nature of Mn^{4+} in the discharged $Li_xMn_2O_4$, solvent oxidation can also occur at the cathode interface. Since this process is not reversible (only the two characteristic 4V $LiMn_2O_4$ features are observed during the subsequent lithiation step), this film corresponds to a thick permanent film grown on the $LiMn_2O_4$ surface. During the second charge, the same behaviour is observed, but the onset potential for the irreversible reaction is shifted upwards to 4.4 V *vs.* Li^+/Li, indicating that the film grown during the first irreversible reaction stabilizes the surface to some extent.

For the alumina-coated $LiMn_2O_4$ electrode, the onset of this irreversible reaction is 4.4 V *vs.* Li^+/Li from the first cycle, indicating that the 1 nm of ALD Al_2O_3 stabilizes the surface in a similar manner as the film grown

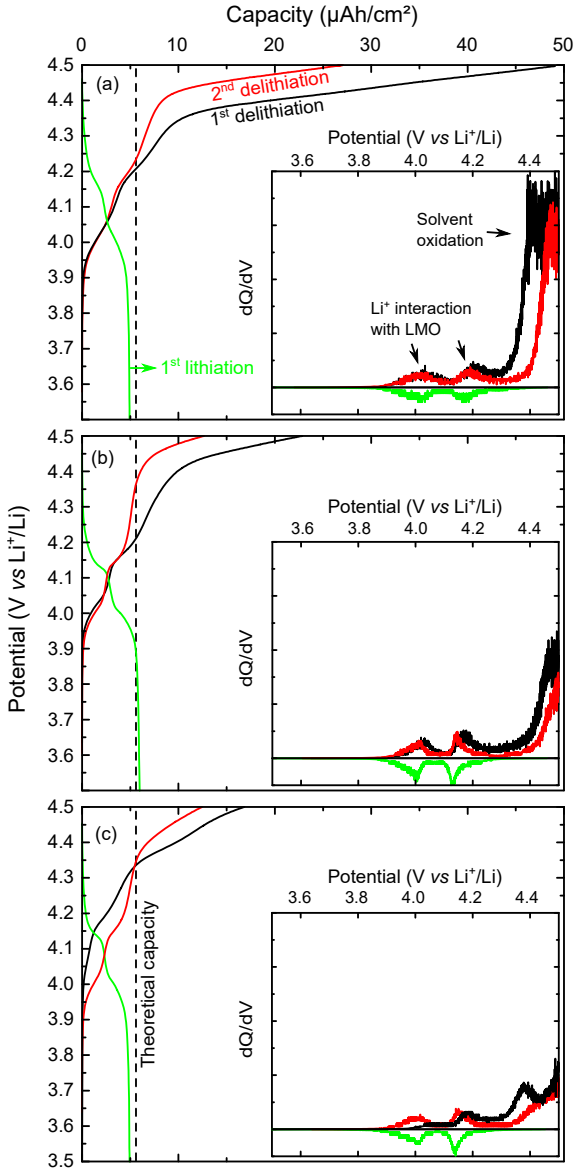

Figure 14.12: Potential profiles of the first delithiation, first lithiation and second delithiation of the (a) uncoated $LiMn_2O_4$, (b) $LiMn_2O_4$ coated with 1 nm of ALD Al_2O_3 and (c) $LiMn_2O_4$ coated with 5 nm of ALD TiO_2. A current of 3 μA was used, corresponding to 0.5C. The insets show the derivative of the charge profile as a function of potential.

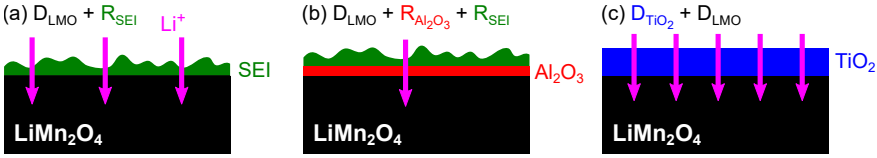

Figure 14.13: Schematic representation of the rate-determining factors for (a) uncoated $LiMn_2O_4$, (b) ALD Al_2O_3 coated $LiMn_2O_4$ and (c) ALD TiO_2 coated $LiMn_2O_4$. D represents diffusion, and R represents charge-transfer resistance.

during the first cycle of the uncoated $LiMn_2O_4$, but without the irreversible loss of charge resulting in a very low Coulombic efficiency for the uncoated $LiMn_2O_4$. Furthermore, the extent of irreversible lithium consumption is less for the alumina-coated $LiMn_2O_4$ than for the uncoated $LiMn_2O_4$. It's important to note that this is not caused by an iR drop over the coating, since the peak positions for the lithium insertion and extraction of the $LiMn_2O_4$ as not shifted compared to the uncoated films. Finally, the $LiMn_2O_4$ coated with 5 nm of ALD TiO_2 shows a slightly different behaviour. While the irreversible reaction above 4.3 V *vs.* Li^+/Li is clearly suppressed, even more so than was the case for the alumina-coated $LiMn_2O_4$, the two plateaus corresponding to the fingerprint of $LiMn_2O_4$ are shifted upwards almost 0.2 V for the first delithiation. During the subsequent lithiation and delithiation, the peaks are on their expected positions around 4 V *vs.* Li^+/Li and 4.2 V *vs.* Li^+/Li. This may indicate that the 5 nm of ALD TiO_2 needs to be 'activated' during the first delitiation cycle to allow lithium to pass through from the $LiMn_2O_4$ into to electrolyte, and once 'activated' it acts as a protective coating.

The presence of the irreversible reaction above 4.3 V *vs.* Li^+/Li for the uncoated $LiMn_2O_4$, and the suppression of it on the $LiMn_2O_4$ coated with 5 nm of ALD TiO_2, explains the improvement in kinetics observed in the Peukert plot in figure 14.11. Figure 14.13 summarizes the effect of the coatings in this case. For unprotected $LiMn_2O_4$, an SEI-layer is formed, posing an interface resistance as an additional rate-determining step (fig 14.11(a)). In the case of ALD Al_2O_3 coated $LiMn_2O_4$, this SEI formation is not suppressed, but a third rate-limiting step is present from the Al_2O_3 coating itself, further reducing the kinetics (fig 14.11(c)).

The reduced kinetics using the $LiMn_2O_4$ coated with 1 nm of ALD Al_2O_3 can be further explained when the layers are examined after the electrochemical tests in the scanning electron microscope. Figure 14.14 shows cross sections of the layers, as received and post-cycling. On the as-received $LiMn_2O_4$ (figure 14.14 (a)), we can clearly distinguish the silicon substrate at the bottom, the 60 nm TiN and 80 nm Pt making up the current

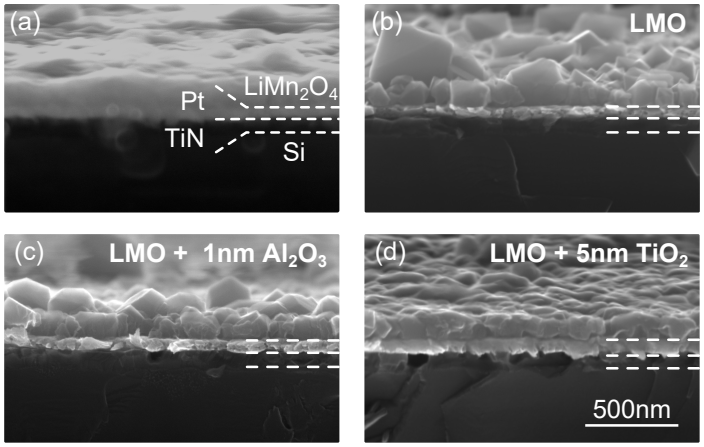

Figure 14.14: Cross section SEM images of (a) the as-recieved $LiMn_2O_4$, and the samples post-electrochemical cycling: (b) uncoated $LiMn_2O_4$, (c) $LiMn_2O_4$ coated with 1 nm of ALD Al_2O_3 and (d) $LiMn_2O_4$ coated with 5 nm of ALD TiO_2.

collector, and the 100 nm $LiMn_2O_4$ at the top, which is a relatively smooth layer. The cycled $LiMn_2O_4$ in figure 14.14 (b) still shows the clearly defined current collector layers, but the $LiMn_2O_4$ layer has developed a substantial amount of surface roughness and particle-like structures on the surface, likely related to this irreversible behaviour above 4.3 V *vs.* Li^+/Li. The $LiMn_2O_4$ coated with 1 nm of ALD Al_2O_3 in figure 14.14 (c) still shows this effect of severely enhanced roughening, so even though the 1 nm of ALD Al_2O_3 layer can delay the formation of the solid electrolyte interface layer and accompanying surface roughness by 0.1 V, it still happens under the conditions studied here. This results in the poorest kinetics, due to the combination of a double kinetic bottleneck: lithium has to pass both the solid electrolyte interface layer and the resistive Al_2O_3 layer. Finally, the ALD TiO_2 layer does not exhibit the extreme roughening of the surface, as can be seen from figure 14.14(d). Electrochemically, the signature of the solvent oxidation at high potentials is not completely suppressed (figure 14.12(c)), but the surface morphology is clearly more pristine than the uncoated and Al_2O_3-coated $LiMn_2O_4$ electrodes. As shown in figure 14.11(c), this lack of imposition of a rate-determining step other than the diffusion through the TiO_2 layer itself, which is not a kinetically limiting factor as was demonstrated from the experiments on thin film TiO_2, gives us a better understanding of the improved kinetics the ALD TiO_2-coated $LiMn_2O_4$ compared to the uncoated $LiMn_2O_4$ in the case of overcharging.

CONCLUSIONS

In this work, we studied the effect of ultra-thin (<10 nm) coatings on electrodes. Thin-film electrodes were used as model systems as they ensure simple one-dimensional current flow and avoid the influence of binders and conductive agents that are required in traditional powder-based electrodes. An ideal model system, thin-film anatase TiO_2, showed that ALD Al_2O_3 coatings are a kinetic barrier for lithium, which is detrimental for the electrode kinetics even for very thin coatings. As soon as the Al_2O_3 films are made too thick (>2 nm), they are completely blocking for lithium ions and display capacitive properties. ALD TiO_2 coatings on the other hand were shown to be never blocking in the investigated thickness regime, and only generate an interfacial resistance. As no bulk resistance was found, the TiO_2 does not constitute and impediment during charging and discharging. The performance of these coatings on a non-ideal system was examined by artificially overcharging thin-film $LiMn_2O_4$ up to 4.5 V *vs.* Li^+/Li. In that case, we find that an Al_2O_3 coating again worsens the kinetics of the electrode dramatically, while a TiO_2 coating remarkably improves it. The improvement was shown to be related to a strong reduction of a solid electrolyte interface formation above 4.3 V *vs.* Li^+/Li, in combination with the lithium conducting nature of the TiO_2 coating. This enables us to conclude that, even though the most investigated ALD coating for lithium ion batteries remains Al_2O_3, this coating material will not work for high-power electrodes due to kinetic limitations. Lithium-conducting coating materials such as TiO_2 can provide interfacial protection while maintaining far superior electrode kinetics.

15

SUPPLEMENTARY TO PAPER V

CYCLIC VOLTAMMETRY

To examine the electrode kinetics, cyclic voltammetry at a range of sweep rates was performed. The sweep rate was varied between $1\,\mathrm{mV\,s^{-1}}$ and $100\,\mathrm{mV\,s^{-1}}$ in the potential range between $0.8\,\mathrm{V}$ *vs.* $\mathrm{Li^+/Li}$ and $3.2\,\mathrm{V}$ *vs.* $\mathrm{Li^+/Li}$. Peak potentials V_p and peak currents I_p of the electrochemical lithiation and delithiation can be extracted from the cyclic voltammetry experiments as described above. The peak potential can be deconstructed to a contribution of the electrode potential U_p, which is the energy of the redox reaction of lithium with the $\mathrm{TiO_2}$ ($\mathrm{Li^+ + e^- + TiO_2 \longleftrightarrow LiTiO_2}$) and a factor related to resistance R, as follows:

$$V_p = U_p + I_p \times R \tag{15.1}$$

Raising the scan rate implies higher currents and more shifted potentials. By performing CV measurements are varying scan rates, an array of V_p-I_p couples can be extracted, and a resistance R can thus be found as the slope of the peak current versus peak potential, for every sample, and the intercept with the potential axis will correspond to U_p. Due to the potential-driven and non-equilibrium nature of the cyclic voltammetry, this does not correspond to an actual impedance of the layer, but rather gives an indication of the barriers that have to be overcome for lithium insertion and extraction.

The validity of this approach was verified by evaluating the peak current and peak potentials, and linear behaviour was found at scan rates below $10\,\mathrm{mV\,s^{-1}}$, as is shown in figure 15.1. For some samples, iR drops at the high scan rates resulted in peak shifting beyond the measured potential borders, which were not considered further to extract parameters. While the peak current varied with scan rate according to a power law (see main article), the peak potential displayed a step at scan rates of $10\,\mathrm{mV\,s^{-1}}$. We observe that the low scan rates (and low currents) are iR controlled, while the high currents and scan rates are kinetically controlled. High

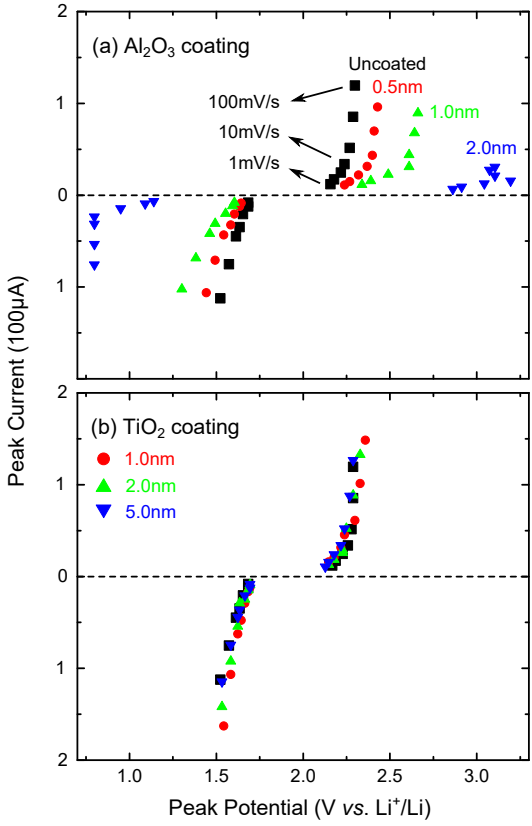

Figure 15.1: Peak current and peak potentials for the TiO_2 electrodes coated with (a) ALD Al_2O_3 and (b) ALD TiO_2, extracted from the cyclic voltammetry experiments performed at a range of scan rates between $1\,mV\,s^{-1}$ and $100\,mV\,s^{-1}$.

currents seem to change the applied potential so far from the electrodepotential that an electrostatic barrier can be overcome, which prevents further change in the applied potential in respect to the electrodepotential. To extract a resistance from an iR-like relation, only the lower range of scan rates ($\leq 10\,mV\,s^{-1}$) were considered. Figure 15.2 shows the evolution of the electrochemical potential and relative resistance change compared to the uncoated electrode as a function of coating thickness for the ALD Al_2O_3- and ALD TiO_2-coated electrodes. The electrode potentials remain constant for the ALD TiO_2-coated electrodes, and are decreased/increased by the ALD Al_2O_3 coating due to the iR drop for lithium insertion/extraction, respectively. The average between the insertion and extraction electrode potentials remains constant, independent of the coating, indi-

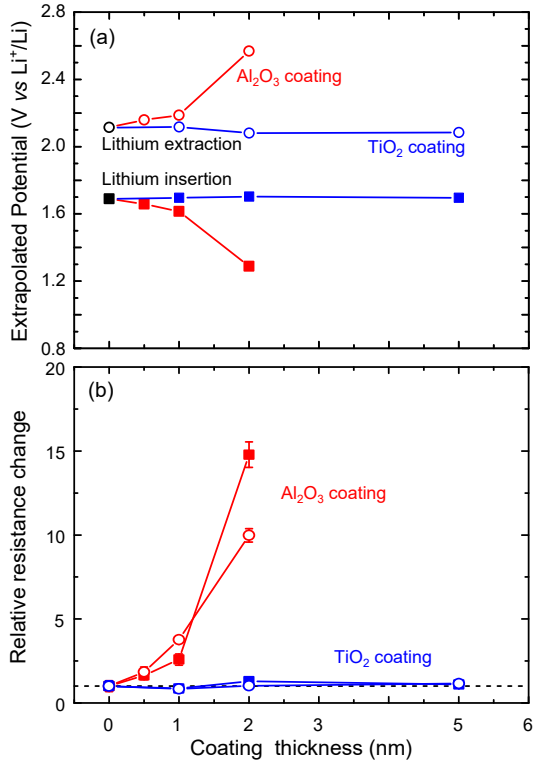

Figure 15.2: Extrapolated peak potentials (top) and relative resistance change (bottom) according to equation 15.1, extracted from the cyclic voltammetry experiments at varying scan rates.

cating that the electrochemical potential is irrelevant of the coatings and the electrode is unchanged by the coating process. Figure 15.2 (b) reveals the same conclusion: the resistance for lithium goes up dramatically for the ALD Al_2O_3 coating with thickness, while the ALD TiO_2 layer barely modifies the resistance.

ELECTROCHEMICAL IMPEDANCE SPECTROSCOPY

In the main paper, electrochemical impedance spectroscopy is performed on ALD Al_2O_3-coated thin-film TiO_2 electrodes. There, the spectra are presented up to 50 kΩ for clarity. For completeness, the fits to the same spectra are presented here in the full examined frequency range, and plotted up to 700 kΩ. Figure 15.3 shows these spectra and the equivalent circuit they are fitted to.

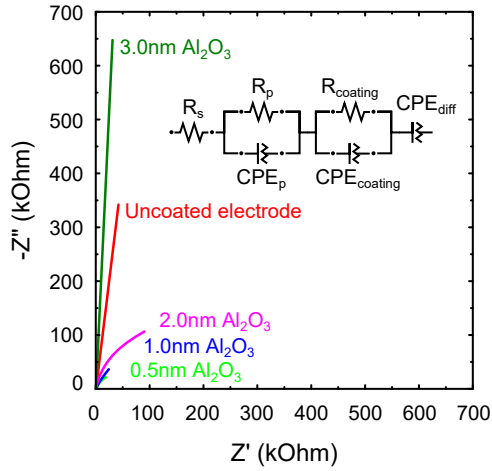

Figure 15.3: Fitted electrochemical impedance spectra of the ALD Al_2O_3-coated electrodes between 100 kHz and 0.1 Hz, using a 10 mV perturbation around the open circuit potentials of the uncharged films. The fits are made to the equivalent circuit shown as inset.

16

PAPER VI

HETEROGENEOUS TiO_2/V_2O_5/CARBON NANOTUBE ELECTRODES FOR LITHIUM-ION BATTERIES

Mert Kurttepeli,[*a] Shaoren Deng,[*b] Felix Mattelaer,[*b] Daire J. Cott,[c] Philippe M. Vereecken,[c] Jolien Dendooven,[b] Christophe Detavernier,[b] and S. Bals[a]

Published in *ACS Applied Materials & Interfaces* (2017). Doi: 10.1021/acsami.6b12759

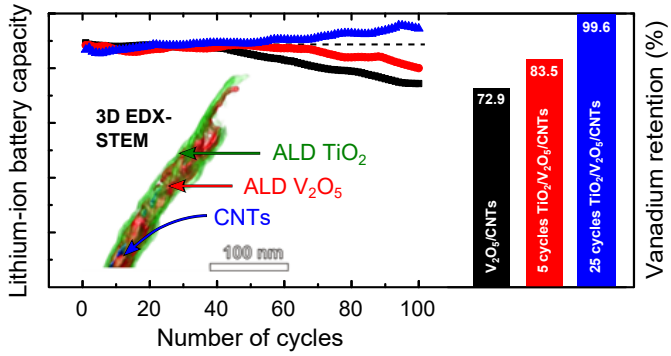

[*] *Contributed equally to this paper.*
[a] *Department of Physics, University of Antwerp, Groenenborgerlaan 171, Antwerp, Belgium,*
[b] *Department of Solid State Sciences, Ghent University, Krijgslaan 281 S1, 9000 Gent, Belgium,*
[c] *imec, Kapeldreef 75, 3001 Leuven, Belgium*

ABSTRACT

Vanadium pentoxide (V_2O_5) is proposed and investigated as a cathode material for lithium-ion (Li-ion) batteries. However, the dissolution of V_2O_5 during the charge/discharge remains as an issue at the V_2O_5-electrolyte interface. In this work, we present a heterogeneous nanostructure with carbon nanotubes supported V_2O_5/titanium dioxide (TiO_2) multilayers as electrodes for thin-film Li-ion batteries. Atomic layer deposition of V_2O_5 on carbon nanotubes provides enhanced Li storage capacity and high rate performance. An additional TiO_2 layer leads to increased morphological stability and in return higher electrochemical cycling performance of V_2O_5/carbon nanotubes. The physical and chemical properties of TiO_2/V_2O_5/carbon nanotubes are characterized by cyclic voltammetry and charge/discharge measurements as well as electron microscopy. The detailed mechanism of the protective TiO_2 layer to improve the electrochemical cycling stability of the V_2O_5 is unveiled.

INTRODUCTION

Lithium ion batteries (LIBs) are excellent power sources for a variety of applications, such as wearables, medical implants, wireless sensors and smart textiles due to their small form factor and high energy density [398]. By using thin films as electrodes, the ionic and electronic pathways in the battery are much shorter and more efficient, which enables the use of high power applications that require fast charging and discharging. The disadvantage of using thin films is their low storage capacity due to their limited thickness. However, this can be overcome by the application of thin-film electrodes on a complex 3D substrate, with an enhancement of the capacity enabled by the available surface enhancement [64, 186, 399, 400]. In this respect, carbon nanotubes (CNTs) are a well-known template for high-energy and high-power applications, because of their high surface area and their ability to function as an excellent current collector. However, a fully conformal coating technique is required to enable the use of CNTs as a template for 3D thin film LIBs. As a result of the self-limiting nature of the reactions between the gas-phase precursor and the substrate, atomic layer deposition (ALD) is the ideal technique to reach this goal [69, 71, 72, 75, 401]. Indeed, ALD metal oxide layers, such as vanadium pentoxide (V_2O_5) or titanium dioxide (TiO_2), deposited onto CNTs templates have already been proven to be useful as electrode materials [30, 80, 81, 84, 265, 266, 310].

Vanadium oxides and more specifically V_2O_5 have been widely investigated as LIB cathode materials. V_2O_5 layers are of great interest due to their high specific capacity, natural abundance, and lower toxicity in comparison to currently used cathode materials [28, 38, 218, 219, 402, 403]. Generally, vanadium pentoxide is not considered ideal as a cathode for a classical lithium ion battery due to its moderate electronic conductivitiy (10×10^{-3} S cm to 10×10^{-2} S cm) and low lithium diffusion coefficients (10×10^{-13} cm^2 s^{-1} to 10×10^{-12} cm^2 s^{-1}) [233, 404–406]. For short diffusion paths, such as thin-film cathodes, on top of good conductivity 3D templates, such as CNTs, these limitations can be overcome [407, 408]. In fact, summarized in a recent review by Huang et al, nanostructuring is one of the three main strategies to enable the use of vanadium pentoxides, alongside carbon hybridization and cation doping [283]. Up to 3 lithium ions can be stored in V_2O_5, yielding a theoretical capacity of 442 mA h g^{-1}, well above the capacity of $LiCoO_2$, which is traditionally used as cathode in commercial LIBs. However, only the insertion of one lithium ion is found to be reversible, due to breaking of chemical bonds upon further lithiation, initiating vanadium dissolution and breakdown of the crystal structure [221, 223]. Metal ion dissolution is not only an issue for V_2O_5, but is a significant factor in capacity fade in many cathode materials, for example in $LiMn_2O_4$ [397].

Protective coatings have been found to alleviate this issue largely. So far, Al_2O_3 buffer layers have been mostly used, since these layers have a protective function against solid-electrolyte interphase (SEI) formation at the anode side [348, 349, 409] and metal dissolution at the cathode side [355, 356]. However, Al_2O_3 is essentially ionically blocking, so this coating is a kinetic bottleneck that can only offer the desired protective function if the layer is made ultra-thin (<1 nm) [356, 410]. Thus, the protective function of Al_2O_3 ensuring no loss in energy density causes a loss in power density. Other coating materials that are not ionically blocking, such as TiO_2, can also be deposited using ALD and they show similar protective functions, while the compromise in power density can be avoided [310, 341, 349, 367]. For example, it was shown that applying a 2 nm to 3 nm layer of ALD TiO_2 on graphite improves the diffusion coefficient for lithium ions [349]. It was furthermore shown that a layer of up to 30 nm TiO_2 enhances the rate performance and the capacity retention in graphite, indicating that the TiO_2 layer does not become a kinetic bottleneck even at higher thicknesses, while at the same time the capacity retention properties are improved [367]. Recently, Xie et al reported the first work dealing with ALD TiO_2 on amorphous V_2O_5 coated on CNTs as a protective coating to deal with the vanadium dissolution [310]. They showed improvement in

cyclability in the 1.5 V to 4.0 V *vs* Li^+/Li region, however, within this potential region TiO_2 itself also inserts lithium, degrading the stability over long term electrochemical cycling [355].

Here, we investigate CNT-supported ALD crystalline V_2O_5 cathodes in the medium charge-discharge regime (down to 2.0 V *vs* Li^+/Li, lithiating V_2O_5 to $Li_2V_2O_5$). This paper reports the balance between performance and capacity as a function of the thickness of ALD deposited TiO_2 layers on V_2O_5/CNTs cathodes. By using advanced electron microscopy techniques, such as energy dispersive X-ray spectroscopy-scanning transmission electron microscopy (EDX-STEM) tomography, the complex 3D structure and composition of the TiO_2 and V_2O_5 layers is characterized. Our results show that a remarkable rate capability and stable electrochemical cyclic performance is achieved from these TiO_2/V_2O_5/CNTs layered nanomaterials. Our measurements furthermore reveal that the thickness of the TiO_2 layer has a significant effect on the stability of the V_2O_5/CNTs cathodes by affecting the phase transition of V_2O_5, as well as resolving the vanadium dissolution issues.

EXPERIMENTAL

Carbon nanotubes growth on Silicon substrate

Multiwalled CNTs (MWCNTs) were grown from a 1 nm (nominal) Co catalyst layer deposited on a Si wafer with a diameter of 200 mm. To avoid diffusion of the Co into the Si, a 70 nm TiN was first sputter deposited onto the Si surface (Endura PVD tool, Applied Materials, USA). MWCNTs were grown in a microwave (2.45 GHz) plasma enhanced chemical vapor deposition chamber (PECVD, TEL, Japan). In a typical experiment the Co catalyst layer was exposed to a NH_3 plasma for 5 minutes to transform the film into active metal nanoparticles for CNT growth. Then a C_2H_4/H_2 mixture was flowed into the chamber at a temperature $>550\,^{\circ}C$ for 30 minutes [411].

ALD-based coatings of TiO_2-VO_x-TiO_2 layers

MWCNTs were loaded into a homemade ALD system with a base pressure of 2×10^{-7} mbar. Metalorganic precursors and water (for VO_x)/ozone (for TiO_2) were alternatively pulsed into the chamber while the MWCNTs sample was heated up to 150°C in case of VO_x and 100 °C in case of TiO_2. Tetrakis-(ethylmethylamino) vanadium (TEMAV) (Air Liquide) and Tetrakis-(dimethylamido) titanium (TDMAT) (99.9 %, Sigma Aldrich)

were used as metal precursors for VO_x and TiO_2, respectively [412, 413]. To achieve a conformal coating on the MWCNTs forest, 20 s to 30 s precursor pulses at a pressure of 0.4 mbar to 0.5 mbar were applied. The pumping time was chosen as twice the pulse time to ensure sufficient evacuation of the residual precursor vapor and reaction products, thus avoiding chemical vapor deposition inside the forest of CNTs. 85 ALD-cycles have been applied on the CNTs template for VO_x coating. In a home-modified *in situ* XRD system (Bruker D-8) with heating stage, prior to ALD of TiO_2, VO_x/CNTs arrays were annealed from 20 °C to 325 °C at a rate of $5\,^{\circ}\,min^{-1}$ in air and kept at 325 °C for 1 hour for the phase transformation of VO_x coating into V_2O_5. Subsequently, 5 and 25 ALD-cycles have been applied on the V_2O_5/CNTs for TiO_2 coating in order to obtain different thicknesses. The schematic representation of the synthesis route applied to the materials investigated here can be found in the supplementary information (SI) Figure 17.1.

SEM and TEM characterizations

Cross-sections of the uncoated V_2O_5/CNTs and TiO_2/V_2O_5/CNTs were characterized using a scanning electron microscope (SEM-FEI Quanta) in order to resolve the morphology of the nanotube forests. Transmission electron microscopy (TEM) specimens were prepared from the samples and studied with a variety of techniques in order to obtain more detailed information. Samples were prepared by scraping off the Si wafer surface and suspending the resulting powder in ethanol. A drop of this suspension was deposited on a carbon coated TEM grid. High-resolution TEM (HRTEM) was performed using a FEI Osiris operated at 200 kV. High-angle annular dark field scanning TEM (HAADF-STEM) images and energy-dispersive X-ray (EDX) elemental maps were collected using an aberration corrected cubed FEI Titan operated at 200 kV, equipped with a Super-X detector for EDX analysis.

EDX-STEM tomography experiments

An aberration corrected cubed FEI Titan microscope equipped with a Super-X detector was used to acquire EDX elemental maps and to perform simultaneous HAADF-STEM at an acceleration voltage of 120 kV. Tilt series were acquired using an advanced tomography holder from Fischione Instruments (Model 2020). The hybrid nanomaterial system in our study consists of constitutional elements such as C, O, Ti, and V with atomic numbers (Z) of 6, 8, 22 and 23, respectively. Elemental maps were

obtained by scanning of individual frames of same location and summing multiple frames with a constant dwell time for different tilt angles. Data acquisition consisted of a EDX-STEM tomography procedure where each 256Œ256 pixel elemental map was acquired for constant collection times using Bruker Esprit^{TM} software together with simultaneous HAADF-STEM images. The elemental maps were acquired at a beam current of 0.2 nA. The total acquisition time was ∼4 h which is the total duration for simultaneous HAADF- and EDX-STEM tilt series acquisition including the tracking/focusing. Each tomography tilt series consisted of 31 HAADF images and EDX maps for each element acquired over a tilt range of ±75° using a tilt increment of 5°. Alignment of the data was carried out by cross correlation as implemented in the FEI Inspect3D software package. The reconstruction was performed using the t'Simultaneous Iterative Reconstruction Technique' (SIRT) with 25 iterations implemented in FEI Inspect3D. Amira (Visage Imaging GmbH) was used for visualization of the reconstructed volume.

Electrochemical testing of TiO_2/V_2O_5/CNTs electrodes

Electrochemical measurements were performed using a custom-built three-electrode Teflon cell. The Teflon cell was clamped onto 2 cm × 2 cm samples using a Viton O-ring. The geometrical surface area of the exposed electrode was 0.9503 cm^2. A lithium metal sheet and a wire were used as a counter and reference electrode, respectively. The Li reference electrode was placed in a capillary with the tip placed less than 1 mm from the electrode surface. Contact was made to the bare TiN underlayer with a crocodile clip at the edge of the sample (outside of the glass cell). The electrolyte used was 1.0 M $LiClO_4$ in propylene carbonate (PC) (99 %, ioli-tec). All of the operations on the cell assembly were carried out in a glove box filled with argon gas in which both the water and oxygen concentrations were less than 1ppm. A potentiostat/galvanostat Autolab PGSTAT302 (Metrohm Autolab) was used to perform all of the electrochemical experiments, which were controlled through Nova 1.8 software. All of the voltages are given versus the Li^+/Li.

Cyclic voltammograms (CV) were recorded starting from the open-circuit potential between 4.00 V and 2.00 V *vs* Li^+/Li at a scan rates of 10 mV s^{-1}. Subsequently, galvanostatic cycling was performed between 4.00 V to 2.00 V *vs* Li^+/Li at various current densities (C-rates) to evaluate the rate and electrochemical cycle performance. For the charging rate, 1C was determined based on the charge calculated from the discharge capacity with a 0.5 mV s^{-1} CV. To account for variations in the CNT densities on the sub-

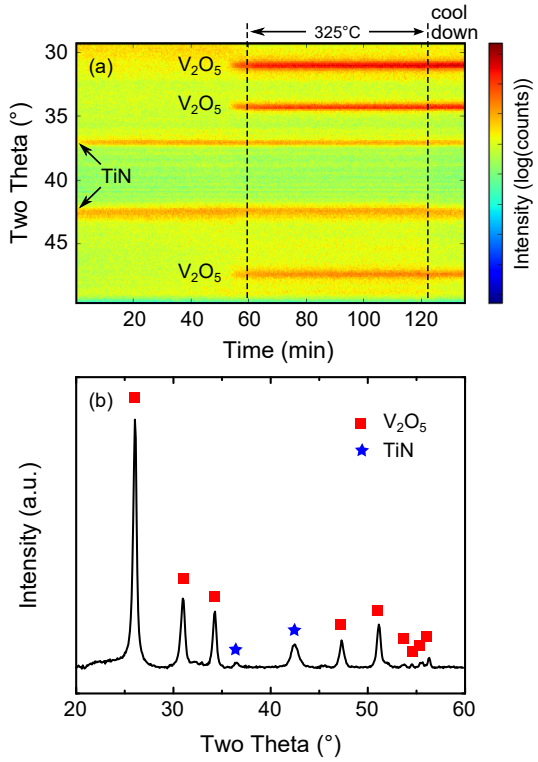

Figure 16.1: *In situ* (a) and ex situ (b) XRD results of VO_x coated CNTs annealed in air at 325 °C for 1 hour.

strate, the measured capacities were scaled to the amount of vanadium deposited, as determined by XRF. Unscaled capacities are shown in the supporting information (figures 17.2 - 17.3).

RESULTS AND DISCUSSION

Structure and morphology of the V_2O_5-coated CNTs

To crystallize the VO_x, ALD coated MWCNTs samples were loaded into a home modified *in situ* XRD system and annealed in air at 325 °C for 1 hour. The diffraction peaks were monitored during the annealing, as shown in Figure 16.1(a). The isothermal process at 325 °C was specifically chosen to crystalize the VO_x to V_2O_5 but not to oxidize the MWCNTs and the TiN layer underneath, since in a previous study, it was shown that the oxidation temperature of VO_x coated MWCNTs is about ~400 °C

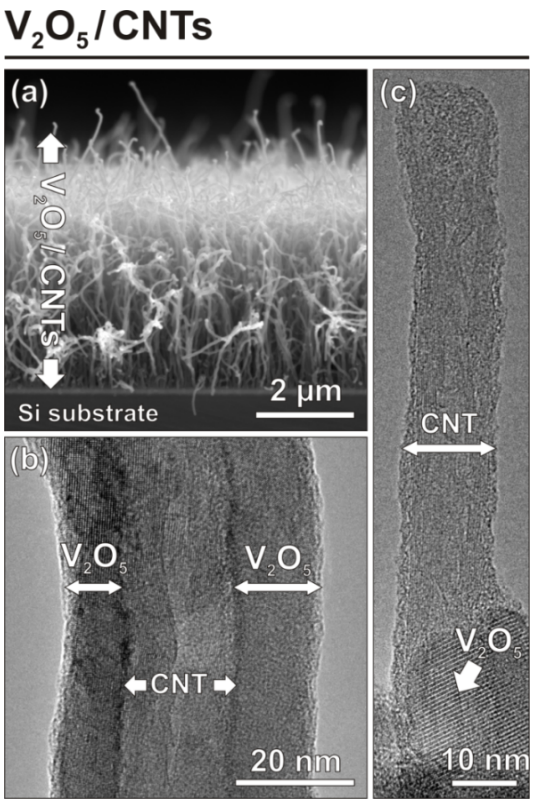

Figure 16.2: (a) SEM image of uncoated V_2O_5/CNTs from cross-sectional view is given. HRTEM images given at (b) and (c) reveal the structure of V_2O_5/CNTs before the LIB tests.

[413]. It can be seen in Figure 16.1(a) that the V_2O_5 peaks appear when the temperature reaches 325 °C whereas the peaks from the TiN layer do not disappear during the annealing. The diffraction peaks in the ex situ XRD pattern as shown in Figure 16.1(b) indicate that VO_x was crystallized into V_2O_5 with *Pmmm* space group and since no detectable TiO_2 peaks were observed, a good preservation of TiN is expected.

A SEM image of the 85 cycles ALD V_2O_5 coated CNTs arrays on the $TiN/SiO_2/Si$ substrate after annealing in air environment is presented in Figure 16.2(a). From the cross-sectional SEM image, it can be seen that the material constitutes a porous structure composed of thin, tubular and branched features occasionally linked to each other. A more detailed investigation of the sample was performed by TEM. From the HRTEM image (see Figure 16.2(b)), it is clear that the graphitic layers of CNTs are sur-

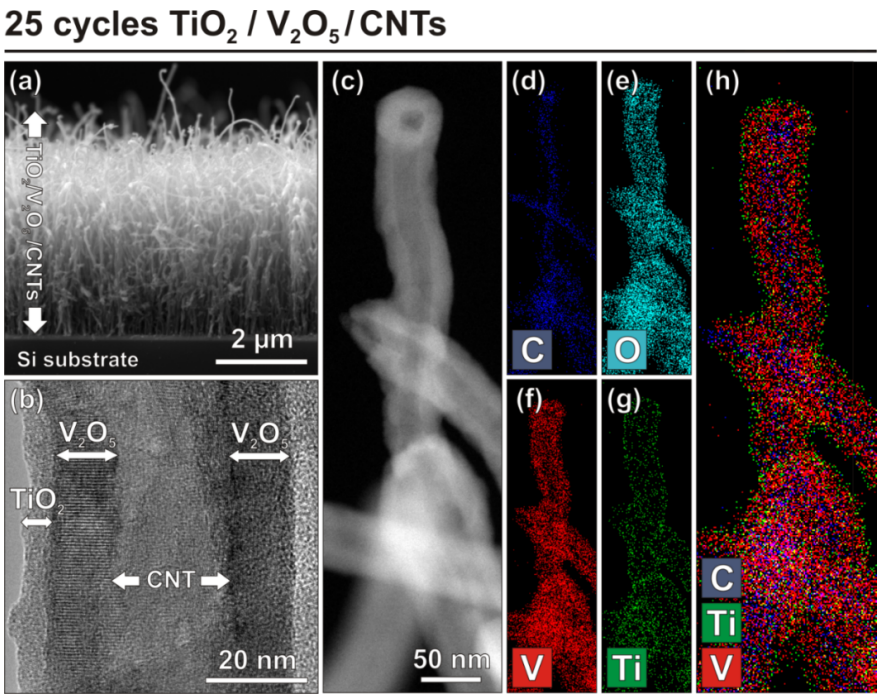

Figure 16.3: (a) SEM image of 25 ALD cycles TiO_2coated V_2O_5/CNTs from cross-sectional view is given. HRTEM image of 25 ALD cycles TiO_2coated V_2O_5/CNTs given at (b) reveals the structure of both $TiO_2$and V_2O_5 coatings before the LIB tests. (c) HAADF-STEM image shows individual TiO_2/V_2O_5/CNTs. (d) Carbon, (e) oxygen, (f) vanadium and (g) titanium compositions of the nanotubes can be seen on (h) EDX mixed color elemental map.

rounded by a thin, crystalline coating. The interplanar spacing between two layers in CNTs corresponds approximately to 0.34 nm, which is the typical distance between two graphene layers in graphite. Such appearance of graphene layers suggests the preservation of MWCNTs subsequent to the annealing process. In addition, HRTEM indicates that the annealing of the as-deposited VO_x on CNTs in air environment results in the transformation from amorphous VO_x into V_2O_5 crystalline form, while the MWCNTs are preserved. On the other hand, HRTEM showed that the ALD VO_x coating was not completely uniform, and that MWCNTs without coated regions are occasionally observed, as shown in Figure 16.2(c).

ALD coating of TiO_2 on V_2O_5/CNTs

As stated earlier, by changing the number of ALD cycles between 5 and 25, TiO_2layers with varying thicknesses were deposited onto V_2O_5/CNTs. For instance, after 25 ALD cycles of TiO_2deposition, a structure as illustrated by the SEM image in Figure 16.3(a) is obtained. The SEM image shows that the overall forest-type morphology was preserved after ALD of TiO_2. A HRTEM image (see Figure 16.3(b)) from the same sample reveals that an amorphous TiO_2layer is surrounding the crystalline V_2O_5/CNTs. In a similar way, 5 ALD cycles TiO_2 coating appeared to be in its amorphous form, which was revealed by TEM. In terms of crystallinity, ALD of TiO_2 hereby shows similar result with respect to one of our previous studies, in which the as-deposited ALD processed TiO_2 film on a carbon nanosheet template showed likewise no crystallinity upon its deposition [414]. The HAADF-STEM image in Figure 16.3(c) shows the presence of tubular-shaped nanostructures. To illustrate the distribution of the elements in the sample, elemental mapping by EDX was performed for the region indicated in Figure 16.3(c). Figure 16.3(d-h) shows the local elemental distributions of C, O, V and Ti at the sample. From the results, the TiO_2coating appears to be uniformly surrounding the V_2O_5 coated CNTs. However, it should be noted that these images and elemental maps only correspond to 2D projections of a 3D object. Therefore, in order to retrieve the correct 3D (chemical) information, EDX-STEM tomography was used.

During such an experiment, 2D EDX elemental maps are collected simultaneously with HAADF-STEM images. The results of the 3D HAADF-STEM and 3D EDX-STEM reconstructions from 25 ALD cycles TiO_2 coated V_2O_5/CNTs sample prior to electrochemical cycling tests are presented in Figure 16.4. The individual 3D elemental distributions of Ti (green), V (red) and C (blue) as well as the superposition of the Ti, V and C signals are also shown (See Figure 16.4(cf)). The HAADF-STEM reconstruction illustrates the morphology of the tubes, but due to the small HAADF-STEM contrast between the different elements, no chemical information can be extracted from individual C, Ti and V containing layers (see Figure 16.4(a-b)). On the other hand, the 3D EDX-STEM results demonstrate fine coatings of Ti and V surrounding the C containing interior (see Figure 16.4(c-f)). The layers are found to be comparably homogenous although sections without coatings are also observed (see Figure 16.4(d) and (e)). Such inhomogeneity at the nanoscale can be expected, since ALD is known to cause the appearance of pinholes and uncoated sections for both TiO_2, and VO_x depositions due to overlap of CNTs in MWCNTs forests [412,

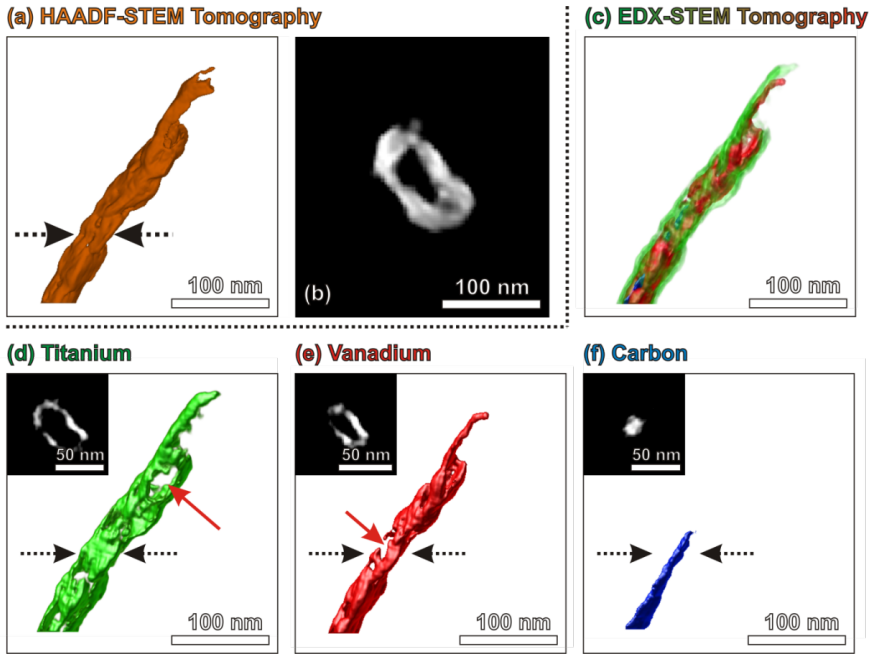

Figure 16.4: 3D visualizations of HAADF-STEM and EDX-STEM reconstructions from 25 ALD cycles TiO_2 coated V_2O_5/CNTs sample. (a) 3D visualization obtained by HAADF-STEM tomography and (b) an orthoslice through the 3D reconstruction. (c) Superimposition of 3D elemental distributions of Ti, V and C and individual 3D elemental distribution of (d) titanium, (e) vanadium and (f) carbon. The orthoslices of EDX-STEM reconstructions for each element are given at insets from positions indicated at the 3D visualizations by black arrows. Red arrows indicate the uncoated regions.

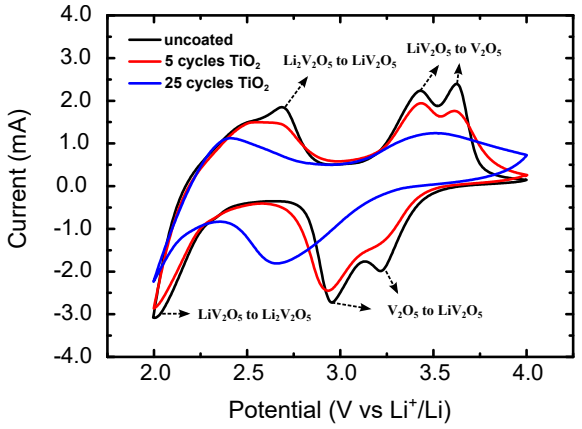

Figure 16.5: The third cyclic voltammograms of uncoated and 5 and 25 cycles TiO_2 coated V_2O_5/CNTs at 10 mV s^{-1}.

413]. However, such defects can be beneficial when using these materials as cathodes, since these areas may facilitate Li^+ insertion/extraction.

Electrochemical and rate performance improvement of TiO_2/V_2O_5/CNTs electrodes

The electrochemical performance of CNT-supported V_2O_5 as lithium-ion battery cathode was examined, and compared to that of the TiO_2-coated cathodes. Cyclic voltammetry was employed to evaluate the potential window for insertion and extraction of lithium in uncoated V_2O_5/CNTs as well as 5 and 25 ALD cycles TiO_2 on V_2O_5/CNTs. Figure 16.5 shows the CV at a scan rate of 10mVs1 in the voltage window of 2.00 V to 4.00 V *vs* Li^+/Li. This potential range was carefully chosen to allow the (de)intercalation of two lithium ions per V_2O_5 unit cell [221, 223], while remaining well above the intercalation window for TiO_2 as for not involving it to participate in the electrochemical lithiation/delithiation cycles [415]. The intercalation of two lithium ions per V_2O_5 unit cell is reported to be much less reversible than intercalation of just one, but yields a higher theoretical capacity [223]. From the CV scans of the uncoated V_2O_5/CNTs it is observed that three reduction-oxidation peak couples are present: two centered above 3.0V *vs* Li^+/Li corresponding to the two-stage (de)intercalation of one lithium into V_2O_5 [219, 221, 311, 416] and another centered around 2.4V *vs* Li^+/Li corresponding to (de)intercalation of a second lithium into LiV_2O_5. The same holds for the 5 and 25 ALD cycles TiO_2

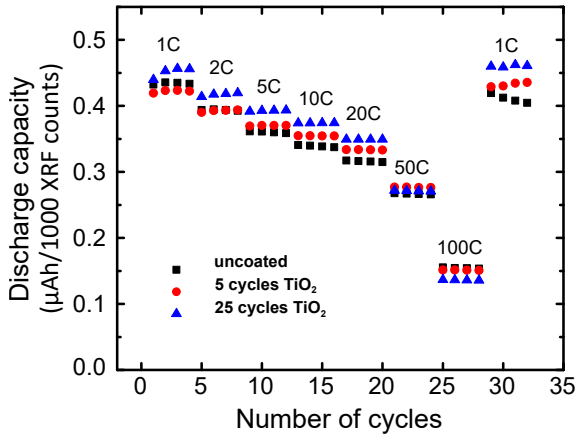

Figure 16.6: Discharge capacity of the kinetics at 1-100C for 30 electrochemical cycles of uncoated and 5 and 25 ALD cycles TiO_2 coated V_2O_5/CNTs. C-rates were calculated based on the measured vanadium content of the samples.

on V_2O_5/CNT samples: only the peaks corresponding to (de)intercalation into V_2O_5 are present, indicating that the TiO_2 ALD film does not contribute in the (de)intercalation reactions. For the 5 ALD cycles TiO_2 on V_2O_5/CNT sample, we observe that the peaks are slightly suppressed, and more so for the 25 ALD cycles TiO_2 on V_2O_5/CNT sample. Furthermore, the overpotential is higher for both samples, indicating the TiO_2 films may cause a kinetic bottleneck during the first electrochemical cycles.

To further investigate this effect, 4 galvanostatic charge-discharges were performed on the same samples at different C-rates (1-100C). The current applied for each C-rate was determined from the theoretical capacity for insertion of two lithium ions into V_2O_5 (294.7mAh/g) and the amount of V_2O_5 present in each sample calculated from equivalent V_2O_5 thicknesses derived from vanadium XRF measurements. Figure 16.6 plots the discharge capacity for varying C-rates of uncoated, 5 and 25 ALD cycles TiO_2 coated V_2O_5/CNTs cathodes. Good kinetics were observed for all samples, with only 20 % to 25 % loss upon charging in 20C compared to 1C. Coating with 5 or 25 ALD cycles of TiO_2 improves the capacity retention noticeably up to 20C, but for high C-rates such as 100C, it is seen that the uncoated sample has a higher available discharge capacity. Therefore, it can be concluded that the TiO_2 coating slightly enhanced the kinetics of the lithiation/delithiation process at low and intermediate C-rates, and only slows down the kinetics at very high C rate. This is significantly different from reported ALD coatings on V_2O_5: Al2O3 in which ALD was

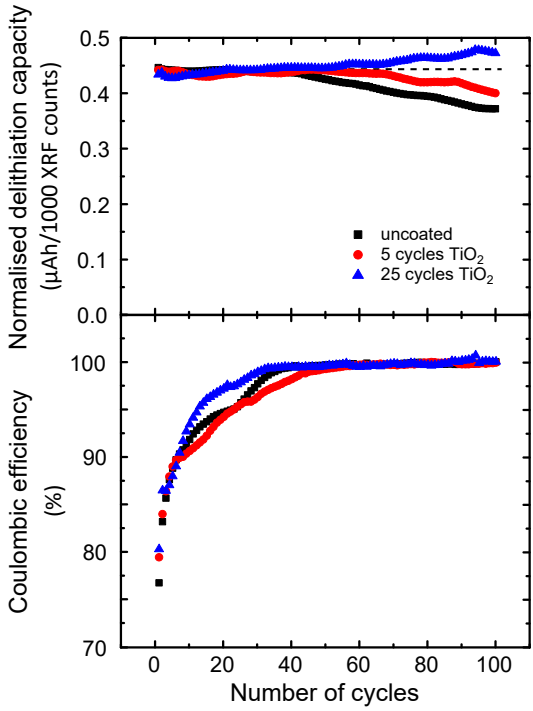

Figure 16.7: Cyclability testing of uncoated V_2O_5/CNTs and of 5 and 25 ALD cycles TiO_2 on V_2O_5/CNTs samples at a current corresponding to 2C between 2.0 and 4.0V *vs* Li^+/Li.

shown to improve the electrochemical cyclability of hydrous vanadium oxide but at the same time impose a kinetic bottleneck.41 While a TiO_2 ALD coating on V_2O_5/CNTs has already been reported to have good rate retention in the 3 lithium intercalation regime (84 % at 2.3C) [310], the kinetics shown here in the 2 lithium intercalation regime are more than 5 times better (85 % at 10C), enabling the use of this material as high-rate cathode.

Finally, we investigated the effect of the coating on the electrochemical cyclability of the cathodes. Because of the chosen potential range, two lithium per V_2O_5 were inserted into the samples, which is beyond the reported range of full reversibility. The delithiation capacity and Coulombic efficiency evolution at 2C for the samples under investigation are shown in Figure 16.7. Indeed, we see a significant decrease in capacity for the uncoated V_2O_5/CNTs upon electrochemical cycling, losing almost 17 % of the available delithiation capacity after 100 cycles. There are clearly

two stages in the evolution of the uncoated V_2O_5/CNTs. During the first 40 electrochemical cycles, the capacity remains almost constant, while the Coulombic efficiency is increasing from 76.7 % during the first cycle to 99.5 % at the 40th charge/discharge cycle. After the 40th cycle, the Coulombic efficiency varies between 99.5 and 100 %, while the capacity fades. In fact, the fraction of the capacity that is lost during the last 60 cycles matches very well with the fraction of Coulombic efficiency missing from 100 %, indicating that a fraction of the available active material between 0.05 and 0.5 % is lost every cycle. For the sample coated with 5 ALD cycles of TiO_2, a similar two-stage behavior is seen: up to 65 charge/discharge cycles the capacity remains constant, while the Coulombic efficiency slowly rises to close to 100 %, and after the 65th cycle the latter remains constant while the capacity starts decreasing. It is reported for V_2O_5 that the capacity loss is related to vanadium dissolution upon overcharging. The low coulombic efficiency during the first stage indicates that more lithium is incorporated than extracted, building more and more lithium into the samples and gradually overcharging it. At a certain point, this excess buildup of lithium is completed (40th cycle for the uncoated V_2O_5/CNTs and 65th cycle for the sample coated with 5 cycles of ALD TiO_2), upon which the capacity starts fading by the dissolution mechanism. Coating the V_2O_5/CNTs with 5 cycles of ALD TiO_2 seems to delay this mechanism, but does not prevent the loss of capacity completely. For the sample coated with 25 cycles of ALD TiO_2, no such two-stage mechanism is seen. Instead, the coulombic efficiency rises much faster, indicating much less excess lithium buildup or a more efficient extraction of lithium. Instead of a drop in available capacity, the capacity increases gradually during the 100 charge/discharge cycles to almost 9 % above the initial capacity.

Discussion of the capacity retention improvements

We observe capacity loss for the uncoated V_2O_5/CNTs and the V_2O_5/CNTs coated with 5 cycles of TiO_2. The electrochemical performance (including electrochemical cyclability) of the nanostructured V_2O_5 is limited by vanadium dissolution [229]. As mentioned previously, further performance improvement of the nanostructured V_2O_5-based cathode is aimed by introducing an additional TiO_2 layer onto the V_2O_5/CNTs with various thicknesses (ALD cycles). To evaluate the effect of preventing vanadium dissolution by ALD coating, the vanadium loss induced by electrochemical cycling was examined by applying XRF characterizations on the V_2O_5/CNTs samples before and after the LIB cyclability test. The percentages of the

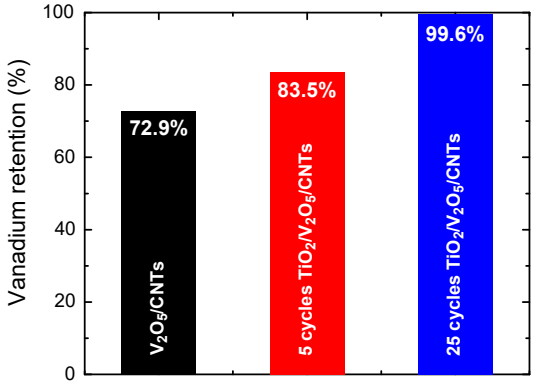

Figure 16.8: XRF characterizations determined vanadium retention for V_2O_5/CNTs, 5 TiO_2/V_2O_5/CNTs and 25 TiO_2/V_2O_5/CNTs samples after the cyclability test.

vanadium retention were determined to be 72.9 %, 83.5 % and 99.6 % after 100 electrochemical cycles charge/discharge for the cases of uncoated V_2O_5/CNTs, 5 ALD cycles TiO_2 coated V_2O_5/CNTs and 25 ALD cycles TiO_2 coated CNTs, respectively (see Figure 16.8). This demonstrates that a TiO_2 coating consisting of 25 ALD cycles is very efficient in alleviating the vanadium dissolution, without imposing a kinetic bottleneck on the cathode.

While the capacity retention in the coated V_2O_5/CNTs is explained by the vanadium dissolution function of the coating, the capacity of the 25 TiO_2/V_2O_5/CNTs is not only retained, but also increased almost 9 % over the 100 charge-discharge cycles. This can be explained by an evolution from crystalline to amorphous structure. The charge-discharging profiles of these three cases are shown in Figure 16.9, and their derivatives (dQ/dV) in supplementary information (Figures 17.4 to 17.6). During the first electrochemical cycles, three clear plateaus (or sharp peaks in the dQ/dV plots) can be seen for all samples, corresponding to the three-stage (de)lithiation of V_2O_5 as shown on the cyclic voltammograms. For the 25 ALD cycles-coated V2O5/CNTs the first lithiation plateau at 3.4V is shifted to lower potential, but still identifiable from the dQdV profile (Figure 17.6). These sharply aligned (de)lithiation regions are present due to the crystalline nature of the V_2O_5, and correspond to the overcoming of energy barriers within the crystal lattice. After 100 electrochemical charge-discharge cycles, the uncoated and 5 ALD cycles-coated V_2O_5/CNTs samples still show the characteristic plateaus and corresponding peaks in the charge-discharge profiles and dQ/dVs, respectively. In the 25 cycles ALD

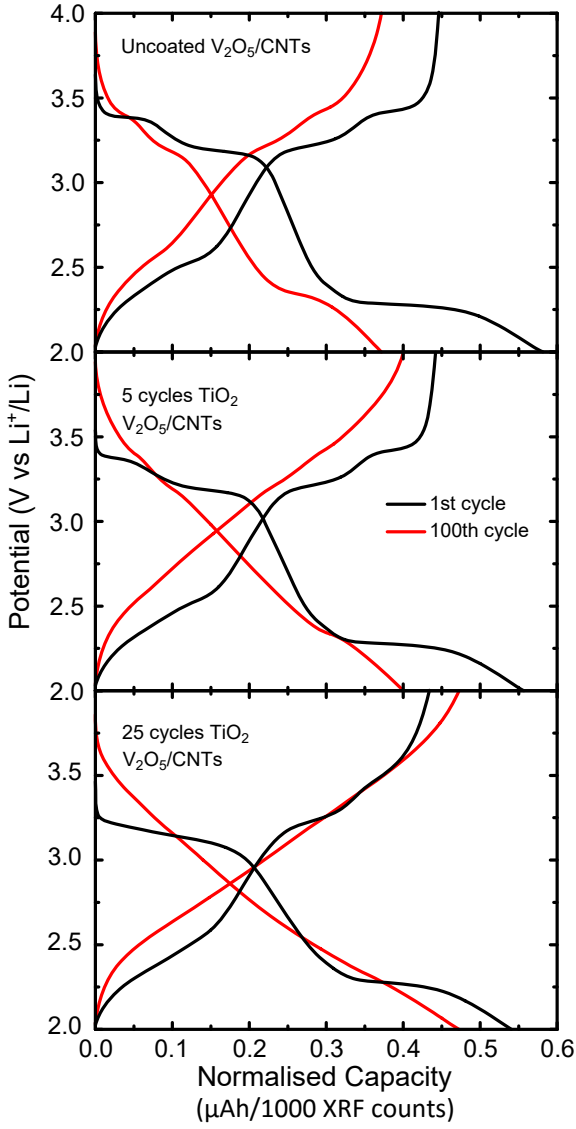

Figure 16.9: Charge-discharge profiles of the first and last cycle of the cyclability experiment

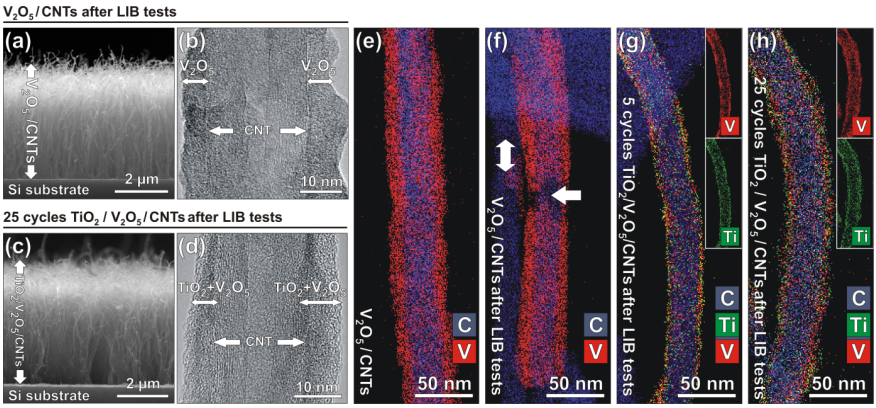

Figure 16.10: (a) SEM image of V_2O_5/CNTs from cross-sectional view after the cyclic voltammetry is given. HRTEM image given at (b) reveals the structure of V_2O_5/CNTs after the cyclic voltammetry tests. (c) SEM image of TiO_2/V_2O_5/CNTs from cross-sectional view after the cyclic voltammetry tests is given. HRTEM image given at (d) reveals the structure of both TiO_2 and V_2O_5 coatings after the cyclic voltammetry tests. (e-h) shows the EDX mapping of V_2O_5/CNTs sample before and V_2O_5/CNTs, 5 cycles and 25 cycles TiO_2 coated V_2O_5/CNTs samples after cyclability test.

TiO_2 coated V_2O_5/CNTs, all signs of those are lost. This indicates no crystal structure is left after 100 (de)lithiation cycles for the latter. For many materials, it has been shown that an amorphous material is able to store more lithium and has faster kinetics than the crystalline counterpart [243, 248, 310, 312]. The amorphisation of V_2O_5 when coated with 25 cycles of ALD TiO_2 thus explains the rise in capacity upon cycling and gradual amorphisation. Since these films are also coated with ALD TiO_2, the vanadium dissolution is also inhibited, preventing capacity loss while at the same time improving the kinetics upon cycling.

To investigate this amorphisation, the post-cycling samples were investigated by SEM, TEM and XRD in the same manner as for as-synthesized samples. SEM image of the uncoated V_2O_5/CNTs sample after the LIB tests shows that the morphology of the material was substantially preserved (see Figure 16.10(a)). HRTEM indicates that the crystalline V_2O_5 coating became amorphous (see Figure 16.10(b)), contrary to what was expected from the electrochemical measurements. Investigations of the samples with 5 and 25 cycles TiO_2 on V_2O_5/CNTs show similar results. SEM image of the 25 cycles TiO_2 on V_2O_5/CNTs reveals that the overall forest-type morphology is preserved (see Figure 16.10(c)) and from the HRTEM image (see Figure 16.10(d)) the amorphous V_2O_5 coating can be

observed, which was also the case for both uncoated V_2O_5/CNTs and 5 cycles TiO_2 on V_2O_5/CNTs samples. As seen in Figure 16.10(e-h), EDX mapping on the samples with TiO_2 coated V_2O_5/CNTs indicates that the VO_x/CNTs are still perfectly protected by TiO_2 without structural collapse. EDX-STEM analysis hereby indicated that the morphology and chemistry of the TiO_2 coated V2O5/CNTs did not change significantly, when the individual EDX elemental maps before and after the cyclability test were compared (see Figure 16.3(d-h)).

To further investigate the degree of crystallinity post-cycling, XRD patterns of the samples were investigated (see Figure 16.11). It is clear that all samples remain crystalline to some extent, although direct comparison before and after electrochemical cycling was not possible due to sample handling. However, a sample-to-sample comparison allows elaborating to the degree of crystallinity left in the samples. A peak identification was performed, and much more V_2O_5 peaks are visible post- electrochemical cycling compared to before (see Figure 16.1), indicating restructuring of the V_2O_5 upon deep lithiation. Some peaks on figure 16.11 have not been identified, but could be assigned to lithiated V_2O_5. However, due to the richness of crystalline V_2O_5 phases, singular identification was not possible. Finally, no peaks from crystalline TiO_2 were observed, indicating that the TiO_2 coatings remain amorphous after electrochemical cycling. As amorphous TiO_2 tends to crystallize upon lithiation and delithiation [417, 418], this is an additional indication that they are not participating in the electrochemical storage mechanism, but merely act as a solid electrolyte. The two overlapping peaks of V_2O_5 around 51° in 2theta were chosen to integrate as to not have any interference from other diffraction peaks from lithiated vanadium pentoxide, and the resulting integrated peak intensity shows that the uncoated V_2O_5/CNTS is clearly much more crystalline after cycling when compared to the coated samples. This result suggests that the TiO_2 ALD layer does not only act as vanadium dissolution barrier, but also assists in gradually amorphisizing the underlying V_2O_5. We hypothesize that this may be related to internal stress building within these films. Upon charging, the vanadium oxide undergoes a volume expansion due to the insertion of lithium. The coated samples could buffer this volume expansion to some extent, which causes the vanadium oxide films to be stressed, possibly contributing to the amorphisization upon cycling. As elaborated earlier, this also enhances the kinetics, which yields higher capacities at high C-rates. This result explains the increase in capacity observed for the 25 cycles TiO_2 V_2O_5/CNTs seen in Figure 16.7.

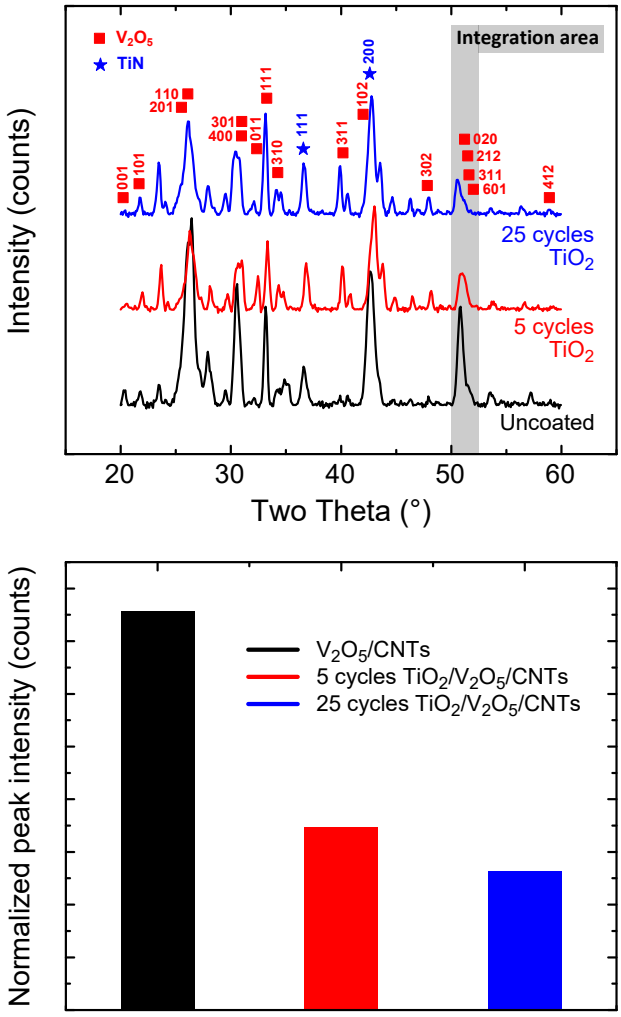

Figure 16.11: (top) XRD pattern of the post-cycling (after 100 charge-discharge cycles, discharged galvanostatically to 4.00 V *vs* Li^+/Li)uncoated and coated V_2O_5/CNTs samples. The XRD intensity was normalized to the amount of vanadium remaining after cycling, to allow for direct comparison. The gray area was used to integrate the neighboring (020), (212), (511) and (601) peaks and integrated intensities are plotted (bottom).

CONCLUSIONS

Heterogeneous TiO_2/V_2O_5/CNTs electrodes were prepared with 5-25 ALD cycles of TiO_2 onto V_2O_5/CNTs, and their electrochemical performance as the cathode electrode of LIBs was evaluated. Different TEM techniques were performed to explain the structural and morphological changes that occurred during the electrochemical tests. A MWCNT-forest template was used as a conductive layer between the substrate and active material (V_2O_5), providing both mechanical support and an increased surface area. Cyclic voltammetry showed faster kinetics for uncoated and 5 ALD cycles TiO_2 coated V_2O_5/CNT samples and slower kinetics for 25 ALD cycles TiO_2 on V_2O_5/CNTs sample. 25 ALD cycles TiO_2 on V_2O_5/CNTs sample also exhibited broad peaks in the CV, which might be an indication of homogeneous filling of V_2O_5. This was also observed with discharge capacity experiments between 1-100C, which showed highest capacity for 25 ALD cycles TiO_2 on V_2O_5/CNTs sample. The delithiation capacity of the electrodes were tested by electrochemical cycling at 2C and showed higher capacity retention for 25 ALD cycles TiO_2 on V_2O_5/CNTs after 100 electrochemical cycles than for uncoated and 5 ALD cycles TiO_2 coated V_2O_5/CNTs. Furthermore, EDX-STEM analysis showed that introducing an additional TiO_2 layer onto V_2O_5/CNTs led to a barrier to the vanadium dissolution. Amorphisation of the V_2O_5 over electrochemical cycling, induced by this lack of vanadium dissolution, enables better kinetics and thus higher available capacity after electrochemical cycling.

17

SUPPLEMENTARY TO PAPER VI

SYNTHESIS OF ALD-COATED V_2O_5/CNTS

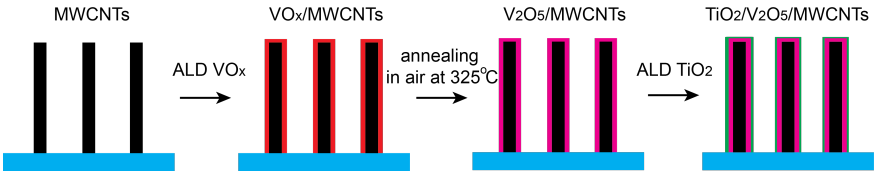

Figure 17.1: Overview of the synthesis route for obtaining heterogeneous TiO_2/V_2O_5/MWCNTs as discussed in this paper.

Figure 17.1 shows a schematic overview of the synthesis route for the electrodes tested in the paper. VO_x metal oxide were coated on MWCNTs by ALD. Subsequent annealing in air at 325 °C causes the transformation of the VO_x coating into V_2O_5 without the removal of MWCNTs. An extra layer of TiO_2 were coated onto VO_x/MWCNTs, which resulted in obtaining the heterogeneous TiO_2/V_2O_5/MWCNTs material. A HAAFD-STEM and XEDS-STEM tomography movie (M1) can be found at this link.

NON-SCALED ELECTROCHEMICAL DATA

In paper VI, the capacities measured are scaled to the amount of vanadium measured on the samples to allow for direct comparison, since the CNT density is not uniform across the samples. To give an impression of what the capacity per footprint area is for these samples, the un-scaled values are given in figures 17.2 (rate capability) and 17.3 (cyclability).

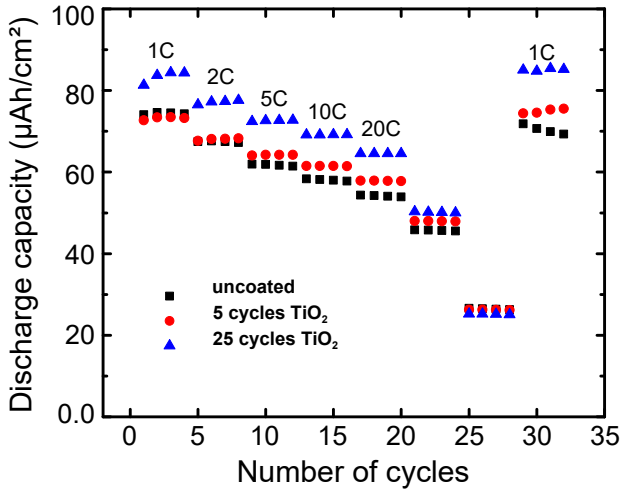

Figure 17.2: Discharge capacity of the kinetics at 1-100C for 30 electrochemical cycles of uncoated and 5 and 25 ALD cycles TiO_2 coated V_2O_5/CNTs. C-rates were calculated based on the measured vanadium content of the samples.

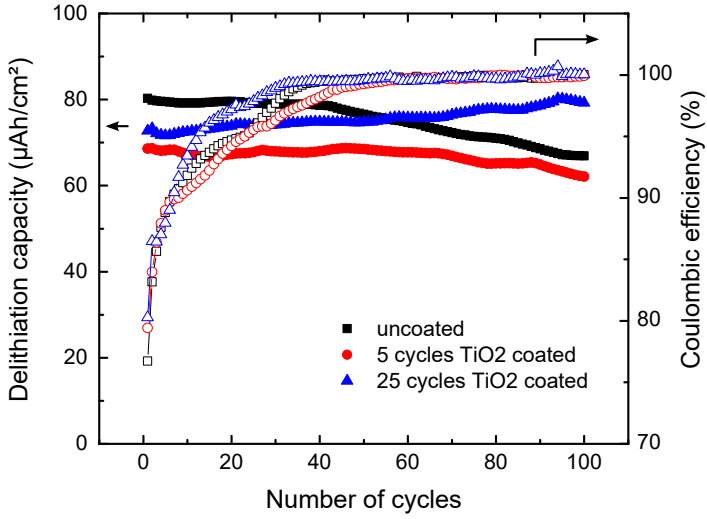

Figure 17.3: Cyclability testing of uncoated V_2O_5/CNTs and of 5 and 25 ALD cycles TiO_2 on V_2O_5/CNTs samples at a current corresponding to 2C between 2.0 V to 4.0 V *vs* Li^+/Li.

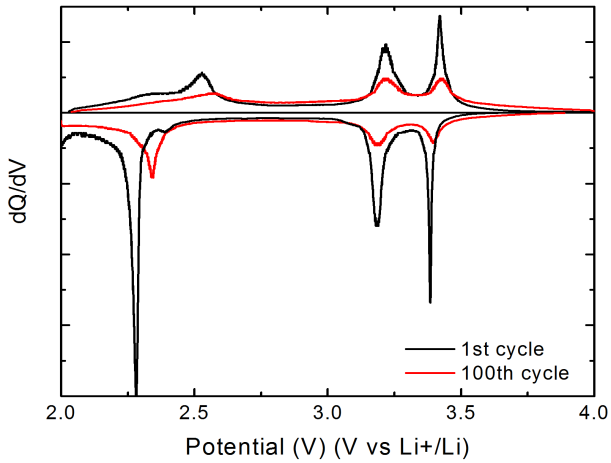

Figure 17.4: Derivative potential profile of the uncoated V_2O_5/CNTS during the first and 100th lithiation (negative dQdV) and delithiation (positive dQdV).

DERIVATIVE POTENTIAL PROFILES

To allow a more thorough interpretation of the charge-discharge profiles, their derivatives are provided here. A plateau in the charge-discharge profile translates into a peak into the derivative profile, and plateaus that are almost undistinguishable from the charge-discharge profiles are often revealed using derivatives.

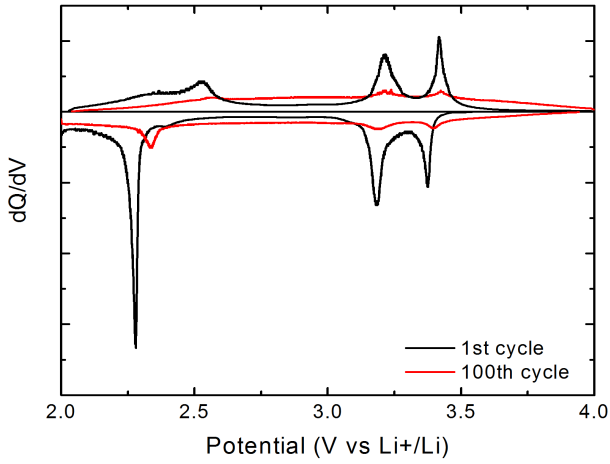

Figure 17.5: Derivative potential profile of the 5 ALD cycles TiO_2 coated V_2O_5/CNTS during the first and 100th lithiation (negative dQdV) and delithiation (positive dQdV).

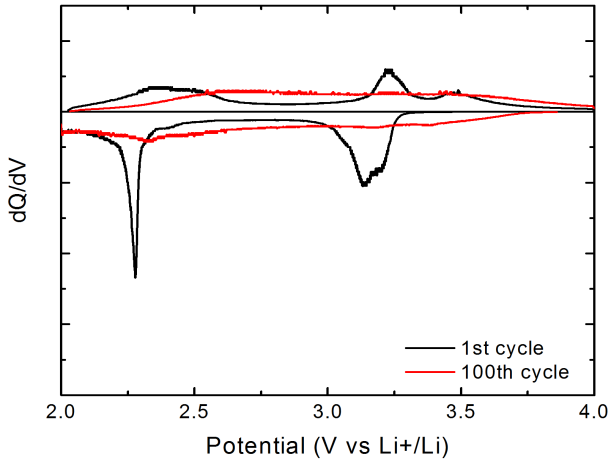

Figure 17.6: Derivative potential profile of the 25 ALD cycles TiO_2 coated V_2O_5/CNTS during the first and 100th lithiation (negative dQdV) and delithiation (positive dQdV).

Part V

CONCLUSION

18

CONCLUSIONS AND FUTURE PROSPECTS

In this work, thin films have been deposited using atomic layer deposition for energy applications, more specifically, for lithium-ion battery applications, and the goal of this work is to illustrate the strengths and weaknesses, the highlights and pitfalls, and the advantages and drawbacks of using ALD in lithium-ion battery development. The conclusions drawn from this work are summarised here.

18.1 ATOMIC LAYER DEPOSITION FOR THIN-FILM ELECTRODES

Atomic layer deposition is an interesting deposition technique for thin-film batteries when 3D-structured electrodes are envisioned. These electrodes can provide both reasonable storage capacity per footprint area, on account of the 3D structuring, and high power, which is inherited from the thin-film nature of the electrodes. These electrodes find their applications in on-chip storage, where their combination with an intermittent energy harvester can for example autonomize sensors. The conformality and thickness control during ALD growth, and the high-quality nature of ALD-grown films, validates the investigation of ALD for these applications.

18.1.1 *Atomic layer deposition of manganese oxides*

18.1.1.1 *Influencing the phase by choice of process parameters*

In part iii, ALD processes are reported for the deposition of manganese oxides. MnO_2 could be deposited using the $Mn(thd)_3$ precursor and ozone, but with a low growth rate between 0.1 and 0.2 Å/cycle. Plasma-enhanced ALD was investigated, as this is known to enable higher growth rates in ALD processes. Three new ALD processes were developed the using $Mn(thd)_3$ precursor and NH_3 plasma, H_2 plasma or H_2O plasma. We found enhanced deposition rates for the plasma processes: the growth

rate was 0.2 Å/cycle independently of the growth temperature. The film quality was found to be excellent, with low roughness and impurities. The oxidative or reductive nature of the plasma or reaction gas determined the oxidation state of the film, and with a single precursor chemistry MnO_2, Mn_3O_4, MnO and a mixed-phase Mn_3O_4/MnO were deposited.

18.1.1.2 *Influencing the phase by post-deposition annealing*

The oxidation and reduction behaviour of these thin-film manganese oxides was studied using *in-situ* X-ray diffraction in controlled ambients: a reducing ambient (H_2), an inert ambient (He) and oxidative ambients (air, O_2). We found that by careful choice of temperature and ambient, all manganese oxide phases in the MnO-MnO_2 series could be obtained, including the Mn_2O_3 phase which would not be obtained directly from (PE-)ALD growth. Mn_2O_3 could be obtained by annealing a MnO_2 film in inert atmosphere above 410 °C. At high temperature in a reducing ambient, metallic manganese was even obtained above 700 °C, which then formed manganese silicates or silicides, depending on the substrate.

18.1.1.3 *Thin-film manganese oxides as lithium-ion battery electrodes*

The broadness of manganese oxide thin-film composition that could be obtained, either by deposition or by post-deposition annealing, allowed us to study applications of the different flavours of manganese oxide. The as-deposited films were all tested as thin-film lithium-ion battery electrode. They all displayed lithium-storage behaviour, but in different potential ranges. MnO_2 could be activated by continuous cycling to a 2.9 V *vs* Li^+/Li positive electrode with up to 71 % of the theoretical capacity (and still rising when the measurement was halted). The lower-valent oxides provided lower potential electrodes, and the MnO-containing electrodes displayed activity below 1.0 V *vs* Li^+/Li as conversion anodes. Unfortunately, the poor conformality of this ALD process did not allow the demonstration of 3D thin-film lithium ion electrodes.

18.1.1.4 *ALD manganese oxide as an ultra-thin seed layer for electrodeposition*

Electrodeposition of manganese oxides in acidic environments suffers from the oxidation of current collectors such as TiN, rendering the deposited films disconnected from their current collector. To overcome this, 1–2 nm ALD MnO_2 seed layers were deposited on the current collectors. The oxidation behaviour was supressed by the seed layer, which also aided in adhesion to the current collector, allowing the electrodeposition of MnO_2

electro-active films up to 1 µm, while the deposition on the uncoated current collector was limited to ∼400 nm, and were deactivated due to current collector oxidation.

18.1.1.5 *Prospects & future work*

The $Mn(thd)_3$ precursor is not an ideal precursor for thin-film electrodes, due to the low growth rates (even with plasma-enhanced ALD) and poor conformality. A maximum film thickness of 30nm could be deposited in a reasonable time frame in this work due to the low growth rates. Besides energy storage, other applications of these films are envisioned, such as thin-film catalysis or the use of these high-quality layers as seed layers to growing thicker films with other deposition techniques, such as electrodeposition.

To obtain higher conformality and higher growth rates, other precursors can be investigated. At the start of this PhD, only two manganese precursors were reported. Now, that number has already doubled. Clever precursor engineering may enable higher growth rates and better conformality.

Finally, manganese oxides become interesting cathode materials when the 4 V *vs* Li^+/Li region is activated, as this significantly enhances the energy density of these films. To do so, the chemical surrounding and structure of these films needs to be altered. Direct deposition of spinel $Li_xMn_2O_4$ has been demonstrated with $Mn(thd)_3$ [419], but can be sped up by visiting smaller precursors. Another way to raise the electrode potential is moving from oxides to phosphates, which can be done by using a third phosphorous-contained ALD precursor [92, 293].

18.1.2 *ALD vanadium oxides as 3D thin-film electrodes*

18.1.2.1 *Vanadium oxide crystallisation and phase control*

Amorphous VO_2 ALD deposition was reported using the TEMAV precursor, with water or ozone as a reagent. The crystallisation and phase change behaviour of these two flavours of amorphous VO_2 were investigated, and the influence of the substrate, temperature, ambient and initial flavour of VO_2 were unravelled. All crystalline phases in the Wadsley series (VO_2-V_2O_5) were obtained. The influences of the different parameters are summarized here.

- The as-deposited flavour of VO_2 determined the lattice of the crystalline VO_2 film, based on density arguments.

- The film deposited using ozone oxidized at lower temperatures to higher oxidation states.
- Higher temperature and higher oxygen partial pressures triggered phase changes to higher oxidation states of vanadium.
- An oxidizible component in the substrate can act as an oxygen drain, and retard the oxidation of the films to higher vanadium oxides.

18.1.2.2 *Vanadium oxides as thin-film electrodes*

The crystalline films were all investigated as thin-film electrodes. All crystalline films in the Wadsley series showed good electrochemical activity. VO_2(M1), outside of the Wadsley series, showed poor performance, possibly due to the high density of this phase. Very high capacities were found for V_3O_7 and V_4O_9, at 1255 mA h cm^{-3} and 1380 mA h cm^{-3}, respectively, almost double that of the best commercially available compound ($LiNi_{0.8}Co_{0.15}Al_{0.05}O_2$, ~700 mA h cm^{-3}). Insertion of one lithium into V_2O_5 clearly results in the best cycle life and rate capability, but the capacity is only 448 mA h cm^{-3}, too low to be considered as an electrode in lithium-ion batteries. Inserting more lithium into V_2O_5 increases the storage capacity, but is dramatic for the cycle life and rate capability. VO_2(B) is a best-of-both-worlds case, as it displays excellent cycle life, reasonable rate capability (75 % at 10C) and a good capacity (805 mA h cm^{-3}).

18.1.2.3 *Amorphous vanadium oxides as high-rate electrodes*

The low-temperature nature of atomic layer deposition enables the deposition of amorphous films. This presented the opportunity to study amorphous and crystalline films side by side. A low-temperature ALD process for the deposition of amorphous V_2O_5 was established at 85 °C using TEMAV as a vanadium precursor and short oxygen plasma pulses as reagent, which yielded C-free amorphous films with vanadium in the +5 oxidation state.

Having established ALD and PE-ALD processes for the deposition of amorphous and crystalline films of both VO_2 and V_2O_5, an in-depth electrochemical benchmarking of these films was performed as thin-film lithium-ion battery electrodes. The best kinetics and cyclability were still found for insertion of one lithium into crystalline V_2O_5, but at the cost of low storage capacity. The conclusions of this benchmarking are summarised:

- The capacity of the amorphous compounds is generally higher than their crystalline counterparts.

- The rate capability of the amorphous compounds is generally higher than their crystalline counterparts: thanks to better diffusion coefficients their rate performance is almost twice as good.
- Extremely high storage capacities wrtr found for amorphous VO_2; up to 1.4 A h cm^{-3}, which could be related to both interstitial storage in an amorphous compound and high availability of storage sites in a low-density compound such as amorphous VO_2. In general, the amorphous compounds have a higher storage capacity compared to their crystalline counterparts in the same potential ranges.
- Cyclability is excellent for shallow lithiation of crystalline V_2O_5, but very poor for further lithiation. Excellent cycle life was found for crystalline VO_2(B). Cyclability is good, but not perfect, for the amorphous vanadium oxides, with most capacity fading related to vanadium dissolution at high state-of-charge.

18.1.2.4 *3D-microstructured and 3D-nanostructured thin-film electrodes*

Unlike the manganese oxide ALD processes, the vanadium oxide ALD processes can be deposited conformally. Unfortunately, amorphous V_2O_5 could not be deposited using the process developed here, as the longer pulse times required to obtain conformality resulted in (partial) crystallisation of the films. Other ALD process chemistries have been demonstrated to deposit conformal amorphous V_2O_5 [266].

The deposition of amorphous VO_2, and the crystallisation of it to VO_2(B) and V_2O_5, was demonstrated on silicon micropillar structures: 50 µm high pillars with a diameter and interpillar spacing of 2 µm. The excellent kinetics of the thin-film electrodes was maintained, while the footprint capacity for 40 nm films was enhanced by a factor of the surface enhancement (∼20x) from ∼1.5–5 µA h cm^{-2} up to ∼30–100 µA h cm^{-2}.

Similarly, the deposition of amorphous VO_2 was carried out on a carbon nanotube forest substrate. Similar footprint capacities were obtained for thinner films (only 85 cycles) and a lower 3D structure (only 85 µm high), thank to the much higher surface enhancement factor of these CNTs.

18.1.2.5 *Prospects & future work*

The crystalline vanadium oxides show staggeringly high capacities and relatively good kinetics. However, their average electrode potential is typically between 2-3V *vs* Li^+/Li, which reduces their energy density somewhat. Phosphates are known to have higher electrode potentials compared

to oxides, due to the chemical surrounding of the transition metal ions. Revisiting vanadium-based ALD from a phosphate angle could potentially raise the electrode potential, and further enhance the energy density.

The amorphous vanadium oxides have excellent properties, but some capacity fading is still present, mostly due to vanadium dissolution. Various ways to tackle these issues are proposed:

- Surface coating has been shown to aid in the stabilisation of dissoluble species. In this work, this has been examined on crystalline vanadium oxides, but the same study can be performed on amorphous vanadium oxides, as they generally posses superior electrode performance characteristics.
- An initial study was performed to examine the influence of the depth of discharge on the cycle life for amorphous V_2O_5, in parallel with the phenomena observed on crystalline V_2O_5. Indeed, much better stability was observed when lithiation was halted at 2.0 V *vs* Li^+/Li, rather than complete charge up to 1.5 V *vs* Li^+/Li, at the cost of lower capacity. A trade-off can always be found between capacity and cyclability, which has not been examined completely for amorphous V_2O_5 and VO_2.
- These films are envisioned for 3D thin-film all-solid-state batteries. In this work, only the electrodes are tested. Challenges are expected for the integration into full devices, which need to be investigated and overcome.

18.2 ATOMIC LAYER DEPOSITION FOR SURFACE MODIFICATIONS

Surface modification has been investigated as a way to extend the lifetime of lithium-ion battery electrodes. For this application, atomic layer deposition has been investigated heavily in the past decade. Here, we used thin-film model systems to study the effect of well-known coatings on the interfaces of lithium-ion battery electrodes, and applied that knowledge to a 3D-nanostructured thin-film electrode.

18.2.0.1 *The kinetic effect of ultra-thin films on an ideal electrode*

A 40 nm anatase TiO_2 film was used as a model system for an ideal electrode, i.e. an electrode without inherent problems such as SEI formation, metal dissolution of large volume changes. This electrode was coated with up to 5 nm amorphous films: ALD Al_2O_3 and ALD TiO_2. The ALD Al_2O_3 film proved detrimental for the kinetics, while ALD TiO_2

maintained the kinetics of the underlying electrode almost perfectly. The blocking nature of ALD Al_2O_3 was studied, and it was found that films with a thickness above 2 nm acted purely capacitively, while thinner films transferred lithium but impose an impedance of $\sigma_{Li^+} = 6.7 \times 10^{-13}\,S\,cm^{-1}$, meaning that these films are only usable when made very thin. As a consequence, the rate performance decreases dramatically by a significant iR-drop across the coating.

18.2.0.2 *The protective effect of ultra-thin films on an non-ideal electrode*

A 100 nm $LiMn_2O_4$ film was used as a model system for electrolyte decomposition. By cycling the film between 3.5–4.5 V *vs* Li^+/Li, the solvent decomposes at high potentials; as PC decomposition is expected above 4.0 V *vs* Li^+/Li. Indeed, above 4.3 V *vs* Li^+/Li a clear solvent decomposition signature is seen from the electrochemical measurements. Based on the arguments above, an ultra-thin ALD Al_2O_3 coating (1 nm) and a thicker ALD TiO_2 coating (5 nm) were chosen to protect the electrode from this electrode ageing mechanism. We found that the ultra-thin ALD Al_2O_3 coating still allowed solvent decomposition, and significantly degraded the rate capability because of the imposed impedance of both the coating and the SEI layer formed. The ALD TiO_2 on the other hand succeeded in reducing the solvent decomposition, and since the coating in itself did not impose a kinetic barrier, significantly improved the rate capability of the $LiMn_2O_4$ electrode.

18.2.0.3 *Improving the cycle life of a high-performance 3D nanostructured thin-film electrode*

The real strength of ALD lies in the conformal nature of the deposited films. To demonstrate this, a 3D-nanostructured electrode was made by coating ALD vanadium oxide onto carbon nanotubes (CNTs). Crystalline V_2O_5 suffers from capacity fading upon cycling, which was shown to be mostly related to vanadium dissolution into the electrolyte. To mediate this, a second conformal coating was placed as a protective barrier. ALD TiO_2 was chosen for its good lithium diffusion, as to maintain the kinetics of the nanostructured electrode. Indeed, the excellent kinetics (20–25 % drop from 1C to 20C) were maintained by the coating. 100 charge-discharge cycles at 2C showed a decreasing capacity for the uncoated V_2O_5/CNTs, and a stabilized for the coated V_2O_5/CNTs electrodes. Moreover, for 25 cycles of ALD TiO_2, the capacity increased over cycling. These effects were attributed to two factors:

- the vanadium dissolution observed for the uncoated V_2O_5/CNTs was decreased by 5 cycles of ALD TiO_2, and almost completely alleviated by 25 cycles of ALD TiO_2. This explained the better capacity retention for the coated electrodes.

- The coated V_2O_5/CNTs were found to be less crystalline upon cycling compared to the uncoated V_2O_5/CNTs. The TiO_2 coating in some way aided in the gradual amorphisation of the V_2O_5 film upon cycling, without allowing the dissolution of it into the electrolyte. Interestingly, in the previous sections it was shown that amorphous vanadium oxides shows a better rate performance than their crystalline counterparts. The increase in capacity may therefore be attributed to an increase in rate capability, as these films are cycled at a rate of 2C.

18.2.0.4 *Prospects & future work*

Atomic layer deposition is clearly an interesting choice to stabilize the surface of lithium-ion battery electrodes. By depositing the coating directly on the composite electrodes, as was done in this work, little concern was given to the electronic conductivity of the coating. However, two remarks can be made related to this

- The electronic conductivity is indeed still an important factor. Most ageing mechanisms, such as solvent decomposition and metal dissolution, are driven by electron transfer. The ideal coating for surface stabilisation is thus an electronic insulator and an ionic conductor, applied directly on the composite electrodes. Solid electrolytes, such as nitrogen-doped lithium phosphates, are ideal for this, but their deposition is not straightforward, and investigations in that direction are an upcoming field in the research on ALD for lithium-ion battery applications.

- A coating on the composite electrode is not always an option, and in the commercialisation stage the choice may be made to apply the coating on the particles rather than on the electrodes. In this case, electronic conductivity is of paramount importance to maintain the electronic network between the particles and the current collector. However, ionic conductivity remains a critical factor. For coatings directly on the electrode particles, dual-conductive coatings are thus required.

18.3 General conclusions and prospects

Atomic layer deposition for lithium-ion battery applications was examined in this work. On the one hand, thin-film electrodes can be deposited by atomic layer deposition, but the slow growth rate of the deposition process limits the film thickness, and thus the capacity of the electrodes, even when 3D nanoscaling concepts are taken into account. In this work, we were able to obtain electrodes showing a capacity of approximately $100\,\mu A\,h\,cm^{-2}$ on two different 3D substrates, i.e. silicon nanopillars and carbon nanotubes. This footprint capacity could be further enhanced by thicker film, i.e. more cycles, or higher surface-area substrates. The former method will decrease the rate capability of the battery, while the latter will make the deposition conditions more demanding. Both options will be very time- and precursor-consuming and reach a maximum at around $1\,mA\,h\,cm^{-2}$, based on feasibility and cost arguments.

While it is in principle possible to deposit the electrodes with atomic layer deposition, this may not be the best option, especially considering that true conformality is not an unyielding condition for the electrode. However, ALD of electrodes still finds its use in core-shell particles, as model electrodes, or for niche applications.

Where true conformality is a hard requirement, is for surface coating. For this application, only a few cycles can suffice to stabilize the interface, so precursor cost and deposition time are not as much a bottleneck as is the case for electrode deposition. Furthermore, as these coatings need to be conformal and uniform across the entire electrode interface, here, atomic layer deposition is ideally (and almost uniquely) suited.

In this work, all depositions were done lithium-free. Atomic layer deposition of lithium-containing films is being investigated, but is not straightforward, as lithium tends to alter the process chemistry and growth modes of the ALD processes drastically. However, to obtain ALD solid electrolytes, and to demonstrate the worlds first all-ALD all-solid-state thin-film lithium-ion battery, further development of the deposition of lithium and lithium-containing films by atomic layer deposition will be paramount.

REFERENCES

1. Whittingham, M. S. History, Evolution, and Future Status of Energy Storage. *Proceedings of the IEEE* **100,** 1518–1534 (2012).
2. *Batteries for Electric Cars. Challenges, Opportunities and the Outlook to 2020* tech. rep. (The Boston Consulting Group, 2010).
3. Zahid Kausar, A. S. M. *et al.* Energizing wireless sensor networks by energy harvesting systems: Scopes, challenges and approaches. *Renewable and Sustainable Energy Reviews* **38,** 973–989 (2014).
4. Linden, D. & Reddy, T. B. *Handbook of Batteries* (McGraw-Hill, 2002).
5. Whittingham, M. S. & Gamble, F. R. The lithium intercalates of the transition metal dichalcogenides. *Materials Research Bulletin* **10,** 363–371 (1975).
6. Whittingham, M. S. The Role of Ternary Phases in Cathode Reactions. *J. Electrochem. Soc.* **123,** 315–320 (Mar. 1976).
7. Mizushima, K. *et al.* Li_xCoO_2 ($0<x<1$): A new cathode material for batteries of high energy density. *Materials Research Bulletin* **15,** 783–789 (June 1980).
8. Yoshino, A. The Birth of the Lithium-Ion Battery. *Angew. Chem. Int. Ed.* **51,** 5798–5800 (June 2012).
9. TechSci Research. *Global Lithium-ion Battery Market By Type (Lithium Nickel Manganese Cobalt (Li-NMC), Lithium Iron Phosphate (Li-IP), Lithium Cobalt Oxide (Li-CO), etc.), By End User, By Region, Competition Forecast and Opportunities, 2011 2021* tech. rep. (July 2016).
10. Christophe Pillot. *Battery Market Development for Consumer Electronics, Automotive, and Industrial: Materials Requirements and Trends* tech. rep. (May 2015).
11. Molenda, J. & Mole, M. in *Metal, Ceramic and Polymeric Composites for Various Uses* (ed Cuppoletti, J.) (InTech, July 2011).
12. *Advances in Lithium-Ion Batteries* (eds van Schalkwijk, W. A. & Scrosati, B.) (Springer US, Boston, MA, 2002).
13. Nazri, G.-A. & Pistoia, G. *Lithium Batteries, Science and Technology* (Springer, 2003).

14. Moore, G. Progress In Digital Integrated Electronics [Technical literaiture, Copyright 1975 IEEE. Reprinted, with permission. Technical Digest. International Electron Devices Meeting, IEEE, 1975, pp. 11-13.] *IEEE Solid-State Circuits Newsletter* **20,** 36–37 (Sept. 2006).

15. Cosmin Laslau, Christopher Robinson & Lilia Xie. *The Next-Generation Battery Roadmap: Quantifying How Solid-State, Lithium-Sulfur, and Other Batteries Will Emerge After 2020* State of the market report (Lux Research, Oct. 2015).

16. Nitta, N. *et al.* Li-ion battery materials: present and future. *Materials Today* **18,** 252–264 (2015).

17. Wang, Y. *et al.* Solid Electrolyte Interphase Formation on Lithium-Ion Electrodes: A Li Nuclear Magnetic Resonance Study. *Electrochemical and Solid-State Letters* **4,** 68–70 (2001).

18. Zhang, S. *et al.* Understanding Solid Electrolyte Interface Film Formation on Graphite Electrodes. *Electrochemical and Solid-State Letters* **4,** 206–208 (2001).

19. Zhang, S. S., Xu, K. & Jow, T. R. EIS study on the formation of solid electrolyte interface in Li-ion battery. *Electrochimica Acta* **51,** 1636–1640 (2006).

20. Verma, P., Maire, P. & Novák, P. A review of the features and analyses of the solid electrolyte interphase in Li-ion batteries. *Electrochimica Acta* **55,** 6332–6341 (Sept. 2010).

21. Obrovac, M. N. & Christensen, L. Structural Changes in Silicon Anodes during Lithium Insertion/Extraction. *Electrochem. Solid-State Lett.* **7,** A93–A96 (May 2004).

22. Larcher, D. *et al.* Recent findings and prospects in the field of pure metals as negative electrodes for Li-ion batteries. **17,** 3759–3772 (Sept. 2007).

23. Xu, W. *et al.* Lithium metal anodes for rechargeable batteries. **7,** 513–537 (Jan. 2014).

24. Williard, N. *et al.* Lessons Learned from the 787 Dreamliner Issue on Lithium-Ion Battery Reliability. *Energies* **6,** 4682–4695 (Sept. 2013).

25. Lu, J. *et al.* The role of nanotechnology in the development of battery materials for electric vehicles. *Nat Nano* **11,** 1031–1038 (Dec. 2016).

26. Bruce, P. G., Scrosati, B. & Tarascon, J.-M. Nanomaterials for rechargeable lithium batteries. *Angew. Chem. Int. Ed. Engl.* **47,** 2930–2946 (2008).

27. Aricó, A. S. *et al.* Nanostructured materials for advanced energy conversion and storage devices. *Nat Mater* **4,** 366–377 (May 2005).

28. Wang, Y. & Cao, G. Developments in Nanostructured Cathode Materials for High-Performance Lithium-Ion Batteries. *Advanced Materials* **20,** 2251–2269 (June 2008).

29. Wang, Y. *et al.* Nanostructured Vanadium Oxide Electrodes for Enhanced Lithium-Ion Intercalation. *Advanced Functional Materials* **16,** 1133–1144 (June 2006).

30. Moriguchi, I. *et al.* A Mesoporous Nanocomposite of TiO_2 and Carbon Nanotubes as a High-Rate Li-Intercalation Electrode Material. *Adv. Mater.* **18,** 69–73 (Jan. 2006).

31. Ortiz, G. F. *et al.* Alternative Li-Ion Battery Electrode Based on Self-Organized Titania Nanotubes. *Chem. Mater.* **21,** 63–67 (Jan. 2009).

32. Liu, D. & Cao, G. Engineering nanostructured electrodes and fabrication of film electrodes for efficient lithium ion intercalation. *Energy & Environmental Science* **3,** 1218 (2010).

33. Chan, C. K. *et al.* High-performance lithium battery anodes using silicon nanowires. *Nature Nanotechnology* **3,** 31–35 (Jan. 2008).

34. Korgel, B. A. Nanomaterials Developments for Higher-Performance Lithium Ion Batteries. *The Journal of Physical Chemistry Letters* **5,** 749–750 (Feb. 2014).

35. Zhang, W.-J. A review of the electrochemical performance of alloy anodes for lithium-ion batteries. *Journal of Power Sources* **196,** 13–24 (Jan. 2011).

36. Obrovac, M. N. *et al.* Alloy Design for Lithium-Ion Battery Anodes. *J. Electrochem. Soc.* **154,** A849–A855 (Sept. 2007).

37. Beaulieu, L. Y. *et al.* Colossal Reversible Volume Changes in Lithium Alloys. *Electrochem. Solid-State Lett.* **4,** A137–A140 (Sept. 2001).

38. Yu, D. *et al.* Mesoporous vanadium pentoxide nanofibers with significantly enhanced Li-ion storage properties by electrospinning. **4,** 858–861 (Mar. 2011).

39. Lotfabad, E. M. *et al.* Si nanotubes ALD coated with TiO_2, TiN or Al_2O_3 as high performance lithium ion battery anodes. *J. Mater. Chem. A* **2,** 2504–2516 (Jan. 2014).

40. Lahiri, I. *et al.* Ultrathin alumina-coated carbon nanotubes as an anode for high capacity Li-ion batteries. *J. Mater. Chem.* **21,** 13621–13626 (Aug. 2011).

41. Guan, C. *et al.* Highly Stable and Reversible Lithium Storage in SnO2 Nanowires Surface Coated with a Uniform Hollow Shell by Atomic Layer Deposition. *Nano Lett.* **14,** 4852–4858 (Aug. 2014).

42. Yu, S.-H. *et al.* Conversion Reaction-Based Oxide Nanomaterials for Lithium Ion Battery Anodes. *Small* **12,** 2146–2172 (Apr. 2016).

43. Liu, N. *et al.* A pomegranate-inspired nanoscale design for large-volume-change lithium battery anodes. *Nat Nano* **9,** 187–192 (2014).

44. Vissers, D. R. *et al.* Role of Manganese Deposition on Graphite in the Capacity Fading of Lithium Ion Batteries. *ACS Appl. Mater. Interfaces* **8,** 14244–14251 (June 2016).

45. Wu, Y. P., Rahm, E. & Holze, R. Carbon anode materials for lithium ion batteries. *Journal of Power Sources* **114,** 228–236 (2003).

46. Fu, L. J. *et al.* Surface modifications of electrode materials for lithium ion batteries. *Solid State Sciences* **8,** 113–128 (Feb. 2006).

47. Riley, L. A. *et al.* Conformal Surface Coatings to Enable High Volume Expansion Li-Ion Anode Materials. *ChemPhysChem* **11,** 2124–2130 (May 2010).

48. Zhu, B. *et al.* Interfacial stabilizing effect of ZnO on Si anodes for lithium ion battery. *Nano Energy* **13,** 620–625 (Apr. 2015).

49. Bettge, M. *et al.* Improving high-capacity $Li_{1.2}Ni_{0.15}Mn_{0.55}Co_{0.1}O_2$-based lithium-ion cells by modifiying the positive electrode with alumina. *Journal of Power Sources* **233,** 346–357 (July 2013).

50. Li, C. *et al.* Cathode materials modified by surface coating for lithium ion batteries. *Electrochimica Acta* **51,** 3872–3883 (2006).

51. Khan, Y. *et al.* Monitoring of Vital Signs with Flexible and Wearable Medical Devices. *Adv. Mater.* **28,** 4373–4395 (June 2016).

52. Yan, C. & Lee, P. S. Stretchable Energy Storage and Conversion Devices. *Small* **10,** 3443–3460 (Sept. 2014).

53. Wu, H. *et al.* Energy Harvesters for Wearable and Stretchable Electronics: From Flexibility to Stretchability. *Adv. Mater.* n/a–n/a (Sept. 2016).

54. Létiche, M. *et al.* Atomic Layer Deposition of Functional Layers for on Chip 3D Li-Ion All Solid State Microbattery. *Adv. Energy Mater.* **7,** 1601402–n/a (2016).

55. Sapunkov, O. *et al.* Quantifying the promise of beyond Liion batteries. *Transl. Mater. Res.* **2,** 045002 (2015).

56. Tarascon, J.-M. & Armand, M. Issues and challenges facing rechargeable lithium batteries. *Nature* **414,** 359–367 (Nov. 2001).

57. Yu, X. *et al.* A Stable Thin-Film Lithium Electrolyte: Lithium Phosphorus Oxynitride. *J. Electrochem. Soc.* **144,** 524–532 (Feb. 1997).

58. Dudney, N. J. & Neudecker, B. J. Solid state thin-film lithium battery systems. *Current Opinion in Solid State and Materials Science* **4,** 479–482 (Oct. 1999).

59. Sundmaeker, H. *et al. Vision and challenges for realising the Internet of things* (EUR-OP, Luxembourg, 2010).

60. Miorandi, D. *et al.* Internet of things: Vision, applications and research challenges. *Ad Hoc Networks* **10,** 1497–1516 (Sept. 2012).

61. Brecht Put. *Nanoscale characterization of materials for thin film batteries* PhD thesis (KU Leuven, Oct. 2015).

62. Armand, M. & Tarascon, J.-M. Building better batteries. *Nature* **451,** 652–657 (Feb. 2008).

63. Notten, P. H. L. *et al.* 3-D Integrated All-Solid-State Rechargeable Batteries. *Adv. Mater.* **19,** 4564–4567 (Dec. 2007).

64. Baggetto, L. *et al.* High Energy Density All-Solid-State Batteries: A Challenging Concept Towards 3D Integration. *Advanced Functional Materials* **18,** 1057–1066 (Apr. 2008).

65. Bruce, P. G. *et al.* LiO2 and LiS batteries with high energy storage. *Nature Materials* **11,** 19–29 (Dec. 2011).

66. Zhang, T. & Imanishi, N. in *Nanoscale Technology for Advanced Lithium Batteries* (eds Osaka, T. & Ogumi, Z.) 227–241 (Springer New York, 2014).

67. Song, J. *et al.* Mapping the Challenges of Magnesium Battery. *The Journal of Physical Chemistry Letters* **7,** 1736–1749 (May 2016).

68. George, S. M., Ott, A. W. & Klaus, J. W. Surface Chemistry for Atomic Layer Growth. *J. Phys. Chem.* **100,** 13121–13131 (Jan. 1996).

69. George, S. M. Atomic Layer Deposition: An Overview. *Chem. Rev.* **110,** 111–131 (Jan. 2010).

70. Puurunen, R. L. A Short History of Atomic Layer Deposition: Tuomo Suntola's Atomic Layer Epitaxy. *Chem. Vap. Deposition* **20,** 332–344 (Dec. 2014).

71. Leskelä, M. & Ritala, M. Atomic Layer Deposition Chemistry: Recent Developments and Future Challenges. *Angewandte Chemie International Edition* **42,** 5548–5554 (2003).

72. Puurunen, R. L. Surface chemistry of atomic layer deposition: A case study for the trimethylaluminum/water process. *Journal of Applied Physics* **97,** 121301 (June 2005).

73. Detavernier, C. *et al.* Tailoring nanoporous materials by atomic layer deposition. *Chem. Soc. Rev.* **40,** 5242–5253 (Oct. 2011).

74. Profijt, H. B. *et al.* Plasma-Assisted Atomic Layer Deposition: Basics, Opportunities, and Challenges. *Journal of Vacuum Science & Technology A: Vacuum, Surfaces, and Films* **29,** 050801 (2011).

75. Miikkulainen, V. *et al.* Atomic layer deposited lithium aluminum oxide: (In)dependency of film properties from pulsing sequence. *Journal of Vacuum Science & Technology A* **33,** 01A101 (Jan. 2015).

76. Longrie, D., Deduytsche, D. & Detavernier, C. Reactor concepts for atomic layer deposition on agitated particles: A review. *Journal of Vacuum Science & Technology A* **32,** 010802 (Jan. 2014).

77. Badot, J. C. *et al.* Atomic Layer Epitaxy of Vanadium Oxide Thin Films and Electrochemical Behavior in Presence of Lithium Ions. *Electrochem. Solid-State Lett.* **3,** 485–488 (Oct. 2000).

78. Snyder, M. Q. *et al.* Synthesis and characterization of atomic layer deposited titanium nitride thin films on lithium titanate spinel powder as a lithium-ion battery anode. *Journal of Power Sources* **165,** 379–385 (Feb. 2007).

79. Knoops, H. C. M. *et al.* Atomic layer deposition for nanostructured Li-ion batteries. *Journal of Vacuum Science & Technology A* **30,** 010801 (Jan. 2012).

80. Meng, X., Yang, X.-Q. & Sun, X. Emerging Applications of Atomic Layer Deposition for Lithium-Ion Battery Studies. *Advanced Materials* **24,** 3589–3615 (July 2012).

81. Liu, J. & Sun, X. Elegant design of electrode and electrode/electrolyte interface in lithium-ion batteries by atomic layer deposition. *Nanotechnology* **26,** 024001 (Jan. 2015).

82. Meng, X. Towards high-energy and durable lithium-ion batteries via atomic layer deposition: elegantly atomic-scale material design and surface modification. *Nanotechnology* **26,** 020501 (Jan. 2015).

83. Guan, C. & Wang, J. Recent Development of Advanced Electrode Materials by Atomic Layer Deposition for Electrochemical Energy Storage. *Adv. Sci.* **3,** n/a–n/a (2016).

84. Ahmed, B., Xia, C. & Alshareef, H. N. Electrode surface engineering by atomic layer deposition: A promising pathway toward better energy storage. *Nano Today* **11,** 250–271 (Apr. 2016).

85. Ma, L. *et al.* Atomic Layer Deposition for Lithium-Based Batteries. *Adv. Mater. Interfaces,* n/a–n/a (Sept. 2016).

86. Put, B. *et al.* Electrical Characterization of Ultrathin RF-Sputtered LiPON Layers for Nanoscale Batteries. *ACS Appl. Mater. Interfaces* **8,** 7060–7069 (2016).

87. Kozen, A. C. *et al.* Atomic Layer Deposition of the Solid Electrolyte LiPON. *Chem. Mater.* **27,** 5324–5331 (Aug. 2015).

88. Jung, Y. S. *et al.* Improved Functionality of Lithium-Ion Batteries Enabled by Atomic Layer Deposition on the Porous Microstructure of Polymer Separators and Coating Electrodes. *Adv. Energy Mater.* **2,** 1022–1027 (Aug. 2012).

89. Kelly, P. J & Arnell, R. D. Magnetron sputtering: a review of recent developments and applications. *Vacuum* **56,** 159–172 (2000).

90. Depla, D. *Magnetrons, Reactive Gases and Sputtering* (Diederik Depla, July 2015).

91. *Reactive sputter deposition* (eds Depla, D. & Mahieu, S.) *Springer series in materials science* **109.** OCLC: 254590268 (Springer, Berlin, 2008).

92. Dobbelaere, T. *et al.* Atomic Layer Deposition of Aluminum Phosphate Based on the Plasma Polymerization of Trimethyl Phosphate. *Chem. Mater.* **26,** 6863–6871 (Dec. 2014).

93. Xie, Q. *et al.* Atomic layer deposition of TiO_2 from tetrakis-dimethyl-amido titanium or Ti isopropoxide precursors and H_2O. *Journal of Applied Physics* **102,** 083521 (Oct. 2007).

94. Musschoot, J. *et al.* Atomic layer deposition of titanium nitride from TDMAT precursor. *Microelectronic Engineering* **86,** 72–77 (Jan. 2009).

95. Dendooven, J. *et al.* Conformality of Al_2O_3 and AlN Deposited by Plasma-Enhanced Atomic Layer Deposition. *J. Electrochem. Soc.* **157,** G111–G116 (Apr. 2010).

96. Dendooven, J. *et al.* Low-Temperature Atomic Layer Deposition of Platinum Using (Methylcyclopentadienyl)trimethylplatinum and Ozone. *The Journal of Physical Chemistry C* **117,** 20557–20561 (2013).

97. Xie, Q. *et al.* Growth Kinetics and Crystallization Behavior of TiO[sub 2] Films Prepared by Plasma Enhanced Atomic Layer Deposition. *Journal of The Electrochemical Society* **155,** H688 (2008).

98. Rampelberg, G. *et al.* Crystallization and semiconductor-metal switching behavior of thin VO_2 layers grown by atomic layer deposition. *Thin Solid Films* **550,** 59 –64 (2014).

99. Rampelberg, G. *et al.* Semiconductor-metal transition in thin VO_2 films grown by ozone based atomic layer deposition. *Applied Physics Letters* **98,** 162902 (Apr. 2011).

100. Nilsen, O., Fjellvåg, H. & Kjekshus, A. Growth of manganese oxide thin films by atomic layer deposition. *Thin Solid Films* **444,** 44–51 (Nov. 2003).

101. Nilsen, O. *et al.* Effect of substrate on the characteristics of manganese(IV) oxide thin films prepared by atomic layer deposition. *Thin Solid Films* **468,** 65–74 (Dec. 2004).

102. Mattelaer, F. *et al.* Manganese oxide films with controlled oxidation state for water splitting devices through a combination of atomic layer deposition and post-deposition annealing. *RSC Advances* **6,** 98337–98343 (2016).

103. Yasaka, M. X-ray thin-film measurement techniques: X-ray reflectivity measurement. *The Rigaku Journal* **26,** 1–9 (2010).

104. Tiilikainen, J *et al.* Accuracy in x-ray reflectivity analysis. *J. Phys. D: Appl. Phys.* **40,** 7497 (2007).

105. Kiessig, H. Untersuchungen zur Totalreflexion von Röntgenstrahlen. *Annalen der Physik* **402,** 715–168 (1931).

106. Yokoyama, D *et al.* Horizontal orientation of linear-shaped organic molecules having bulky substituents in neat and doped vacuum-deposited amorphous films. *Organic Electronics* **10,** 127–137 (Feb. 2009).

107. Butt, H.-J., Cappella, B. & Kappl, M. Force measurements with the atomic force microscope: Technique, interpretation and applications. *Surf. Sci. Rep.* **59,** 1 –152 (2005).

108. Raposo, M., Ferreira, Q. & a. Ribeiro, P. A Guide for Atomic Force Microscopy Analysis of Soft- Condensed Matter. *Modern Research and Educational Topics in Microscopy,* 758–769 (2007).

109. *Electron microscope* `wikipedia.org/wiki/Electron_microscope`. Accessed: Jan. 2017.

110. Kortright, J. B. & Thompson, A. C. *X-Ray Data Booklet* X-Ray emission energies table.

111. *X-ray Crystallography* `wikipedia.org/wiki/X-ray_crystallography`. Accessed: Jan. 2017.

112. Bard, A. J. & Faulkner, L. R. *Electrochemical Methods, Fundamentals and Applications* (John Wiley and sons inc., 2001).

113. Evans, D. H. *et al.* Cyclic voltammetry. *Journal of Chemical Education* **60,** 290 (Apr. 1983).

114. Heinze, J. Cyclic VoltammetryElectrochemical Spectroscopy. New Analytical Methods (25). *Angew. Chem. Int. Ed. Engl.* **23,** 831–847 (Nov. 1984).

115. Wen, C. J. *et al.* Use of electrochemical methods to determine chemical-diffusion coefficients in alloys: application to LiAI. *Int. Met. Rev.* **26,** 253–268 (Jan. 1981).

116. Li, J. *et al.* Potentiostatic Intermittent Titration Technique for Electrodes Governed by Diffusion and Interfacial Reaction. *J. Phys. Chem. C* **116,** 1472–1478 (Jan. 2012).

117. Wen, C. J. *et al.* Thermodynamic and Mass Transport Properties of LiAl. *J. Electrochem. Soc.* **126,** 2258–2266 (Dec. 1979).

118. Julien, C. & Yebka, B. in *New Trends in Intercalation Compounds for Energy Storage* (eds Julien, C., Pereira-Ramos, J. P. & Momchilov, A.) 253–268 (Springer Netherlands, Dordrecht, 2002).

119. Park, M. *et al.* A review of conduction phenomena in Li-ion batteries. *Journal of Power Sources* **195,** 7904–7929 (Dec. 2010).

120. Macdonald, J. R. Impedance spectroscopy. *Ann Biomed Eng* **20,** 289–305 (May 1992).

121. Brug, G. *et al.* The analysis of electrode impedances complicated by the presence of a constant phase element. *Journal of Electroanalytical Chemistry and Interfacial Electrochemistry* **176,** 275–295 (Sept. 1984).

122. Barsoukov, E. *et al.* Universal battery parameterization to yield a non-linear equivalent circuit valid for battery simulation at arbitrary load. *Journal of Power Sources* **83,** 61–70 (1999).

123. Grundy, A. N., Hallstedt, B. & Gauckler, L. J. Assessment of the Mn-O system. *JPE* **24,** 21–39 (Feb. 2003).

124. Stobbe, E., de Boer, B. & Geus, J. The reduction and oxidation behaviour of manganese oxides. *Catalysis Today* **47,** 161–167 (Jan. 1999).

125. Fritsch, S. & Navrotsky, A. Thermodynamic Properties of Manganese Oxides. *Journal of the American Ceramic Society* **79,** 1761–1768 (July 1996).

126. Young, M. J. *et al.* Rapid Growth of Crystalline Mn_5O_8 by Self-Limited Multilayer Deposition using $Mn(EtCp)_2$ and O_3. *ACS Applied Materials & Interfaces* **8,** 18560–18569 (July 2016).

127. Ma, J. *et al.* Catalysis by Manganese Oxide Monolayers Part 2: Zirconia Support. *Berichte der Bunsengesellschaft für physikalische Chemie* **100,** 585–593 (May 1996).

128. Craciun, R. & Dulamita, N. Influence of La_2O_3 promoter on the structure of MnO_x/SiO_2 catalysts. *Catalysis Letters* **46,** 229–234 (July 1997).

129. Gorlin, Y. & Jaramillo, T. F. A Bifunctional Nonprecious Metal Catalyst for Oxygen Reduction and Water Oxidation. *J. Am. Chem. Soc.* **132,** 13612–13614 (2010).

130. Calegaro, M., Lima, F. & Ticianelli, E. Oxygen reduction reaction on nanosized manganese oxide particles dispersed on carbon in alkaline solutions. *Journal of Power Sources* **158,** 735–739 (July 2006).

131. Diab, N. & Schuhmann, W. Electropolymerized manganese porphyrin/ polypyrrole films as catalytic surfaces for the oxidation of nitric oxide. *Electrochimica Acta* **47,** 265–273 (Sept. 2001).

132. Singoredjo, L. *et al.* Alumina supported manganese oxides for the low-temperature selective catalytic reduction of nitric oxide with ammonia. *Applied Catalysis B: Environmental* **1,** 297–316 (Dec. 1992).

133. Kang, M. *et al.* Manganese oxide catalysts for NO_x reduction with NH_3 at low temperatures. *Applied Catalysis A: General* **327,** 261–269 (Aug. 2007).

134. Qi, G. & Yang, R. T. Low-temperature selective catalytic reduction of NO with NH_3 over iron and manganese oxides supported on titania. *Applied Catalysis B: Environmental* **44,** 217–225 (Aug. 2003).

135. Hasan, M. A. *et al.* Promotion of the hydrogen peroxide decomposition activity of manganese oxide catalysts. *Applied Catalysis A: General* **181,** 171–179 (May 1999).

136. Einaga, H., Ibusuki, T. & Futamura, S. Performance evaluation of a hybrid system comprising silent discharge plasma and manganese oxide catalysts for benzene decomposition. *IEEE Transactions on Industry Applications* **37,** 1476–1482 (Oct. 2001).

137. Li, W. & Oyama, S. T. Mechanism of Ozone Decomposition on a Manganese Oxide Catalyst. 2. Steady-State and Transient Kinetic Studies. *J. Am. Chem. Soc.* **120,** 9047–9052 (Sept. 1998).

138. Luan, X., Guan, D. & Wang, Y. Enhancing High-Rate and Elevated-Temperature Performances of Nano-Sized and Micron-Sized $LiMn_2O_4$ in Lithium-Ion Batteries with Ultrathin Surface Coatings. *Journal of Nanoscience and Nanotechnology* **12,** 7113–7120 (Sept. 2012).

139. Wu, M.-S. & Chiang, P.-C. J. Electrochemically deposited nanowires of manganese oxide as an anode material for lithium-ion batteries. *Electrochemistry Communications* **8,** 383–388 (Mar. 2006).

140. Kordesh, K. & Weissenbacher, M. Rechargeable alkaline manganese dioxide/zinc batteries. *Journal of Power Sources* **51,** 61–78 (Aug. 1994).

141. Martha de Souza, C. C. B., Corrêa de Oliveira, D. & Tenório, J. A. S. Characterization of used alkaline batteries powder and analysis of zinc recovery by acid leaching. *Journal of Power Sources* **103,** 120–126 (Dec. 2001).

142. Landorf, R. W. & Licht, S. J. Sputtered Manganese Dioxide as Counterelectrodes in Thin Film Capacitors. *J. Electrochem. Soc.* **119,** 430–433 (Apr. 1972).

143. Zhang, H. *et al.* Growth of Manganese Oxide Nanoflowers on Vertically-Aligned Carbon Nanotube Arrays for High-Rate Electrochemical Capacitive Energy Storage. *Nano Lett.* **8,** 2664–2668 (Sept. 2008).

144. Hu, C. Ideal capacitive behavior of hydrous manganese oxide prepared by anodic deposition. *Electrochemistry Communications* **4,** 105–109 (Feb. 2002).

145. Babakhani, B. & Ivey, D. G. Anodic deposition of manganese oxide electrodes with rod-like structures for application as electrochemical capacitors. *Journal of Power Sources* **195,** 2110–2117 (Apr. 2010).

146. Silva, R. M. *et al.* Coating of Vertically Aligned Carbon Nanotubes by a Novel Manganese Oxide Atomic Layer Deposition Process for Binder-Free Hybrid Capacitors. *Adv. Mater. Interfaces* **3,** n/a–n/a (Nov. 2016).

147. Dagotto, E., Hotta, T. & Moreo, A. Colossal magnetoresistant materials: the key role of phase separation. *Physics Reports* **344,** 1–153 (Apr. 2001).

148. Smith, K. S. & Huyck, H. L. An overview of the abundance, relative mobility, bioavailability, and human toxicity of metals. *The environmental geochemistry of mineral deposits* **6,** 29–70 (1999).

149. Thackeray, M. M. Manganese oxides for lithium batteries. *Progress in Solid State Chemistry* **25,** 1–71 (1997).

150. Thackeray, M. M. *et al.* Spinel Electrodes from the Li-Mn-O System for Rechargeable Lithium Battery Applications. *J. Electrochem. Soc.* **139,** 363–366 (Feb. 1992).

151. Wang, E. I., Lin, L. & Bowden, W. L. *pat.* US5482796 A (1996).

152. Julien, C. M. *et al.* Comparative Issues of Cathode Materials for Li-Ion Batteries. *Inorganics* **2,** 132–154 (Mar. 2014).

153. Fang, X. *et al.* Electrode reactions of manganese oxides for secondary lithium batteries. *Electrochemistry Communications* **12,** 1520–1523 (Nov. 2010).

154. Wang, D. *et al.* β-MnO_2 as a cathode material for lithium ion batteries from first principles calculations. *Physical Chemistry Chemical Physics* **15,** 9075 (2013).

155. Etman, A. S. *et al.* Effect of Film Morphology on the Li Ion Intercalation Kinetics in Anodic Porous Manganese Dioxide Thin Films. *J. Phys. Chem. C* **118,** 9889–9898 (May 2014).

156. Wang, G., Zhang, L. & Zhang, J. A review of electrode materials for electrochemical supercapacitors. **41,** 797–828 (Jan. 2012).

157. Young, M. J. *et al.* Charge Storage in Cation Incorporated α-MnO2. *Chem. Mater.* **27,** 1172–1180 (Feb. 2015).

158. Put, B. *et al.* High Cycling Stability and Extreme Rate Performance in Nanoscaled $LiMn_2O_4$ Thin Films. *ACS Appl. Mater. Interfaces* **7,** 22413–22420 (2015).

159. Xia, Y., Zhou, Y. & Yoshio, M. Capacity Fading on Cycling of 4V $Li/LiMn_2O_4$ Cells. *J. Electrochem. Soc.* **144,** 2593–2600 (Aug. 1997).

160. Song, M. Y., Ahn, D. S. & Park, H. R. Capacity fading of spinel phase LiMn2O4 with cycling. *Journal of Power Sources* **83,** 57–60 (1999).

161. Dai, Y., Cai, L. & White, R. E. Capacity Fade Model for Spinel $LiMn_2O_4$ Electrode. *J. Electrochem. Soc.* **160,** A182–A190 (Jan. 2013).

162. Yu, X. Q. *et al.* Nanocrystalline MnO thin film anode for lithium ion batteries with low overpotential. *Electrochemistry Communications* **11,** 791–794 (Apr. 2009).

163. Zhong, K. *et al.* MnO powder as anode active materials for lithium ion batteries. *Journal of Power Sources* **195,** 3300–3308 (May 2010).

164. Pang, S.-C., Anderson, M. A. & Chapman, T. W. Novel Electrode Materials for Thin-Film Ultracapacitors: Comparison of Electrochemical Properties of Sol-Gel-Derived and Electrodeposited Manganese Dioxide. *Journal of The Electrochemical Society* **147,** 444 (2000).

165. Chigane, M. & Ishikawa, M. Manganese Oxide Thin Film Preparation by Potentiostatic Electrolyses and Electrochromism. *J. Electrochem. Soc.* **147,** 2246–2251 (June 2000).

166. Neishi, K. *et al.* Formation of a manganese oxide barrier layer with thermal chemical vapor deposition for advanced large-scale integrated interconnect structure. *Applied Physics Letters* **93,** 032106–032106–3 (2008).

167. Nakamura, T. *et al.* Spectroscopic Study on Metallorganic Chemical Vapor Deposition of Manganese Oxide Films. *Journal of The Electrochemical Society* **152,** C584–C587 (Sept. 2005).

168. Nilsen, O. *et al.* Growth of nano-needles of manganese(IV) oxide by atomic layer deposition. *J Nanosci Nanotechnol* **8,** 1003–1011 (Feb. 2008).

169. Lu, H. *et al.* Thin MnO and NiO films grown using atomic layer deposition from ethylcyclopentadienyl type of precursors. *Journal of Crystal Growth* **310,** 5464–5468 (Dec. 2008).

170. Burton, B., Fabreguette, F. & George, S. Atomic layer deposition of MnO using Bis(ethylcyclopentadienyl)manganese and H_2O. *Thin Solid Films* **517,** 5658–5665 (Aug. 2009).

171. Mattelaer, F. *et al.* Deposition of MnO Anode and MnO_2 Cathode Thin Films by Plasma Enhanced Atomic Layer Deposition Using the $Mn(thd)_3$ Precursor. *Chem. Mater.* **27,** 3628–3635 (May 2015).

172. Jin, H., Hagen, D. & Karppinen, M. Low-temperature atomic layer deposition of crystalline manganese oxide thin films (Sept. 2016).

173. Klesko, J. P. *et al.* Unusual stoichiometry control in the atomic layer deposition of manganese borate films from manganese bis(tris-(pyrazolyl) borate) and ozone. *Journal of Vacuum Science & Technology A: Vacuum, Surfaces, and Films* **34,** 051515 (Sept. 2016).

174. Lee, Y. *et al.* Atomic Layer Deposition of Metal Fluorides Using HF-Pyridine as the Fluorine Precursor. *Chem. Mater.* **28,** 2022–2032 (Apr. 2016).

175. Riha, S. C. *et al.* Atomic Layer Deposition of MnS: Phase Control and Electrochemical Applications. *ACS Appl. Mater. Interfaces* **8,** 2774–2780 (Feb. 2016).

176. Miikkulainen, V. *et al.* Atomic Layer Deposition of Spinel Lithium Manganese Oxide by Film-Body-Controlled Lithium Incorporation for Thin-Film Lithium-Ion Batteries. *J. Phys. Chem. C* **118,** 1258–1268 (Jan. 2014).

177. Young, M. J. *et al.* Band Diagram and Rate Analysis of Thin Film Spinel $LiMn_2O_4$ Formed by Electrochemical Conversion of ALD-Grown MnO. *Adv. Funct. Mater.* n/a–n/a (Sept. 2016).

178. Pickrahn, K. L. *et al.* Active MnO_x Electrocatalysts Prepared by Atomic Layer Deposition for Oxygen Evolution and Oxygen Reduction Reactions. *Adv. Energy Mater.* **2,** 1269–1277 (2012).

179. Strandwitz, N. C. *et al.* Photoelectrochemical Behavior of n-type Si(100) Electrodes Coated with Thin Films of Manganese Oxide Grown by Atomic Layer Deposition. *J. Phys. Chem. C* **117,** 4931–4936 (2013).

180. Morita, M., Iwakura, C. & Tamura, H. The anodic characteristics of massive manganese oxide electrode. *Electrochimica Acta* **24,** 357–362 (Apr. 1979).

181. Nelson, A. J., Reynolds, J. G. & Roos, J. W. *Core-level satellites and outer core-level multiplet splitting in Mn model compounds* in *The 46th international symposium of the american vacuum society* **18** (AVS, Seattle, Washington (USA), 2000), 1072–1076.

182. Di Castro, V. & Polzonetti, G. XPS study of MnO oxidation. *Journal of Electron Spectroscopy and Related Phenomena* **48,** 117–123 (1989).

183. Foord, J. S., Jackman, R. B. & Allen, G. C. An X-ray photoelectron spectroscopic investigation of the oxidation of manganese. *Philosophical Magazine A* **49,** 657–663 (1984).

184. Timmermans, M. *et al. Electrodeposition of Thick MnO_2 Films on Restrictive Substrates* in *Meeting Abstracts* (The Electrochemical Society, 2015), 936–936.

185. Timmermans, M. *et al.* Electrochemical deposition of thick and adherent MnO_2 films for energy storage devices. *In preparation.*

186. Oudenhoven, J. F. M., Baggetto, L. & Notten, P. H. L. All-Solid-State Lithium-Ion Microbatteries: A Review of Various Three-Dimensional Concepts. *Advanced Energy Materials* **1,** 10–33 (2011).

187. Long, J. W. *et al.* Three-Dimensional Battery Architectures. *Chemical Reviews* **104,** 4463–4492 (Oct. 2004).

188. Dudney, N. J. Solid-state thin-film rechargeable batteries. *Materials Science and Engineering: B. Thin Films and Nanomaterials for energy Conversion and Storage* **116,** 245–249 (Feb. 2005).

189. Vereecken, P. M. & Huyghebaert, C. (Invited) Conformal Deposition for 3D Thin-Film Batteries. *ECS Transactions* **58,** 111–118 (Aug. 2013).

190. Boukhalfa, S., Evanoff, K. & Yushin, G. Atomic layer deposition of vanadium oxide on carbon nanotubes for high-power supercapacitor electrodes. *Energy Environ. Sci.* **5,** 6872–6879 (Apr. 2012).

191. Langereis, E. *et al.* In situ spectroscopic ellipsometry as a versatile tool for studying atomic layer deposition. *J. Phys. D: Appl. Phys.* **42,** 073001 (Apr. 2009).

192. Putkonen, M. & Niinistö, L. in *Precursor Chemistry of Advanced Materials* (ed Fischer, R. A.) *Topics in Organometallic Chemistry* 9, 125–145 (Springer Berlin Heidelberg, Jan. 2005).

193. Nilsen, O., Fjellvåg, H. & Kjekshus, A. Inexpensive set-up for determination of decomposition temperature for volatile compounds. *Thermochimica Acta* **404,** 187–192 (Sept. 2003).

194. Hahn, W. C. & Muan, A. Studies in the system Mn-O–The Mn_2O_3-Mn_3O_4 and Mn_3O_4-MnO equilibria. *Am J Sci* **258,** 66–78 (Jan. 1960).

195. Li, X. *et al.* Tin Oxide with Controlled Morphology and Crystallinity by Atomic Layer Deposition onto Graphene Nanosheets for Enhanced Lithium Storage. *Adv. Funct. Mater.* **22,** 1647–1654 (Apr. 2012).

196. *NIST atomic spectra database - version 5* 2014.

197. Camacho, J. J. *et al.* Optical emission spectroscopy of oxygen plasma induced by IR CO2 pulsed laser. *J. Phys. D: Appl. Phys.* **41,** 215206 (Nov. 2008).

198. Pearse, R. W. B. & Gaydon, A. G. *The identification of molecular spectra* (Chapman and Hall, Dec. 1976).

199. Miikkulainen, V. *et al.* Crystallinity of inorganic films grown by atomic layer deposition: Overview and general trends. *Journal of Applied Physics* **113,** 021301–021301–101 (2013).

200. Ramírez, A. *et al.* Evaluation of MnOx, Mn_2O_3, and Mn_3O_4 Electrodeposited Films for the Oxygen Evolution Reaction of Water. *J. Phys. Chem. C* **118,** 14073–14081 (July 2014).

201. Indra, A. *et al.* Active Mixed-Valent MnO_x Water Oxidation Catalysts through Partial Oxidation (Corrosion) of Nanostructured MnO Particles. *Angew. Chem. Int. Ed.* **52,** 13206–13210 (Dec. 2013).

202. Rongé, J. *et al.* Monolithic cells for solar fuels. *Chem. Soc. Rev.* **43,** 7963–7981 (Feb. 2014).

203. Li, Y. W. *et al.* Influence of post-annealing on structural, electrical and optical properties of manganese oxide thin films grown by atomic layer deposition. *Thin Solid Films* **574,** 115–119 (Jan. 2015).

204. Zaki, M. I. *et al.* Thermochemistry of manganese oxides in reactive gas atmospheres: Probing redox compositions in the decomposition course MnO_2 MnO. *Thermochimica Acta* **303,** 171–181 (Oct. 1997).

205. Barner, H. E. & Mantell, C. L. Kinetics of Hydrogen Reduction of Manganese Dioxide. *Ind. Eng. Chem. Proc. Des. Dev.* **7,** 285–294 (Apr. 1968).

206. Knaepen, W. *et al.* In-situ X-ray Diffraction study of Metal Induced Crystallization of amorphous silicon. *Thin Solid Films* **516,** 4946–4952 (June 2008).

207. Rampelberg, G. *et al.* In situ X-ray diffraction study of the controlled oxidation and reduction in the VO system for the synthesis of VO_2 and V_2O_3 thin films. *J. Mater. Chem. C* **3,** 11357–11365 (2015).

208. Trotochaud, L., Mills, T. J. & Boettcher, S. W. An Optocatalytic Model for SemiconductorCatalyst Water-Splitting Photoelectrodes Based on In Situ Optical Measurements on Operational Catalysts. *J. Phys. Chem. Lett.* **4,** 931–935 (2013).

209. Katzke, H., Toledano, P. & Depmeier, W. Theory of morphotropic transformations in vanadium oxides. *Phys. Rev. B* **68,** 024109 (July 2003).

210. Keränen, J *et al.* Preparation, characterization and activity testing of vanadia catalysts deposited onto silica and alumina supports by atomic layer deposition. *Applied Catalysis A: General* **228,** 213–225 (2002).

211. Keränen, J. *et al.* Preparation by atomic layer deposition and characterization of active sites in nanodispersed vanadia/titania/silica catalysts. *Catalysis Today. Innovation in Selective Oxidation 2003* **9192,** 67–71 (July 2004).

212. Gervasini, A. *et al.* Surface characteristics and activity in selective oxidation of o-xylene of supported V_2O_5 catalysts prepared by standard impregnation and atomic layer deposition. *Catalysis Today. Selective Catalytic Oxidation: Fundamentals, Application and Environmental Impacts-ACS National Meeting, New York, 7-11 September 2003* **96,** 187–194 (2004).

213. Bahlawane, N. & Lenoble, D. Vanadium Oxide Compounds: Structure, Properties, and Growth from the Gas Phase. *Chem. Vap. Deposition* **20,** 299–311 (Sept. 2014).

214. MOTT, N. F. Metal-Insulator Transition. *Rev. Mod. Phys.* **40,** 677–683 (1968).

215. Stegemann, B. *et al.* Switching adhesion forces by crossing the metal-insulator transition in Magnéli-type vanadium oxide crystals. *Beilstein Journal of Nanotechnology* **2,** 59–65 (2011).

216. Ko, C., Yang, Z. & Ramanathan, S. Work Function of Vanadium Dioxide Thin Films Across the Metal-Insulator Transition and the Role of Surface Nonstoichiometry. *ACS Appl. Mater. Interfaces* **3,** 3396–3401 (Sept. 2011).

217. Yang, Z., Ko, C. & Ramanathan, S. Oxide Electronics Utilizing Ultrafast Metal-Insulator Transitions. *Annual Review of Materials Research* **41,** 337–367 (Aug. 2011).

218. Whittingham, M. S. *et al.* Some transition metal (oxy)phosphates and vanadium oxides for lithium batteries. *Journal of Materials Chemistry* **15,** 3362 (2005).

219. Murphy, D. W. *et al.* Lithium incorporation by vanadium pentoxide. *Inorganic Chemistry* **18,** 2800–2803 (1979).

220. Dickens, P. G. *et al.* Phase relationships in the ambient temperature $Li_xV_2O_5$ system ($0.1 < x < 1.0$). *Materials Research Bulletin* **14,** 1295–1299 (1979).

221. Delmas, C. *et al.* The $Li_xV_2O_5$ system: An overview of the structure modifications induced by the lithium intercalation. *Solid State Ionics* **69,** 257–264 (Aug. 1994).

222. Liu, Y. *et al.* V_2O_5 Nano-Electrodes with High Power and Energy Densities for Thin Film Li-Ion Batteries. *Adv. Energy Mater.* **1,** 194–202 (2011).

223. Leger, C. *et al.* Structural and Electrochemical Properties of $\omega Li_xV_2O_5$ ($0.4 < x < 3$) as Rechargeable Cathodic Material for Lithium Batteries. *Journal of The Electrochemical Society* **152,** A236–A241 (Jan. 2005).

224. Cohen, Y. S. & Aurbach, D. Surface films phenomena on vanadium-pentoxide cathodes for Li and Li-ion batteries: in situ AFM imaging. *Electrochem. Commun.* **6,** 536 –542 (2004).

225. Pan, A. *et al.* Synthesis of Hierarchical Three-Dimensional Vanadium Oxide Microstructures as High-Capacity Cathode Materials for Lithium-Ion Batteries. *ACS Applied Materials and Interfaces* **4,** 3874–3879 (2012).

226. Chou, S.-L. *et al.* High Capacity, Safety, and Enhanced Cyclability of Lithium Metal Battery Using a V_2O_5 Nanomaterial Cathode and Room Temperature Ionic Liquid Electrolyte. *Chem. Mater.* **20,** 7044–7051 (2008).

227. Ganganagappa, N. & Siddaramanna, A. One step synthesis of monoclinic VO_2(B) bundles of nanorods: Cathode for Li ion battery. *Mater. Charact.* **68,** 58–62 (2012).

228. Yan, Y. *et al.* Vanadium based materials as electrode materials for high performance supercapacitors. *Journal of Power Sources* **329,** 148–169 (Oct. 2016).

229. West, K. *et al.* Vanadium oxides as electrode materials for rechargeable lithium cells. *Journal of Power Sources* **20.** 3rd International Meeting on Lithium Batteries, 165 –172 (1987).

230. Manthiram, A. & Kim, J. Low Temperature Synthesis of Insertion Oxides for Lithium Batteries. *Chemistry of Materials* **10,** 2895–2909 (1998).

231. Wilhelmi, K.-A. *et al.* A Refinement of the Crystal Structure of V_6O_{13}. *Acta Chemica Scandinavica* **25,** 2675–2687 (1971).

232. Sakurai, Y. *et al.* Electrochemical behaviour of amorphous V_2O_5(-P_2O_5) cathodes for lithium secondary batteries. *Journal of Power Sources* **20,** 173–177 (July 1987).

233. Lantelme, F. *et al.* Electrochemical Study of Phase Transition Processes in Lithium Insertion in V_2O_5 Electrodes. *Journal of The Electrochemical Society* **150,** A1202 (2003).

234. Liu, Y. *et al.* V_2O_5 Nano-Electrodes with High Power and Energy Densities for Thin Film Li-Ion Batteries. *Advanced Energy Materials* **1,** 194–202 (Mar. 2011).

235. Østreng, E. *et al.* High power nano-structured V_2O_5 thin film cathodes by atomic layer deposition. *J. Mater. Chem. A* **2,** 15044–15051 (2014).

236. Zhou, S. *et al.* A Nanonet-Enabled Li Ion Battery Cathode Material with High Power Rate, High Capacity, and Long Cycle Lifetime. *ACS Nano* **6,** 919–924 (Jan. 2012).

237. Murphy, D. W. & Christian, P. A. Solid State Electrodes for High Energy Batteries. *Science* **205,** 651–656 (Aug. 1979).

238. Murphy, D. W. *et al.* Lithium Incorporation by V_6O_{13} and related vanadium (+4,+5) oxide cathode materials. *Journal Electrochem. Soc.* **128,** 2053–2060 (1981).

239. Murphy, D. W. *et al.* Vanadium Oxide Cathode Materials for Secondary Lithium Cells. *J. Electrochem. Soc.* **126,** 497–499 (Mar. 1979).

240. Christian, P. A. *et al.* Vanadium Oxide Cathode Materials for Secondary Lithium Cells. *J. Electrochem. Soc.* **126,** 497–499 (1979).

241. Whittingham, M. S. Lithium Batteries and Cathode Materials. *Chemical Reviews* **104,** 4271–4302 (2004).

242. Van der Ven, A., Bhattacharya, J. & Belak, A. A. Understanding Li Diffusion in Li-Intercalation Compounds. *Accounts of Chemical Research* **46,** 1216–1225 (May 2013).

243. Julien, C. & Nazri, G.-A. *Solid State Batteries: Materials Design and Optimization* (ed Tuller, H. L.) (Springer US, Boston, MA, 1994).

244. Machida, N., Fuchida, R. & Minami, T. Electrochemical insertion of lithium ions into V_2O_5 glasses containing transition-metal oxides. *Solid State Ionics* **35,** 295–298 (Sept. 1989).

245. Lee, J. *et al.* Unlocking the Potential of Cation-Disordered Oxides for Rechargeable Lithium Batteries. *Science* **343,** 519–522 (Jan. 2014).

246. Tossici, R. *et al.* Study of amorphous and crystalline $Li_{1+x}V_3O_8$ by FTIR, XAS and electrochemical techniques. *Solid State Ionics* **57,** 227–234 (1992).

247. Bates, J. B. *et al.* Fabrication and characterization of amorphous lithium electrolyte thin films and rechargeable thin-film batteries. *Journal of Power Sources. This volume contains the Proceedings of the 6th International Meeting on Lithium Batteries* **43,** 103–110 (1993).

248. Fang, H.-T. *et al.* Comparison of the rate capability of nanostructured amorphous and anatase TiO_2 for lithium insertion using anodic TiO_2 nanotube arrays. *Nanotechnology* **20,** 225701 (June 2009).

249. Sabi, Y. *et al.* A new class of amorphous cathode active material $Li_xM_yPO_z$ (M = Ni, Cu, Co, Mn, Au, Ag, Pd). *Journal of Power Sources* **258,** 54–60 (July 2014).

250. Uchaker, E. *et al.* Better than crystalline: amorphous vanadium oxide for sodium-ion batteries. *J. Mater. Chem. A* **2,** 18208–18214 (Sept. 2014).

251. Passerini, S. *et al.* High rate electrodes of V_2O_5 aerogel. *Electrochimica Acta* **44,** 2209–2217 (Feb. 1999).

252. Chae, O. B. *et al.* Reversible Lithium Storage at Highly Populated Vacant Sites in an Amorphous Vanadium Pentoxide Electrode. *Chem. Mater.* **26,** 5874–5881 (2014).

253. Blanquart, T. *et al.* Atomic layer deposition and characterization of vanadium oxide thin films. *RSC Advances* **3,** 1179–1185 (Dec. 2012).

254. Premkumar, P. A. *et al.* Process Study and Characterization of VO_2 Thin Films Synthesized by ALD Using TEMAV and O_3 Precursors. *ECS Journal of Solid State Science and Technology* **1,** P169–P174 (Jan. 2012).

255. Wang, X. *et al.* Atomic layer deposition of vanadium oxide thin films from tetrakis(dimethylamino)vanadium precursor. *Journal of Materials Research* **32,** 37–44 (Jan. 2017).

256. Mattelaer, F. *et al.* Atomic layer deposition of vanadium oxides for thin-film lithium-ion battery applications. *RSC Adv.* **6,** 114658–114665 (2016).

257. Geert Rampelberg. *Thin Film Synthesis of VO_2 and VN by Gas-Solid Reactions And Atomic Layer Deposition* PhD thesis (UGent, 2016).

258. Tangirala, M. *et al.* Physical Analysis of VO_2 Films Grown by Atomic Layer Deposition and RF Magnetron Sputtering. *ECS J. Solid State Sci. Technol.* **3,** N89–N94 (Jan. 2014).

259. Mattelaer, F. *et al.* Amorphous And Crystalline Vanadium Oxides As High-Energy And High-Power Cathodes For 3D Thin-Film Lithium Ion Batteries. *To be published.*

260. Baddour-Hadjean, R. *et al.* A Raman study of the lithium insertion process in vanadium pentoxide thin films deposited by atomic layer deposition. *J. Raman Spectrosc.* **33,** 631–638 (Aug. 2002).

261. Le Van, K. *et al.* Amorphous vanadium oxide films synthesised by ALCVD for lithium rechargeable batteries. *Journal of Power Sources* **160,** 592–601 (Sept. 2006).

262. Musschoot, J. *et al.* ALD of Vanadium Oxide. *ECS Trans.* **25,** 29–37 (Sept. 2009).

263. Musschoot, J. *et al.* Comparison of Thermal and Plasma-Enhanced ALD/CVD of Vanadium Pentoxide. *J. Electrochem. Soc.* **156,** P122–P126 (July 2009).

264. Banerjee, P. *et al.* Mixed mode, ionic-electronic diode using atomic layer deposition of V_2O_5 and ZnO films. **21,** 15391–15397 (Sept. 2011).

265. Chen, X. *et al.* Cathodic ALD V_2O_5 thin films for high-rate electrochemical energy storage. **3,** 4294–4302 (Mar. 2013).

266. Chen, X. *et al.* MWCNT/V_2O_5 Core/Shell Sponge for High Areal Capacity and Power Density Li-Ion Cathodes. *ACS Nano* **6,** 7948–7955 (Sept. 2012).

267. Chen, X. *et al.* Ozone-Based Atomic Layer Deposition of Crystalline V_2O_5 Films for High Performance Electrochemical Energy Storage. *Chem. Mater.* **24,** 1255–1261 (Apr. 2012).

268. Østreng, E., Nilsen, O. & Fjellvåg, H. Optical Properties of Vanadium Pentoxide Deposited by ALD. *J. Phys. Chem. C* **116,** 19444–19450 (Sept. 2012).

269. Keränen, J *et al.* Calorimetric measurements of the acidity of supported vanadium oxides prepared by ALE and impregnation. *Thermochimica Acta. Calorimetry and Thermal Effects in catalysis. A Collection of Papers from the Second International Symposium on Calorimetry and Thermal Effects in Catalysis Lyon, France, 5-7 July 2000* **379,** 233–239 (Nov. 2001).

270. Dagur, P., Mane, A. U. & Shivashankar, S. A. Thin films of VO_2 on glass by atomic layer deposition: microstructure and electrical properties. *Journal of Crystal Growth* **275,** 1223–1228 (2005).

271. Povey, I. M. *et al.* Atomic layer deposition for the fabrication of 3D photonic crystals structures: Growth of Al_2O_3 and VO_2 photonic crystal systems. *Surface and Coatings Technology. Euro CVD 1616th European Conference on Chemical Vapor Deposition* **201,** 9345–9348 (Sept. 2007).

272. Willinger, M.-G. *et al.* Vanadium Oxide Sensing Layer Grown on Carbon Nanotubes by a New Atomic Layer Deposition Process. *Nano Letters* **8,** 4201–4204 (2008).

273. Silversmit, G., Poelman, H. & De Gryse, R. Influence of magnetron deposition parameters on the stoichiometry of sputtered V_2O_5 films. *Surf. Interface Anal.* **36,** 1163–1166 (2004).

274. Poelman, H. *et al.* V_2O_5 thin films deposited by means of d.c. magnetron sputtering from ceramic V_2O_3 targets. *Surf. Interface Anal.* **34** (2002).

275. Cazzanelli, E. *et al.* Raman and XPS characterization of vanadium oxide thin films deposited by reactive RF sputtering. *Solar Energy Materials and Solar Cells* **56,** 249–258 (Jan. 1999).

276. Watanabe, H., Itoh, K.-i. & Matsumoto, O. Properties of V_2O_5 thin films deposited by means of plasma MOCVD. *Thin Solid Films* **386,** 281–285 (2001).

277. Beke, S. A review of the growth of V_2O_5 films from 1885 to 2010. *Thin Solid Films* **519,** 1761–1771 (Jan. 2011).

278. Ryabova, L. A., Serbinov, I. A. & Darevsky, A. S. Preparation and Properties of Pyrolysis of Vanadium Oxide Films. *J. Electrochem. Soc.* **119,** 427–429 (Apr. 1972).

279. Silversmit, G. *et al.* Determination of the V2p XPS binding energies for different vanadium oxidation states (V^{5+} to V^{0+}). *Journal of Electron Spectroscopy and Related Phenomena* **135,** 167 –175 (2004).

280. Kobe Geryl. *Atomic layer deposition of vanadium oxides for lithium-ion batteries* Master's dissertation (Ghent University, 2014).

281. Wang, Y. *et al.* Design principles for solid-state lithium superionic conductors. *Nature Materials* **14,** 1026–1031 (2015).

282. Wriedt, H. A. The O-V (Oxygen-Vanadium) system. *Bulletin of Alloy Phase Diagrams* **10,** 271–277 (June 1989).

283. Huang, X. *et al.* Vanadium Pentoxide-Based Cathode Materials for Lithium-Ion Batteries: Morphology Control, Carbon Hybridization, and Cation Doping. *Particle & Particle Systems Characterization* **32,** 276–294 (Mar. 2015).

284. Jiang, J. *et al.* Recent Advances in Metal Oxide-based Electrode Architecture Design for Electrochemical Energy Storage. *Adv. Mater.* **24,** 5166–5180 (2012).

285. Musil, J. *et al.* Reactive magnetron sputtering of thin films: present status and trends. *Thin Solid Films* **475,** 208–218 (Mar. 2005).

286. Hanlon, T. J *et al.* Comparison between vanadium dioxide coatings on glass produced by sputtering, alkoxide and aqueous solgel methods. *Thin Solid Films* **405,** 234–237 (Feb. 2002).

287. Peter, A. P. *et al.* Metal-Insulator Transition in ALD VO_2 Ultrathin Films and Nanoparticles: Morphological Control. *Advanced Functional Materials* **25,** 679–686 (Feb. 2015).

288. Mendialdua, J., Casanova, R. & Barbaux, Y. XPS studies of V_2O_5, V_6O_{13}, VO_2 and V_2O_3. *J. Electron Spectrosc. Relat. Phenom.* **71,** 249–261 (Apr. 1995).

289. Leroux, C., Nihoul, G. & Van Tendeloo, G. From VO_2(B) to VO_2(R): Theoretical structures of VO_2 polymorphs and in situ electron microscopy. *Phys. Rev. B* **57,** 5111–5121 (9 1998).

290. Ebin, B., Battaglia, V. & Gürmen, S. Comparison of 4V and 3V electrochemical properties of nanocrystalline $LiMn_2O_4$ cathode particles in lithium ion batteries prepared by ultrasonic spray pyrolysis. *Ceramics International* **40,** 7029–7035 (June 2014).

291. SNE Research. *LIBs for EV-Technology Issue and Market Forecast (2011~2020)* tech. rep. (May 2013).

292. Zargouni, Y. *et al.* Electrodeposition and Characterization of Manganese Dioxide Thin Films on Silicon Pillar Arrays for 3D Thin-Film Lithium-Ion Batteries. *ECS Trans.* **61,** 29–41 (Aug. 2014).

293. Dobbelaere, T. *et al.* Plasma-Enhanced Atomic Layer Deposition of Iron and Titanium Phosphates as Electrode Materials for 3D-Structured Lithium-Ion Microbatteries. *ECS Trans.* **75,** 35–44 (Aug. 2016).

294. Xia, X. *et al.* Three-dimensional graphene and their integrated electrodes. *Nano Today* **9,** 785–807 (Dec. 2014).

295. Chao, D. *et al.* A V_2O_5/Conductive-Polymer Core/Shell Nanobelt Array on Three-Dimensional Graphite Foam: A High-Rate, Ultrastable, and Freestanding Cathode for Lithium-Ion Batteries. *Adv. Mat.* **26,** 5794–5800 (Sept. 2014).

296. Xia, X. *et al.* VO_2 nanoflake arrays for supercapacitor and Li-ion battery electrodes: performance enhancement by hydrogen molybdenum bronze as an efficient shell material. *Mater. Horiz.* **2,** 237–244 (2015).

297. Goodenough, J. B. & Kim, Y. Challenges for Rechargeable Li Batteries. *Chem. Mater.* **22,** 587–603 (Feb. 2010).

298. Kang, K. *et al.* Electrodes with High Power and High Capacity for Rechargeable Lithium Batteries. *Science* **311,** 977–980 (Feb. 2006).

299. Lu, Z., MacNeil, D. D. & Dahn, J. R. Layered $Li[Ni_xCo_{12x}Mn_x]O_2$ Cathode Materials for Lithium-Ion Batteries. *Electrochemical and Solid-State Letters* **4,** A200 (2001).

300. Rougier, A. Optimization of the Composition of the $Li_{1-z}Ni_{1+z}O_2$ Electrode Materials: Structural, Magnetic, and Electrochemical Studies. *Journal of The Electrochemical Society* **143,** 1168 (1996).

301. Rougier, A. *et al.* Effect of cobalt substitution on cationic distribution in $LiNi_{1-y}Co_yO_2$ electrode materials. *Solid State Ionics* **90,** 83–90 (Sept. 1996).

302. Zhou, T. *et al.* Surface Engineering and Design Strategy for Surface-Amorphized TiO_2 @Graphene Hybrids for High Power Li-Ion Battery Electrodes. *Advanced Science* **2,** 1500027 (Sept. 2015).

303. Manthiram, A., Kim, J. & Tsang, C. in *Materials for Electrochemical Energy Storage and Conversion Ii-Batteries, Capacitors and Fuel Cells* (eds Ginley, D. S. *et al.*) WOS:000075187200059, 421–426 (Materials Research Society, Warrendale, 1998).

304. LampeÖnnerud, C. *et al.* The Performance of Single-Phase V_6O_{13} in the Lithium/Polymer Electrolyte Battery. *J. Electrochem. Soc.* **142,** 3648–3651 (Nov. 1995).

305. Liu, H. *et al.* Design and synthesis of a novel nanothorn VO_2(B) hollow microsphere and their application in lithium-ion batteries. *J. Mater. Chem.* **19,** 2835–2840 (Apr. 2009).

306. Nethravathi, C. *et al.* N-Doped GrapheneVO_2(B) Nanosheet-Built 3D Flower Hybrid for Lithium Ion Battery. *ACS Appl. Mater. Interfaces* **5,** 2708–2714 (Apr. 2013).

307. Zhang, S. *et al.* Novel Flowerlike Metastable Vanadium Dioxide (B) Micronanostructures: Facile Synthesis and Application in Aqueous Lithium Ion Batteries. *J. Phys. Chem. C* **113,** 15058–15067 (Aug. 2009).

308. Li, G. *et al.* Synthesis of Urchin-like VO_2 Nanostructures Composed of Radially Aligned Nanobelts and Their Disassembly. *Inorg. Chem.* **48,** 1168–1172 (Feb. 2009).

309. Ren, G. *et al.* Vertically aligned VO_2(B) nanobelt forest and its three-dimensional structure on oriented graphene for energy storage. *J. Mater. Chem. A* **3,** 10787–10794 (May 2015).

310. Xie, M. *et al.* Stabilizing an amorphous V_2O_5/carbon nanotube paper electrode with conformal TiO_2 coating by atomic layer deposition for lithium ion batteries. *J. Mater. Chem. A* **4,** 537–544 (2016).

311. Koltypin, M. *et al.* The Study of Carbon-Coated V[sub 2]O[sub 5] Nanoparticles as a Potential Cathodic Material for Li Rechargeable Batteries. *Journal of The Electrochemical Society* **154,** A605 (2007).

312. McGraw, J. Next generation V_2O_5 cathode materials for Li rechargeable batteries. *Solid State Ionics* **113-115,** 407–413 (Dec. 1998).

313. Machida, N., Fuchida, R. & Minami, T. Behavior of Rapidly Quenched V_2O_5 Glass at Cathode in Lithium Cells. *J. Electrochem. Soc.* **136,** 2133–2136 (Aug. 1989).

314. Zhao, D. *et al.* Lithium Storage in Microstructures of Amorphous Mixed-Valence Vanadium Oxide as Anode Materials. *ChemSusChem* **8,** 2212–2222 (July 2015).

315. Zhao, D. *et al.* Amorphous Vanadium Oxide/Molybdenum Oxide Hybrid with Three-Dimensional Ordered Hierarchically Porous Structure as a High-Performance Li-Ion Battery Anode. *Chem. Mater.* **28,** 4180–4190 (June 2016).

316. McGraw, J. M. *et al.* Li Ion diffusion measurements in crystalline and amorphous V_2O_5 thin-film battery cathodes. *MRS Proceedings* **575** (Jan. 1999).

317. Dendooven, J. *et al.* Modeling the Conformality of Atomic Layer Deposition: The Effect of Sticking Probability. *J. Electrochem. Soc.* **156,** P63–P67 (Apr. 2009).

318. Cremers, V. *et al.* Monte Carlo simulations of atomic layer deposition on 3D large surface area structures: Required precursor exposure for pillar- versus hole-type structures. *Journal of Vacuum Science & Technology A: Vacuum, Surfaces, and Films* **35,** 01B115 (Jan. 2017).

319. Vetter, J. *et al.* Ageing mechanisms in lithium-ion batteries. *Journal of Power Sources* **147,** 269–281 (Sept. 2005).

320. Waldmann, T. *et al.* Temperature dependent ageing mechanisms in Lithium-ion batteries A Post-Mortem study. *Journal of Power Sources* **262,** 129–135 (Sept. 2014).

321. Barré, A. *et al.* A review on lithium-ion battery ageing mechanisms and estimations for automotive applications. *Journal of Power Sources* **241,** 680–689 (Nov. 2013).

322. Agubra, V. & Fergus, J. Lithium Ion Battery Anode Aging Mechanisms. *Materials* **6,** 1310–1325 (Mar. 2013).

323. Broussely, M. *et al.* Main aging mechanisms in Li ion batteries. *Journal of Power Sources* **146,** 90–96 (Aug. 2005).

324. Wohlfahrt-Mehrens, M, Vogler, C & Garche, J. Aging mechanisms of lithium cathode materials. *Journal of Power Sources* **127,** 58–64 (Mar. 2004).

325. Sarre, G., Blanchard, P. & Broussely, M. Aging of lithium-ion batteries. *Journal of Power Sources* **127,** 65–71 (Mar. 2004).

326. Broussely, M *et al.* Aging mechanism in Li ion cells and calendar life predictions. *Journal of Power Sources* **97-98,** 13–21 (July 2001).

327. Julien, C. *et al.* Surface modification of positive electrode materials for lithium-ion batteries. *Thin Solid Films* **572,** 200–207 (Dec. 2014).

328. Edström, K., Gustafsson, T. & Thomas, J. O. The cathodeelectrolyte interface in the Li-ion battery. *Electrochimica Acta. Polymer Batteries and Fuel Cells:Selection of Papers from First International Conference* **50,** 397–403 (Nov. 2004).

329. Ein-Eli, Y. A New Perspective on the Formation and Structure of the Solid Electrolyte Interface at the Graphite Anode of Li-Ion Cells. *Electrochem. Solid-State Lett.* **2,** 212–214 (1999).

330. Wang, D. *et al.* Atomic layer deposited coatings to significantly stabilize anodes for Li ion batteries: effects of coating thickness and the size of anode particles. *J. Mater. Chem. A* **2,** 2306–2312 (Jan. 2014).

331. Liu, X. H. *et al.* Anisotropic Swelling and Fracture of Silicon Nanowires during Lithiation. *Nano Lett.* **11,** 3312–3318 (Aug. 2011).

332. Liu, Y. *et al.* In Situ Transmission Electron Microscopy Observation of Pulverization of Aluminum Nanowires and Evolution of the Thin Surface Al_2O_3 Layers during LithiationDelithiation Cycles. *Nano Lett.* **11,** 4188–4194 (2011).

333. Chen, Z. *et al.* Role of surface coating on cathode materials for lithium-ion batteries. *J. Mater. Chem.* **20,** 7606–7612 (Aug. 2010).

334. Zuo, D. *et al.* Recent progress in surface coating of cathode materials for lithium ion secondary batteries. *Journal of Alloys and Compounds* **706,** 24–40 (June 2017).

335. Ahmed, B. *et al.* Surface Passivation of MoO_3 Nanorods by Atomic Layer Deposition toward High Rate Durable Li Ion Battery Anodes. *ACS Appl. Mater. Interfaces* **7,** 13154–13163 (June 2015).

336. Jung, Y. S. *et al.* Ultrathin Direct Atomic Layer Deposition on Composite Electrodes for Highly Durable and Safe Li-Ion Batteries. *Adv. Mater.* **22,** 2172–2176 (2010).

337. Woo, J. H. *et al.* Nanoscale Interface Modification of $LiCoO_2$ by Al_2O_3 Atomic Layer Deposition for Solid-State Li Batteries. *Journal of the Electrochemical Society* **159,** A1120–A1124 (Jan. 2012).

338. Kim, J. W. *et al.* Surface chemistry of $LiNi_{0.5}Mn_{1.5}O_4$ particles coated by Al_2O_3 using atomic layer deposition for lithium-ion batteries. *Journal of Power Sources* **274,** 1254–1262 (Jan. 2015).

339. Riley, L. A. *et al.* Electrochemical effects of ALD surface modification on combustion synthesized $LiNi_{1/3}Mn_{1/3}Co_{1/3}O_2$ as a layered-cathode material. *Journal of Power Sources* **196,** 3317–3324 (2011).

340. Kim, J. W. *et al.* Unexpected high power performance of atomic layer deposition coated $Li[Ni_{1/3}Mn_{1/3}Co_{1/3}]O_2$ cathodes. *Journal of Power Sources* **254,** 190–197 (2014).

341. Laskar, M. R. *et al.* Atomic Layer Deposition of $Al_2O_3Ga_2O_3$ Alloy Coatings for $Li[Ni_{0.5}Mn_{0.3}Co_{0.2}]O_2$ Cathode to Improve Rate Performance in Li-Ion Battery. *ACS Applied Materials & Interfaces* **8,** 10572–10580 (Apr. 2016).

342. Jackson, D. H. K. *et al.* Optimizing AlF_3 atomic layer deposition using trimethylaluminum and TaF_5: Application to high voltage Li-ion battery cathodes. *Journal of Vacuum Science & Technology A: Vacuum, Surfaces, and Films* **34,** 031503 (May 2016).

343. Jung, Y. S. *et al.* Effects of Atomic Layer Deposition of Al_2O_3 on the $Li[Li_{0.20}Mn_{0.54}Ni_{0.13}Co_{0.13}]O_2$ Cathode for Lithium-Ion Batteries. *J. Electrochem. Soc.* **158,** A1298–A1302 (Jan. 2011).

344. Zhang, X. *et al.* Structural and Electrochemical Study of Al_2O_3 and TiO_2 Coated $Li_{1.2}Ni_{0.13}Mn_{0.54}Co_{0.13}O_2$ Cathode Material Using ALD. *Adv. Energy Mater.* **3,** 1299–1307 (2013).

345. Zhao, J., Aziz, S. & Wang, Y. Hierarchical functional layers on high-capacity lithium-excess cathodes for superior lithium ion batteries. *Journal of Power Sources* **247,** 95–104 (Feb. 2014).

346. Yan, P. *et al.* Atomic to Nanoscale Investigation of Functionalities of an Al_2O_3 Coating Layer on a Cathode for Enhanced Battery Performance. *Chem. Mater.* **28,** 857–863 (Feb. 2016).

347. Zhao, J. & Wang, Y. Surface modifications of Li-ion battery electrodes with various ultrathin amphoteric oxide coatings for enhanced cycleability. *J Solid State Electrochem* **17,** 1049–1058 (Dec. 2012).

348. Xiao, X. *et al.* Atomic layer coating to mitigate capacity fading associated with manganese dissolution in lithium ion batteries. *Electrochemistry Communications* **32,** 31–34 (July 2013).

349. Wang, H.-Y. & Wang, F.-M. Electrochemical investigation of an artificial solid electrolyte interface for improving the cycle-ability of lithium ion batteries using an atomic layer deposition on a graphite electrode. *Journal of Power Sources* **233,** 1–5 (July 2013).

350. Kang, E. *et al.* Fe_3O_4 Nanoparticles Confined in Mesocellular Carbon Foam for High Performance Anode Materials for Lithium-Ion Batteries. *Adv. Funct. Mater.* **21,** 2430–2438 (July 2011).

351. Hu, T. *et al.* Porous Fe_2O_3 nanorods anchored on nitrogen-doped graphenes and ultrathin Al_2O_3 coating by atomic layer deposition for long-lived lithium ion battery anode. *Carbon* **76,** 141–147 (Sept. 2014).

352. Piper, D. M. *et al.* Reversible High-Capacity Si Nanocomposite Anodes for Lithium-ion Batteries Enabled by Molecular Layer Deposition. *Adv. Mater.* **26,** 1596–1601 (2014).

353. Ahn, D. & Xiao, X. Extended lithium titanate cycling potential window with near zero capacity loss. *Electrochemistry Communications* **13,** 796–799 (Aug. 2011).

354. Lee, J.-T. *et al.* Low-temperature atomic layer deposited Al_2O_3 thin film on layer structure cathode for enhanced cycleability in lithium-ion batteries. *Electrochimica Acta* **55,** 4002–4006 (Apr. 2010).

355. Cheng, H.-M. *et al.* Enhanced Cycleabity in Lithium Ion Batteries: Resulting from Atomic Layer Depostion of Al_2O_3 or TiO_2 on LiCoO2 Electrodes. *J. Phys. Chem. C* **116,** 7629–7637 (Apr. 2012).

356. Li, X. *et al.* Significant impact on cathode performance of lithium-ion batteries by precisely controlled metal oxide nanocoatings via atomic layer deposition. *Journal of Power Sources* **247,** 57–69 (Feb. 2014).

357. Park, J. S. *et al.* Ultrathin Lithium-Ion Conducting Coatings for Increased Interfacial Stability in High Voltage Lithium-Ion Batteries. *Chem. Mater.* **26,** 3128–3134 (2014).

358. Su, Y. *et al.* Enhancing the High-Voltage Cycling Performance of LiNio.5Mno.3Coo.2O2 by Retarding Its Interfacial Reaction with an Electrolyte by Atomic-Layer-Deposited Al_2O_3. *ACS Appl. Mater. Interfaces* **7,** 25105–25112 (Nov. 2015).

359. Guan, D., Jeevarajan, J. A. & Wang, Y. Enhanced cycleability of LiMn2O4 cathodes by atomic layer deposition of nanosized-thin Al_2O_3 coatings. *Nanoscale* **3,** 1465–1469 (Apr. 2011).

360. Guan, D. & Wang, Y. Ultrathin surface coatings to enhance cycling stability of LiMn2O4 cathode in lithium-ion batteries. *Ionics* **19,** 1–8 (Apr. 2012).

361. Kohandehghan, A. *et al.* Silicon nanowire lithium-ion battery anodes with ALD deposited TiN coatings demonstrate a major improvement in cycling performance. *J. Mater. Chem. A* **1,** 12850–12861 (Oct. 2013).

362. Liu, J. *et al.* Ultrathin atomic layer deposited ZrO_2 coating to enhance the electrochemical performance of $Li_4Ti_5O_{12}$ as an anode material. *Electrochimica Acta* **93,** 195–201 (2013).

363. Zhao, J. *et al.* Low temperature preparation of crystalline ZrO_2 coatings for improved elevated-temperature performances of Li-ion battery cathodes. *Chemical Communications* **48,** 8108 (2012).

364. Zhao, J. & Wang, Y. Atomic layer deposition of epitaxial ZrO_2 coating on $LiMn_2O_4$ nanoparticles for high-rate lithium ion batteries at elevated temperature. *Nano Energy* **2,** 882–889 (Sept. 2013).

365. Kong, J.-Z. *et al.* Enhanced electrochemical performance of $LiNi_{0.5}Co_{0.2}Mn_{0.3}O_2$ cathode material by ultrathin ZrO_2 coating. *Journal of Alloys and Compounds* **657,** 593–600 (Feb. 2016).

366. Yesibolati, N. *et al.* SnO_2 Anode Surface Passivation by Atomic Layer Deposited HfO_2 Improves Li-Ion Battery Performance. *Small* **10,** 2849–2858 (July 2014).

367. Lee, M.-L. *et al.* Atomic layer deposition of TiO_2 on negative electrode for lithium ion batteries. *Journal of Power Sources. 16th International Meeting on Lithium Batteries (IMLB)* **244,** 410–416 (Dec. 2013).

368. Lee, J.-H. *et al.* The effect of TiO_2 coating on the electrochemical performance of ZnO nanorod as the anode material for lithium-ion battery. *Appl. Phys. A* **102,** 545–550 (Nov. 2010).

369. Lotfabad, E. M. *et al.* ALD TiO_2 coated silicon nanowires for lithium ion battery anodes with enhanced cycling stability and coulombic efficiency. *Phys. Chem. Chem. Phys.* **15,** 13646–13657 (July 2013).

370. Kong, J.-Z. *et al.* Ultrathin ZnO coating for improved electrochemical performance of $LiNi_{0.5}Co_{0.2}Mn_{0.3}O_2$ cathode material. *Journal of Power Sources* **266,** 433–439 (Nov. 2014).

371. Kong, J.-Z. *et al.* Improved electrochemical performance of $Li_{1.2}Mn_{0.54}Ni_{0.13}Co_{0.13}O_2$ cathode material coated with ultrathin ZnO. *Journal of Alloys and Compounds* (Oct. 2016).

372. Ban, C. & George, S. M. Molecular Layer Deposition for Surface Modification of Lithium-Ion Battery Electrodes. *Adv. Mater. Interfaces,* n/a–n/a (2016).

373. Park, J. S. *et al.* Amorphous Metal Fluoride Passivation Coatings Prepared by Atomic Layer Deposition on $LiCoO_2$ for Li-Ion Batteries. *Chem. Mater.* **27,** 1917–1920 (2015).

374. Xiao, B. *et al.* Unravelling the Role of Electrochemically Active $FePO_4$ Coating by Atomic Layer Deposition for Increased High-Voltage Stability of $LiNi_{0.5}Mn_{1.5}O_4$ Cathode Material. *Adv. Sci.* **2,** n/a–n/a (2015).

375. Lin, C.-F. *et al.* Solid Electrolyte Lithium Phosphous Oxynitride as a Protective Nanocladding Layer for 3D High-Capacity Conversion Electrodes. *ACS Nano* **10,** 2693–2701 (Feb. 2016).

376. Nisula, M. & Karppinen, M. Atomic/Molecular Layer Deposition of Lithium Terephthalate Thin Films as High Rate Capability Li-Ion Battery Anodes. *Nano Lett.* (Jan. 2016).

377. Li, X. *et al.* Atomic layer deposition of solid-state electrolyte coated cathode materials with superior high-voltage cycling behavior for lithium ion battery application. *Energy Environ. Sci.* **7,** 768–778 (Jan. 2014).

378. Riley, L. A. *et al.* Improved Mechanical Integrity of ALD-Coated Composite Electrodes for Li-Ion Batteries. *Electrochem. Solid-State Lett.* **14,** A29–A31 (Mar. 2011).

379. Shim, J.-H. *et al.* Mixed Electronic and Ionic Conductor-Coated Cathode Material for High-Voltage Lithium Ion Battery. *ACS Appl. Mater. Interfaces* **8,** 12205–12210 (2016).

380. Aaltonen, T. *et al.* Atomic Layer Deposition of $Li_2OAl_2O_3$ Thin Films. *Chem. Mater.* **23,** 4669–4675 (Nov. 2011).

381. Aaltonen, T. *et al.* Lanthanum titanate and lithium lanthanum titanate thin films grown by atomic layer deposition. *J. Mater. Chem.* **20,** 2877–2881 (Mar. 2010).

382. Perng, Y.-C. *et al.* Synthesis of ion conducting $Li_xAl_ySi_zO$ thin films by atomic layer deposition. *J. Mater. Chem. A* **2,** 9566–9573 (June 2014).

383. Hu, Y. *et al.* Electrical characterization of amorphous $LiAlO_2$ thin films deposited by atomic layer deposition. *RSC Adv.* **6,** 60479–60486 (2016).

384. Hämäläinen, J. *et al.* Study of amorphous lithium silicate thin films grown by atomic layer deposition. *Journal of Vacuum Science & Technology A* **30,** 01A106 (Jan. 2012).

385. Hämäläinen, J. *et al.* Lithium Phosphate Thin Films Grown by Atomic Layer Deposition. *J. Electrochem. Soc.* **159,** A259–A263 (Jan. 2012).

386. Nisula, M. *et al.* Atomic Layer Deposition of Lithium Phosphorus Oxynitride. *Chem. Mater.* **27,** 6987–6993 (2015).

387. Cao, Y., Meng, X. & Elam, J. W. Atomic Layer Deposition of Li_xAl_yS Solid-State Electrolytes for Stabilizing Lithium-Metal Anodes. *ChemElectroChem* **3,** 858–863 (June 2016).

388. Liu, J. *et al.* Atomic layer deposited aluminium phosphate thin films on N-doped CNTs. *RSC Adv.* **3,** 4492–4495 (Mar. 2013).

389. Wang, B. *et al.* Atomic layer deposition of lithium phosphates as solid-state electrolytes for all-solid-state microbatteries. *Nanotechnology* **25,** 504007 (2014).

390. *Li-ion Cathode & Anode Electrode Sheets | NEI Corporation*

391. Li, Y. *et al.* Tuning electrochemical performance of Si-based anodes for lithium-ion batteries by employing atomic layer deposition alumina coating. *J. Mater. Chem. A* **2,** 11417–11425 (July 2014).

392. Aurbach, D. *et al.* Design of electrolyte solutions for Li and Li-ion batteries: a review. *Electrochimica Acta* **50,** 247–254 (Nov. 2004).

393. Moitzheim, S. *Comparison of Amorphous TiO_2 with Anatase Thin-Films Grown By ALD in Terms of Rate Performance and Capacity for Li^+-Insertion* in (Ecs, July 2015).

394. Landi, B. J. *et al.* Carbon nanotubes for lithium ion batteries. **2,** 638–654 (June 2009).

395. Basch, A. & Albering, J. H. Preparation and characterization of core-shell battery materials for Li-ion batteries manufactured by substrate induced coagulation. *J Power Sources* **196,** 3290–3295 (Mar. 2011).

396. Li, H. & Zhou, H. Enhancing the performances of Li-ion batteries by carbon-coating: present and future. **48,** 1201–1217 (Jan. 2012).

397. Yi, T.-F. *et al.* A review of recent developments in the surface modification of LiMn2O4 as cathode material of power lithium-ion battery. *Ionics* **15,** 779–784 (Dec. 2009).

398. Bates, J. B *et al.* Thin-film lithium and lithium-ion batteries. *Solid State Ionics. Proceedings of the 12th International Conference on Solid State* **135,** 33–45 (Nov. 2000).

399. Roberts, M. *et al.* 3D lithium ion batteriesfrom fundamentals to fabrication. *J. Mater. Chem.* **21,** 9876–9890 (June 2011).

400. Jiang, J. *et al.* Recent Advances in Metal Oxide-based Electrode Architecture Design for Electrochemical Energy Storage. *Advanced Materials* **24,** 5166–5180 (2012).

401. Leskelä, M. & Ritala, M. Atomic layer deposition (ALD): from precursors to thin film structures. *Thin Solid Films* **409,** 138–146 (Apr. 2002).

402. Chan, C. K. *et al.* Fast, Completely Reversible Li Insertion in Vanadium Pentoxide Nanoribbons. *Nano Lett.* **7,** 490–495 (Feb. 2007).

403. Fang, W.-C. & Fang, W.-L. Fast and reversible surface redox reduction in V_2O_5 dispersed on CNx nanotubes, 5236–5238 (Oct. 2008).

404. Coustier, F. Doped Vanadium Oxides as Host Materials for Lithium Intercalation. *Journal of The Electrochemical Society* **146,** 1355 (1999).

405. Livage, J. Vanadium pentoxide gels. *Chemistry of Materials* **3,** 578–593 (July 1991).

406. Potiron, E. *et al.* Electrochemically synthesized vanadium oxides as lithium insertion hosts. *Electrochimica Acta* **45,** 197–214 (Sept. 1999).

407. Shin, J. *et al.* Carbon-coated V_2O_5 nanoparticles with enhanced electrochemical performance as a cathode material for lithium ion batteries. *Journal of Alloys and Compounds* **589,** 322–329 (Mar. 2014).

408. Pan, A. *et al.* Synthesis of Hierarchical Three-Dimensional Vanadium Oxide Microstructures as High-Capacity Cathode Materials for Lithium-Ion Batteries. *ACS Applied Materials and Interfaces* **4,** 3874–3879 (2012).

409. Lipson, A. L. *et al.* Nanoscale Investigation of Solid Electrolyte Interphase Inhibition on Li-Ion Battery MnO Electrodes via Atomic Layer Deposition of Al_2O_3. *Chem. Mater.* **26,** 935–940 (Jan. 2014).

410. Jung, Y. S. *et al.* Enhanced Stability of LiCoO[sub 2] Cathodes in Lithium-Ion Batteries Using Surface Modification by Atomic Layer Deposition. *Journal of The Electrochemical Society* **157,** A75 (2010).

411. Chiodarelli, N. *et al.* Measuring the electrical resistivity and contact resistance of vertical carbon nanotube bundles for application as interconnects. *Nanotechnology* **22,** 085302 (Feb. 2011).

412. Deng, S. *et al.* Atomic layer deposition-based synthesis of photoactive TiO_2 nanoparticle chains by using carbon nanotubes as sacrificial templates. *RSC Advances* **4,** 11648 (2014).

413. Deng, S. *et al.* Porous nanostructured metal oxides synthesized through atomic layer deposition on a carbonaceous template followed by calcination. *J. Mater. Chem. A* **3,** 2642–2649 (2015).

414. Kurttepeli, M. *et al.* Synthesis and Characterization of Photoreactive TiO $_2$ Carbon Nanosheet Composites. *The Journal of Physical Chemistry C* **118,** 21031–21037 (Sept. 2014).

415. Borghols, W. J. H. *et al.* Lithium Storage in Amorphous TiO[sub 2] Nanoparticles. *Journal of The Electrochemical Society* **157,** A582 (2010).

416. Odani, A. *et al.* Testing Carbon-Coated VOx Prepared via Reaction under Autogenic Pressure at Elevated Temperature as Li-Insertion Materials. *Advanced Materials* **18,** 1431–1436 (June 2006).

417. Xiong, H. *et al.* Self-Improving Anode for Lithium-Ion Batteries Based on Amorphous to Cubic Phase Transition in TiO $_2$ Nanotubes. *The Journal of Physical Chemistry C* **116,** 3181–3187 (Feb. 2012).

418. González, J. R. *et al.* Relationships between the length of self-organized titania nanotube, adsorbed solvents and its electrochemical reaction with lithium. *Journal of Solid State Electrochemistry* **19,** 3013–3018 (Oct. 2015).

419. Miikkulainen, V. *et al.* Atomic Layer Deposition of Spinel Lithium Manganese Oxide by Film-Body-Controlled Lithium Incorporation for Thin-Film Lithium-Ion Batteries. *J. Phys. Chem. C* **118,** 1258–1268 (Jan. 2014).

ACKNOWLEDGEMENTS

I'd like to start the acknowledgement section with a quote from a famous inventor-scientist-engineer that lived in the 19th century, Thomas Edison. In February 1883, Edison published the following lines of text in The Electrician:

"The storage battery is, in my opinion, a catchpenny, a sensation, a mechanism for swindling the public by stock companies. The storage battery is one of those peculiar things which appeals to the imagination, and no more perfect thing could be desired by stock swindlers than that very selfsame thing... Just as soon as a man gets working on the secondary battery it brings out his latent capacity for lying... Scientifically, storage is all right, but, commercially, as absolute a failure as one can imagine."

I'd like to think the last couple of decades have proved him wrong, and that this work moves the truth just that little bit further from that idea. And that my work the past 5 years haven't brought out my *latent capacity for lying* too dramatically!

While my name is the one on the front cover of this booklet, none of this would have been possible without tremendous help and support. Behind every researcher is a battery of people (pun intended) for him to lean on, to learn from, to cooperate with and to draw support from. Here, I'd like to take the time to thank some people I've met along the road or that have helped me walk it.

First of all, I'd like to acknowledge my promotors, Christophe and Jolien, for enabling me to do this work, providing the infrastructure to do my work and the freedom to let my mind run free and explore what is truly a very small corner of the unexplored universe. On top of that, I'd like to thank them both especially for the tremendous help with writing the articles and reading through this work more than several times. If there's one thing I was taught that will stick around, it is how to incorporate the word *unicorn* in a work of this magnitude.

Secondly, working at the S1 would have been much more dull without the presence of some very nice colleagues. *All work and no play makes Jack a dull boy*, and all that. Thank you for providing a nice working environment to everyone in the department, and within cocoon especially. A special thanks goes out to Jan & Jevgenij for the shared passion for spirits, Filip &

The Electrician (London) Feb. 17, 1883, p. 329
It's true, go and find it!

Jeroen for providing terrible puns by the truckload, Kevin & Kilian for the plentiful Friday distractions and Delphine & Frank for the lovely dinners. Over the years, you all have become much more than colleagues, you've become true friends.

Of course, work is still work, but the work wouldn't get done without some help. I'd like to extend a word thanks to those that have aided me with the technical and scientific aspect of it. Stefaan, thanks for being such a great guy and a man that can get (almost) every done with a broad smile on your face. Davy and Geert, for solving most problems just by walking in the room (and walking in at the right time), and for solving the rest shortly after. Olivier, Nico, Matthias, Karl for helping with SEM and XPS measurements. I'm sure I'm forgetting plenty of people here, and that, if you owe my gratitude I don't always express it properly, but know that I do greatly appreciate every bit of help I get and got. A special work of thanks goes out here to my thesis students over the years, and one in particular: Kobe, you've done some great work during your thesis years, and I'm sure you'll recognize much of it here in some form. Good job, and thanks!

Life isn't just lived at the S1, no matter what your bosses might claim. I would like to thank my father and mother for always being there when I needed, and for being such great grandparents. Thank you Arthur, for broadening my horizon from time to time, and teaching me to appreciate the little things. A big thanks goes out to all my friends from Kortrijk, most of whom I've known for the better part of my life. It's great to unwind with a good beer, some gaming or just some solid conversation and laughter! Finally, I'd like to thank Nele, for the tremendous support she has been over the years, and for filling our house with the warmth I can't always give it. And thank you for being such an amazing mom to Lara. To Lara, I'd like to say this: never stop being as happy and as great as you are now! I love you both with all my heart!

To summarize, thank you all for your contributions, of for just being there for me in general. I couldn't have done this without you all!

Felix Mattelaer
March 31st, 2017